# RELATIONSHIP BETWEEN PROCESSING, STRUCTURE, AND PROPERTIES OF TITANIUM ALLOYS PRODUCED BY HYDROGEN SINTERING AND PHASE TRANSFORMATION (HSPT)

by

James D. Paramore

A dissertation submitted to the faculty of
The University of Utah
in partial fulfillment of the requirements for the degree of

Doctor of Philosophy

Department of Metallurgical Engineering

The University of Utah

December 2015

**The University of Utah Graduate School**

# STATEMENT OF THESIS APPROVAL

The dissertation of **James D. Paramore**

has been approved by the following supervisory committee members:

| | | |
|---|---|---|
| **Zhigang Zak Fang** | , Chair | **9/23/2015** Date Approved |
| **Ravi Chandran** | , Member | **9/23/2015** Date Approved |
| **Sivaraman Guruswamy** | , Member | **9/23/2015** Date Approved |
| **Mark C. Koopman** | , Member | **9/23/2015** Date Approved |
| **Don Li** | , Member | **9/24/2015** Date Approved |

and by **Manoranjan Misra** , Chair of the Department of **Metallurgical Engineering**

and by David B. Kieda, Dean of The Graduate School.

## ABSTRACT

In this dissertation, the process-structure-property relationships of titanium alloys, specifically Ti-6Al-4V, produced via hydrogen sintering and phase transformation (HSPT) is investigated. HSPT is a low-cost, blended elemental (BE), press-and-sinter process for producing titanium alloys that have mechanical properties that are competitive with wrought titanium alloys. Throughout this dissertation, the wrought-like microstructures that are possible by utilizing HSPT with other low-cost postsintering thermal processes, such as solution treatment and ageing (STA) heat treatments, are discussed. Additionally, the exceptional mechanical properties that result from the range of microstructures produced are presented.

Currently, wrought processing is the state of the art for producing titanium alloys with the mechanical properties necessary for critical applications. However, wrought processing employs multiple steps of energy-intensive thermomechanical processing (TMP) to both form the shaped products and refine the microstructure. In fact, the majority of cost associated with many titanium products on the market today stems from TMP. Powder metallurgy (PM) has long been sought as a low-cost alternative to wrought processing, owing to its near-net-shape capabilities. However, traditional PM titanium has mechanical properties that are insufficient for many critical applications. In this dissertation, it is shown that HSPT is capable of producing wrought-like microstructures and mechanical properties without resorting to energy-intensive processes such as

pressure-assisted sintering or TMP, which is compulsory for other processing routes.

The as-sintered microstructure and mechanical properties of HSPT Ti-6Al-4V are discussed and compared with wrought and traditional PM Ti-6Al-4V. Additionally, the as-sintered HSPT Ti-6Al-4V was processed with a range of low-cost thermal processing techniques to produce a range of wrought-like microstructures and mechanical properties. Therefore, it is shown that HSPT is capable of producing different microstructures that have been engineered to meet the application-tailored demands for mechanical properties of titanium alloys. Additionally, the physical metallurgical principles and mechanisms behind these capabilities are discussed. The impetus for this research was the development of a low-cost process to produce high-performance titanium alloys. Therefore, a quantitative energy model, which was developed by the author, of the HSPT process is also presented.

**TABLE OF CONTENTS**

## LIST OF TABLES

Tables

## ACKNOWLEDGMENTS

First and foremost, I would like to thank Professor Z. Zak Fang for his years of mentorship, support, and encouragement. Prof. Fang taught the first lecture of the first class that I ever took in this field and hired me as an undergraduate researcher that same year. Prof. Fang's unique teaching style and highly personable nature is the reason I was able to excel in this field. In addition to his invaluable guidance he gave me as an undergraduate, he afforded me opportunities and trusted me with responsibilities far beyond what professors typically provide their undergraduate assistants. After finishing my master's degree at MIT, I went to work for the U.S. Army Research Laboratory in Maryland. However, after a couple of years working as an engineer, Prof. Fang convinced me to sacrifice my very comfortable salary to join his group again in pursuit of my PhD. Now, many packs of ramen noodles later, I am exceedingly grateful for his encouragement and never-ending support.

I would also like to thank Prof. K.S. Ravi Chandran for his guidance during my doctoral studies. Prof. Chandran was a P.I. on my research project as well as a member of my thesis committee. His knowledge of titanium physical metallurgy and honest guidance and comments were very helpful. I would also like to thank Prof. Mark Koopman, who managed this project, guided me on a daily basis in my research, and always had a hilarious story to entertain me with. Without his constant hard work and advice, our project would never have reached its full potential. Also on my committee was Prof. Siva Guruswamy,

who is probably one of the best educators I have ever had the pleasure of teaching me. I always looked forward to his lectures as both an undergraduate and a graduate student, and he never failed to bewilder me with his vast knowledge of metallurgy. Finally, I would like to thank Dr. Don Li, who joined my committee at the last moment due to scheduling conflicts with another member. I cannot express enough my gratitude for his selfless willingness to take on this unobligated task on such short notice and the invaluable advice he has contributed to my research.

I also want to thank all of my colleagues who provided me countless hours of support and comradery both in the lab and outside of it. I want to specifically express my appreciation to Matt Dunstan, who nearly sacrificed a limb helping me to polish hundreds of fatigue bars, and for being a great friend these last few years. I also want to thank Pei Sun for his constant willingness to go out of way to help with whatever task was at hand. I want to thank Brady Butler of the United States Army Research Laboratory, a fellow alum of our department and very close friend, who provided hours of support, advice, and help in pursuit of this degree, not to mention his years of unmatched loyalty and true friendship. Finally, I would like to thank all of my other lab mates who helped immensely with this project: Lu Yang, Pankaj Kumar, Fei Cao, Andrew Jamieson, and Gustavo Saboia Silveira, just to name a few.

I come from a truly excellent household with a family whose love and care are unmatched in this world. My parents provided me with an almost unbelievable childhood and prepared me for nothing but success in this world. As a child, my father would wake up before 5 A.M. to cook us a full, hot breakfast, every single day. At lunch, I would go to my grandfather's house every day from elementary school for a hot lunch. Then, my

mother would come home from work every night and prepare a family meal. My parents worked tirelessly to bestow family values and work ethic into every one of their children. I got my technical brain from my father, my book smarts and sense of humor from my mother, and no form of laziness from either of them. I live a truly blessed life, and I have my family to thank for it. To this day, I live with a constant sense of security, because I know that my parents are always there to help me with any unexpected hurdle life throws my way.

Last and certainly not least, I need to thank my beautiful girlfriend, who makes life worth living and brightens every moment. She has made countless sacrifices for me over the last 8 years in my pursuit of education. She has moved over 2,000 miles away from her family for years at a time not once, but twice, to support me in my endeavors. She has put her own goals on hold so I could pursue mine, and she has been my biggest supporter the entire time. I cannot imagine life without her, and I am forever grateful for every moment I get to spend with her.

Finally, I would like to acknowledge the funding and support that made this research possible. My research project was funded by the US Department of Energy, Innovative Manufacturing Initiative (DEEE0005761), through the Advanced Manufacturing Office and the Office of Energy Efficiency and Renewable Energy. Titanium hydride and master alloy powders were provided by Reading Alloys (AMETEK). Lastly, the United States Army Research Laboratory was an invaluable partner during this research project, providing valuable insight as well as access to microscopy and X-ray diffraction equipment.

# CHAPTER 1

# INTRODUCTION

## 1.1 Background

The goal of this dissertation is to determine the relationship between processing, structure, and properties of titanium alloys that are produced by hydrogen sintering and phase transformation (HSPT). This process has been under active research at the University of Utah as well as the United State Army Research Laboratory (ARL) for about 5 years. Therefore, the concept of HSPT being a viable methodology for the production of low-cost titanium alloys that meet the strict standards for structural titanium alloys has been proven. However, fundamental understanding of the mechanisms behind HSPT is still being developed. This knowledge has important implications not only for this burgeoning process, but also for titanium metallurgy as a whole.

HSPT is a blended elemental (BE), powder metallurgy (PM), press and sinter process for the production of titanium alloys[1–17]. During this process, compacts of hydrogenated titanium, metallic titanium, and/or master alloy powders are sintered under a dynamically controlled hydrogen partial pressure. The use of hydrogenated powder and the presence of hydrogen in solution during sintering has been shown in several studies to significantly improve purity and densification of PM titanium alloys[17–22]. However, HSPT differs from other PM processes in that a dynamically controlled hydrogen partial pressure is used to

control the hydrogen content within the alloy during sintering. This is done as a means to refine the microstructure during sintering via phase transformations in the Ti-H alloy systems. The goal of HSPT is to produce engineered microstructures and application-tailored mechanical properties in the as-sintered state, thereby eliminating thermomechanical processing (TMP) compulsory to traditional titanium processing routes.

Figure 1.1 is a theoretical flow sheet of processing steps necessary to produce titanium alloys with high strength and ductility via melt-wrought processing, traditional PM, and HSPT. PM has long been sought as a means to decrease the cost of titanium alloys[23]. As a convention, titanium PM can be grouped into two generalized processes: blended elemental (BE) and pre-alloyed (PA). In BE processing, the desired alloy chemistry is obtained by mechanical mixing powders of the parent metal (i.e. titanium) with powders of the required alloy constituents. During PA processing, as the name suggests, some type of pyrometallurgical process is utilized during power production to produce the desired alloy in powder form[14]. PA generally produces better mechanical properties, but the PA powders tend to be relatively expensive due to the energy-intensive processes that are required. Additionally, pre-alloyed powders are inherently hard and difficult to press, meaning high temperature compaction methods, such as hot isostatic pressing (HIP), are generally required with PA powders. On the other hand, BE titanium alloys tend to have relatively poor mechanical properties in the as-sintered state due to high interstitial concentrations, residual porosity, and undesirable microstructures[14,23–25]. These properties can be improved through the implementation of special powder handling techniques to minimize oxygen content, pressure-assisted sintering such as HIPing to improve densification, and thermo-mechanical work after sintering to close porosity and refine the

microstructure through recrystalization[25]. However, these additional processing steps tend to be energy-intensive and increase cost. Therefore, the goal of HSPT is to maximize the performance-to-cost ratio of titanium by eliminating the need for these types of processing steps in a BE process[14]. Finally, in other PM titanium processes vacuum is the preferred sintering atmosphere[26], limiting sintering to a batch process. Conversely, HSPT can be conducted at atmospheric pressure. Because of this, the possibility exists for HSPT to be commercialized as a continuous process.

HSPT should not be confused with hydrogen sintering processes used commercially for other alloy systems such as steels, tungsten alloys, etc. During sintering of these alloys, hydrogen is chosen for its reducing character[27]. However, titanium lies below hydrogen on the Ellingham diagram[28]. As such, hydrogen is not a viable reducing agent for titanium and plays a very different role in HSPT. As mentioned above, the hydrogen partial pressure is used to control the hydrogen content within the titanium alloy during sintering. Because the phase equilibria and transformation kinetics of titanium alloys varies as a function of hydrogen content, the hydrogen partial pressure is employed as an additional parameter to control microstructural evolution during sintering and heat treatments. The mechanisms and implications of these phenomena are discussed in this dissertation.

As mentioned above, the overall goal of HSPT research is to maximize the performance-to-cost ratio of titanium alloys. Up to 90% of the cost associated with typical titanium products result from the energy intensive and low-yield thermo-mechanical steps necessary for wrought processing[29–33]. HSPT aims to produce titanium alloys via PM, an inherently low-cost means of metals production, while achieving the superior properties of wrought titanium alloys. Because of this, a quantitative energy model has also been

developed to investigate the potential cost savings of HSPT versus wrought process. This model has predicted a significant decrease in energy required per ton of titanium alloy produced. The results of the energy model are presented in CHAPTER 3. Additionally, this dissertation will present HSPT's ability to produce titanium alloys that not only meet but often exceed the mechanical properties of titanium alloys produced via wrought processing.

## 1.2 Research Scope and Objectives

The ability of HSPT to produce ultrafine grained (UFG) microstructures and exceptional static mechanical properties in the as-sintered state had been previously demonstrated[1,8,15,17]. However, it has been hypothesized that the as-sintered microstructure may be further heat treated to produce a range of wrought-like microstructures via simple heat treatments and thermal processing. Therefore, the goal of this research is to understand the process-structure-property relationship of Ti-6Al-4V produced via HSPT and subsequent thermal processing. These properties will be compared with those produced by the conventional processes of wrought processing and traditional powder metallurgy. Additionally, because the motivation for this research is the development of a low-cost alternative to wrought process, it is necessary to evaluate the energy-saving potential of this process via a quantitative energy model. Therefore, this research has a three prong approach:

(1) Develop a quantitative energy model of the HSPT process as well as a typical wrought process to determine the potential energy and cost savings of the HSPT process compared with traditional titanium production technologies

(2) Determine the relationship between processing and microstructure of both HSPT and vacuum-sintered Ti-6Al-4V and the mechanisms by which the microstructure evolves

(3) Determine the relationship between microstructure and mechanical properties of HSPT and vacuum-sintered Ti-6Al-4V with various microstructures, including the mechanisms behind the strength, ductility, and failure

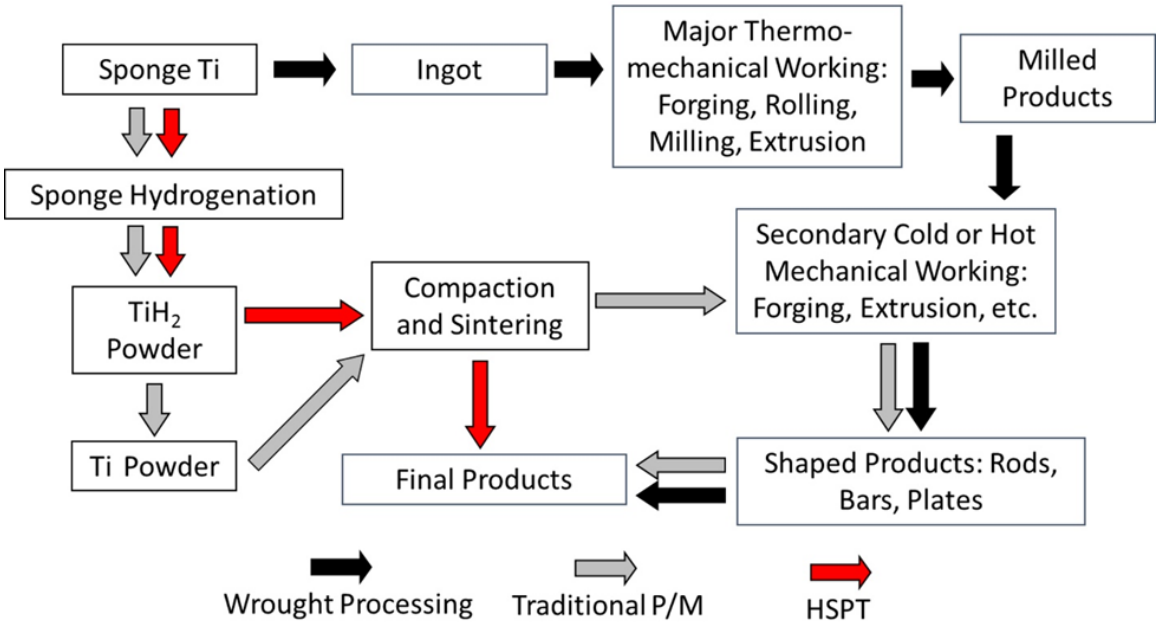


Figure 1.1: Flow sheet of a titanium melt-wrought process, a traditional PM process, and the HSPT process.

# CHAPTER 2

# BACKGROUND AND LITERATURE REVIEW

Understanding the thermodynamics and kinetics of the hydrogenation reactions as well as the phase transformations that occur in hydrogen-containing titanium alloys is necessary to explain the unique structures and properties that are available via HSPT. Therefore, this chapter will focus on the history of using hydrogen in titanium processing as well as the thermodynamics and kinetics of reactions that occur during HSPT processing and traditional titanium processing. Additionally, the process-structure-property relationships, as reported in the literature, of α+β titanium alloys such as Ti-6Al-4V will be summarized.

## 2.1 Brief Description of Titanium Alloys and Phases

In general, titanium alloys have two main phases: α phase and β phase. The α phase has a hexagonal close-packed (HCP) crystal structure. The β phase, on the other hand, has a body-centered cubic (BCC) crystal structure. Of these two phases, α tends to be the softer phase while β tends to the stronger yet less ductile phase[34–37]. In addition to these two main phases, there are two other phases which will be discussed in this dissertation. If the hydrogen content of titanium is sufficiently high, the δ hydride phase will form[38]. The δ phase has a face centered cubic (FCC) crystal structure but is extremely brittle. Lastly, if the α phase becomes supersaturated with aluminum, it will form a brittle intermetallic

phase called $\alpha_2$ with the chemical formula $Ti_3Al$. This is also an HCP phase with a crystal structure very similar to α, but with a highly ordered structure due to the high fraction of aluminum[34–37].

To date, HSPT research has focused on two alloy systems: commercially pure titanium (CP-Ti) and Ti-6Al-4V. However, the results presented in this dissertation are limited to Ti-6Al-4V, which is by far the most common commercial alloy. In general, titanium alloys are classified by the primary phases present when the alloy is in use. The three general classes of titanium alloys are α/near-α alloys, α+β alloys, and β alloys. The class of alloy is determine by the alloying elements. Alloys with a large fraction of β stabilizers (e.g. Mo or V) will form structures of primarily β grains, alloys with a large fraction of α stabilizers (e.g. Al or O) will form structures of primarily α grains, and alloys with balanced fractions of α and β stabilizers will form structures with α and β grains[34–37]. Because Ti-6Al-4V is an α+β alloy, the process-structure-property relationships of α+β alloys will be discussed in this dissertation.

## 2.2 History of Using Hydrogen in Titanium Processing

Hydrogen embrittles titanium and is, therefore, generally an undesirable component in titanium alloys. However, because of rapid diffusion and the reversible nature of the hydrogenation reaction, hydrogen can be easily removed by annealing under vacuum or an inert gas atmosphere. Additionally, the presence of hydrogen can result in benefits with regards to sintering and phase evolution during heat treatments. As such, there is a long history of using hydrogen in titanium processing.

### 2.2.1 History of Using Hydrogenated Titanium in a Powder Metallurgy Process

The hydride-dehydride (HDH) process is a well-known, commercial process for titanium powder production. HDH takes advantage of the brittleness of titanium hydride to improve comminution behavior in powder production[39]. However, hydrogenated titanium is also employed in sintering processes. The use of hydrogenated titanium versus metallic titanium results in better control of oxygen content in the sintered sample[40,41]. Additionally, titanium hydride exhibits exceptional compaction behavior, resulting in excellent green density and green strength[17,42]. Finally, densification during sintering is significantly improved when hydrogenated titanium powder is used[43]. For these reasons, there is a long history of hydrogenated titanium being used as the feedstock material for a sintering process.

The first patent to use hydrogenated titanium in a sintering process, filed by Gregory, dates back nearly 50 years to 1967[44]. This patent describes a method in which titanium hydride powder is used in the production of niobium-based superconductor alloys. Shortly afterwards, a process to produce titanium alloys and metal matrix composites using titanium hydride powder was developed at the United States Army Materials and Mechanics Research Center. This process was called “decomposition powder metallurgy” and was first reported in 1970 by Greenspan et al. as a means to produce titanium alloys and metal matrix composites via hot pressing[45,46]. The first press and sinter process to produce titanium alloys from titanium hydride was patented by the Japanese team of Obara et al. in 1974[47]. In the Japanese process, sintering was achieved under vacuum or inert gas atmospheres. Following these pioneering publications and patents, a wide variety of processes have been published and/or patented that use hydrogenated titanium powder.

These processes include both pressure-assisted (i.e. hot pressing or hot isostatic pressing) as well as press and sinter methods, and have been used to produce a range of products including titanium alloys[42,48–54], sputtering targets[55], decorative titanium products[56], and shape memory alloys[57]. Since 2000, a significant amount of work regarding vacuum sintering of hydrogenated titanium powder has been reported by Ivasishin et al.[18,19,22,40,43,58–61]. This work has led to a series of processes developed and commercialized by an Ohio-based company called The Advanced Material Group (ADMA). ADMA has patented several processes for the production of hydrogenated titanium powder as well as vacuum sintering of these powders to produce titanium alloys and metal matrix composites[41,62–66].

### 2.2.2 Thermohydrogen Processing (THP) of Titanium Alloys

Utilizing the phase transformations in the Ti-H system as a means to refine microstructure and improve mechanical properties of titanium alloys has a history in the literature as well. Thermo-hydrogen processing (THP) and thermo-chemical processing are the names given to a group of processes during which hydrogen is used as a temporary alloying element. In some processes, hydrogen is used to improve the workability of titanium. In others, THP utilizes the phase transformations in the Ti-H system to refine the microstructure of titanium alloys. During THP, bulk titanium alloys are hydrogenated, subjected to heat treatments and/or hot working, and subsequently dehydrogenated.

The use of hydrogen as a temporary alloying element was first patented in 1959 by Zwicker et al. as a means to improve the workability and deformability of titanium during hot working[67]. The first studies to investigate THP as a means to refine microstructure via

phase transformations and the effect on mechanical properties were conducted by Kerr et al. in the late 1970s and early 1980s[68,69]. Since then, many investigations of THP have been published[70–91], including a review paper by Froes et al. published in 2004[92]. THP has been used on both wrought material and sintered PM material as a means to refine the microstructure and improve mechanical properties. Across these studies, THP consistently increased strength in both wrought and PM titanium. In some studies, the increase in strength was accompanied by a decrease in ductility[70,71,73,88,90,91]. However, other studies reported an increase in strength as well as ductility[69,79,84].

## 2.3 Thermodynamics and Kinetics of Ti(alloy)-H Phase Transformations

The phase equilibria and transformation kinetics of hydrogen-containing titanium alloys are strongly dependent on the hydrogen concentration during processing. Additionally, the hydrogen concentration is strongly dependent on both temperature and partial pressure of hydrogen in the atmosphere. Therefore, understanding how the hydrogen concentration varies during a thermal treatment, such as sintering or heat treating, and then understanding how this, in turn, affects the phase evolution of the alloy is necessary to explain the microstructures that are produced via HSPT.

### 2.3.1 Ti-H Phase Diagram

When studying the Ti-H phase diagram (Figure 2.1)[38], one realizes it bears a resemblance to the Fe-C system. In particular, the Ti-H system has a eutectoid reaction similar to the famous eutectoid reaction that is responsible for the vast array of steel microstructures available from the Fe-C system. As mentioned in the previous section,

these phase transformations were the motivation for THP research. A hypothesis and concept was thus proposed that the effects of hydrogen on phase transformations could be incorporated in sintering of titanium to control microstructural evolution during sintering. This was the intellectual basis around which the HSPT processed was developed.

As mentioned above, the Ti-H system contains a eutectoid transformation. Therefore, when cooling a Ti-H alloy below the eutectoid temperature at a controlled rate and with a controlled concentration of hydrogen in the system, a eutectoid decomposition of the β-phase will occur. If this is done at a sufficient rate, a high degree of undercooling will provide significant driving force to precipitate α-Ti and δ-$TiH_2$, but limit grain growth in the new phases. Other phase transformations are also possible, such as the formation of pro-eutectoid α and pro-eutectoid δ-$TiH_2$ for hypoeutectoid and hypereutectoid compositions, respectively. Additionally, $\alpha_2$-$Ti_3Al$ will precipitate if the temperature is held below the $\alpha_2$ solvus temperature[34], or if α becomes supersaturated with aluminum[34] due to large volume fractions of β and δ-$TiH_2$ caused by the presence of hydrogen. Because hydrogen is a β stabilizer, the volume fractions of β and δ-$TiH_2$ are directly related to hydrogen concentration[5]. Additionally, this also means the β-transus temperature is dependent on the hydrogen concentration. Therefore, all of these phase transformations may be controlled by adjusting the hydrogen concentration as a function of temperature and hydrogen partial pressure in the atmosphere during sintering and subsequent cooling.

### 2.3.2 Controlling Hydrogen Concentration Within Titanium

The hydrogen concentration within titanium changes as a function of both temperature and hydrogen partial pressure. As an example, the equilibrium hydrogen partial pressure of β-Ti(H) (β phase with dissolved hydrogen) is given in Eq. 2.1. In this equation, $p_{H_2}$ is

the equilibrium partial pressure of hydrogen, *C* is the H/Ti ratio, and *T* is absolute temperature[93].

$$\ln\left(p_{H_2}\right) = 15.84 + 0.7C + 2\ln\left(\frac{C}{2-C}\right) - \frac{16.0 \times 10^3}{T} \qquad \text{Eq. 2.1}$$

Because hydrogen is a volatile alloying element, using the phase diagram to design heat treatments is not as straightforward for Ti-H as it is with other eutectoid systems, such as Fe-C. To subject a steel specimen to a purely eutectoid reaction, one would simply prepare an alloy of the eutectoid composition, austenitize the material by holding above the eutectoid temperature, and then cool the material below the eutectoid temperature. However, because the composition of the Ti-H system is dependent on hydrogen partial pressure, the phase equilibria and transformation kinetics change as a function of hydrogen partial pressure as well as temperature. Therefore, controlling phase transformations in the Ti-H system requires dynamic control of the atmosphere in addition to temperature.

> **Example**: Assume a titanium specimen was held above the eutectoid temperature in the β-Ti(H) phase field under a hydrogen partial pressure and temperature that corresponded to the eutectoid composition. Upon cooling, the hydrogen concentration within the specimen would increase if the atmosphere was unchanged. Therefore, a cooling curve superimposed on the phase diagram would fall to the right of the eutectoid point, and pro-eutectoid δ-$TiH_2$ would form. If it was desired that the cooling curve passed through the eutectoid point to produce a fully eutectoid reaction, the hydrogen partial pressure must be simultaneously decreased with temperature to maintain the eutectoid composition during cooling.

This additional process parameter, coupled with the rapid diffusion rates of hydrogen,

is a unique advantage to working with the Ti-H system. While this certainly makes designing a process more complicated, it also offers an additional degree of freedom to control the microstructural evolution during sintering and heat treatments. Gas carburization of steel is an analogous phenomenon[94]. However, the relatively slow diffusion kinetics of carbon in steel limit that process to surface treatments, and the carbon is not a temporary alloying element. Because the diffusion of hydrogen in titanium is rapid, processes such as HSPT are capable of engineering bulk properties of titanium alloys.

### 2.3.3 Pseudo-Binary Phase Diagram for Ti-6Al-4V-xH

The phase diagram shown in Figure 2.1 is only valid as a reference for unalloyed titanium. In order to fully understand and predict the phase transformations of an alloy during HSPT, such as Ti-6Al-4V, one needs a pseudo-binary phase diagram. In such a diagram, the abscissa is the hydrogen concentration within the alloy and the origin represents the pure alloy free of hydrogen. It is important to realize that in actuality a pseudo-binary phase diagram represents a system with more than two components. Therefore, by Gibb's Phase Rule, the number of phases possible in each field is increased by the number of additional components in the alloy beyond titanium and hydrogen. As an example, the (Ti-6Al-4V)-H diagram can have phase fields with four phases in equilibrium.

Since the 1980s, several studies have endeavored to generate the (Ti-6Al-4V)-H pseudo-binary phase diagram as a reference tool for thermo-hydrogen processing (THP) studies[68,75,83,95]. However, generating such a phase diagram is difficult, resulting in contradictory findings between the publications. As mentioned above, the equilibrium concentration of hydrogen within the alloy varies as a function of temperature and pressure,

meaning care must be taken to determine the instantaneous concentration of hydrogen within the alloy at a given temperature. One study endeavored to stabilize the hydrogen concentration by oxidizing the sample surface after hydrogenation to create a hydrogen diffusion barrier[83]. However, the rapid diffusion of hydrogen in titanium would likely result in an appreciable degree of dehydrogenation during the oxidation step. Additionally, when small samples are studied, oxygen, which is an α stabilizer, will diffuse into the sample at high temperatures and affect the phase transformations. Furthermore, quenching is not a viable solution to this problem due to the rapid diffusion. Therefore, even with quenching, the actual resulting hydrogen concentration is difficult to control. Lastly, rapid phase changes during cooling make observation of the high-temperature phases very difficult without in-situ methods.

To address the difficulty in obtaining a reliable phase diagram and the contradictory findings in the literature for the (Ti-6Al-4V)-H system, extensive experimentation was performed by the author's research group to observe the real-time phase evolution of this system as a function of temperature and hydrogen concentration. These data were then used to produce an improved (Ti-6Al-4V)-H phase diagram. These results were a main topic in the doctoral dissertation of the author's colleague, Pei Sun[6]. Therefore, these results will only be briefly summarized in this dissertation.

To observe the phase evolution in (Ti-6Al-4V)-H, experiments were performed using in-situ X-ray diffraction (XRD). A custom designed tube furnace with atmospheric control was installed in the beamline of the synchrotron at the Advanced Photon Source (Beamline 11-ID-C) located at Argonne National Lab. The increased resolution of the synchrotron was necessary to effectively differentiate between α-Ti and $\alpha_2$-$Ti_3Al$ peaks, which lie

nearly on top of one another on the diffractogram. Complimentary experiments were also conducted using a Panalytical X-ray diffractometer with an installed hot-stage at the Army Research Laboratory by the author. Additionally, extensive experimentation was performed using thermogravimetric analysis (TGA) and differential scanning calorimetry (DSC). By combining the real-time XRD phase data with the equilibrium hydrogen concentration data from TGA, an updated pseudo-binary phase diagram has been generated. The results of these experiments were published in 2015 and are presented as an improved pseudo-binary phase diagram in Figure 2.2[5].

#### 2.3.3.1 Phase Transformations during HSPT

For convenience, the phase transformation thermodynamics and kinetics of the Ti-H alloy systems are discussed in this chapter in the context of the eutectoid reaction. However, as shown in Figure 2.2, the actual phase transformations that occur during the HSPT process are much more complicated than a simple eutectoid reaction. In fact, the majority of the microstructural refinement produced by the HSPT process is achieved at a temperature above which the eutectoid reaction occurs. The actual phase evolution during vacuum sintering and the HSPT process of the Ti-6Al-4V-H system are outlined as dashed lines on Figure 2.2. The thermal processes used to produce these phase transformations are discussed in CHAPTER 4.

### 2.3.4 Phase Transformation Kinetics

Another important consideration regarding microstructural evolution during HSPT is the kinetics of the phase transformations. It has been reported that the kinetics of the phase transformations in (Ti-6Al-4V)-H change as a function of hydrogen concentration. Qazi

et al. reported that for the time-temperature-transformation (TTT) curve of the eutectoid reaction the nose temperature is decreased linearly with hydrogen concentration (Eq. 2.2) and the nose time is increased proportional to the square of the hydrogen concentration (Eq. 2.3)[83]. Therefore, as hydrogen concentration is increased, the kinetics slow and the degree of undercooling required to maximize kinetics is increased.

$$T_N = 731 - 5.0C_H \quad \text{Eq. 2.2}$$

$$t_N = 2.8(C_H)^2 \quad \text{Eq. 2.3}$$

The dependence of hydrogen concentration on temperature and atmosphere adds an additional degree of complication to the problem of kinetics as well. If the hydrogen partial pressure is held constant, according to Eq. 2.1, the hydrogen concentration in titanium is increased as the temperature is decreased. However, as the hydrogen concentration is increased, the nose temperature of the TTT curve is simultaneously decreased. Therefore, when trying to identify the temperature at which transformation kinetics are maximized, one is chasing a moving target. To overcome this complication and determine the temperature at which transformation kinetics are maximized, a curve for the hydrogen concentration as a function of temperature at a constant hydrogen partial pressure (Figure 2.3-A) and a curve for the nose temperature as a function of hydrogen concentration (Figure 2.3-B) are needed. The intersection of these two curves would indicate the temperature at which transformation kinetics are maximized for a given hydrogen partial pressure (Figure 2.3-C).

### 2.4 The Hydrogen Sintering and Phase Transformation (HSPT) Process

As mentioned above, the HSPT process was originally developed at the University of Utah and has been under investigation at the University of Utah and the United States Army Research Laboratory for over five years[1,2,5,8,13,15,17]. The HSPT process is a main topic of this dissertation. Therefore, in this section, a general description of the HSPT process and the underlying theory behind this process are presented. Further information regarding the specific experimental parameters used in this study are available in CHAPTER 4.

Figure 2.4 shows a schematic representation of a typical HSPT sintering profile. For the reader's convenience, the phase evolution of Ti-6Al-4V during sintering via the HSPT process versus traditional vacuum sintering are shown as red and blue lines, respectively, on the pseudo-binary phase diagram given in Figure 2.5. During HSPT, the partial pressure of hydrogen is dynamically controlled throughout the thermal cycle. The desired hydrogen partial pressure is produced either by mixing hydrogen gas with an inert gas at atmospheric pressure or by creating a partial vacuum on a pure hydrogen atmosphere. The thermal profile for an HSPT process consists of three general steps, detailed below:

Step 1 – Sintering: During this step, sintering is achieved at a temperature above the β-transus (1000~1300°C) and a relatively high hydrogen partial pressure, generally 1~100 kPa (0.1~1 atm). Higher hydrogen partial pressures, up to 1 MPa (10 atm), can be used to increase hydrogen content at the sintering temperature, but this is generally not required. At these temperatures and pressures, the material is entirely β-Ti(H), β phase with dissolved hydrogen. The high temperature and presence of hydrogen in solution during this step facilitates near full densification, resulting in less than 1 vol% porosity after sintering.

Step 2 – Homogenization and Phase Transformation: The second step in HSPT refines

the microstructure by taking advantage of phase transformations present in Ti(alloy)-H phase diagrams. During this step, the hydrogen partial pressure is controlled to accommodate a higher or lower hydrogen concentration. Because the thermodynamics and kinetics of the phase transformations are a function of hydrogen concentration, the resulting microstructure can be controlled via the hydrogen partial pressure as well as the temperature profile. At the sintering temperature, titanium has very low hydrogen solubility. Therefore, depending on the alloy and desired microstructure, a homogenization step may be included to increase the overall hydrogen content by homogenizing at a temperature below the sintering temperature but above the phase transformation temperature. The material is then cooled to a multiphase field to allow β-Ti (BCC) to decompose into low temperature phases such as α-Ti (HCP) and δ-$TiH_2$ (FCC). Under certain circumstances, $\alpha_2$-$Ti_3Al$ (ordered HCP) can also form, if desired. Nucleation of the low temperature phases refines the microstructure. Additionally, δ-$TiH_2$ ( $\rho_{TiH_2} = 3.75\ g/cm^3$ ) is significantly less dense than titanium ($\rho_{Ti} = 4.51\ g/cm^3$). Therefore, it is possible that the formation of a significant volume fraction of δ-$TiH_2$ produces internal strain that can lead to subsequent grain refinement due to recrystallization during dehydrogenation or other subsequent heat treatments, though this phenomenon has yet to be conclusively demonstrated.

Step 3 – Dehydrogenation: In the final step of the process, the hydrogen is removed at a temperature below the β-transus under a hydrogen-free atmosphere. This is achieved either by vacuum or by flowing an inert gas essentially free of hydrogen. This step may be performed either in a separate dehydrogenation furnace or in the same furnace immediately following Step 2 by adjusting the atmosphere and temperature (dashed line in

Figure 2.4). During dehydrogenation, further grain refinement is facilitated by the decomposition of δ-$TiH_2$ to α and β. After dehydrogenation, hydrogen levels well below the ASTM standard for Grade 5 T-6Al-4V (150 ppm)[96] are easily achieved using inert gas or low vacuum (>$10^{-1}$ Pa). Hydrogen levels below 10 ppm are consistently achieved by using high vacuum (<$10^{-2}$ Pa).

### 2.5 Mechanisms Behind Microstructural Evolution of Ti-6Al-4V

The process-structure relationships and the general forms of microstructure in α+β alloys are discussed in the following section. However, before discussing these relationships, it is first necessary to understand the mechanisms by which the phases evolve during heat treatments of α+β titanium alloys, such as Ti-6Al-4V. For reference, the pseudo-binary phase diagram for Ti-6Al as a function of vanadium concentration and temperature is given in Figure 2.5[34–37].

In titanium alloys, the α phase that forms from the parent β grains will have an crystallographic relationship of α<0001> || β<110>[34]. The α phase that forms at the heat treatment temperature, and not during cooling, is called primary α ($\alpha_p$). Conversely, the α phase that forms during cooling by transformation of the β phase due to changing phase fractions is logically called transformed β. Also shown on the phase diagram is the martensite start temperature for this alloy, which corresponds to roughly 800 °C for Ti-6Al-4V. This indicates that martensite will begin to form from β grains when Ti-6Al-4V is cooled below 800 °C at a sufficient rate (>1000 °C/min)[34].

In order for the β grains to transform into the low temperature α+β microstructure, the alloying elements must partition into their respective phases[97]. For Ti-6Al-4V, aluminum

will diffuse into the region forming α grains and vanadium will diffuse into the region forming β grains. Therefore, the morphology of the α grains that form during cooling is a function of the cooling rate. Because the alloying elements must partition into their respective phases, the maximum width of the α grains that form during cooling is proportional the diffusion length of alloying elements[98]. If the material is cooled quickly, the diffusion length of the alloying elements will be shorter, resulting in α lamellae with high aspect ratios and vice versa. This phenomenon is shown schematically in Figure 2.6.

As an example, a tie line has been drawn one the phase diagram in Figure 2.5 corresponding to Ti-6Al-4V at 950 °C. According to the lever rule, at this temperature the alloy will be approximately 60% β phase and 40% α phase. Therefore, the maximum fraction of $\alpha_p$ of possible after a heat treatment at 950 °C is approximately 40%. The remainder of the α phase in the final structure will form as transformed β during cooling. Due to the phenomenon shown in Figure 2.6, the morphology of the α grains will be determined by the cooling rate. As a rule of thumb, the description of a globularized grain is an aspect ratio less than 3:1. Therefore, if the cooling rate is sufficiently slow to form α grains with an aspect ratio below 3:1, it is possible to form all equiaxed or globularized α grains in the final microstructure. The specific types of microstructures that are formed during heat treatments of α+β alloys and the controlling parameters are discussed in detail in the following sections.

## 2.6 Process-Structure Relationships of α+β Alloys

The majority of the technical knowledge regarding titanium stems from research into wrought processing. Therefore, the process-structure-property relationships discussed in

the following sections will be for wrought-processed alloys, as that is what is primarily available in the literature. The microstructures of α+β alloys are generally grouped into three categories: fully lamellar, bi-modal (duplex), and fully equiaxed (globularized). Therefore, each of these structures will be discussed individually in the following sections.

### 2.6.1 Fully Lamellar Microstructures

Fully lamellar structures (Figure 2.7-A), are characterized by colonies of lamellar α grains (light phase in optical micrographs) with β (dark phase in optical micrographs) distributed along the α grain boundaries and/or at the triple points of the α colonies. Fully lamellar structures generally result from one of two wrought processing conditions: β-annealed or β-processed condition.

#### 2.3.1.1 β-Annealed

The processing route to achieve the β-annealed condition consists of hot working at an elevated temperature to reduce the flow stress of the alloy. A secondary hot working step may be utilized to decrease the average grain size of the β-phase. The material is then recrystallized above the β-transus temperature. A schematic representation of a typical β-annealing processing route is shown in Figure 2.8[34–36]. Additionally, the important processing parameters and their influence on the resulting microstructure are discussed below and are summarized in Table 2.1[34–37].

The three most important processing parameters for controlling the microstructure in a β-annealed alloy are 1) the isothermal temperature in the deformation/working step, 2) the cooling rate from the recrystallization/transformation step, and 3) the annealing temperature in the annealing/aging step. Using a higher temperature during deformation

(the deformation/working step) will lower the flow stress of the material. However, a higher temperature will result in larger β-grains during deformation and consequently larger α colonies in the resulting microstructure. The next important parameter is the cooling rate from the recrystallization temperature (the recrystallization/transformation step). This cooling rate will affect the size of the α colonies, the width of the α lamellae, and the size the grain boundary α (G.B. α) that grows along the prior β grain boundaries during cooling. Lastly, the annealing temperature (the annealing/aging step) will determine whether or not secondary α within β or $\alpha_2$-$Ti_3Al$ within α is formed during annealing.

Figure 2.9 shows the effect that the cooling rate from the recrystallization temperature has on the resulting microstructure[34]. Figure 2.9-A was cooled at 1 °C/min which results in large α lamellae and a large α colony size, as well as a relatively thick G.B. α layer along the prior β grain boundaries. In comparison, Figure 2.9-B, which was cooled at 100 °C/min, shows much finer α lamellae as well as much thinner G.B. α along the grain boundaries. Finally, Figure 2.9-C shows a sample that was cooled at 8000 °C/min, which is well beyond the critical cooling rate to form martensite of ~1000 °C[34]. Therefore, this structure consists of a very fine acicular martensitic structure and essentially no G.B. α.

2.3.1.2 β-Processed

Another processing route to obtain a fully lamellar structure is β-processing. However, β-processing is used primarily for β alloys and only has limited commercial use in α+β alloys[34]. As such, research on this type of processing for α+β alloys is limited. Therefore, because this dissertation concentrates on α+β microstructures, the details of β-processing will not be discussed.

### 2.6.2 Bi-Modal (Duplex) Microstructures

Bi-modal or duplex microstructures, as the name would suggest, consist of two distinct microstructural constituents. The first constituent is either a lamellar or acicular structure, consisting of either lamellar or acicular α grains and dispersed β between the α grains. However, a significant volume fraction of the bi-modal structure is made up of equiaxed or globularized α grains called primary α ($\alpha_p$) (Figure 2.7-B). The $\alpha_p$ grains are formed at high temperature during heat treatments, hence the name. Conversely, α phase that is formed during cooling is called transformed β, which forms during cooling as β phase transforms to α phase. A schematic representation of typical processing routes used to achieve a bi-modal microstructure via wrought processing is shown in Figure 2.10[34–36]. Additionally, the important processing parameters affecting the bi-modal microstructure are discussed below and summarized in Table 2.2[34–37].

For this type of processing, the cooling rate in the homogenization/solutionizing step will control the width of the α lamellae and the size of the $\alpha_p$ grains. The deformation step will primarily control the texture of the microstructure. The temperature in this step will determine the type of texture, while the degree of deformation will determine the texture intensity and the dislocation density, which will also determine the driving force for recrystallization during subsequent steps. Also during the deformation/working step, the mode of deformation will determine the texture symmetry. During recrystallization, the temperature will determine the vol% of $\alpha_p$ and, therefore, the β grain size in the final microstructure as well as the degree of alloy element partitioning due to a larger or smaller portion of the equilibrium α phase fraction being $\alpha_p$ versus transformed β (lamellar α colonies). The cooling rate from the recrystallization/transformation step will have an

effect on the width of the α lamellae as well. Similar to fully lamellar processing routes, the annealing temperature (the annealing/aging step) will determine whether or not secondary α within β or $\alpha_2$-$Ti_3Al$ within α is formed during annealing.

Figure 2.11[34] shows typical bi-modal microstructures of an α+β alloy produced by a processing route similar to that shown in Figure 2.10. Figure 2.11-A was cooled relatively slowly (~100 °C/min) during the homogenization/solutionizing step, resulting in comparatively large average α lamellae width and $\alpha_p$ grain size. Figure 2.11-B was cooled at a much faster rate (~500 °C/min) and, therefore, has a much finer α lamellae width. The finer α lamellae width results in finer $\alpha_p$ grains formed during the recrystallization step. Therefore, this microstructure is finer with regards to both the size of the α lamellae within the transformed β region as well the size of the equiaxed $\alpha_p$ grains.

Figure 2.12 is a TEM micrograph of a bi-modal microstructure of Ti-6Al-4V that was formed using a recrystallization temperature of 950 ºC[34]. It has been proposed that equiaxed $\alpha_p$ grains are formed when recrystallized β grains penetrate the lamellar α grains along the α/α grain boundaries, thereby forming separated $\alpha_p$ grains[99].

### 2.6.3 Fully Equiaxed Microstructures

A fully equiaxed microstructure is essentially a bi-modal microstructure with the majority of the α phase in the form of equiaxed or globularized grains and all the β phase restricted to the α triple points (Figure 2.7-C). Therefore, the microstructure is mostly free of the lamellar α colonies that form during nonequilibrium transformation of β (i.e. fast cooling rates). A schematic of typical processing routes used to achieve fully equiaxed microstructures is shown in Figure 2.13[34–36]. The important processing parameters and their effect on the resulting microstructure are discussed in the following paragraphs and

are summarized in Table 2.3[34–37].

The temperature used during the recrystallization/transformation step determines the type of recrystallization performed. For a high temperature recrystallization (HTR), the temperature in the recrystallization/transformation step is near the β transus temperature. For a low temperature recrystallization (LTR), a temperature hundreds of degrees Celsius below the β transus temperature is used. For Ti-6Al-4V, typical temperatures for recrystallization are around 950 ºC and 800 ºC for HTR and LTR, respectively[34]. However, the actual temperature used is dependent not only on the alloy composition but on the state of the microstructure before recrystallization. LTR will typically result in a finer equiaxed microstructure (on the order of 10 μm or less)[34]. However, the lower recrystallization temperature requires greater driving force for recrystallization, such as a high dislocation density due to deformation or an ultra-fine lamellar grain size in the starting condition. Such an ultra-fine lamellae width necessary for LTR can be achieved by using a very fast cooling rate during the homogenization/solutionizing step[34].

As mentioned before, the only difference between a fully equiaxed microstructure and a bi-modal microstructure is that essentially all of the α grains are equiaxed or globularized. Therefore, the processing routes used to achieve a fully equiaxed microstructure are similar to bi-modal processing route. This is particularly true for HTR. As discussed in section 2.5, the morphology of α formed during cooling from an HTR temperature is dependent on the cooling rate. Because of this, the vol% of equiaxed or globularized α grains is partially controlled by the cooling rate during the recrystallization/transformation step; a slower cooling rate will result in a larger volume fraction of equiaxed grains and vice versa. Therefore, to achieve a bi-modal microstructure, a faster cooling rate is employed in the

recrystallization/transformation step, whereas a slower cooling rate will result in a fully equiaxed or globularized structure. As mentioned above, the rule of thumb description of a globularized grain is an aspect ratio less than 3:1. For Ti-6Al-4V, a cooling rate from the HTR recrystallization/transformation step less than 30 ºC/min can result in a volume fraction of equiaxed grains high enough to be considered a fully equiaxed microstructure[34].

Figure 2.14 shows two micrographs (optical and TEM) of an ultra-fine equiaxed microstructure that was formed during LTR recrystallization of Ti-6Al-4V[34,100]. This microstructure was formed in a laboratory by using a processing route similar to that shown in Figure 2.13 with a very fast cooling rate during the homogenization/solutionizing step and an LTR temperature of 800 ºC. This treatment resulted in a fully equiaxed microstructure with α grains on the order of 2 μm.

The mechanism to form $\alpha_p$ during HTR is identical to that described in the previous section for a bi-modal structure (Figure 2.12), but to form a fully equiaxed structure, the transformation is given sufficient time (i.e. slow cooling rate) for globularized α to form during cooling and consume the majority of the material's remaining volume. However, during LTR, a different mechanism has been proposed to form the $\alpha_p$ grains. The mechanism proposed for HTR relies on a high equilibrium phase fraction of β when the temperature is near the β transus. However, during LTR the temperature is much lower, and the relative phase fractions are reversed. Therefore, the proposed mechanism for LTR is analogous to the HTR mechanism, just in the opposite direction. That is, $\alpha_p$ grains form by penetration of α along β/β grain boundaries into the recrystallized β grains[34,99]. A TEM micrograph illustrating this mechanism is shown in Figure 2.15[34].

## 2.7 Structure-Property Relationship of α+β Alloys

As with any material, the mechanical properties of α+β alloys are strongly dependent on microstructure. Therefore, the impetus for studying heat treatments of titanium is driven by a possible increase in mechanical performance through microstructural engineering. In this section, the relationship between structure and mechanical properties of α+β titanium alloys will be discussed. The simplest and often preliminary method for comparing mechanical properties is quasi-static tensile testing. However, because titanium alloys are often chosen for critical applications in which long life and a high degree of confidence is required (e.g. aerospace), the dynamic mechanical properties (i.e. fatigue performance) is often the more important consideration.

As discussed in the previous sections, the two extremes for microstructures of α+β alloys are fully lamellar and fully equiaxed. Anything in between these two extremes is termed bi-modal or duplex and typically has an equiaxed α phase fraction between 10 and 50 vol%. By convention, anything beyond 50 vol% and the equiaxed grains begin to interconnect and the material is typically called fully equiaxed[34]. Therefore, these definitions will be used when discussing the structure-property relationships in the following sections.

The two distinct microstructural forms of α phase contribute differently to the overall mechanical properties. Lamellar α grains have greater resistance to slip and tend to increase the material's strength, while equiaxed α grains tend to improve tensile ductility and can have a beneficial effect on high cycle fatigue performance[34,35]. As such, processing that employs recrystallization annealing to form equiaxed α grains is often employed to improve the ductility and/or fatigue performance of commercial alloys[35]. How these

different microstructural forms are utilized to modify the mechanical properties of titanium alloys will be discussed in the following sections.

### 2.7.1 Quasi-Static Mechanical Properties

Table 2.4 gives the static tensile properties of Ti-6Al-4V with respect to the minimum values defined by the ASTM B348 standard[96], typical values for Grade 5 Ti-6Al-4V (standard oxygen content) in the annealed condition[35], typical values for Grade 5 Ti-6Al-4V in the solution treated and aged condition[35], and typical values for Grade 23 (also known as extra low interstitial or ELI grade) Ti-6Al-4V in the annealed condition[35]. From these data, one can see that a simple STA (solution treatment and ageing) heat treatment can significantly affect the tensile properties of the alloy. Compared to typical values for annealed Grade 5 Ti-6Al-4V, after STA, the tensile strength is increased from a maximum typical value of 993 MPa to 1172 MPa (18% increase) and yield strength is increased from a maximum typical value of 924 MPa to 1103 MPa (19% increase). However, the increase in strength is met with a decrease in ductility from 14 %EL to 10 %EL (28% decrease). It should also be noted that the solution strengthening effect of oxygen is apparent in these data. Both the tensile strength and yield strength of annealed Grade 23 (low-oxygen) are about 100 MPa less than annealed Grade 5, though the ductility of Grade 23 is slightly greater.

Figure 2.16 was created from values for strength and ductility of an α+β titanium alloy (IMI 834) reported by Lütjering and Williams[34]. This figure shows how the strength and ductility at different temperatures vary as a function of vol% $\alpha_p$. In this case, 0 vol% $\alpha_p$ corresponds to a fully lamellar structure, while 10, 20, 30, 40 vol% $\alpha_p$ correspond to bi-

modal microstructures with increasing amounts of $\alpha_p$. As the vol% of $\alpha_p$ increases from 0 vol% (fully lamellar) to 20 vol% (bi-modal), both the yield strength and tensile strength of the material increases by about 10% at room temperature. However, when the amount of $\alpha_p$ is further increased to 30 vol%, the yield and tensile strength values begin to decrease, though their values are still higher than those reported for the fully lamellar structure. With regards to ductility, a significant increase in both elongation (%EL) and reduction in area (%RA) is observed for the bi-modal microstructures versus the fully lamellar microstructure. 5 %EL was reported for the fully lamellar structure, while 13 %EL was reported for 20 vol% $\alpha_p$, though no further increase in %EL was reported for 30 vol% $\alpha_p$. The reduction in area, however, increased steadily as the amount of $\alpha_p$ was increased. The three structures experience 12 %RA, 20 %RA, and 26 %RA for 0 vol%, 20 vol%, and 30 vol% $\alpha_p$, respectively[34].

For the high temperature properties, very similar trends to the room temperature properties are reported in the literature. That is, there is a definitive increase in strength in a bi-modal structure versus a fully lamellar one. However, a bi-modal structure with a comparatively moderate amount of $\alpha_p$ (10 vol% versus 40 vol% in these data) will have greater strength than one with a greater amount of $\alpha_p$. That is, an increase in vol% $\alpha_p$ begins to have a deleterious effect on strength beyond a certain point. Both fully lamellar and 10 vol% $\alpha_p$ structures are reported to exhibit 10 %EL, while the 40 vol% $\alpha_p$ material was reported to exhibit 14 %EL. The reduction in area continually increases as the amount of $\alpha_p$ within the microstructure increases, going from 26 %RA for a fully lamellar structure to 36 %RA for a bi-modal structure with 40 vol% $\alpha_p$[34].

### 2.7.2 Dynamic Mechanical Properties

The plot on the left of Figure 2.17 shows the high-cycle fatigue (HCF) behavior of Ti-6Al-4V with respect to different α+β microstructures: fully lamellar, bi-modal (duplex), and fully equiaxed. This figure also illustrates how the relative size of each microstructure has an effect on HCF strength. From this figure, the following general trend for endurance limit with respect to microstructure from greatest to least can be deduced:

Fine Bi-Modal > Fine Equiaxed > Fine Lamellar >

Coarse Equiaxed > Coarse Lamellar

However, when studying the plot on the right of Figure 2.17, which shows the rate of fatigue crack propagation with respect to the stress intensity factor, the relationship is inverse to what would be expected based on the reported endurance limits. For example, the fine equiaxed microstructure is reported to exhibit the fastest crack propagation, despite the fact that it has the second highest endurance limit in the HCF plot.

The apparent disparity between endurance limit and fatigue crack propagation rates is likely due to the fact that HCF properties of a material are governed by both the initiation and the growth of cracks[101,102]. Therefore, the rate at which cracks propagate, and the corresponding fatigue life of the material before failure, is controlled by the material's propensity to initiate cracks as well as the material's ability to resist crack growth[102]. In α+β alloys, cracks tend to initiate more readily within the lamellar regions of the microstructure. An example of crack initiation within the lamellar region of a bi-modal structure is show in Figure 2.18[34]. However, the lamellar grains also tend to have higher strength than $\alpha_p$ grains and should, therefore, exhibit slower crack growth rates[34,35].

Additionally, it has already been shown in the previous section that the presence of $\alpha_p$ grains has a ductilizing effect[34,35]. With all of this considered, it can be deduced that even though the lamellar grains are able to slow down crack growth, their presence likely increases the frequency of crack initiation. Furthermore, the fact that globularized grains make the material more ductile means a greater degree of strain energy can be absorbed by the material near the crack tip in microstructures with globularized α grains[101].

### 2.7.3 Effect of Porosity on Fracture

HSPT is a powder metallurgy process, and powder metallurgy processes are susceptible to porosity[27]. Therefore, despite the mechanical properties of the grain structure, the fatigue performance of a PM specimen will be greatly compromised if the sample contains a pore of sufficient size.

It is well known in fracture mechanics that crack propagation within a material is directly related to the size of a flaw that a force is acting on. At the tip of a crack, the stress applied to the material is intensified proportionally to the size of the flaw within the material. The stress intensity at the tip of a crack is defined as[101]:

$$K = Y\sigma\sqrt{\pi a} \qquad \text{Eq. 2.4}$$

In Eq. 2.4, σ is the applied stress, a is the crack length, and Y is a scaling factor depending on the size and geometry of the crack and specimen. The calculated stress intensity may then be used with Paris' law to calculate fatigue crack growth upon cyclic loading by the following equation[103]:

$$\frac{\mathrm{d}a}{\mathrm{d}N} = C(\Delta K)^m \qquad \text{Eq. 2.5}$$

In Eq. 2.5, N is the number of cycles, C is a material dependent constant, and $\Delta K = K_{max} - K_{min}$ (i.e. the difference between minimum and maximum stress intensity) for each cycle. However, Paris' law only applies when the stress intensity is greater than a threshold value. Therefore, the fatigue crack growth threshold ($\Delta K_{th}$) is the stress intensity under which fatigue crack growth will not occur (i.e. the material will never fail). Therefore, by combining Eq. 2.4 and Eq. 2.7, one may compare the endurance limit of an alloy to fracture caused by a particular flaw in a specimen. This yields the following two relationships for internal pores and surface pores, respectively:

$$\Delta\sigma_{e,\mathrm{interior}} = \frac{\Delta K_{th}}{0.5\sqrt{\pi a}} \qquad \text{Eq. 2.6}$$

$$\Delta\sigma_{e,\mathrm{surface}} = \frac{\Delta K_{th}}{0.65\sqrt{\pi a}} \qquad \text{Eq. 2.7}$$

By using these equations, one may calculate the maximum pore size that can be tolerated without affecting the endurance limit of a Ti-6Al-4V specimen. From Figure 2.17, a fine lamellar structure has an endurance limit of 600 MPa according to the S-N plot. To be conservative, $\Delta K_{th}$ may be estimated from the x-intercept of the crack propagation curve in Figure 2.17 with the lowest $\Delta K$ value, which is approximately 3 MPa-$m^{1/2}$. Plugging these values into Eq. 2.6 and Eq. 2.7, it is calculated that the maximum tolerable pores for a fine lamellar microstructure are 20 μm and 30 μm for surface pore and interior pore, respectively.

Table 2.1: Important processing parameters effecting microstructures of β-annealed alloys. Data from the literature[34–37].

| **Step** | **Parameter** | **Effect on Microstructure** |
|---|---|---|
| Deformation/ Working | Temperature | - Flow stress<br>- β grain size<br>(α colony size) |
| Recrystallization/ Transformation | Cooling rate | - Size of α colonies<br>- Width of α lamellae<br>- GB α layer |
| Annealing/ Aging | Annealing temperature | - $Ti_3Al$ in α<br>- Secondary α in β |

Table 2.2: Important processing parameters effecting properties of bi-modal microstructures. Data from the literature[34–37].

| **Step** | **Parameter** | **Effect on Microstructure** |
|---|---|---|
| Homogenization/ Solutionizing | Cooling rate | - Width of α lamellae<br>- $\alpha_P$ size |
| Deformation/ Working | Deformation temperature<br>Deformation degree<br>Deformation mode | - Texture type<br>- Texture intensity<br>- Dislocation density<br>- Texture symmetry |
| Recrystallization/ Transformation | Recrystallization temperature<br>Cooling rate | - β grain size<br>- Alloy element partitioning<br>- Vol% of $\alpha_P$<br>- Width of α lamellae |
| Annealing/ Aging | Annealing temperature | - $Ti_3Al$ in α<br>- Secondary α in β |

Table 2.3: Important processing parameters effecting properties of fully equiaxed microstructures. Data from the literature[34–37].

| **Step** | **Parameter** | **Effect on Microstructure** |
|---|---|---|
| Homogenization/ Solutionizing | Cooling rate | - Width of α lamellae<br>- $\alpha_P$ size |
| Deformation/ Working | Deformation temperature<br>Deformation degree<br>Deformation mode | - Texture type<br>- Texture intensity<br>- Dislocation density<br>- Texture symmetry |
| Recrystallization/ Transformation | HTR with a slow cooling rate (< 30°C/min)<br>LTR (800~850°C for Ti-6Al-4V) | - Fully equiaxed structure<br>- Fully equiaxed structure<br>- Very fine $\alpha_P$ size |
| Annealing/ Aging | Annealing temperature | - $Ti_3Al$ in α<br>- Secondary α in β |

Table 2.4: Typical tensile properties of Ti-6Al-4V. Data from the literature[35].

| **Grade (Ti-6Al-4V)** | **Condition** | **U.T.S. (MPa)** | **0.2% Y.S. (MPa)** | **Elongation (%)** |
|---|---|---|---|---|
| Grade 5 | ASTM B348 Standard (annealed) | 895 | 828 | 10 |
| Grade 5 | Annealed | 900-993 | 830-924 | 14 |
| Grade 5 | Solution treated and aged | 1172 | 1103 | 10 |
| Grade 23 (ELI) | Annealed | 830-896 | 760-827 | 15 |

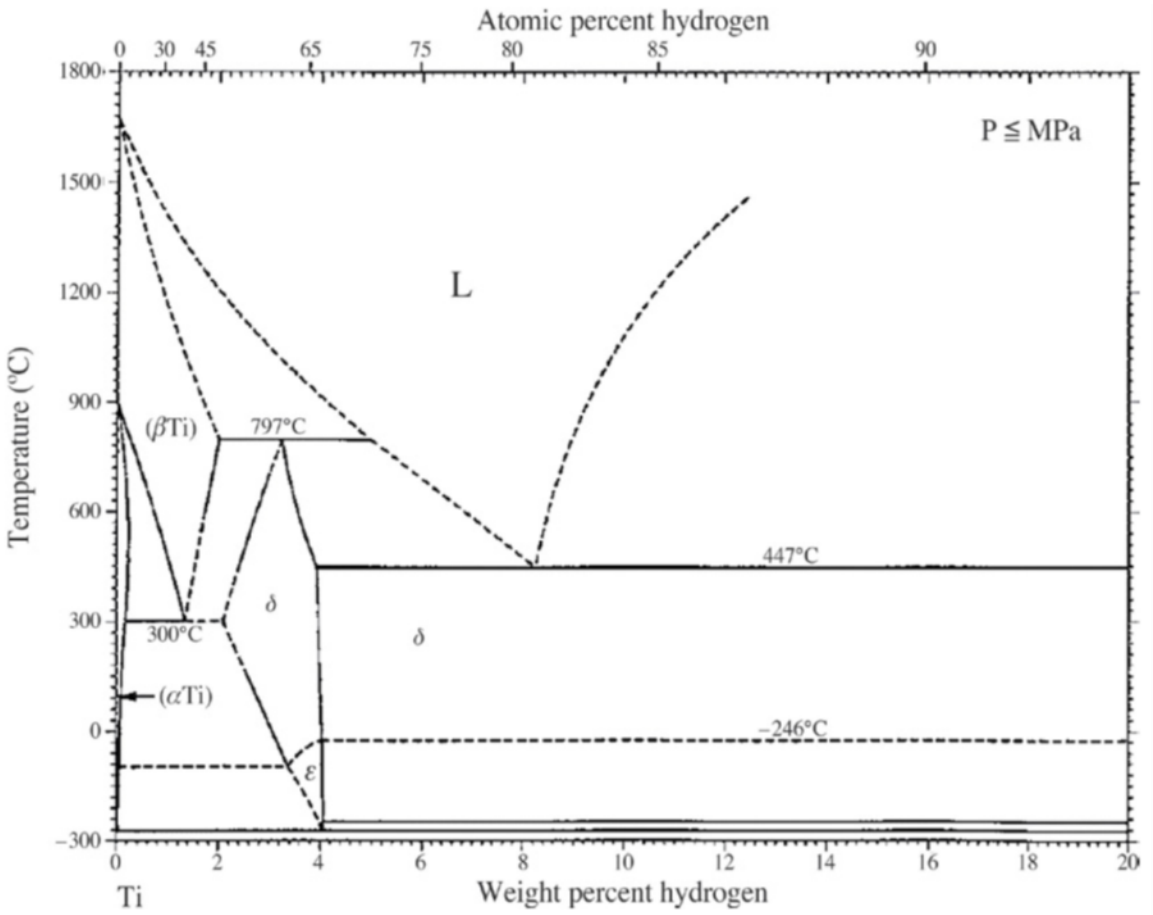


Figure 2.1: Ti-H phase diagram (reproduced with permission of ASM International via Copyright Clearance Center)[38].

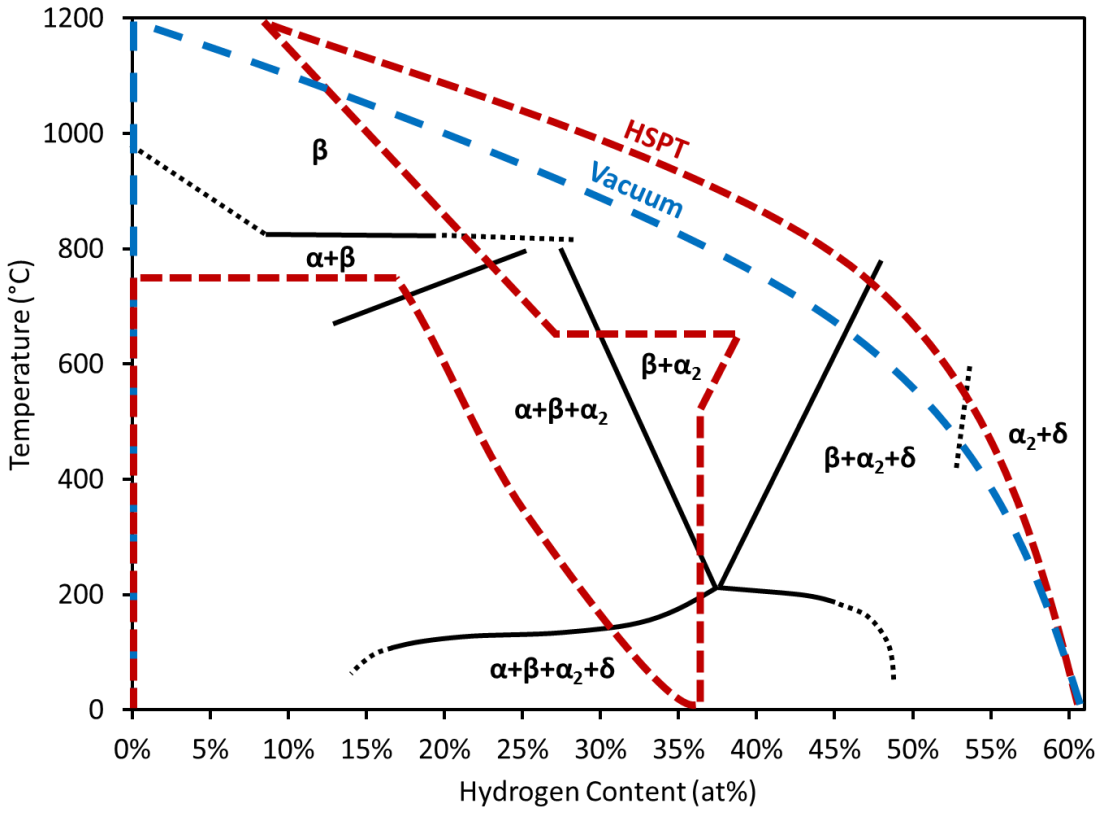


Figure 2.2: Improved (Ti-6Al-4V)-H pseudo-binary phase diagram[5]. Phase evolution curves of (Ti-6Al-4V)-H during the HSPT and vacuum sintering profiles presented in CHAPTER 3 are superimposed on the phase diagram.

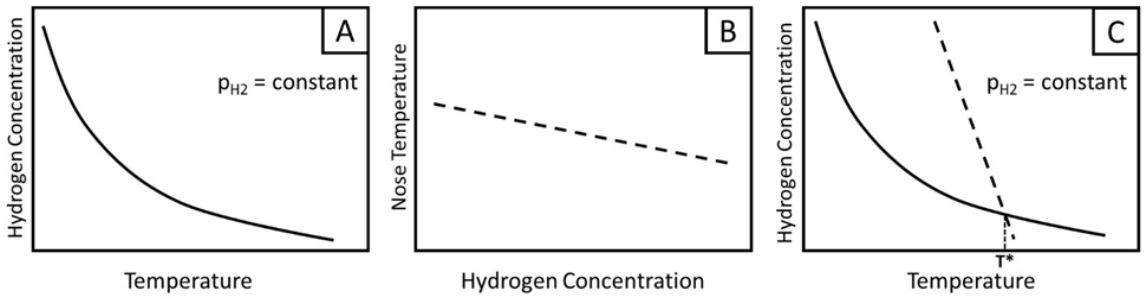


Figure 2.3: Schematic plots of A) equilibrium hydrogen concentration as a function of temperature for a given hydrogen partial pressure, B) nose temperatures of the phase transformation as a function of hydrogen concentration, and C) superimposition of A and B (axes flipped) to determine temperature at which transformation kinetics are maximized. Data from the literature[83].

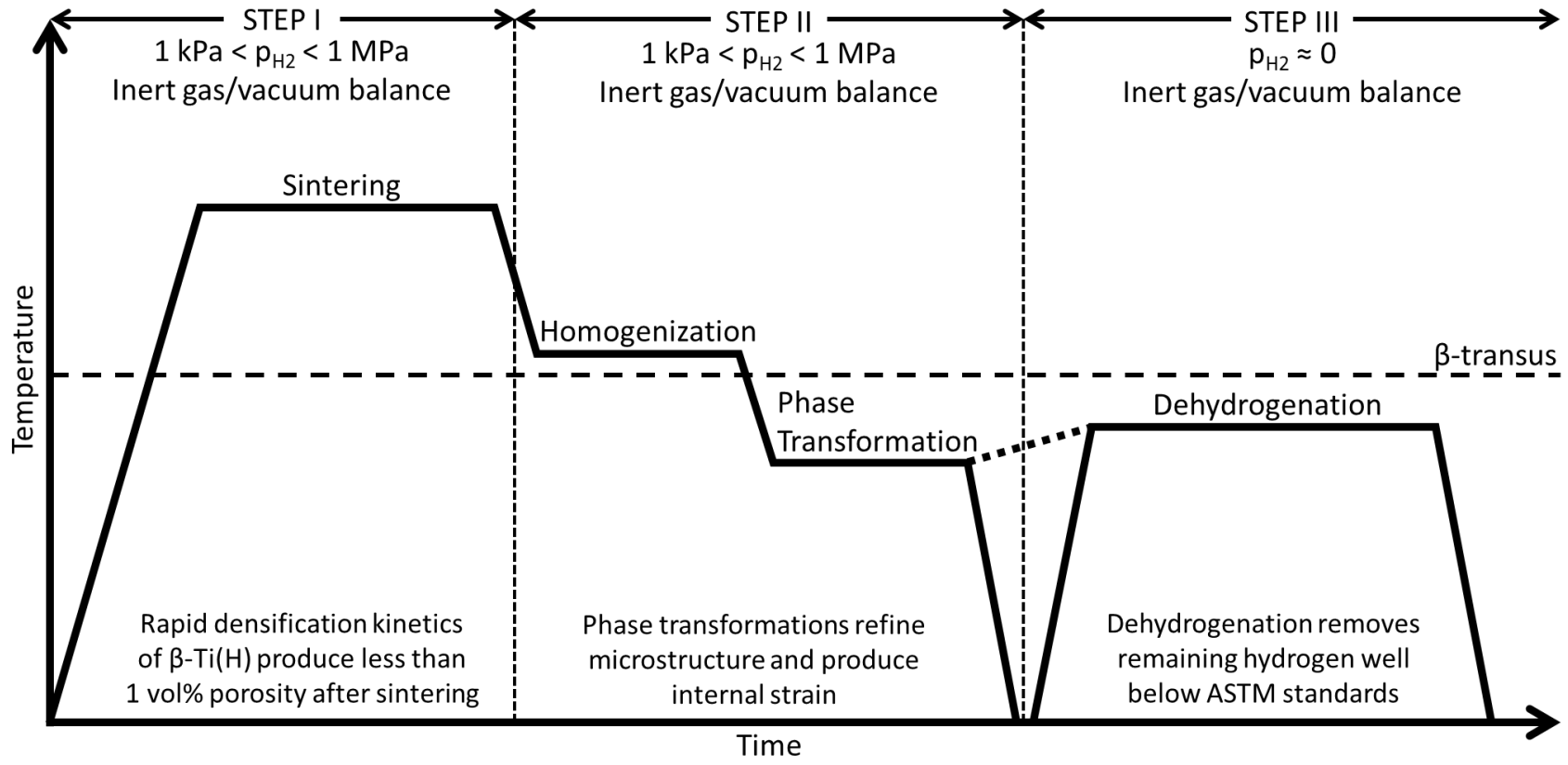


Figure 2.4: Schematic of the sintering and dehydrogenation profiles used during HSPT.

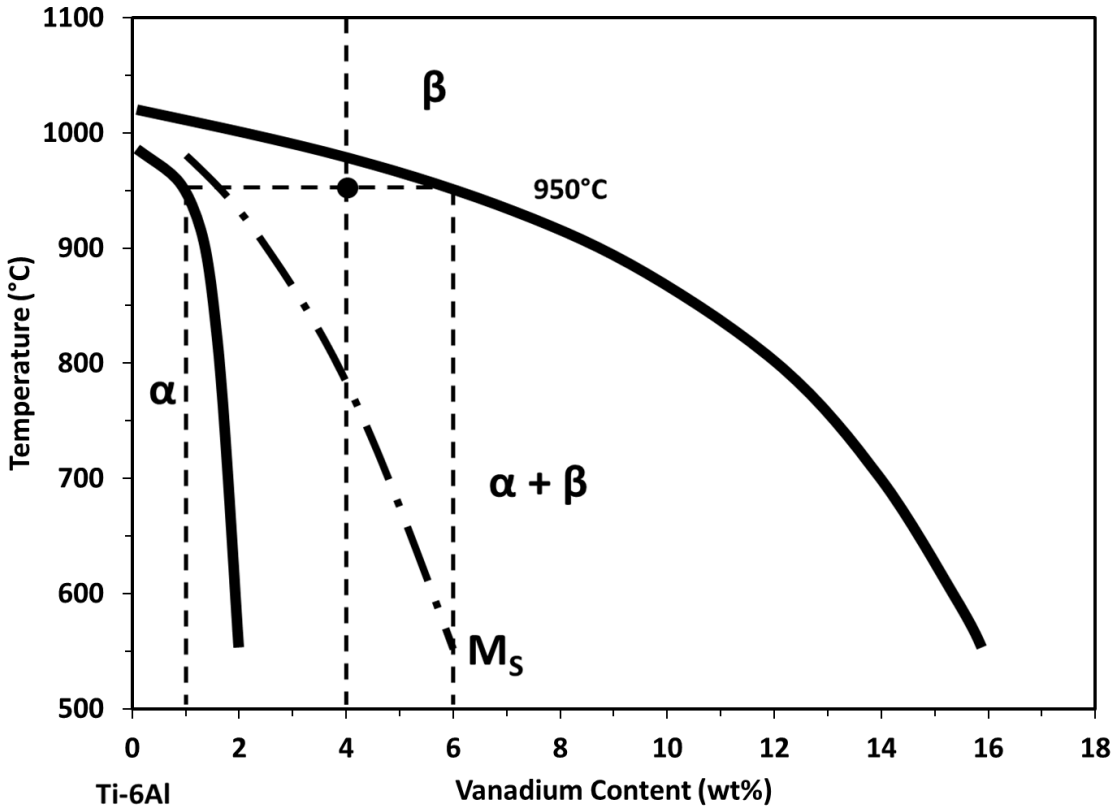


Figure 2.5: Pseudo-binary phase diagram for (Ti-6Al)-V. A tie line at 950°C shows that the material is 60 vol% β phase at a typical heat treatment temperature. Data from the literature[34–36].

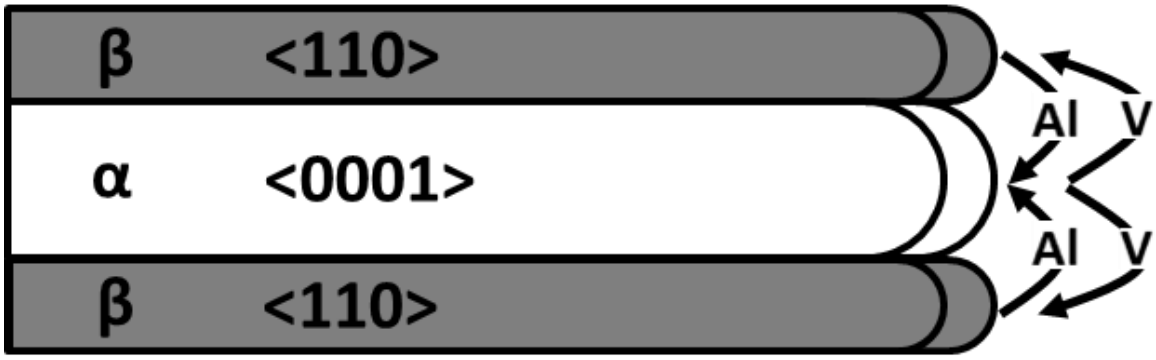


Figure 2.6: Schematic representation of alloying element partitioning in α+β alloys as β grains transform into α+β grains during cooling.

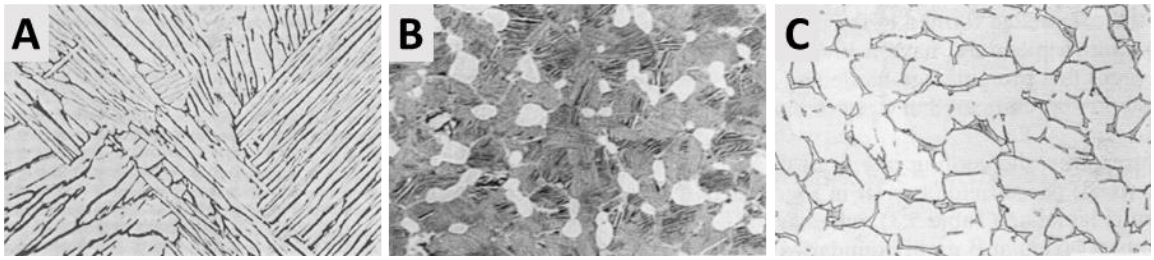


Figure 2.7: Optical micrographs of three types of microstructures generally seen in α+β titanium alloys. A) fully lamellar, B) bi-modal (duplex), and C) fully equiaxed (reproduced with permission of Springer via RightsLink/Copyright Clearance Center)[34].

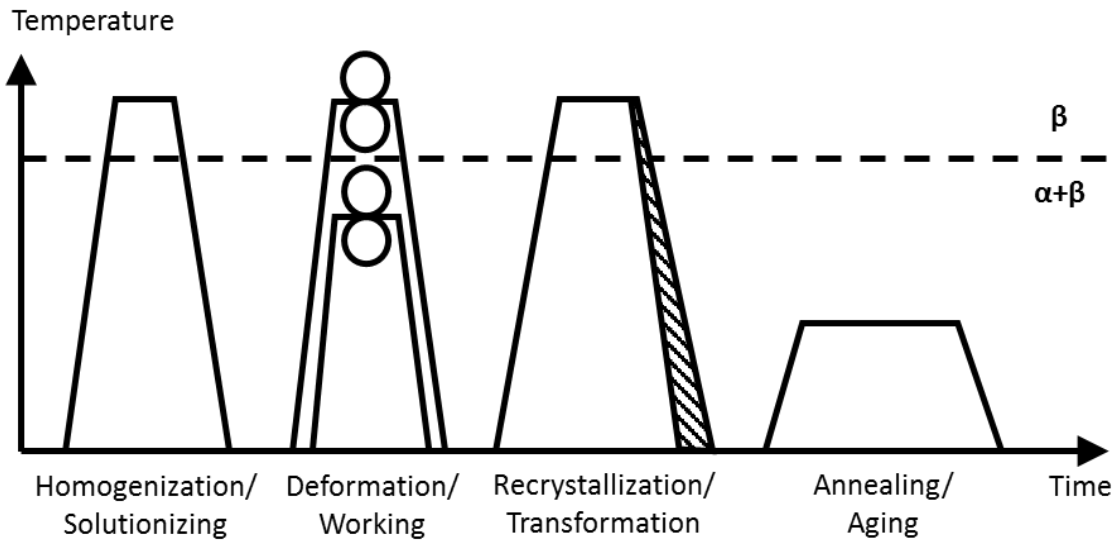


Figure 2.8: Schematic of typical processing routes used to achieve fully lamellar (β-annealed) microstructures. Data from the literature[34–36].

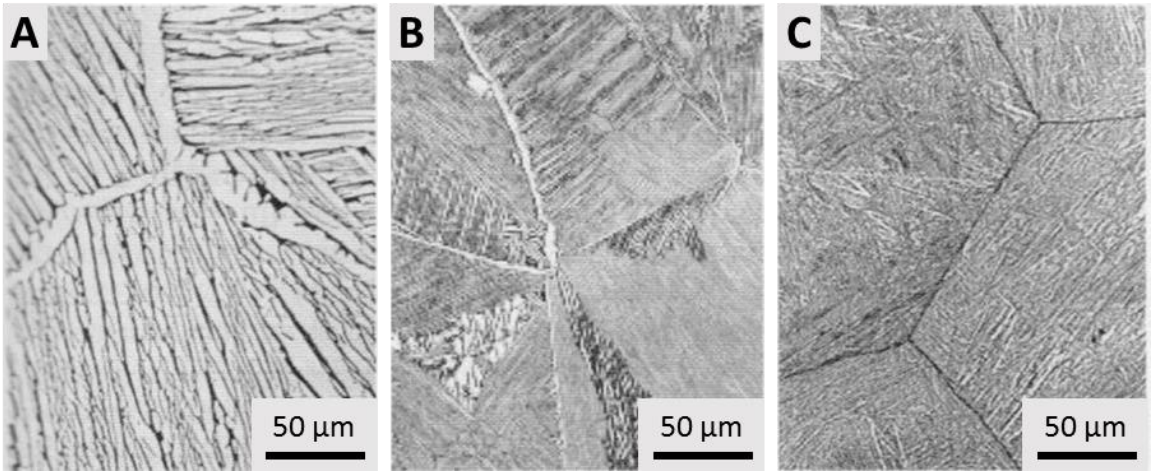


Figure 2.9: Optical micrographs of β-annealed microstructures with varying cooling rates from the recrystallization temperature: A) 1 °C/min, B) 100 °C/min, and C) 8000 °C/min (reproduced with permission of Springer via RightsLink/Copyright Clearance Center)[34].

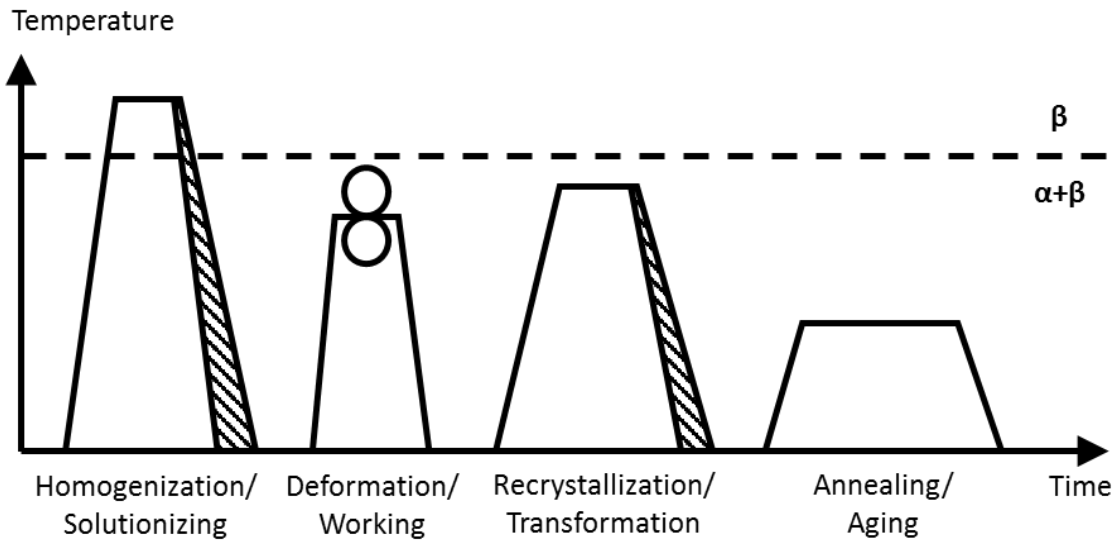


Figure 2.10: Schematic of typical processing routes used to achieve bi-modal microstructures. Data from the literature[34–36].

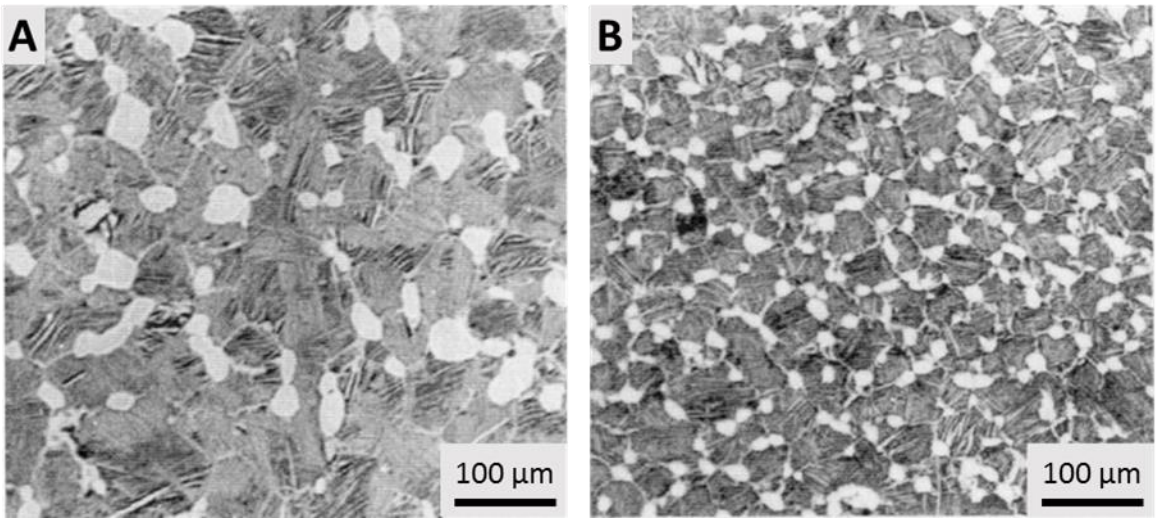


Figure 2.11: Optical micrographs of bi-modal microstructures with varying cooling rates from the homogenization/solutionizing step: A) 100 °C/min, and B) 500 °C/min (reproduced with permission of Springer via RightsLink/Copyright Clearance Center)[34].


Figure 2.12: TEM micrograph of Ti-6Al-4V recrystallized at 950 °C to form a bi-modal microstructure (reproduced with permission of Springer via RightsLink/Copyright Clearance Center)[34].

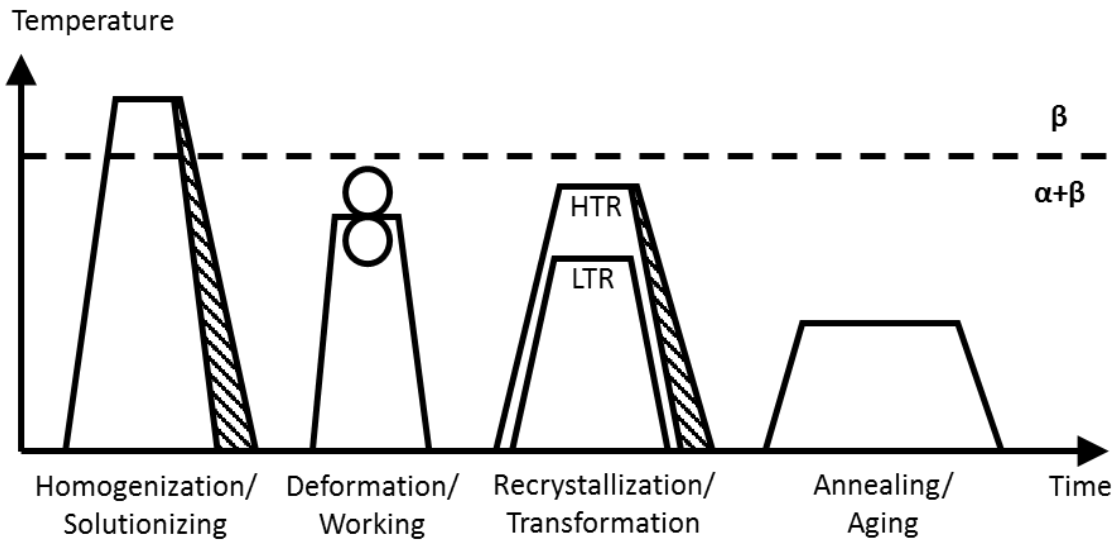


Figure 2.13: Schematic of typical processing routes used to achieve fully equiaxed microstructures. Data from the literature[34–36].

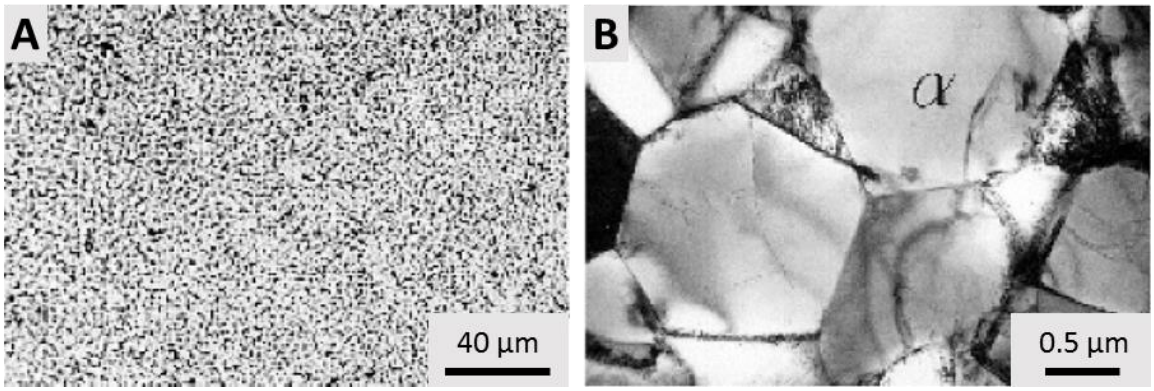


Figure 2.14: Ti-6Al-4V subjected to low temperature recrystallization (LTR) at 800 °C. A) optical micrograph, and B) TEM micrograph (reproduced with permission of Springer via RightsLink/Copyright Clearance Center)[34].

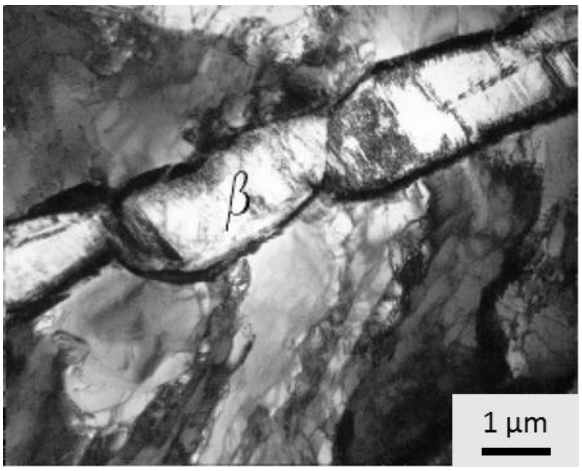


Figure 2.15: TEM micrograph showing low temperature recrystallization in Ti-6Al-4V at 800 °C (reproduced with permission of Springer via RightsLink/Copyright Clearance Center)[34].

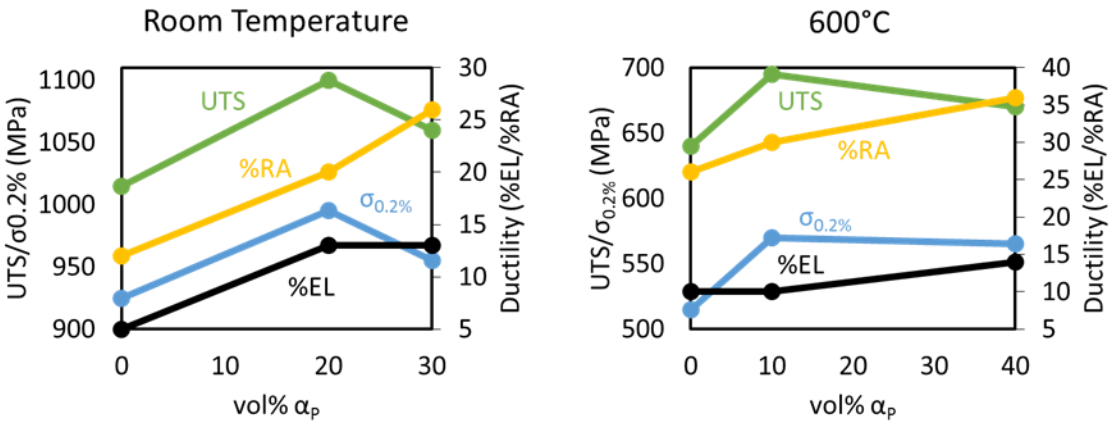


Figure 2.16: Strength and ductility of an α+β titanium alloy (IMI 834) with respect to vol% $\alpha_p$. Data from the literature[34].

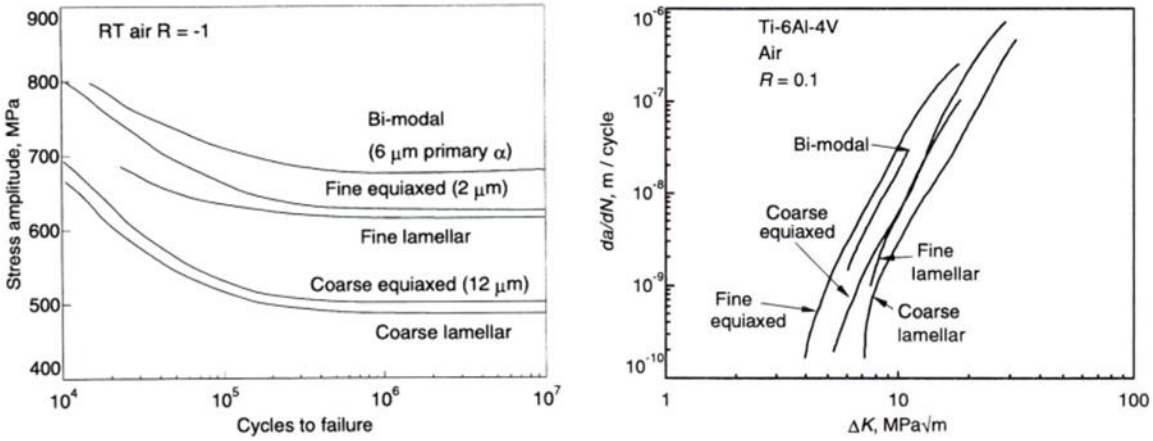


Figure 2.17: S-N plot for HCF (left) and fatigue crack propagation (right) of Ti-6Al-4V (reproduced with permission of ASM International via Copyright Clearance Center)[35].

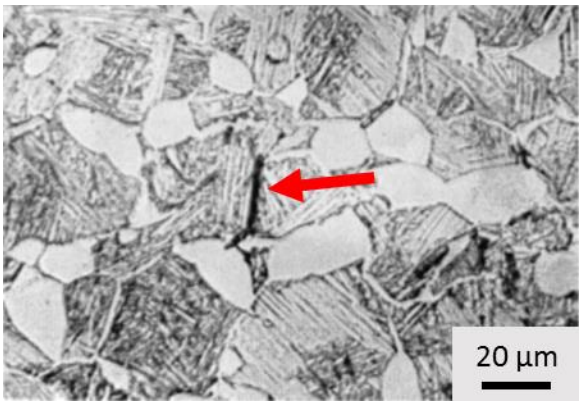


Figure 2.18: Micrograph showing crack nucleation in lamellar region of a bi-modal microstructure (reproduced with permission of Springer via RightsLink/Copyright Clearance Center)[34].

# CHAPTER 3

## ENERGY MODEL

Titanium is traditionally thought of as a sustainability material because of its potential for light-weighting and increasing service life of components which are traditionally made of steel. Additionally, the costs associated with the adoption of titanium in commercial and industrial applications are usually assumed to be predominately related to the extractive process. Therefore, the majority of published studies that discuss titanium with regard to sustainability focus primarily on titanium's impact on energy use in end-user applications[16,33,104–106] and discuss the feasibility of such implementations relying on the reduction in cost of the extractive process (e.g. Kroll Process)[16,20,33,107]. However, this logic fails to consider the primary source of energy consumption in titanium production.

While the energy requirements of the Kroll Process are relatively high, the majority of the energy use and, therefore, cost associated with the production of end-user titanium products is from thermomechanical processing (TMP) in wrought processing[14,32]. These processing steps are often complicated, multistep, and low-yield. In fact, it has been reported that for some mill products over 90% of the cost results from the thermomechanical processing (TMP) steps in wrought processing[108]. Therefore, HSPT has the potential to significantly reduce the embodied energy and cost of titanium components by avoiding TMP, even when the Kroll Process is used to produce the feedstock. To

understand the potential economic and environmental advantages of HSPT, the author has created a comparative energy model for the production of a specific titanium product via traditional melt-wrought processing versus HSPT.

An energy model has been chosen over a cost model for two reasons. First, in practice, energy and cost are directly related. Therefore, the energy consumption is a direct indication of the cost. Second, if this or any other technology is capable of making titanium a viable replacement for steel in many commercial applications, it will cause a dramatic increase in production rates of titanium components. If this happens, the energy required to produce the components themselves will become an important environmental as well economic consideration for the sustainability of titanium as a structural material.

## 3.1 Energy Model Considerations

In order to generate an accurate comparison between the energy efficiency of the HSPT process and a wrought process, it is necessary to identify a specific component to be produced. While complex geometries are best suited to highlight the superior efficiencies of a near-net-shape (NNS) powder metallurgy (PM) process, such as HSPT, a relatively simple geometry of 2 inch round bar stock was chosen to provide a conservative evaluation of HSPT versus wrought processing.

Wrought processing of titanium is a competitive market. Consequently, actual data from the industrial processes are understandably guarded and, therefore, unavailable for this study. Additionally, HSPT has yet to be commercialized and, therefore, actual production-scale data does not exist. Therefore, for this model, the author started with first principles using thermodynamic calculations to model the energy requirements of each step

for each process. The theoretical energy required for each processing step was first calculated to determine a baseline energy comparison for both processes, not accounting for parasitic energy consumption or equipment efficiencies. When available, typical equipment efficiencies were taken from the literature to determine the actual energy requirements for each process step. When published equipment efficiencies were not available or suitable, such as in modeling the HSPT sintering furnace, the actual energy requirements were calculated by solving the entire mass and energy balance of the process. Examples of energy consumption in a sintering process are heat loss through the furnace insulation, heating the furnace hardware and parts as they enter the furnace, heating the gases flowing into the furnace, energy consumed by endothermic reactions during sintering, and embodied energy of gases consumed by the process.

Figure 3.1 is a flow sheet of processes considered for HSPT and wrought processing in this model. The purpose of this model was to determine the relative energy required for HSPT versus wrought processing. It was assumed that the feedstock for each process was titanium sponge produced by the Kroll Process. In this model, the HSPT process has three general processing steps: powder preparation (hydrogenation of titanium sponge to produce $TiH_2$ and ball milling), compaction, and sintering. The modeled wrought process has two general processing steps: ingot formation (vacuum arc remelting or VAR), and forging (21 passes of heating and gyratory forging).

### 3.1.1 HSPT Energy Calculations

The calculations used to determine energy requirements of each step in the HSPT process as shown in Figure 3.1 are detailed in the following sections.

3.1.1.1 Powder Preparation

The starting material assumed in this model is titanium sponge from the Kroll Process. Therefore, in order to prepare the $TiH_2$ powder used in the HSPT process, the Ti sponge must first be hydrogenated to form $TiH_2$ and then ball milled to the appropriate particle size. A typical particle size for commercially available Ti sponge is 19 mm[109]. Therefore, after hydrogenation, the $TiH_2$ would need to be milled from 19 mm down to the required particle size for compaction and sintering (~37 μm).

In forming $TiH_2$, the hydrogenation reaction is highly exothermic ($\Delta H_{\mathrm{Ti+H_2 \rightarrow TiH_2}} = -2.97$ kJ/g)[110]. Therefore, this reaction produces much more energy than that required to heat the Ti to an elevated temperature at which it would react spontaneously with $H_2$ to form $TiH_2$. As such, the energy required to heat the Ti in order to form $TiH_2$ would be negative in any commercial process. To keep this model conservative, this term is simply disregarded in this model. However, in order to form $TiH_2$ from Ti sponge, a significant amount of $H_2$ gas is required. $H_2$ gas has a relatively high embodied energy, due to the energy-intensive processes used to produce it. Therefore, the embodied energy of $H_2$ gas used to form $TiH_2$ has been considered.

The vast majority of $H_2$ gas used in industry is produced by the decomposition of natural gas (methane). In the most common process, methane is decomposed via a process called plasma-catalyst steam reforming, which requires 186 kJ of electricity per mole of $H_2$ gas produced[111]. Using this value, the embodied energy of hydrogen used in this process can be calculated:

$$E_{H_2} = 186\,\frac{\text{kJ}}{\text{mol H}_2} \times \frac{1\text{ mol H}_2}{1\text{ mol TiH}_2} \times \frac{1\text{ mol TiH}_2}{49.88\text{ g}} = 3.73\text{ kJ/g} = 1035.76\text{ kWh/ton} \quad \text{Eq. 3.1}$$

The amount of energy required to ball mill a certain material to a required passing size can be calculated from the Bond Work Index ($W_I$) of that material[112]. Unfortunately, the $W_I$ for $TiH_2$ is not published in the literature. However, Haffez has shown that the Bond Work Index of brittle materials is strongly correlated to the elastic modulus ($E$) by the relationship given in Eq. 3.2[113]. The elastic modulus of $TiH_2$ is reported in the literature as 128.2 GPa[114]. Therefore, the $W_I$ of $TiH_2$ can be calculated:

$$W_I\,(\text{kWh/ton}) = 6.3\ln E - 10.6 = 6.3\ln(128.2) - 10.6 = 20.0\text{ kWh/ton} \quad \text{Eq. 3.2}$$

Therefore, the amount of work required to reduce 19 mm $TiH_2$ produced by hydrogenation of sponge to the required size of 37 μm can be estimated using Bond's equation[112]:

$$E_{\text{mill}} = W_I\left(\frac{10}{\sqrt{P_{80}}} - \frac{10}{\sqrt{F_{80}}}\right) = 20.0\left(\frac{10}{\sqrt{37}} - \frac{10}{\sqrt{19000}}\right) = 31.39\text{ kWh/ton} \quad \text{Eq. 3.3}$$

In Eq. 3.3, $P_{80}$ is the size under which 80% of product passes and $F_{80}$ is the size under which 80% of the feedstock passes.

Using the values calculated in Eq. 3.1 and Eq. 3.3, the total energy required for the powder preparation step of the HSPT process can be calculated:

$$E_{\text{powder prep}} = E_{H_2} + E_{\text{mill}} = 1067.15 \text{ kWh/ton} \quad \text{Eq. 3.4}$$

*The energy required to produce $H_2$ gas as well as the energy required for milling are both assumed to be entirely supplied by electricity*.

It should be noted that the energy requirements for the powder preparation step have been calculated per ton of $TiH_2$. However, the final product produced by the HSPT process is Ti metal. Because of this fact, this step will have a yield equal to the mass ratio of Ti to $TiH_2$, which is 96:100 or 96%. This value has been incorporated in Table 3.2 to account for weight loss due to hydrogen evolution during the process.

3.1.1.2 Compaction

To model the compaction energy requirements, it was assumed that the vast majority of energy will be used by the hydraulic pumps to generate the compaction pressure in a cold isostatic press (CIP). In order to calculate the theoretical work required to achieve a specified change in density, one must know how the density of a compact changes as a function of applied pressure. The tap density (starting density) of the milled $TiH_2$ powder has been measured by the author at 2.13 g/cc. Additionally, based on the compaction data presented in section 5.2, it was determined that the green density of $TiH_2$ as a function of CIP pressure agrees nicely with the following compaction equation reported by German[27]:

$$\rho = \rho_0 + AP^{1/3} \quad \text{Eq. 3.5}$$

In Eq. 3.5, $\rho_o$ is initial density, P is the compaction pressure, A is a process dependent constant (calculated as 1.518 kg-m$^{-3}$-Pa$^{-1/3}$ for this powder), and $\rho$ is the green density. Using this equation, one may calculate the *theoretical* work performed during CIP from

tap density of the feedstock powder (2.13 g/cc) to a typical green density (3.2 g/cc):

$$E_{\text{compaction,theo}} = \int PdV = -\int_{2130\frac{\text{kg}}{\text{m}^3}}^{3200\frac{\text{kg}}{\text{m}^3}} \frac{(\rho-\rho_0)^3}{A^3\rho^2}\,d\rho = 10.62\,\frac{\text{kJ}}{\text{kg}} = 2.95\ \text{kWh/ton} \qquad \text{Eq. 3.6}$$

Hydraulic efficiency is generally governed by frictional forces exerted on the pressure medium due to the geometry of the motors, pipelines, and pressure cells[115]. For this model, it was assumed that this process would have a hydraulic efficiency of 75% ($\eta_{\text{hydraulic}} = 0.75$), which is a rule-of-thumb efficiency value commonly used for calculations of hydraulic power consumption[115]. Therefore, taking into account the hydraulic efficiency, one may calculate the *actual* energy required for compaction as:

$$E_{\text{compaction}} = \frac{E_{\text{compaction,theo}}}{\eta_{\text{hydraulic}}} = 3.93\ \text{kWh/ton} \qquad \text{Eq. 3.7}$$

*It is assumed that all energy required for compaction will be supplied in the form of electricity to drive the hydraulic pumps.*

3.1.1.3 Sintering

In order to ensure an accurate furnace design, an industrial furnace manufacturer (Abbott Furnace Co.) was consulted during the preparation of this energy model[116]. During communications with Abbott, the requirements for a commercialized version of the HSPT process were discussed. From these conversations, Abbott either confirmed or corrected assumptions made by the author in developing the theoretical furnace design. Abbott then

provided a detailed quote for a furnace that would meet the requirements of the HSPT process as proposed by the author. Therefore, the design parameters provided in this section have been vetted by experts in sintering furnace design.

While most of the preliminary HSPT research to date achieved dehydrogenation under vacuum, it should be realized that the dehydrogenation thermodynamics and kinetics are ruled purely by the *partial pressure* of hydrogen and not by the total pressure of the environment. This means that dehydrogenation can be achieved under a protective gas at atmospheric pressure (1 bar), assuming the gas has a low enough hydrogen concentration. As such, HSPT can be conducted via a continuous sintering process using flowing argon gas. Therefore, for the HSPT sintering process, a continuous, fuel-fired sintering furnace with a stainless steel conveyor belt and three gas-shielded zones was modeled. Figure 3.2 gives the overall mass and energy balances of the HSPT sintering process designed for this model.

The *theoretical* energy required for sintering titanium by this method is calculated from the energy required to heat $TiH_2$ to the sintering temperature (1200°C) using the heat capacity of $TiH_2$ (0.603 J/g-K)[117], as well as the energy required to overcome the endothermic dehydrogenation reaction ($\Delta H_{TiH_2 \rightarrow Ti + H_2} = 2.97$ kJ/g)[110]:

$$E_{\text{sinter,theo}} = \int_{25℃}^{1200℃} C_{\text{p,TiH}_2} dT + \Delta H_{TiH_2 \rightarrow Ti + H_2}$$
$$= 3682.42 \frac{\text{kJ}}{\text{kg}} = 1022.89 \text{ kWh/ton} \qquad \text{Eq. 3.8}$$

The total sintering energy was calculated by modeling all other energy consumption sources (i.e. energy to heat the parts and the stainless steel conveyor belt, energy to heat

constant flow of shielding gas into each zone, energy to overcome the endothermic dehydrogenation reaction, heat transfer through furnace insulation, and the embodied energy of the gas). The specific energy of the process is strongly dependent on the production rate. Therefore, a single stream production rate of 434.9 kg/hr of Ti parts was chosen. In order to accommodate this production rate, it was assumed that a three zone furnace with a 314 stainless steel conveyor belt measuring 76.2 cm wide by 1 cm thick and moving at a rate of 2.54 cm/min was loaded with an average of 39.01 g/cm$^2$ of green parts to be sintered.

The next necessary determination for this calculation is the size and operating temperatures of each zone in the furnace. Using the current sintering profile for HSPT, one knows that the parts must sinter at 1200°C for 4 hours, they must go through the phase transformation step at 650°C for 4 hours, and then must be dehydrogenated at 750°C for 8 hours. Therefore, using the belt rate of 2.54 cm/min and the required dwell times, one may determine the length of each zone in the furnace to be 6.1 m each for Zone 1 and Zone 2, and 12.2 m for Zone 3. Based on the proposed belt width of 76.2 cm along with the literature reported dimensions for similar belt-driven furnaces[118] and the information provided by Abbott[116], the proposed furnace will have an interior muffle height of 17.78 cm and width of 81.28 cm.

The first energy consideration in modeling the sintering furnace is the enthalpy required to heat the parts and conveyor belt in each zone. This "ramp power" ($P_{ramp}$) can be calculated from reported heat capacity values for $TiH_2$ (0.603 J/g-K), Ti (0.524 J/g-K), and 314 stainless steel (SS) (0.5 J/g-K)[117,119] along with the mass flow rates of parts ($\mu_{parts}$ = 125.85 g/s) and belt ($\mu_{belt}$ = 7.9 g/s) into each zone:

$$P_{\text{ramp}} = \int_{25℃}^{1200℃} \left(\mu_{\text{parts}} C_{\text{p,TiH}_2} + \mu_{\text{belt}} C_{\text{p,SS}}\right) dT + \int_{1200℃}^{650℃} \left(\mu_{\text{parts}} C_{\text{p,Ti}} + \mu_{\text{belt}} C_{\text{p,SS}}\right) dT + \int_{650℃}^{750℃} \left(\mu_{\text{parts}} C_{\text{p,Ti}} + \mu_{\text{belt}} C_{\text{p,SS}}\right) dT = 57.88 \text{ kW} \quad \text{Eq. 3.9}$$

The second energy consideration is the power required to overcome the endothermic dehydrogenation reaction. This can be calculated from the literature-reported enthalpy of formation for $TiH_2$ ($\Delta H_{\text{TiH}_2 \rightarrow \text{Ti} + \text{H}_2} = 2.97$ kJ/g)[110] and the same mass flow rate of parts used in the previous calculation:

$$P_{\text{dehydro}} = \mu_{\text{parts}} \Delta H_{\text{TiH2} \rightarrow \text{Ti} + \text{H2}} = 374.27 \text{ kW} \quad \text{Eq. 3.10}$$

The third energy consideration will be the power required to heat the protective gases in each zone. These gases are required to both protect the parts and control the hydrogen concentration in the parts during sintering and phase transformation, as well as facilitate dehydrogenation in the final zone. The gas will run counter-current to the parts. This will allow the gas to be preheated by the parts as they are leaving the hotter zones and will, therefore, allow a large portion of the energy required to initially heat the parts to be reclaimed by the flowing gases.

It should be realized that the amount of $H_2$ contained in $TiH_2$ is more than sufficient to provide all of the $H_2$ gas required in the process. Therefore, only Ar will need to be pumped into the furnace to maintain the required $H_2$ partial pressure. In order to prevent contamination of the zones by back diffusion of gases, a sufficient overall linear velocity

of the Ar gas will be required. In order to determine the amount of Ar used during the process, a mass balance was established between the incoming Ar, the $H_2$ evolved from $TiH_2$, and the exhaust at Zone 3 and Zone 1 (Figure 3.2). It was assumed that the total volume of gas exiting either exhaust is equal. For this model, a carrier gas (Ar) linear velocity of 4 cm/s was assumed to be sufficient to counter back-diffusion. Therefore, the flow rate of Ar must be sufficiently greater than the volume of $H_2$ evolved to create a net linear velocity of the Ar gas of 4 cm/s towards the Zone 1 exhaust. It should be emphasized that 4 cm/s is the net velocity of Ar towards Zone 1, not total velocity of the flowing gas. Therefore, this will create an atmosphere of pure Ar at the Zone 3 exhaust, necessary for dehydrogenation, while creating a concentration gradient of $H_2$ in furnace from 0% at the Zone 3 exhaust up to ~90% at the Zone 1 exhaust. These gas concentrations will maintain a sufficient hydrogen concentration within the Ti parts in Zone 1 and 2 and allow for complete dehydrogenation in Zone 3. Using the necessary linear velocity of Ar out of Zone 1 (4 cm/s) and the internal cross-sectional area of the muffle (1445.16 $cm^2$), a required Ar flow rate of $Q_{Ar,Zone1}$ = 346.84 L/min at the Zone 1 exhaust was calculated:

$$Q_{\mathrm{Ar,Zone1}} = v_{\mathrm{Ar}} \times A_{\mathrm{Muffle}} = 346.84\ \mathrm{L/min} \qquad \text{Eq. 3.11}$$

The rate of $H_2$ evolution is determined by the calculated quantity of $H_2$ in $TiH_2$ (0.49 L $H_2$/g $TiH_2$) and the rate of parts entering the furnace ($\mu_{parts}$ = 125.85 g/s), which calculates to $Q_{H2}$ = 3330.06 L/min:

$$Q_{\mathrm{H_2}} = \mu_{\mathrm{parts}} \times \frac{0.49\ \mathrm{L\ H_2}}{\mathrm{g\ TiH_2}} = 3330.06\ \mathrm{L/min} \qquad \text{Eq. 3.12}$$

Finally, by solving the gas mass balance, the flow rate of Ar into the furnace must be

$Q_{\mathrm{Ar,total}}$ = 4023.74 L/min:

$$Q_{\mathrm{Zone1,total}} = Q_{\mathrm{Zone3,total}} = Q_{\mathrm{Ar,Zone3}} = Q_{\mathrm{H_2}} + Q_{\mathrm{Ar,Zone1}} = 3676.90\ \mathrm{L/min} \quad \text{Eq. 3.13}$$

$$Q_{\mathrm{Ar,total}} = Q_{\mathrm{Ar,Zone1}} + Q_{\mathrm{Ar,Zone3}} = 4023.74\ \mathrm{L/min} \quad \text{Eq. 3.14}$$

The $H_2$ gas is evolved from $TiH_2$ and is, therefore, heated in the solid phase and accounted for in Eq. 3.9. However, the Ar enters the furnace at room temperature and its heat capacity must accounted for. Using the current sintering conditions for HSPT and the heat capacity of Ar reported in the literature ($C_{\mathrm{P,Ar}}$ = 20.79 J/mol-K)[119], the power required to heat the Ar gas can be calculated. For this calculation, it should be realized that all of the Ar needs to be heated to 750 °C in Zone 3. However, as shown above, only 346.84 L/min ($Q_{Ar,Zone1}$) of Ar moves through Zones 1 and 2 and, therefore, must be heated to 1200 °C.

In addition to the energy required to heat the Ar, the embodied energy of Ar must also be determined as a consumable of the process. The embodied energy for Ar was reported in the literature as $E_{\mathrm{Ar}}$ = 16.46 kJ/mol[120]. Therefore, using the heat capacity of Ar, flow rates in each zone, zone temperatures, and the embodied energy of Ar, the total power consumed by the gas can be calculated:

$$P_{\mathrm{gas,heat}} = \frac{1}{24.5\mathrm{L/mol}}\left[Q_{\mathrm{Ar,total}}\left(\int_{25℃}^{750℃} C_{\mathrm{p,Ar}}dT + E_{\mathrm{Ar}}\right) + Q_{\mathrm{Ar,Zone1}}\int_{750℃}^{1200℃} C_{\mathrm{p,Ar}}dT\right] = 65.99\ \mathrm{kW} \quad \text{Eq. 3.15}$$

The last energy consideration will be heat lost due to imperfect insulation of the furnace. This is the most subjective of the calculations, as the efficiency of the insulation can vary widely depending on the design of the furnace and selection of the insulating materials. Therefore, to make a model which is representative of a feasible industrial process, a design was chosen similar to those employed in continuous belt-driven furnaces currently used in the PM industry[118] and consistent with the recommendations of Abbott Furnace Co.[116]. For the proposed furnace, each zone will be insulated by high density (22 lb/ft$^3$ or 0.35 g/cm$^3$)[116,121] insulating fiberboard at a thickness of $t$ = 12 inches (30.48 cm). The thermal conductivity of the insulation will vary with the internal temperature of each zone. Therefore, the following relationship between furnace temperature and thermal conductivity was calculated by the author using technical data for thermal conductivity provided by Refractory Specialties Inc. (RSI), a leading manufacturer of furnace insulation, for their high density fiberboard (Gemcolite® HD FG23-112)[121]:

$$k\ (\text{W/cm-℃}) = 1.434 \times 10^{-6} T(℃) + 1.971 \times 10^{-4} \qquad \text{Eq. 3.16}$$

Based on the muffle height, width, and length of each zone, we know that Zones 1 and 2 will each have an internal surface area of $SA_{\text{Zone1}} = SA_{\text{Zone2}} = 1.21 \times 10^5$ cm$^2$ and Zone 3 will have an internal surface area of $SA = 2.42 \times 10^5$ cm$^2$. Therefore, the surface area, thermal conductivity, and temperature of each zone can be used to calculate the power required to compensate for heat loss ($q$) in each zone through the furnace insulation:

$$P_{\text{insulation}} = q_{\text{Zone1}} + q_{\text{Zone2}} + q_{\text{Zone3}}$$

$$= \frac{k_{1200^\circ\text{C}} SA_{\text{Zone1}}}{t} + \frac{k_{650^\circ\text{C}} SA_{\text{Zone2}}}{t} + \frac{k_{750^\circ\text{C}} SA_{\text{Zone3}}}{t} \qquad \text{Eq. 3.17}$$

$$= 19.61 \text{ kW}$$

By combining the power for each source of heat flow/loss, one may calculate the *total* specific energy required for the sintering process:

$$E_{\text{sinter}} = \frac{P_{\text{ramp}} + P_{\text{dehydro}} + P_{\text{gas}} + P_{\text{insulation}}}{\mu_{\text{Ti,parts}}} \qquad \text{Eq. 3.18}$$

$$= 1190.51 \text{ kWh/ton}$$

*It is assumed that all energy required for sintering will be thermal energy from fuel.*

As opposed to the powder preparation and compacting steps, the specific energy of the sintering step was calculated in Eq. 3.18 based on the mass of Ti parts produced, not the input mass of $TiH_2$. Therefore, the yield of the sintering step in this model is 100%.

### 3.1.2 Wrought Process Energy Calculations

The most common wrought process to produce Ti-6Al-4V bar stock involves ingot formation by vacuum arc remelting (VAR) (most grades are achieved by double or triple melting the material), followed by hot-working near the β-transus to produce the desired geometry (2 inch round bar in this model)[37]. For most commercial wrought processes, additional working and heat treatments would be required to produce a refined microstructure for superior mechanical properties (Figure 1.1). However, a vast number of different working and heat treating processes are used in the industry. For this reason, this model only accounts for the primary thermomechanical work to produce the desired

mill product geometry. Therefore, the actual amount of energy required to produce 2" bar stock via wrought processing with an ultrafine microstructure that would be competitive with the as-sintered HSPT microstructure would be greater than that calculated in this model. However, as previously emphasized, this model has been created to provide a conservative evaluation of HSPT versus wrought processing. Therefore, this underestimation only increases the conservativeness of this model.

3.1.1.4 Ingot Formation - Vacuum Arc Remelting (VAR)

The *theoretical* energy required to VAR a double-melt ingot will be twice the enthalpy required to heat titanium to its melting point and overcome the enthalpy of fusion[119]:

$$E_{\mathrm{VAR,theo}} = 2\left(\int_{25℃}^{1670℃} C_{\mathrm{p,Ti}}\,dT + \Delta H_{\mathrm{fusion,Ti}}\right) = 2315.16\,\frac{\mathrm{kJ}}{\mathrm{kg}} = 643.10\ \mathrm{kWh/ton} \qquad \text{Eq. 3.19}$$

In order to calculate the total electricity requirements of VAR, actual energy requirements for industrial VARs for the production and recycling of iron alloys reported in literature[122] were compared to theoretical energy requirements to heat and melt iron. From this comparison, it has been determined that VARs operate between 23.8% and 31.4% total efficiency. Therefore, a value of 33% has been chosen to give wrought processing the most optimistic evaluation for this model. Taking this efficiency into account, one may calculate the actual energy required for VAR to form an ingot with a standard 28 inch diameter[123]:

$$E_{\mathrm{VAR}} = \frac{E_{VAR,\mathrm{theo}}}{\eta_{\mathrm{VAR}}} = 1948.79 \text{ kWh/ton} \qquad \text{Eq. 3.20}$$

*It is assumed that all energy required for VAR will be supplied in the form of electricity.*

3.1.1.5 Forging

Modeling a forging process is exceedingly difficult due to the myriad parameters which affect the energy consumption of the process. Therefore, in order to simplify the problem, the theoretical energy requirements to heat and mechanically work the material were considered. Then, typical efficiencies reported in literature for the equipment used in these industrial processes were applied. The forging pressure ($P$ = 200 MPa) and temperature (900 °C) used in this model were taken from typical values for Ti-6Al-4V reported in the literature[37,124]. For this model, a standard 71.12 cm (28 inch) diameter ($V$ = 769,231 cm$^3$), 3,400 kg, double-melt ingot[123] produced by VAR was assumed to be the forge feedstock. It was then assumed that the ingot would be worked via multiple passes to produce 2 inch (5.08 cm) diameter round bar stock by a gyratory forging machines (GFM). The *theoretical* mechanical work required to reduce the diameter to 2 inches at 200 MPa can be calculated using the following formula, where F is force, r is the radius, P is pressure, and V is volume:

$$E_{\mathrm{forge,mech,theo}} = \int_{r_\mathrm{i}}^{r_\mathrm{f}} F dr = \int_{r_\mathrm{i}}^{r_\mathrm{f}} \frac{2PV}{r} dr = 2PV \ln\left(\frac{r_\mathrm{f}}{r_\mathrm{i}}\right) = 66.34 \text{ kWh/ton} \qquad \text{Eq. 3.21}$$

In Eq. 3.21, $P$ is the forging pressure (200 MPa), $V$ is the ingot volume (769,231 cm$^3$), $r_\mathrm{i}$ is the initial radius (71.12/2 = 30.56 cm), and $r_\mathrm{f}$ is the final radius (5.08/2 = 2.54 cm).

In this model, it is assumed that the GFMs are hydraulic. Therefore, taking into account the rule-of-thumb hydraulic efficiency of 75% ($\eta_{\text{hydraulic}} = 0.75$)[115], one may calculate the *actual* mechanical work required for forging:

$$E_{\text{forge,mech}} = \frac{E_{\text{forge,mech,theo}}}{\eta_{\text{hydraulic}}} = 88.46 \text{ kWh/ton} \qquad \text{Eq. 3.22}$$

*It is assumed that all energy required for the mechanical work will be supplied in the form of electricity to drive the hydraulic pumps.*

The theoretical energy required to achieve and maintain the required minimum forging temperature (900 °C)[37] is the sum of the initial energy to heat the material from room temperature and the additional energy required to reheat the material after each pass. It has been assumed that the material will cool approximately 200°C between passes[125]. Assuming the volume of the ingot remains constant, one may calculate the initial and final lengths to be 193.6 cm and 379.5 m, respectively. If a typical elongation of 30% is achieved for each pass[124], this forging process will require 21 passes. Therefore, the *theoretical* energy to heat the titanium to the appropriate forging temperature is:

$$E_{\text{forge,heat,theo}} = \int_{25℃}^{900℃} C_{\text{p,Ti}} dT + 21 \int_{700℃}^{900℃} C_{\text{p,Ti}} dT = 738.69 \text{ kWh/ton} \qquad \text{Eq. 3.23}$$

Forge furnaces are reported to operate at 20~60% efficiency[125]. Therefore, to be conservative, it has been assumed the forging furnaces operate at 60% efficiency ($\eta_{\text{furnace}} = 0.60$). Taking this efficiency into consideration, one may calculate the *actual* energy required to heat the material during forging:

$$E_{\text{forge,heat}} = \frac{E_{\text{forge,heat,theo}}}{\eta_{\text{furnace}}} = 1231.16 \text{ kWh/ton} \qquad \text{Eq. 3.24}$$

*It is assumed that all energy required for heating will come from the burning of fuel.*

Traditional titanium forging operations tend to have low yields due to oxide formation and removal[107]. Therefore, a conservative material yield for the forging step of 75% has been considered in the calculation. It should be noted that the removal of the oxide layer is usually performed between forging passes, which would result in greatly increased cooling and reheating energy requirements. However, this consideration has been omitted in the model to maintain an optimistic evaluation of wrought processing.

## 3.2 Energy Model Results

Table 3.1 gives a comparison of the theoretical energy requirements for the two processes when process efficiencies are ignored. This comparison is useful from a standpoint that additional engineering optimizations are always possible for any process, though the thermodynamics of the desired reactions are an insuperable lower boundary for specific energy consumption.

Table 3.2 gives the actual energy requirement comparison for the two processes as calculated in this model, accounting for the efficiency of each step in each process. As mentioned above, the energy required for HSPT sintering was determined by the mass and energy balances of the entire sintering process, whereas the remaining process efficiencies (CIP/forge hydraulics, VAR furnace, and forge furnace) were assumed to be consistent with values reported in literature.

Coal energy equivalence was included in Table 3.2 to normalize the difference between

available thermal energy and electrical energy from fossil fuels with regard to environmental implications. In the United States, the majority of electricity is produced by burning coal[126], which only provides 2000 kWh/ton when converted into electricity, versus 6150 kWh/ton when used for thermal energy. Therefore, taking this phenomenon into consideration is important when considering fossil fuel consumption and greenhouse gas (GHG) emissions. The equivalency could have also been calculated with regard to natural gas or oil volumes with the same result, as power plants all tend to convert fuel thermal energy to electrical energy at approximately a 3:1 ratio, regardless of fuel[126].

Based on this model, wrought processing is approximately 41% more energy intensive than HSPT on a purely *theoretical* level. However, when equipment efficiency, process yields, and electrical generation form fossil fuels are considered, wrought processing becomes more than twice as energy-intensive as HSPT. However, it should be emphasized that great care was taken to provide a very conservative evaluation of HSPT and a very optimistic evaluation of traditional wrought processing. Furthermore, the model above assumes that both processes produce 2 inch round bar stock, a geometry that does not take into account the massive energy and cost savings of producing near-net-shape parts. Even with this bias towards wrought processing within the model, the results are clear that the HSPT process is significantly less energy-intensive. However, it is important to realize that the energy savings from using the HSPT process will be significantly greater than what was predicted in this model if the following important considerations were taken into account:

- Near-net-shape ability of HSPT
    - This would increase the energy efficiency by the factor equaling the

typical buy-to-fly ratio of the wrought-processed part *(up to 20 fold for complex geometries)*

- Recycling of $H_2$ gas
    - It was assumed that *none of the $H_2$ used in the HSPT process was recycled*
    - If $H_2$ was recycled in the HSPT process, it would *decrease the energy consumption of HSPT by as much as 70%*
- Secondary thermomechanical processing (TMP) during wrought processing
    - Secondary TMP is necessary in wrought processing to produce a refined microstructure and superior mechanical properties
    - The bar stock produced by the wrought process proposed in this model would have mechanical properties far inferior to the ultrafine grained (UFG) microstructure produced by the proposed HSPT process

Table 3.1: Theoretical minimum energy requirements of the modeled processes.

| **HSPT** | **(kWh/ton)** | **Wrought Processing** | **(kWh/ton)** |
|---|---|---|---|
| Powder Preparation | 31.39 | | |
| Compaction | 2.95 | VAR | 643.10 |
| Sintering | 1022.89 | Forging | 805.04 |
| **Total** | **1025.84** | **Total** | **1448.14** |

Table 3.2: Calculated energy consumption and equivalent coal consumption of the modeled processes.

| **HSPT** | **Electricity (kWh/ton)** | **Fuel (kWh/ton)** |
|---|---|---|
| Powder Production (kWh/ton) | 1067.15 | 0 |
| Powder Production Yield | 96% | 96% |
| Compaction (kWh/ton) | 3.93 | 0.00 |
| Compaction Yield | 96% | 96% |
| Sintering (kWh/ton) | 51.81 | 1138.70 |
| Sintering Yield | 100% | 100% |
| Total Energy | 1214.07 | 1138.70 |
| Equivalent Coal (ton Coal/ton Ti) | 0.61 | 0.19 |
| **Total Coal (ton Coal per ton Ti)** | **0.79** | |
| **Wrought Processing** | **Electricity (kWh/ton)** | **Fuel (kWh/ton)** |
| VAR (kWh/ton) | 1948.79 | 0.00 |
| VAR Yield | 100% | 100% |
| Forging (kWh/ton) | 88.46 | 1231.16 |
| Forging Yield | 75% | 75% |
| Total Energy | 2716.32 | 1641.54 |
| Equivalent Coal (ton Coal/ton Ti) | 1.36 | 0.27 |
| **Total Coal (ton Coal per ton Ti)** | **1.63** | |

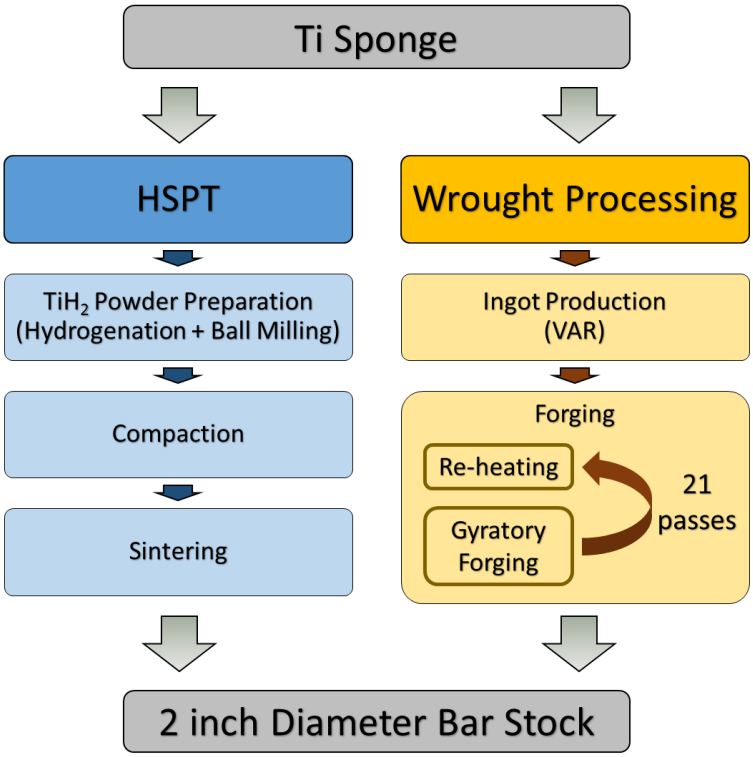


Figure 3.1: Flow sheet of the HSPT and wrought processing steps proposed in the energy model.

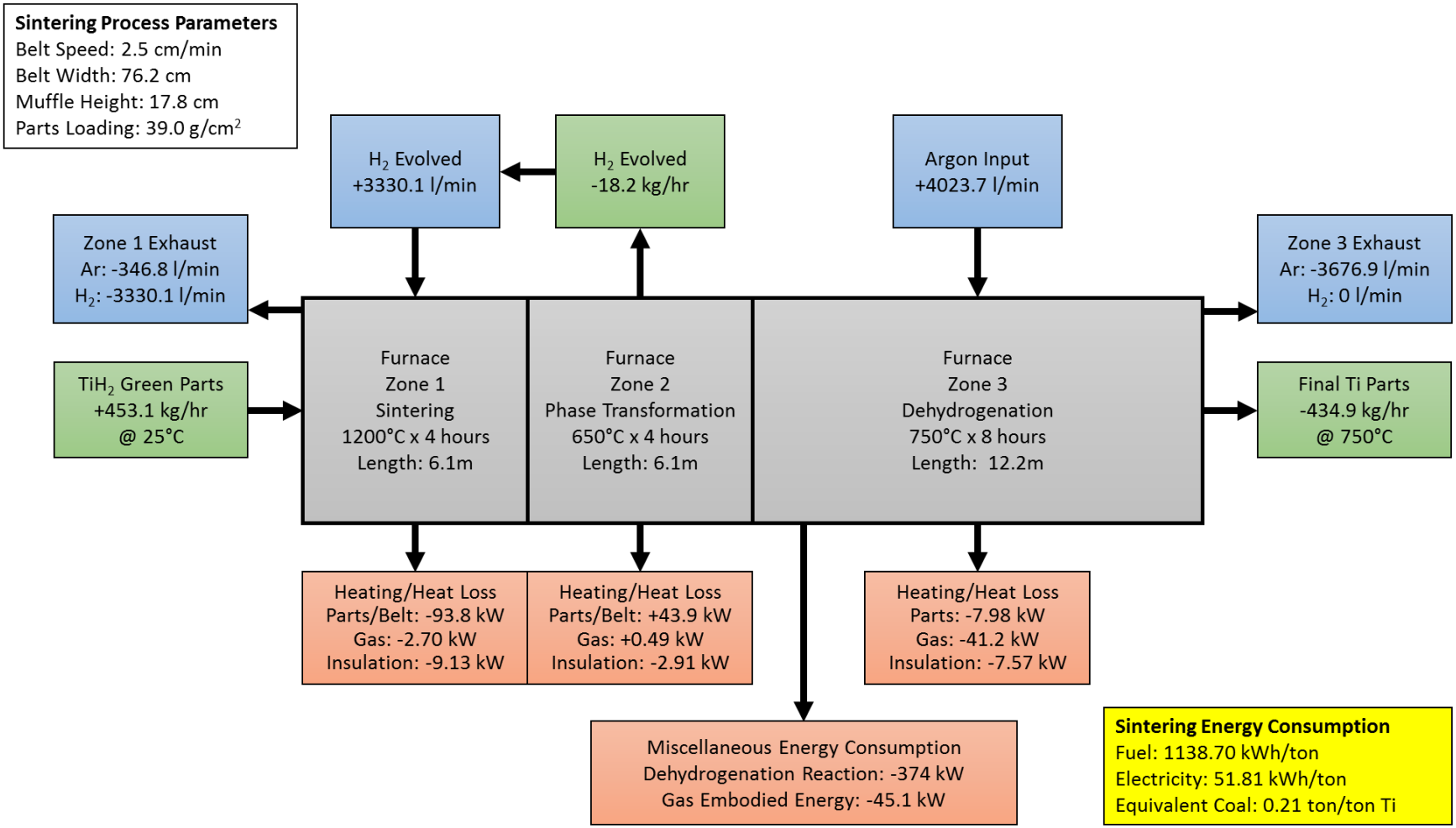


Figure 3.2: Mass and energy balances of the HSPT sintering step proposed in the energy model.

# CHAPTER 4

## EXPERIMENTAL PROCEDURES

Typically, HSPT is a blended elemental (BE) PM process. Of course, pre-alloyed (PA) powders could also be used with HSPT. However, PA powders are generally more expensive and are unnecessary based on current results from the BE method. The most common HSPT practice is to blend a commercially pure titanium hydride (CP-$TiH_2$) powder with a master alloy powder via mechanical mixing to produce the desired titanium alloy. In the case of Ti-6Al-4V, CP-$TiH_2$ is blended with 9.6 wt% 60Al-40V master alloy. Therefore, after dehydrogenation, the alloy will have the appropriate composition (90 wt% Ti, 6 wt% Al, and 4 wt% V). The CP-$TiH_2$ can come from traditional and/or low cost-sources including virgin metal from Kroll or an alternative extractive process, recycled scrap or turnings, and/or sponge fines. It is also possible to use a low-cost, pre-alloyed source, such as Ti-6Al-4V machine turnings that have been hydrogenated[127]. The excellent milling behavior of hydrogenated titanium makes it is easy to produce a powder of the required size from almost any source. Additionally, $TiH_2$ has excellent compaction behavior resulting from the propensity of the powder to crush during compaction, meaning powder with irregular particle morphologies is acceptable for HSPT. Finally, when compared with Ti metal, $TiH_2$ is much less reactive. Therefore, the powder is not prone to contamination from the atmosphere during handling. The only important concern when

sourcing a powder would be the initial cleanliness of the feedstock.

During the research performed in this study, the vast majority of the samples were prepared by the experimental procedure outlined in Figure 4.1. The details of each processing step will be discussed in the following sections of this chapter.

## 4.1 Powder Preparation

The task of studying powder preparation has been largely undertaken by Lu Yang. Ms. Yang was a Masters student working on the same HSPT project as the author. The results of her research were the subject of her Master's thesis[7]. Therefore, the method and results of Ms. Yang's study will not be discussed in any detail in this dissertation. However, based on Ms. Yang's research, a reliable process has been developed for preparing powder of the proper size, morphology, and purity for this study. This process is described in this section.

For this study, -20+60 mesh CP-$TiH_2$ was received from Reading Alloys, an AMETEK company. The large particle size was chosen to minimize the interstitial contaminants in the feedstock powder. The powder was milled in a rolling ball mill under a protective argon atmosphere in a stainless steel jar with a 9.7 cm internal diameter. The jar was loaded with a 60 vol% charge of 6 mm stainless steel balls and a ball to $TiH_2$ powder charge of 10:1 by mass (~5:1 by volume). The powder was then milled at 80 RPM for 30 minutes. After milling, the powder was sieved using an ultrasonic sieve shaker and the -400 mesh (<37 μm) powder was collected. In the earlier stages of this research project, -325 mesh (<44 μm) powder was used. However, results have shown that -400 mesh (<37 μm) powder results in better compaction and densification behavior without a noticeable effect on purity. Therefore, this particle size was chosen for all experiments detailed in this

dissertation.

After sieving, the CP-$TiH_2$ was blended with 9.6 wt% of -325 mesh (<44 μm) 60Al/40V master alloy, also supplied by Reading Alloys (AMETEK). Blending was achieved by combining the powders with the required mass fractions and loaded in either a turbula-style shaker mixer in a 1 L Nalgene bottle, or a V-blender. In both machines, blending was carried out for a minimum of 1 hour to ensure thorough homogenization.

## 4.2 Cold Isostatic Compaction

Green compacts were prepared from the blended powder using a cold isostatic press (CIP). 60 grams of blended powder was loaded into a CIP bag using a funnel. The CIP bags were purchased from Trexler Rubber. The internal dimensions of the CIP bag were 0.75" (19 mm) diameter by 5" (127 mm) long and were made of natural latex rubber to allow for highly elastic behavior of the bag during pressing. The loaded CIP bags were then loaded into the CIP (American Isostatic Presses CP360) and compacted at 350 MPa for 7 minutes.

The loose and tap density of the powder was determined using a graduated cylinder to determine the volume of a known mass of powder before and after tapping. Tap density was determined by using a Quantachrome Dual Autotap™ to tap the powder until the density stopped increases (usually at about 1,000 taps).

The green density of compacts were determined using vacuum impregnation and the Archimedes method. The green samples were first weighed to determine their mass before vacuum impregnation. The samples were then impregnated by submersing the sample in vegetable oil under vacuum, therefore allowing the vegetable oil to penetrate into the open

porosity of the sample. Finally, the samples were weighed when suspended in water to determine the volume of the sample by the Archimedes method of buoyancy.

### 4.3 Thermal Processing

All sintering and dehydrogenation processes, as well as many heat treatments, were conducted in a custom built tube furnace that has been nicknamed Titan. The heating elements and electric enclosure of the tube furnace was purchased from Sentrotech. The furnace was equipped with Eurotherm 2404 temperature controller using a type-S thermocouple that was suspended at the center of the furnace tube. The Eurotherm 2404 was outfitted with a DC temperature transmission module, which transmits the current temperature (process value or PV) of the furnace as a 0-10 V analog signal for real-time data acquisition. The furnace tube was made of Kanthal APM alloy, which is a high temperature Fe-Cr-Al alloy capable of withstanding continuous use in air up to 1300 ºC. The atmosphere of the furnace was controlled using two mass flow controllers (MFC, Allborg GFC): one for ultra-high purity (UHP) $H_2$ and one for UHP Ar. Both MFC's had a range of 0 to 10 L/min with 1.5% full range accuracy. High vacuum was achieved using an Edward Diffstak 100/300 diffusion pump, capable of reaching $10^{-5}$ Pa vacuum levels. The entire vacuum system was custom designed by the author to handle the high flow rates of hydrogen during sintering and dehydrogenation experiments. The vacuum system included a new type of compression fitting for the furnace tube designed by the author.

### 4.3.1 Sintering and Dehydrogenation

For continuity in the data, a "best practice" was determined as the standard HSPT sintering profile in this study. This sintering practice gave the best consistent results in previous research and was, therefore, determined as the baseline for comparing HSPT results with respect to its process parameters and subsequent processing, such as heat treating. This sintering profile is broken up into two individual process: sintering and dehydrogenation. Because vacuum sintering is the industry standard for traditional powder metallurgy (PM) Ti, vacuum sintering of Ti and $TiH_2$ powder was conducted for comparison with the HSPT results. When either of these sintering methods are referred to in this chapter, it can be assumed that the corresponding profile shown in Figure 4.2 for "HSPT" and "Vacuum" was used. Any variations to either of these profiles in an experiment will be explicitly mentioned with the presented data.

### 4.3.2 Dilatometry

Dilatometry experiments were conducted using a Linseis L75 PT horizontal dilatometer (Figure 4.3). During such experiments, instantaneous sample dimensions are determined by displacement of an alumina push rod that is in constant contact with the sample. The push rod is connected to a linear variable differential transformer (LVDT) with 0.125 nm resolution. The contact force between the push rod and the sample is controlled throughout the experiment and programmable up to 1000 mN[128].

Typical HSPT sintering profiles (Figure 2.4) were used to study the change in sample dimensions throughout the thermal profiles. The atmosphere in the dilatometer was controlled using 0-10 L/min MFCs (Aalborg GFC). High vacuum levels were controlled

using a Pfeiffer Hi-Cube Eco vacuum system which incorporates a roughing pump, turbo-molecular tube, and all the necessary control systems in a standalone unit[129].

### 4.3.3 Heat Treating

Heating treating was conducted using Titan (the furnace described at the beginning of section 4.3) when moderate cooling rates are acceptable. However, when quenching was required, the samples were heat treated in a Vulcan 3-550 box furnace to allow for easy removal and prevent unnecessary quench delay. To prevent unnecessary oxidation of the samples during heat treatments in the box furnace, which could to lead to changes in the microstructure and mechanical properties, each sample was coated in a glass frit suspension (Alumlube) to protect it from air. Quenching was performed by quickly unloading the samples from the box furnace and immediately immersing in room temperature water.

Figure 4.4 shows the heat treating profiles used in this study. The heat treating profiles used were based on the solution treatment and ageing (STA) and recrystallization annealing and ageing (RA) treatments that are well established in the industry. The details of these types of heat treatments and the microstructures that result are discussed in detail in CHAPTER 6.

For each of the heat treating experiments, the sample was first sintered and dehydrogenated using the standard HSPT profile (Figure 4.2). Two different dehydrogenation temperatures were used to study the effect of this parameter on the resulting microstructures and mechanical properties. Each heat treated sample was also aged at 550 ºC for 6 hours following heat treatment. Across the heat treating experiments, the effect of dwell temperature and cooling rate was studied. Two different dwell

temperatures were used; 954 ºC was used for high temperature treatments and 825 ºC was used for low temperature treatments. Additionally, three different cooling rates were studied; these cooling rates were furnace cooling (~10 ºC/min), air cooling (~350 ºC/min), and water quenching (>5000 ºC/min).

### 4.3.4 Gaseous Isostatic Forging Technology (GIFT)

While the densification behavior of titanium in the presence of dissolved hydrogen is excellent, the as-sintered material usually has residual porosity on the order of 1 vol% with pores having diameters on the order of 10~100 μm. Therefore, because porosity has a deleterious effect on mechanical properties, specifically fatigue performance, a method to remove the residual porosity after sintering was sought. Traditional thermomechanical processing (TMP) steps, such as high temperature forging, are energy-intensive and not conducive to developing a low-cost process. Additionally, traditional forging results in deformation of the part and is, therefore, not compatible with near-net-shape (NNS) processing. In this study, a nontraditional forging process was used to close the residual porosity and investigate the effect that the pores left after sintering have on mechanical properties. The process used in this study is called gaseous isostatic forging technology (GIFT). GIFT, also known as pneumatic isostatic forging (PIF) in the industry, is currently used commercially by AMETEK to close the porosity of steel and titanium components produced via casting or traditional powder metallurgy processes[130].

GIFT uses isostatic pressure delivered by a gaseous medium to close the residual porosity in PM components. Because the applied forging pressures is isostatic, the shrinkage that occurs during forging is isotropic. Therefore, the components retain their

desired geometry during this process and the NNS capability of the process as a whole is retained.

A schematic flow sheet of a typical GIFT process, based on descriptions available in the literature[130], is given in Figure 4.5. During GIFT, the samples are preheated in a furnace to the desired forging temperature. For titanium alloys, this temperature is typically between 845-900°C to lower the flow stress of the material being processed. The samples are then loaded into the GIFT pressure vessel, which is rapidly pressurized. For titanium alloys, a pressure of 45,000 psi is typically used. A typical GIFT apparatus is capable of pressurizing the sample chamber at a rate between 200 psi/sec to 4,000 psi/sec. Initial pressurization of the vessel is achieved by opening a valve between the sample chamber and gas reservoir, which was previously pressured using a gas booster pump. When the valve is opened, gas rushes from the reservoir to the sample chamber to achieve equilibrium between the two chambers. This initial pressurization is called an "air hammer", due to the high impulse of the gas pressurization. If necessary, the booster pump is then connected to the sample chamber by closing and opening the corresponding valves to increase the sample chamber pressure to the desired maximum forging pressure.

## 4.4 Metallography

Metallography was performed on the samples at various points throughout processing to identify the changes in the evolving microstructure as a function of sintering, dehydrogenation, and heat treatments. Each sample that was chosen for metallographic analysis was first sectioned using a precision sectioning saw (Allied High Tech – TechCut 5). Care was taken to ensure than an interior surface of each sample was exposed by the

sectioning process. This was done by sectioning a cylindrical sample at a thickness that is equal to or greater than the radius of the sample. Therefore, the center of the exposed surface was the maximum possible distance from an exterior surface during processing. This was done to make sure near-surface microstructural features, such as an α case, did not affect the data analysis performed during microscopy.

After sectioning, each specimen was mounted in a conductive copper- or graphite-impregnated mounting resin and mounted in a hot press (Allied High Tech – TechPress 2). The samples were then polished using an automatic polisher (Allied High Tech – MetPrep 3 with AD-5 automatic fluid dispenser). The samples were first ground with 180 grit SiC paper until flat, and then ground with 320 SiC paper to remove the coarse scratches. After grinding, the samples were polished using 9 μm followed by 3 μm diamond suspension in oil. For the final polishing step, the samples were polished for several minutes using an attack polish consisting of 0.04 μm colloidal silica mixed with 25~30 vol% of 30% $H_2O_2$. A small area of each polished sample was then etched to reveal microstructural details. The etchant used was Kroll's solution consisting of hydrofluoric acid, nitric acid, and water (2 mL HF: 3 mL $HNO_3$: 95 mL $H_2O$)[34].

Some samples were prepared for electron backscatter diffraction (EBSD) using electropolishing. Electropolishing was performed using a Struers LectroPol-5[131] with a ~20V potential and a high flow rate of electrolyte at room temperature. The electrolyte used consisted of perchloric acid, butoxyethanol, and methanol (30 mL 70% $HClO_4$: 175 mL $BuOC_2H_4OH$: 300 mL MeOH). This polishing method has a tendency to quickly etch the material. Therefore, a series of short polishes (30 seconds) was conducted on each sample to check for over-etching along the way.

Microstructural analysis was performed using confocal microscopy (Olympus OLS3500) and SEM (FEI Nova NanoSEM, FEI Helios DualBeam NanoLab, and Hitachi S4700 FESEM). Characterization of grain orientation and phase identification were conducted using EBSD (Oxford HKL detector on an FEI DualBeam NanoLab).

### 4.5 Mechanical Testing

Before mechanical testing, samples were sent out for machining into round tensile bars and fatigue bars. All machining was performed by Westmoreland Testing and Research (WMT&R), a NADCAP and A2LA accredited material testing laboratory[132], and Bingham Machine Company (BIMCO), an accredited machine shop that commonly performs work for the Department of Defense. The tensile bars were machined to ASTM E8[133] specifications with a 6.35 mm (0.25") diameter by 25.4 mm (1") long gauge and 3/8"-16 threaded grips. The fatigue bars had a 6.35 mm (0.25") diameter by 12.7 mm (0.5") length gauge with 12.7 mm (0.5") diameter smooth ends. The drawings used to machine the tensile and fatigue bars are shown Figure 4.6. Because surface defects can easily cause erroneous fatigue test results[103], the fatigue samples were polished to a mirror finish before testing (smooth bar). To remove all machining defects, the bars were first ground using 180 grit silicon carbide (SiC) paper to remove approximately 200 μm of material. The bars were then polished using the following series of steps:

60 grit SiC paper → 180 grit SiC paper → 240 grit SiC paper

→ 320 grit SiC paper → 400 grit SiC paper→ 600 grit SiC paper

→ 800 grit SiC paper → 1 μm colloidal $Al_2O_3$

Both tensile tests and fatigue tests were performed using an MTS Landmark Servohydraulic Test System capable of up to 120 kN of force and 60 Hz cyclic loading[134]. Control and data acquisition was accomplished using MTS TestSuite software.

During quasi-static tests, the tensile bars were threaded onto a high strength steel rod mounted within the wedge grips of the MTS. These tests were performed at a strain rate of $3 \times 10^{-4}\ s^{-1}$, as defined by the ASTM standard for testing titanium alloys[96].

Fatigue tests were performed as tensile tests with cyclic loading. These tests were performed at a range of maximum stresses (300~1000 MPa) to produce an S-N plot for each type of sample tested. Fatigue bars were loaded directly into the wedge grips of the MTS, as their grips were not threaded in order to prevent premature failure in the grip section of the bar. The cyclic loading was performed at a maximum of 35 Hz with an R-value of 0.1 to ensure crack closure between cycles.

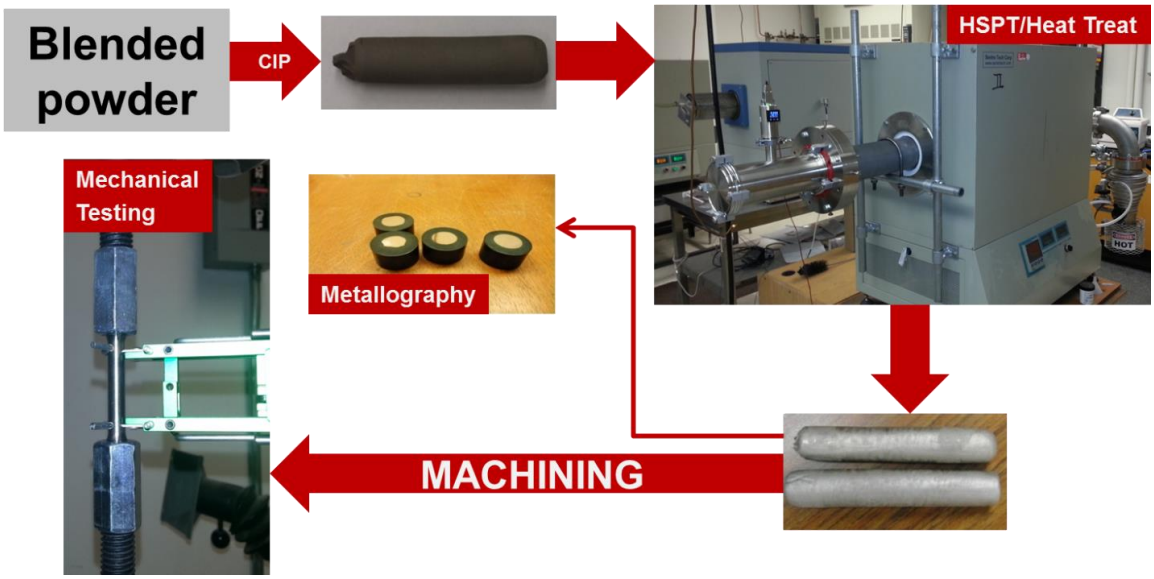


Figure 4.1: Flow sheet of the typical experimental procedure used for samples prepared in this study.

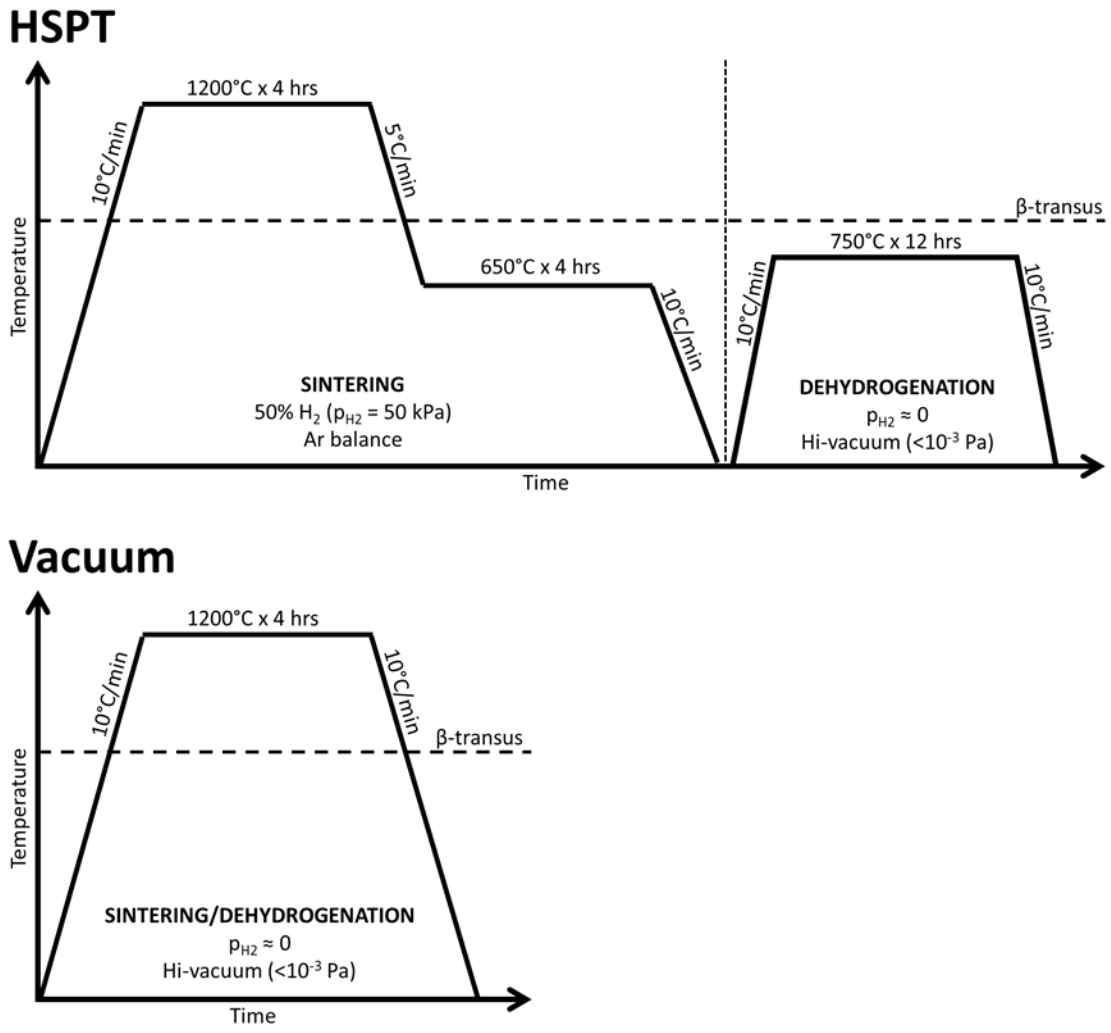


Figure 4.2: Standard sintering profiles used for HSPT and vacuum sintering.


Figure 4.3: Linseis L75 PT horizontal dilatometer.

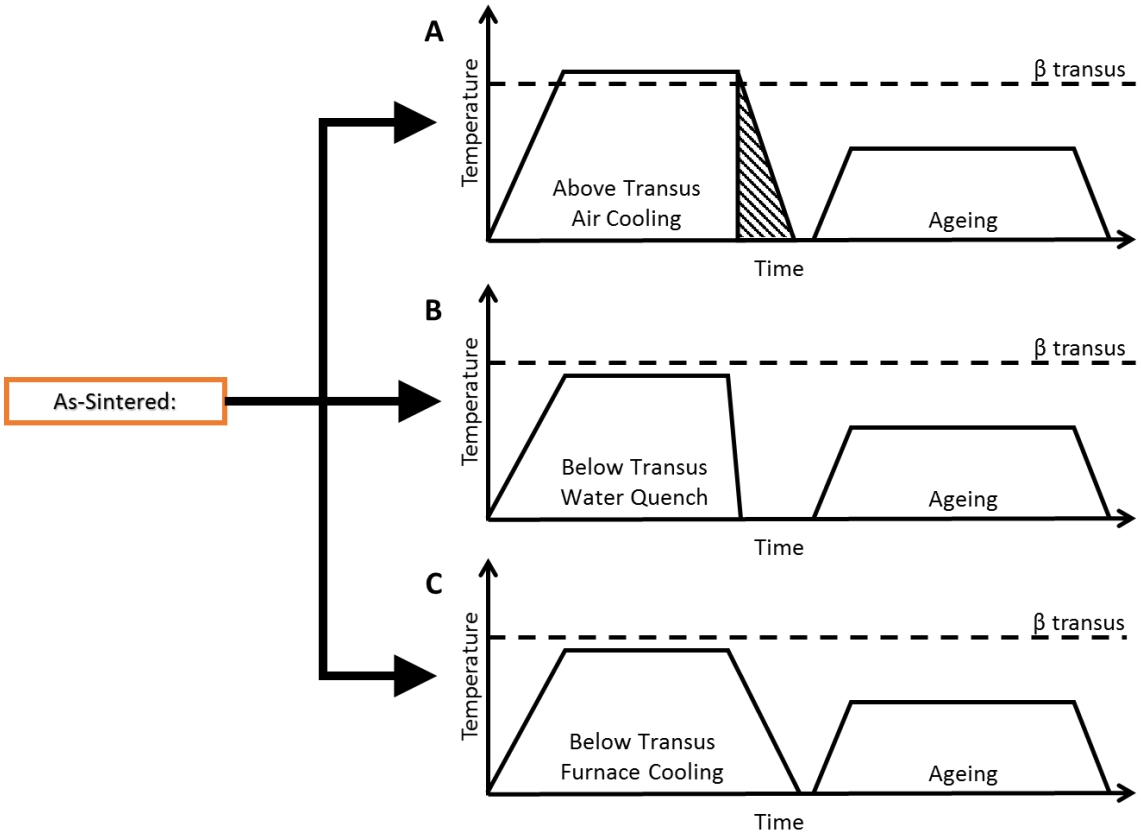


Figure 4.4: Schematic representation of the heat treatment profiles used in this study. A) Above transus heat treatment (typically used to produce a fully lamellar or "β-annealed" microstructure), B) below transus heat treatment with fast cooling (typically used to produce a bi-modal microstructure), and C) below transus heat treatment with slow cooling (typically used to produce a fully equiaxed microstructure). All heat treatments incorporate an aging step following the heat treatment.

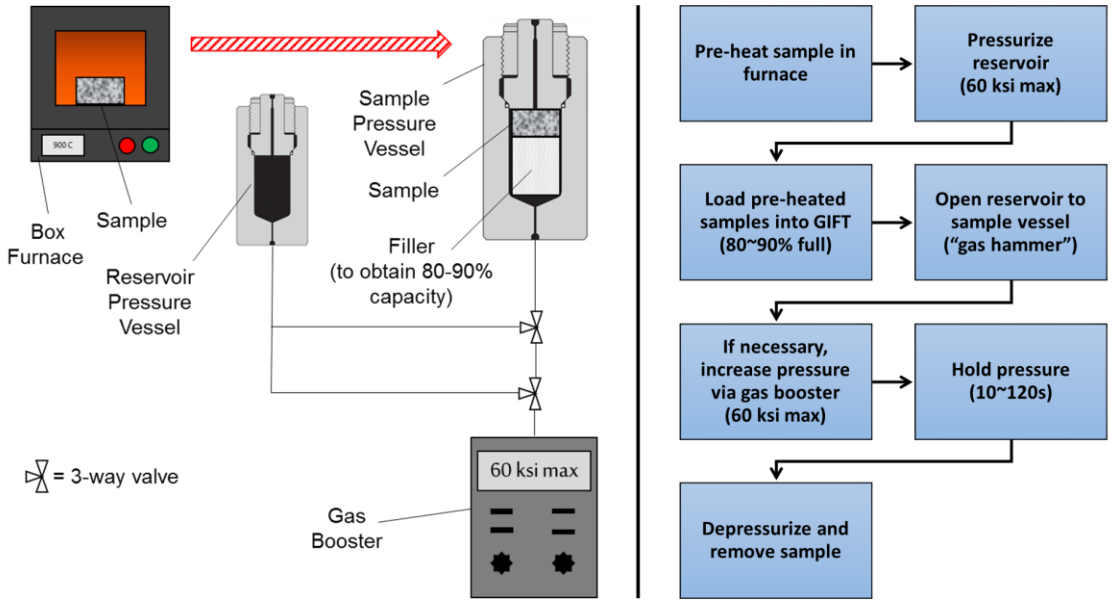


Figure 4.5: Schematic diagram and flow sheet of the GIFT process. Prepared from process descriptions available in the original patent[130].

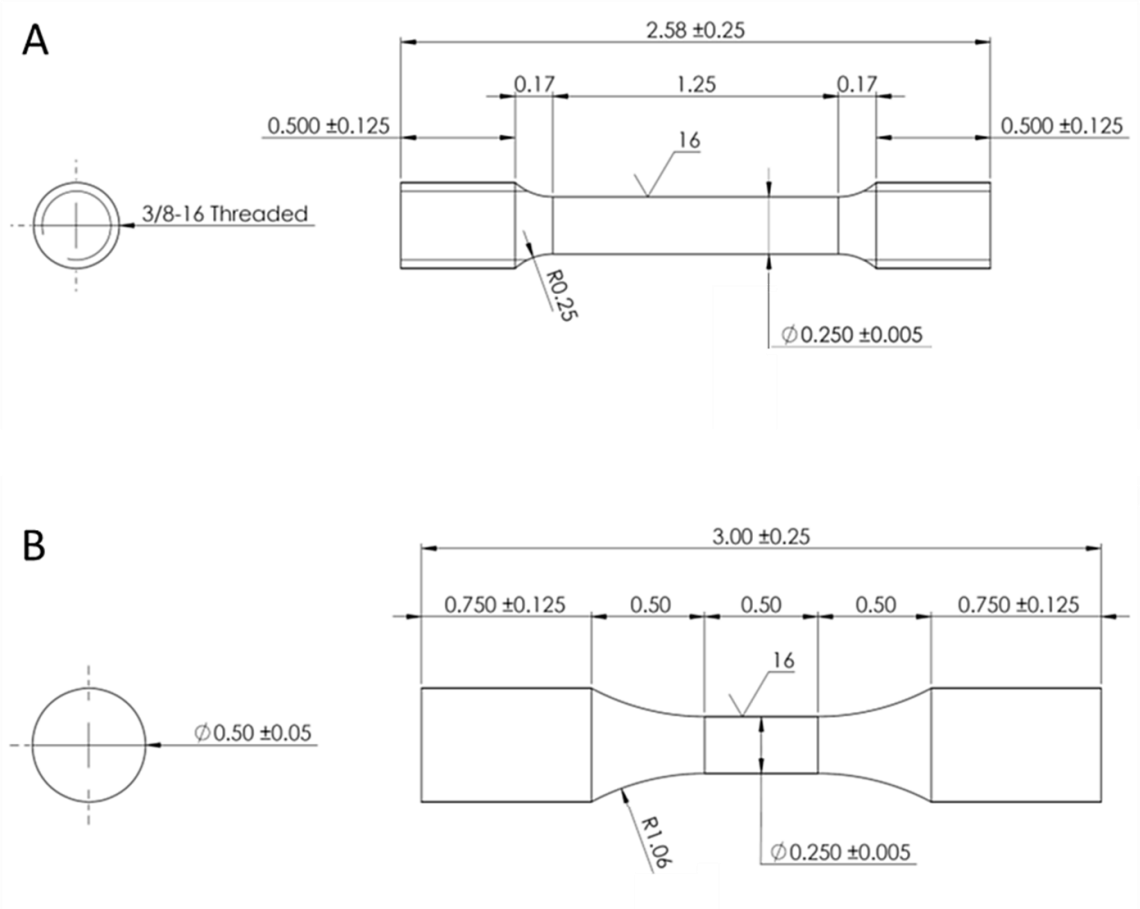


Figure 4.6: Drawing of the A) tensile and B) fatigue bar dimensions used for all mechanical testing discussed in this dissertation (all units are in inches).

# CHAPTER 5

# COMMINUTION, COMPACTION, AND DENSIFICATION RESULTS

In this chapter, the results obtained by the author regarding the characterization of the powder and its behavior during compaction and sintering will be discussed. The first two sections of this chapter will describe the powder that is used for the HSPT process as well as its compaction behavior. Dilatometry work that was performed to study the densification behavior of the alloys during sintering in hydrogen-containing atmospheres will also be presented.

## 5.1 Powder Characterization

Figure 5.1-A is an SEM micrograph of as-milled -325 mesh (<44 μm) CP-$TiH_2$. As mentioned early, during the early stages of this research, -325 mesh (<44 μm) was chosen as the desired particle size for the feedstock. However, subsequent experiments determined that a -400 mesh (<37 μm) particle size produced better results with regards to densification. Typically, the as-sintered density of parts produced via HSPT using -400 mesh (<37 μm) powder produced 99% average relative density versus 98.5% average relative density when -325 mesh (<44 μm) powder was used. However, the overall particle size distribution below 37 μm and the morphology of the two powders are exceedingly similar, and their

appearances under SEM are essentially identical. Therefore, even though -400 mesh (<37 μm) powder was used for the results presented in this study, the micrograph of -325 mesh (<44 μm) powder is valid as an example of the general size and morphology of the powder used in this study.

As visible in the micrographs, $TiH_2$ powder has an irregular angular morphology. This causes the powder to be very abrasive and have poor flowability. However, as discussed in section 5.2, $TiH_2$ powder still exhibits excellent compaction behavior despite these characteristics due to its ability to crush under pressure.

For comparison, CP-Ti powder that was prepared by dehydrogenating -325 mesh (<44 μm) CP-$TiH_2$ is shown in Figure 5.1-B. As seen, dehydrogenation did not affect the size or morphology of the powder. Therefore, the CP-Ti powder in nearly identical to the CP-$TiH_2$ with respect to these characteristics.

There is a strong correlation between specific surface area, which is directed related to particle size, and purity of the powder. Therefore, it is important to account for this tradeoff when determining the appropriate particle size for sintering experiments. In this study, the -400 mesh (<37 μm) powder was identified as the nominal size, accounting for all of these considerations. Figure 5.2 shows the representative particle size distribution of -400 mesh (<37 μm) powder produced via the milling and sieving procedure detailed in section 4.1. Additionally, this powder consistently had a 0.4 $m^2/g$ specific surface area, as measured by Brunauer, Emmett, and Teller (BET) analysis. Using these methods, the titanium samples discussed in this dissertation consistently fell within the oxygen concentration range of 0.2-0.25 wt%. Further data on sample purity as a result of powder preparation and thermal processing (i.e. sintering, heat treating, and GIFT) and how it relates to mechanical

properties are presented in CHAPTER 8.

## 5.2 Compaction Behavior

Hydrogenated titanium powder exhibits attractive compaction behavior, resulting in green compacts with relative density consistently greater than 85% and excellent green strength. It has been proposed that the brittleness of the material leads to crushing of the particles during compaction[17,42]. Therefore, even when using powder with highly irregular particle morphologies, compacts can be produced with excellent green density and strength using moderate compaction pressures (200~400 MPa). Both cold isostatic pressing (CIP) and uniaxial die pressing were investigated in this study with promising results. During die pressing, the abrasive nature of $TiH_2$ caused problematic die wall friction for geometries with large die wall surface area and high compaction pressures. However, die wall lubricants such as zinc stearate and Acrawax were successfully used to overcome this issue during the production of large parts[9].

Because of its implications for a PM process, an experiment was conducted to compare the flowability and compaction behavior of CP-$TiH_2$ compared to CP-Ti. The relative density data of the two powders when loose, tapped, and compacted at three different pressures are given in Figure 5.3. As seen in the micrographs in Figure 5.1, both powders have the same particle size distribution and morphology. This is important in order to provide a fair comparison, as the size and morphology of a powder will significantly affect its compaction behavior[27]. As seen in the data, the loose and tap densities are very similar. However, despite having the same size and morphology, the green density of CP-$TiH_2$ is improved versus CP-Ti for all three compaction pressures. This is to be expected, as the

loose and tap densities are determined purely by the flowability. However, the tendency of $TiH_2$ to crush under pressure caused it to have improved green density versus Ti. The hydride achieved a relative density of nearly 80% after compaction at 138 MPa (20 ksi) and over 85% after compaction at 414 MPa (60 ksi), whereas the metal powder produced a relative density of only 73% after compaction at 414 MPa (60 ksi).

### 5.3 Dilatometry

It is well documented that sintering $TiH_2$ in vacuum exhibits excellent densification and purity after sintering[17,42]. However, the densification behavior of $TiH_2$ alloys in a hydrogen-containing atmosphere has not been previously discussed in the literature. Therefore, dilatometry experiments were conducted on both CP-$TiH_2$ as well as blended $TiH_2$-60Al/40V powder to produce bulk CP-Ti and Ti-6Al-4V, respectively.

For both sets of experiments, -325 mesh (<44 μm) powder was die pressed at 350 MPa into cylindrical samples measuring 16.2 mm in diameter by approximately 10 mm in height. These samples were then sintered using an HSPT sintering profile in the dilatometer. For the CP-Ti, it was theorized that the transformation temperature would have to be much lower due to the relatively low β-transus temperature on the Ti-H phase diagram. Therefore, a transformation temperature of 250 ºC was chosen for CP-Ti. Due to the low transformation temperature and likelihood of slow hydrogenation kinetics, a dwell at 550 ºC for 3 hours was added to the sintering profile to increase and homogenize the hydrogen content within the sample before transformation. Therefore, the CP-Ti samples were sintered at 1200 ºC for 4 hours, 550 ºC for 3 hours, and 650 ºC for 4 hours (Figure 5.4). The Ti-6Al-4V samples were sintered at 1200 °C for 4 hours followed by 650 °C for 4

hours (Figure 5.5). In order to study the effect of the hydrogen partial pressure on sintering behavior, four different gas mixtures were used during these experiment by flowing mixtures of $H_2$ and Ar gas (10, 20, 30, and 40% $H_2$). When the samples cool below a certain temperature, continued hydrogen pickup in the samples will cause them to crack due to formation of excess δ-$TiH_2$. As an example, this phenomenon is shown in the 10% $H_2$ curve of Figure 5.5 and is marked with a "Crack initiation" label. Therefore, to prevent this from happening, the $H_2$ mass flow controller was turned off in all other experiments before cooling below a certain temperature.

Figure 5.4 shows four shrinkage curves for CP-$TiH_2$ sintered in hydrogen-containing atmospheres. All samples expand during the initial stages of the heat-up due to thermal expansion. As the temperature reaches approximately 450~500°C, the hydride begins to rapidly decompose causing the samples to begin to shrink. It should be noted that during sintering of hydrogenated powder, shrinkage will occur due to hydrogen evolution as well as sintering; decoupling these mechanisms to determine shrinkage due to sintering alone can be challenging. As seen, most of the densification occurs during heat-up, before the sintering temperature is reached. During the high temperature hold, a small amount of additional shrinkage is observed. As the material is cooled, the hydrogen concentration increases. During cooling, shrinkage due to thermal expansion is greater than expansion due to hydrogen absorption, resulting in net shrinkage. However, when the samples are held at the lower temperatures, measurable expansion due to hydrogen absorption is visible in the data.

As visible in the shrinkage curves, the increased hydrogen partial pressure has an apparently positive effect on densification. That is, the samples under the higher partial

pressure of hydrogen exhibit more shrinkage during the dwell. As the samples cool, the effect of $H_2$ partial pressure has a clear effect causing the samples to expand. The samples under a high hydrogen partial pressure absorb more hydrogen during cooling, causing significantly more expansion of the sample. This has important implications for the phase transformation step, as the phase equilibria and transformation kinetics are strongly dependent on hydrogen concentration as discussed in section 2.3.

Figure 5.5 shows the shrinkage curves for $TiH_2$-60Al/40V sintered in the same four different hydrogen-containing atmospheres. The shrinkage curves during heat-up in these experiments are very similar to those with CP-Ti. However, as the high temperature hold is reached, the blended powder begins to behave differently. The alloying elements seem to play a definitive role in the densification behavior of the alloy, as the relationship between hydrogen partial pressure and shrinkage is inverted when compared to CP-Ti. That is, the Ti-6Al-4V samples under a higher hydrogen partial pressure show decreased overall shrinkage during the 1200 ºC hold compared to the CP-Ti samples. Additionally, where the CP-Ti exhibited a large amount of expansion due to hydrogen absorption in the ramp down segments, a significantly smaller amount of expansion was recorded with Ti-6Al-4V. While the mechanisms behind this phenomenon are currently unclear, it is apparent that the alloying elements play a significant role in hydrogen adsorption of titanium during sintering.

While the dilatometry curves show a difference in density among the samples as a function of hydrogen partial pressure at the end of the dilatometry experiment, this is purely an artifact of hydrogen concentration as a function of hydrogen partial pressure. After dehydrogenation, the samples of the same alloy have very similar densities regardless of

hydrogen partial pressure used during sintering. It should be noted, however, that CP-Ti typically densifies more than Ti-6Al-4V. From the dilatometry experiments, the Ti-6Al-4V samples usually have a final relative density around 98.9%, whereas CP-Ti samples usually have a final relative density around 99.3%. This is caused by the alloying elements having a deleterious effect on diffusion due to the alloying elements partitioning into their respective phases during sintering.

### 5.4 Density of As-sintered and As-GIFT'd Samples

In order to close porosity, many samples produced both via HSPT and vacuum sintering were processed using gaseous isostatic forging technology (GIFT). As discussed in CHAPTER 4, GIFT is a specialized technology currently used commercially by AMETEK to close porosities that form as a result of defects from casting or sintering processes[130]. GIFT is unique from other forging technologies in that it is near-net-shape compatible, owing to its isostatic nature. During GIFT, samples are first heated to lower the flow stress of the material and allow for further densification when pressure is applied. During this process, Ti-6Al-4V is heated to 845~900 °C and held at this temperature for several minutes to allow for plastic flow of the material as pneumatic pressure of up to 45,000 psi is applied. Because of the high temperatures used during GIFT, the microstructure before and after this process was studied to document the change in density and porosity as well as any changes in the grain structure of the material. The metallographic analysis of samples before and after GIFT are discussed in CHAPTER 6.

For all the samples presented in this study, GIFT processing was outsourced to AMETEK, as the necessary equipment was not currently available at the University of

Utah. Unfortunately, the specific parameters used during GIFT are proprietary and protected by AMETEK. Therefore, the exact values for the temperatures, times, and pressures used during GIFT were not available to author. However, the ranges reported for temperature and pressure, as discussed in the previous paragraph, were made available. Therefore, with this knowledge, the author has designed an apparatus, along with Matt Dunstan at the University of Utah, to perform these experiments independently. Mr. Dunstan will be studying this process in depth to determine the effect of the specific GIFT parameters on the microstructure and mechanical properties of titanium alloys as part of his doctoral research.

In the literature, the theoretical density for Ti-6Al-4V is reported as 4.42 to 4.43 g/cm$^3$, depending on the concentration of aluminum and vanadium in the alloy. As-sintered Ti-6Al-4V produced from hydrogenated powder via HSPT or vacuum sintering typically have relative densities greater than 99%, assuming a theoretical density of 4.426 g/cm$^3$ for Ti-6Al-4V. Therefore, despite the excellent densification behavior of $TiH_2$, there is still up to 1 vol% porosity after sintering. However, these pores can all be closed very effectively using GIFT.

Figure 5.6 shows the average relative density of samples produced via HSPT and vacuum sintering, before and after the GIFT process. The data in this figure represent averages calculated from 28 vacuum-sintered samples and 51 HSPT samples. All samples were produced from -400 mesh (<37 μm) $TiH_2$ powder blended with 9.6 wt% 60Al/40V master alloy. The density was determined for the as-sintered samples using the Archimedes method in water. These samples were then sent out for GIFT processing by AMETEK, after which the density was again measured to determine the change.

The average as-sintered density for HSPT samples was 4.38 g/cm$^3$ with a standard deviation of 0.007 g/cm$^3$, and the average as-sintered density for vacuum-sintered samples was 4.395 g/cm$^3$ with a standard deviation of 0.006 g/cm$^3$. The average density of HSPT samples after GIFT was 4.426 g/cm$^3$ with a standard deviation of 0.003 g/cm$^3$, and the average density of vacuum-sintered samples after GIFT was 4.426 g/cm$^3$ with a standard deviation of 0.005 g/cm$^3$. Therefore, because both HSPT and vacuum-sintered samples consistently had the same average density after GIFT, this value was taken as the theoretical density of Ti-6Al-4V produced via the blended elemental method used in this study. This value was then used to calculate the relative densities reported in Figure 5.6. Using this value for the theoretical density of Ti-6Al-4V produced via this method, HSPT produces as as-sintered density of 99.0% while vacuum sintering produces as as-sintered density of 99.3%. After GIFT, the relative density is consistently increased to 100%.

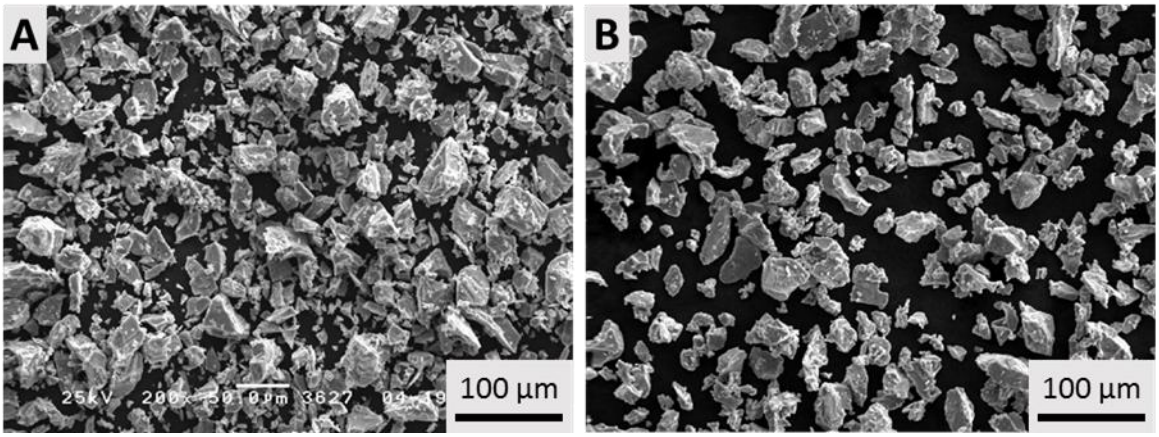


Figure 5.1: SEM micrographs of A) as-milled -325 mesh CP-$TiH_2$ and B) as-dehydrogenated -325 mesh CP-Ti.

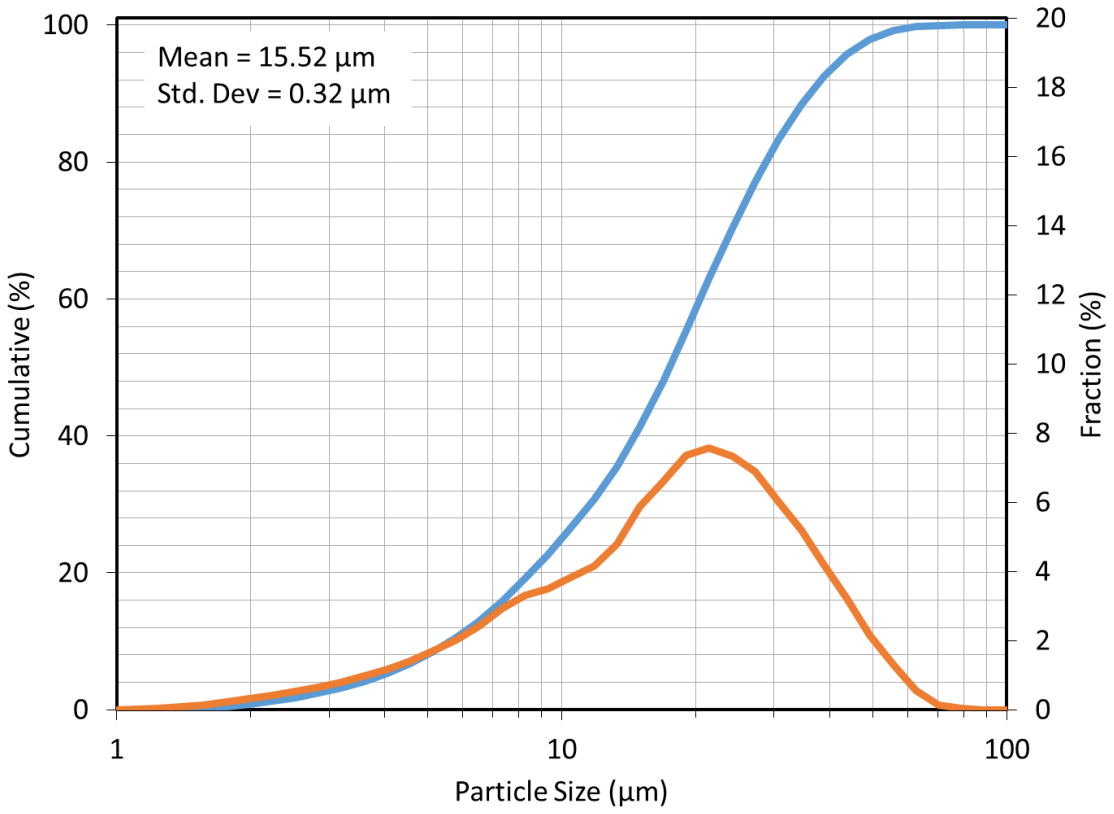


Figure 5.2: Typical particle size distribution of powder with 0.4 $m^2/g$ specific surface area.

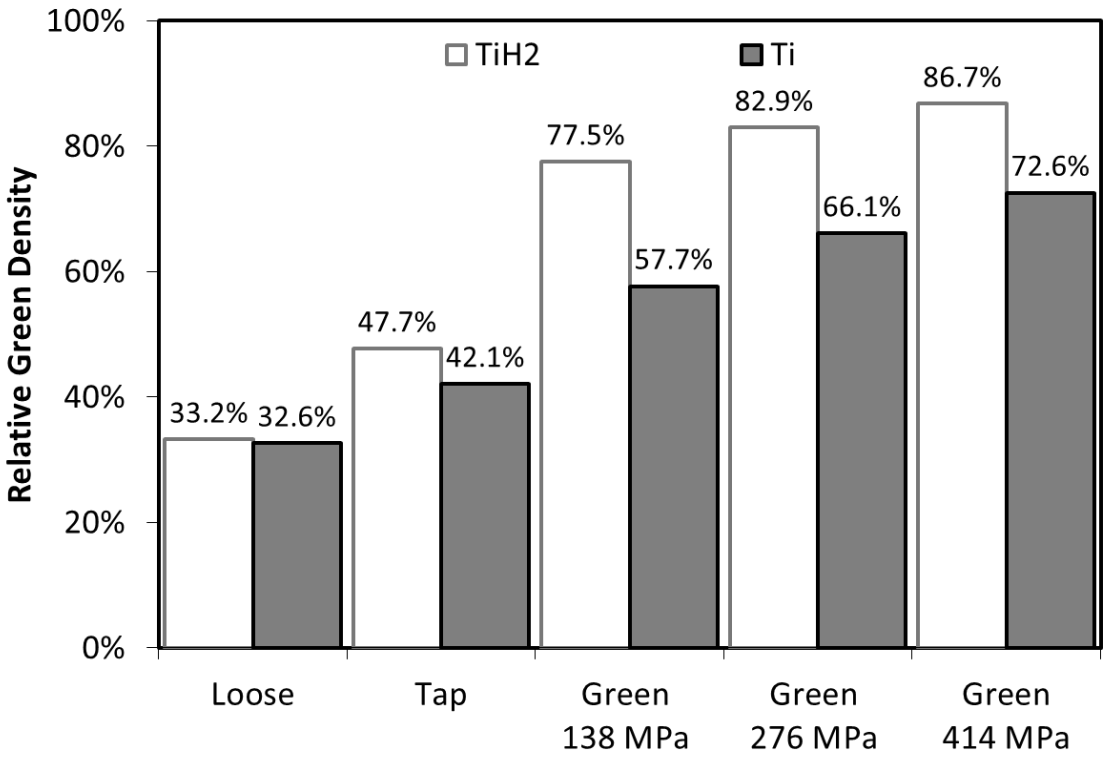


Figure 5.3: Density comparisons of -325 mesh CP-$TiH_2$ and CP-Ti as powder (loose and tapped) and green compacts after CIP at three different pressures.

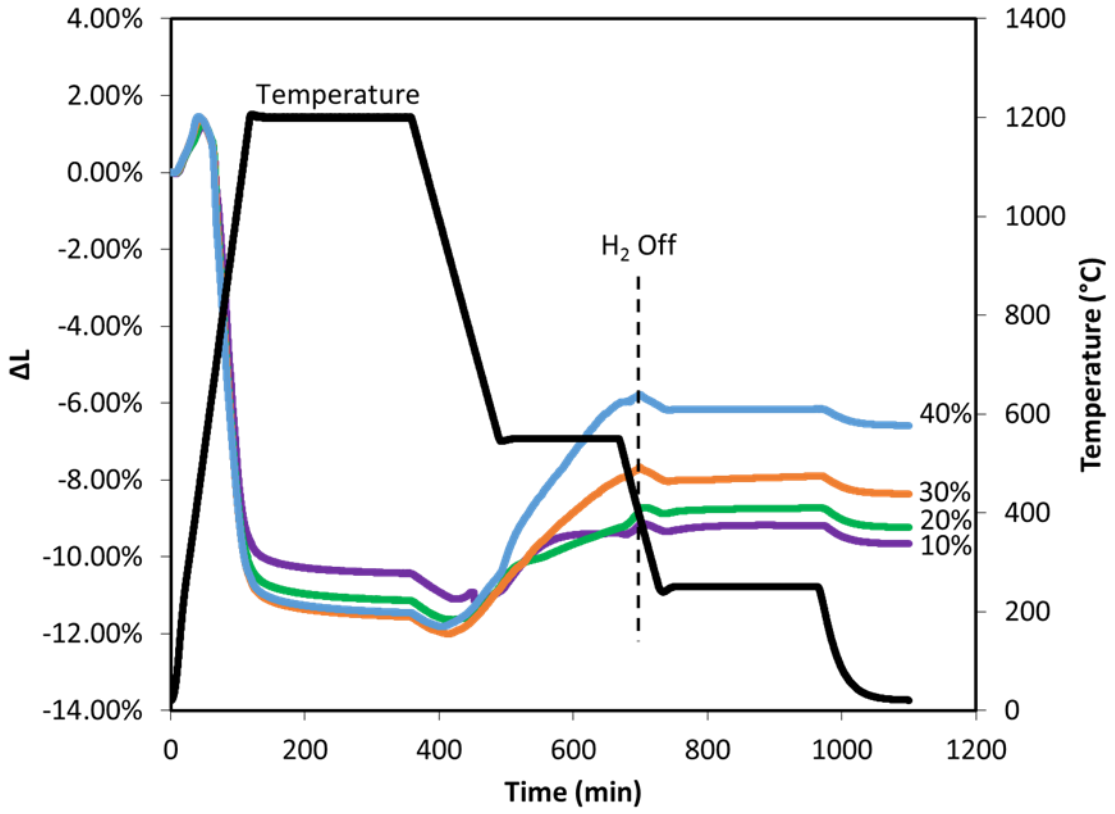


Figure 5.4: Shrinkage curves of CP-$TiH_2$ sintered in 10, 20, 30, and 40% $H_2$.

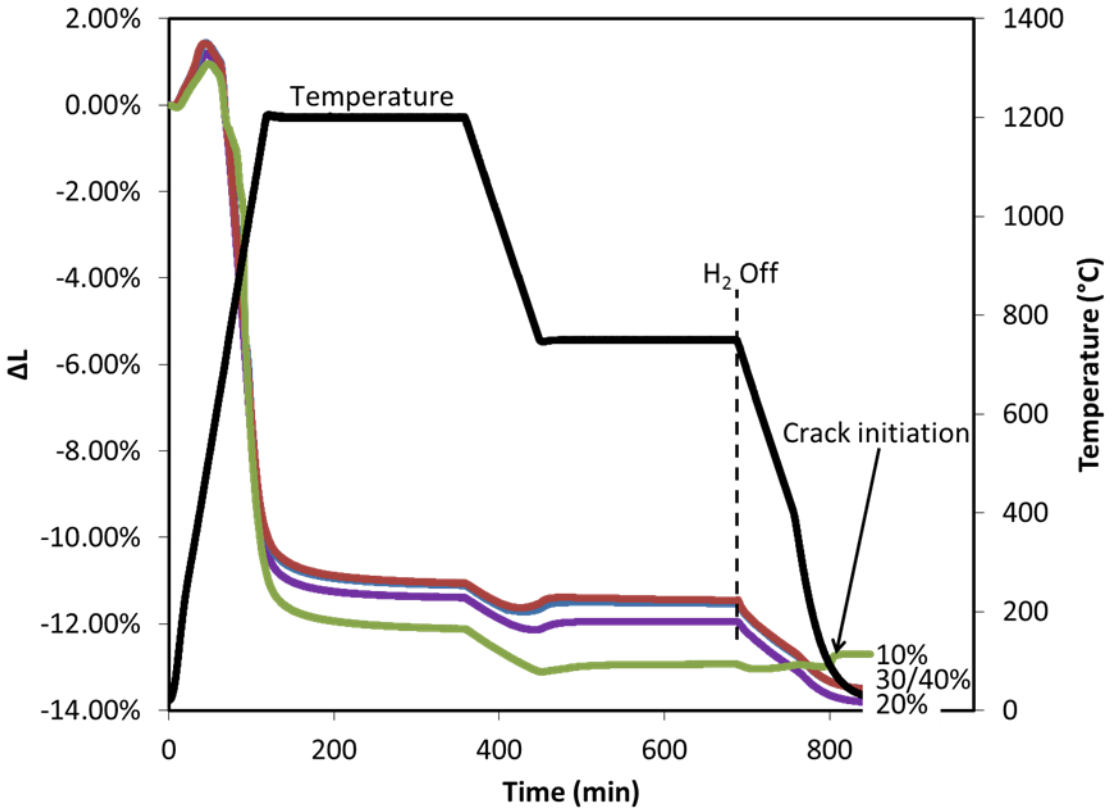


Figure 5.5: Shrinkage curves of CP-$TiH_2$ with 9.6 wt% 60Al/40V sintered in 10, 20, 30, and 40% $H_2$ (balance Ar at atmospheric pressure). Note: the curves for 30% (blue) and 40% (red) $H_2$ are very closely overlapping.

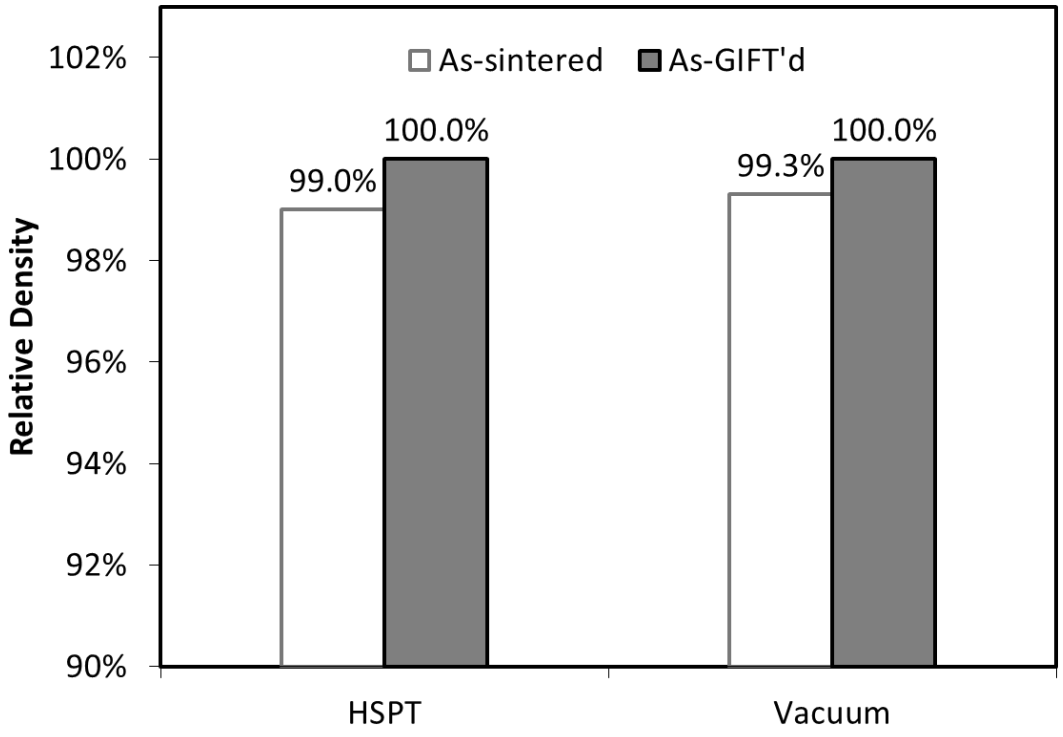


Figure 5.6: Average relative density of Ti-6Al-4V samples produced via HSPT versus vacuum sintering before and after GIFT.

# CHAPTER 6

## RELATIONSHIP BETWEEN PROCESSING AND MICROSTRUCTURE OF Ti-6Al-4V PRODUCED VIA HSPT

The greatest emphasis of this research was on understanding the microstructural evolution and resulting mechanical properties of Ti-6Al-4V during the HSPT process and subsequent heat treatments. Ti-6Al-4V is chosen as the workhorse in the titanium industry not because it is the best material for any particular application, but because it is extremely versatile with regards to its ability to have a wide range of mechanical properties achieved through different processing treatments. Therefore, any commercially viable alternative to wrought processing for the production of Ti-6Al-4V would need to have the ability to produce a range of microstructures and mechanical properties. While this is easily achieved via thermomechanical processing (TMP) routes, those processes are energy-intensive and contribute the majority of cost in most titanium components produced commercially. Therefore, an important attribute of HSPT is the ability of this process to produce Ti-6Al-4V with a wide range of wrought-like mechanical properties using low-cost feedstock materials, low-energy processing routes, and doing so with near-net-shape capabilities.

In this chapter, the range of microstructures available via HSPT and the mechanisms

that make them possible are discussed in detail. Additionally, throughout the chapter, the microstructures produced via HSPT and subsequent heat treatments are compared to samples produced via vacuum sintering using identical powder, compaction, and thermal processing, aside from the obvious difference in sintering method.

All samples were prepared as cylindrical blanks, which were pressed as green parts using cold isostatic pressing (CIP) before sintering. Sintering was performed using the standard HSPT or vacuum sintering profiles shown in Figure 4.2, followed by GIFT and/or heat treatments, when applicable. The GIFT process is shown schematically in Figure 4.5. All heat treatments followed one of the three basic heat treatment profiles presented in Figure 4.4, which have all been borrowed from typical heat treatments used in wrought processing as defined in the literature[34,35].

### 6.1 As-sintered Microstructure of HSPT vs. Vacuum Sintering

The micrographs shown in Figure 6.1 are from three samples produced using three different blended elemental (BE) methods to produce Ti-6Al-4V: vacuum sintering of Ti powder, vacuum sintering of $TiH_2$ powder, and HSPT of $TiH_2$ powder. All three samples are Ti-6Al-4V and were sintered using the profiles shown for their respective processes in Figure 4.2. Additionally, all three samples were prepared from powder with similar size distributions as those shown in Figure 5.2 and were all compacted using a cold isostatic press (CIP) at 350 MPa (50.8 ksi) for 7 minutes.

Figure 6.1-A was prepared from CP-Ti powder blended with 10 wt% 60Al-40V master alloy and sintered under high vacuum at 1200°C for 4 hours (Figure 4.2-Vacuum). As is evidenced by the micrograph, densification was relatively poor, resulting in ~96% relative

density. Additionally, the high temperatures and long hold times necessary for densification resulted in a coarse lamellar α plate colony structure typical of PM Ti-6Al-4V. The microstructure and properties of this sample could be improved by incorporating pressure-assisted sintering to increase densification and thermomechanical processing (TMP) to remove porosity and refine the microstructure. However, these additional steps would increase energy consumption and cost in a commercial process.

Figure 6.1-B was prepared from CP-$TiH_2$ blended with 9.6 wt% 60Al-40V master alloy and sintered under high vacuum at 1200°C for 4 hours (Figure 4.2-Vacuum). Despite having an identical thermal profile and atmosphere, densification is significantly improved versus Figure 6.1-A due to the presence of solvated hydrogen during sintering. As such, this sample has a relative density of ~99%. However, the sintering conditions still result in the same coarse lamellar microstructure, which is undesirable for mechanical properties and would require energy-intensive post-processing to refine.

Figure 6.1-C was prepared from CP-$TiH_2$ blended with 9.6wt% 60Al-40V master alloy and sintered using HSPT (Figure 4.2-HSPT). After sintering, the sample was dehydrogenated under high vacuum at 750°C for 12 hours. The relative density of this sample was also ~99%. Residual porosity, though none is visible on the micrograph, is on the order of 10~20 μm in diameter. The microstructure is still lamellar. However, α plates (dark colored phase) are substantially finer; α plate widths are submicron and α plate lengths are on the order of 1~5 μm. Additionally, the β phase (light colored phase) is discontinuous and dispersed, as opposed to the continuous β phase visible in the other two micrographs. The discontinuous β phase is advantageous with regard to mechanical properties and is a necessary precursor for heat treatments, as discussed in section 6.3.

### 6.1.1 High Angle Grain Boundaries

As discussed in CHAPTER 2, the α grains in a single colony tend to be oriented parallel to one another. Even though α grains are often separated by a layer of β, the two phases share two slip systems that are exactly parallel and two more within 10º. There is little resistance to slip between α grains of similar orientation[34]. Therefore, while the microstructures of as-dehydrogenated HSPT samples have very fine lamellar α grains, the strengthening due to grain size reduction will not necessarily be a function of the size of the individual α lamellae. Rather, the slip length and, therefore, mechanical properties will be determined by the mean path between high angle grain boundaries (HAGBs). For α colony structure, such as seen in the lamellar microstructure presented in this dissertation, the HAGBs usually correspond with the boundaries of the α colonies, not the boundaries of the individual lamellae within the colony.

Electron backscatter diffraction (EBSD) was used to study the orientations of α grain in an as-dehydrogenated HSPT microstructure. Figure 6.2-A shows an SEM micrograph of as-dehydrogenated Ti-6Al-4V produced via HSPT for comparison with the EBSD maps. Figure 6.2-B shows an Euler map of grain orientations collected via EBSD (Oxford HKL detector on FEI Helios DualBeam NanoLab). The color designations in an Euler map show the relative orientations of the grains. However, it should be noted that grain orientations are determined by three axes. Therefore, similar colors do not always indicate grains that are nearly parallel with respect to all three axes. Because of this, an algorithm provided with the EBSD analysis software (Oxford Channel 5) was used to calculate misorientations of adjacent grains. The HAGBs, as determined by this method, are highlighted in red in Figure 6.2-C.

When comparing Figure 6.2-A and Figure 6.2-C, it is apparent that the distance between HAGBs corresponds well with the size of the α colonies in Figure 6.2-A. While the α colonies are larger than the individual α grains, the size of the colonies themselves in an HSPT-produced microstructure are still very fine. The distance between HAGBs (i.e. the average effective slip length) is between 2 to 5 μm, as shown in Figure 6.2-C.

### 6.1.2 Microstructural Evolution During HSPT

Figure 6.3 shows micrographs of Ti-6Al-4V that was produced via HSPT in the as-sintered condition before dehydrogenation. These images have been colorized and lightened to help highlight the microstructural features.

The microstructure before dehydrogenation is significantly different than as-dehydrogenated specimens. According to the (Ti-6Al-4V)-H phase diagram shown in Figure 2.2[5], the phases present in this microstructure should be α, $\alpha_2$-$Ti_3Al$, β, and δ-$TiH_2$. The hydrogen rich phases (β and δ-$TiH_2$) are either not present, in the case of the hydride phase, or present in much smaller quantities when the hydrogen is removed. Therefore, as shown in the micrographs, the microstructure should be significantly different than the as-dehydrogenated α+β material. This is especially true when a higher dehydrogenation temperature is used, as the α phase tends to coarsen at the higher temperatures. As such, before dehydrogenation the microstructure is much more acicular in morphology and has very thin, needle-like grains with a high aspect ratio. However, lower dehydrogenation temperatures produce a microstructure similar to the state be dehydrogenation (Figure 6.4). This microstructure generated before dehydrogenation has been reported to be a result of homogenous precipitation of $\alpha_2$-$Ti_3Al$ during the phase transformation step (Figure 2.4),

followed by formation of α-Ti and then δ-$TiH_2$ as the material absorbs more hydrogen during cooling from the phase transformation step to room temperature[2]. Phase evolution during the HSPT sintering profile is shown schematically on the phase diagram in Figure 2.2.

It should be mentioned that the microstructure before dehydrogenation does not contain coarse grain boundary α grains (G.B. α) that are typical of lamellar Ti-6Al-4V, as discussed in section 2.6.1. G.B. α is, however, consistently observed in HSPT Ti-6Al-4V after dehydrogenation. Therefore, it can be concluded that G.B. α forms and coarsens significantly during the dehydrogenation step. This is an important consideration, as G.B. α is known to have deleterious effects on mechanical properties[34–37]. As such, one could theoretically minimize the presence and/or size of G.B. α by modifying the dehydrogenation step. The feasibility of this practice has been investigated by the author and is discussed in the following section.

#### 6.1.2.1 Effect of Dehydrogenation Temperature

The dehydrogenation temperature was theorized to have a significant effect on the grain size after dehydrogenation. Additionally, as mentioned in the previous section, it has been observed that G.B. α is coarsened primarily during dehydrogenation. Therefore, Ti-6Al-4V samples prepared via HSPT were dehydrogenated at different temperatures to study the effect of this processing parameter on structure.

SEM micrographs of two samples, dehydrogenated at different temperatures, are shown in Figure 6.4. Both samples were sintered using the standard HSPT profile (Figure 4.2). Figure 6.4-A was dehydrogenated at the standard temperature of 750 ºC for 12 hours.

However, Figure 6.4-B was dehydrogenated at 650 ºC for 24 hours. As visible from the micrographs, the sample dehydrogenated at 650 ºC has a much finer and more acicular microstructure than 750 ºC. In addition to the dehydrogenation step, subsequent heat treatments also have profound effect on G.B. α, as the high temperature hold used during the heat treatments tends to cause these grains to grow and form a thicker layer of G.B. α along the prior β grain boundary. Therefore, the effect of dehydrogenation temperature on the resulting microstructures after subsequent heat treatments is an important consideration. Therefore, these results are discussed in detail in section 6.2.2.1.

As would be expected, the temperature during dehydrogenation was observed to have a significant effect on dehydrogenation kinetics. That is, utilizing a lower dehydrogenation temperature would slow the process of removing hydrogen. Therefore, lower dehydrogenation temperatures were observed to require longer dehydrogenation times to reach similar hydrogen concentrations. To address this issue, chemical analysis of samples dehydrogenated at different temperatures and times was performed to measure the resulting hydrogen content. Hydrogen content was measured along with oxygen and nitrogen content via the inert gas fusion instrument (LECO TCH-600). Several samples were dehydrogenated using different temperatures and times to determine a qualitative trend for complete dehydrogenation. A summary of the results from these experiments is given in Table 6.1.

From the chemical analysis study, it was found that the hydrogen level after 12 hours at 650 °C under high vacuum yielded a hydrogen level of 143 ppm. It should be noted that this value meets the ASTM standard for grade 5 Ti-6Al-4V[96]. Therefore, using the ASTM standard as a guide, 12 hours is sufficient to dehydrogenate the alloy at 650 °C. However,

the hydrogen concentration is typically lower than 10 ppm when 750 °C is used. Therefore, further experiments were conducted to determine the time necessary to achieve similar hydrogen levels when 650 °C is used. It was found that doubling the dehydrogenation time to 24 hours achieved this result. However, it should be emphasized that obtaining this hydrogen level is superfluous with regards to the ASTM standard. Additional experiments found that a hydrogen level below 100 ppm was achieved after on 2 hours at 825 °C. Therefore, from these experiments, it was observed that sufficient dehydrogenation could be achieved in about 12 hours at 650 °C while an increase of less than 200 °C reduces this time by nearly an order of magnitude.

### 6.2 Heat Treatments to Produce Wrought-like Microstructures

In this section, the wrought-like microstructures that result from HSPT with subsequent heat treatments are discussed and compared to results obtained from vacuum-sintered material subjected to identical heat treatments. These results are presented chronologically, showing the iterative process that was used to investigate the heat-treatability of HSPT and vacuum-sintered specimens. Therefore, the first section will discuss the preliminary results obtained from the first heat treatment experiments. The following sections will present in-depth results obtained using different heat treatments. Additionally, results obtained from heat treating vacuum-sintered Ti-6Al-4V are presented as well for comparison. From this comparison, it has been determined that obtaining wrought-like microstructures via heat treatments without thermomechanical processing (TMP) is unique to HSPT. Therefore, the final sections of this chapter show microscopic evidence of the mechanisms by which the microstructure evolves during HSPT sintering and subsequent heat treatments to

explain this unique ability.

### 6.2.1 Preliminary Heat Treating Results

Preliminary heat treating experiments were performed on as-dehydrogenated Ti-6Al-4V produced using the standard HSPT method (Figure 4.2). The starting microstructure for these heat treatments was the ultra-fine grained lamellar structure typical of HSPT (Figure 6.2-A and Figure 6.4-A). The first heat treatment selected was a standard solution treatment and aging (STA) consisting of a 954 ºC treatment for 1 hour, followed by a water quench, and ageing at 550 ºC for 6 hours (Figure 4.4-B). Micrographs of samples produced with this heat treatment are shown in Figure 6.5 and Figure 6.6.

The sample shown in Figure 6.5 was prepared by electropolishing, which was chosen to retain a clean surface suitable from EBSD analysis. Figure 6.5-A is a high-tilt SEM micrograph. This micrograph was taken as a representation of the topographical surface just before an EBSD scan. This is the reason for the high-tilt, as the sample must be tilted for EBSD analysis. A corresponding EBSD scan of this microstructure is shown in Figure 6.5-B. This microstructure clearly shows a bi-modal microstructure with approximately 40 vol% globularized $\alpha_p$ formed as a result of the heat treatment. The EBSD orientation map shows the boundaries and relative orientation of the $\alpha_p$ grains. It can be seen from the grain orientations that adjacent $\alpha_p$ grains are generally misoriented with their neighbors. The black regions in Figure 6.5-B correspond to regions with poor indexing. This EBSD scan was taken using a step size of 50 nm. Therefore, either the step size was too large for the microstructure between the $\alpha_p$ grains or this area had too much strain to properly index.

Figure 6.6-A shows a high resolution SEM micrograph of a mechanically polished and

chemically etched surface of the same sample shown in Figure 6.5. Figure 6.6-B is given as a visual reference between the two types of polishing and imaging procedures. These micrographs clearly show regions of extremely fine lamellar grains that are indicative of transformed-β between the $\alpha_p$ grain.

6.2.1.1 Formation of Acicular α Grains During Water Quenching

Synchrotron X-ray diffraction was performed using the Advanced Photon Source (APS Beamline 11-ID-C) at Argonne National Laboratory (ANL). Using this technique, XRD was performed on samples before after the 954 °C heat treatment with water quench. The results of these experiments are shown in Figure 6.7. As seen, the water quench causes the α peaks to broaden, while the β peaks completely disappear. The transformed β structure in Ti-6Al-4V that forms by the growth of lamellar or acicular α grains always leaves at least some retained β. However, the very high resolution and highly sensitive synchrotron XRD patterns indicate that the sample is completely devoid of β grains after the water quench. Therefore, these data indicate that the β grains present at high temperature are transformed during the water quench via a diffusionless reaction (i.e. martensite reaction)[98], as typical diffusion reactions would leave some retained β. As such, it was concluded that the water quench forms acicular martensite grains. However, after aging, the XRD patterns shown broad α peaks (consistent with acicular grains) and a return of the β peaks. Additionally, the SEM micrographs show an acicular morphology of the α grains after the 550 ºC aging. Therefore, it was concluded that the aging temperature was sufficient to allow decomposition of the metastable martensite grains into α and β, though the grains maintained an acicular morphology. As such, the resulting microstructure from this heat

treatment consists of globularized $\alpha_p$ grains and ultrafine-grained (UFG) acicular α with a small fraction of retained β between the acicular grains.

### 6.2.2 Effect of HSPT and Heat Treating Parameters on Ti-6Al-4V

After the success of producing a clearly bi-modal microstructure using a simple heat treatment at 954 °C with water quenching, a further study was performed to study the effect of the various HSPT and heat treatment parameters on the resulting microstructure. The parameters tested were the dehydrogenation temperature during HSPT as well as the cooling rate and dwell temperature during subsequent heat treatment. The results gained from this study will be presented in this section.

#### 6.2.2.1 Effect of Dehydrogenation Temperature on Heat Treatments

Because the dehydrogenation temperature has a strong affect on the as-dehydrogenated microstructure (Figure 6.4), it was theorized that the finer microstructure would in turn have a significant effect on phase evolution during heat treatments. Therefore, heat treatments were performed on samples dehydrogenated at 750 ºC and 650 ºC, respectively. These heat treating experiments used a high temperature (954 ºC) STA treatment with a water quench (Figure 4.4-B). The results of this study are shown in Figure 6.8.

Figure 6.8 shows ultraviolet laser confocal micrographs of the as-quenched microstructures of two samples that were dehydrogenated at 750 ºC (Figure 6.8-A) and 650 ºC (Figure 6.8-B). The amount and morphology $\alpha_p$ grains was the primary area of interest in this study. As shown in the previous section, aging was observed to have little effect on the morphology of the remaining microstructure. It should be noted that the apparent

difference in surface topography of the two samples is most likely an artifact of the imaging technique used. Figure 6.8-A is a compiled image made from 3-D profilometry scans. During these scans, the z-height of the sample stage is moved while sequential laser scans of the surface are performed. This generates an image with excellent depth of field and topographical information. Figure 6.8-B is an image collected using a single height laser scan of the surface.

Both samples shown in Figure 6.8 have a clearly bi-modal microstructure. However, the $\alpha_p$ grains in the 750 ºC sample seem to be coarser and more globularized (lower aspect ratio) on average. It is believed this is caused by the starting microstructure of the 650 ºC sample being more acicular (Figure 6.4-B), with long needle-like grains. Figure 6.8-B also shows G.B. α with parallel α grains emanating from the boundary. This branch-like structure of the G.B. α appears to be controlled by the dehydrogenation temperatures, as the samples dehydrogenated at 750 ºC form G.B. α that is continuous along the prior β grain boundary and mostly separated from adjacent α grains. Therefore, the dehydrogenation temperatures appears to be an important parameter for controlling the size and morphology of G.B. α grains both in the as-sintered and heat-treated microstructures.

#### 6.2.2.2 Effect of Cooling Rate

As discussed in section 2.6, the cooling rate from the solutionizing and recrystallization temperatures tends to have a profound effect on the microstructure of α+β alloys. It is well known that the vol% of globularized α in a heat-treated microstructure is controlled by the cooling rate from the recrystallization temperature[34]. Therefore, to achieve a fully equiaxed microstructure with greater than 50~60 vol% globularized α grains, a slow

cooling rate is needed during recrystallization. In order to study this phenomenon for HSPT Ti-6Al-4V, a series of experiments were conducted in which the cooling rate was varied from heat treatments at 954 ºC (Figure 4.4).

The confocal micrographs shown in Figure 6.9 represent three samples that were all dehydrogenated at 750 ºC, heat treated at 954 ºC for 1 hour, and cooled at three different rates. Figure 6.9-A was water quenched from 954 ºC. No means for measuring temperature were available during quenching, but it is safely assumed that the cooling rate was greater than 1000 ºC/min. Figure 6.9-B was air cooled from 954 ºC. Non-contact infrared temperature measurements during this experiment indicated a cooling rate of approximately 350 ºC/min for the first 500 °C of cooling. Figure 6.9-C was furnace cooled, which corresponded to about 10 ºC/min for the first 500 °C of cooling.

The air cooled sample in Figure 6.9 shows a definitive increase in vol% of globularized α versus the water quenched sample. While the general form of the α grains is similar in the water quenched and air cooled samples, an observable difference is shown between the two conditions. The slower cooling rate seems to result in a greater fraction of grains with a more globularized morphology. As the cooling rate is lowered further, this effect become even more apparent. The microstructure in the furnace cooled sample has a very high volume fraction of globularized α. Additionally, the α grains appear uniformly equiaxed, with an aspect of ratio greater than 2:1 being a rare occurrence. This is in line with the theory of globularized α formation. Because the morphology of forming α grains is dependent on cooling rate, due to diffusion of alloying elements during cooling, fast cooling generally results in in a more lamellar structure due to the short diffusion lengths available to the alloying elements. This phenomenon was discussed in section 2.5.

The combined effect of cooling rate as well as dehydrogenation temperature was also studied. The results of this study are shown in Figure 6.10. Both of these samples were dehydrogenated at 650 ºC and heat treated at 954 ºC for 1 hour. The sample shown in Figure 6.10-A was water quenched and Figure 6.10-B was water cooled. The same trend from cooling rate is observed in samples dehydrogenated at 650 ºC. As the cooling rate is decreased, both the volume fraction of globularized α and the degree of globularization of the grains increase. However, the morphology of the α grains in the furnace cooled microstructure are more elongated than those seen from higher dehydrogenation temperatures (Figure 6.9-C). Again, this phenomenon is likely a result of the acicular morphology of samples dehydrogenated at 650 ºC (Figure 6.4-B).

6.2.2.3 Effect of Heat Treatment Dwell Temperature

During heat treatments of α+β alloys, the heat treatment temperature can have a profound effect on the size of globularized α grains in the resulting microstructure. In fact, one study reported the formation of a fully equiaxed microstructure with α grains on the order of 2 μm when the samples were deformed and recrystallized at 800 ºC[100]. Therefore, the effect of the dwell temperature on the heat treated microstructures of HSPT samples was studied.

Figure 6.11 shows two confocal micrographs of samples that were dehydrogenated at 750 ºC and heat treated. Figure 6.11-A was treated at 954 ºC for 1 hour, while Figure 6.11-B was treated at 825 ºC for 1 hour. Slower cooling rates seemed to have the greatest effect on the resulting microstructure in the previous experiments. Therefore, for both of these samples, furnace cooling was chosen to highlight the different in heat treatment

temperature on the resulting microstructure.

As is shown in the micrographs, the dwell temperature has a significant effect on the microstructure. The sample treated at 954 ºC shows a significant change resulting from the heat treatment versus the as-dehydrogenated structure. The sample treated at 825 ºC, however, is remarkably less transformed. There are some isolated areas on the micrograph that appear to be very small globularized α grains (<5 μm). However, the majority of the microstructure exhibits the lamellar structure that is indicative of as-dehydrogenated HSPT samples (Figure 6.2-A and Figure 6.4-A).

### 6.2.3 Comprehensive Heat Treatments of HSPT and Vacuum-Sintered Ti-6Al-4V

After determining the effect of the various dehydrogenation and heat treating parameters on the resulting microstructure, a study was undertaken to investigate the feasibility of forming the three general types of microstructures of Ti-6Al-4V produced via wrought processing discussed in section 2.6: fully equiaxed (globularized), bi-modal, and fully lamellar (β-annealed). A key point to this effort was to avoid thermomechanical processing (TMP), which is compulsory in wrought processing to break up the coarse microstructure and induce a driving force for recrystallization by creating a high dislocation density. Additionally, to determine whether or not the ability to form wrought-like microstructures via simple heat treatments was unique to HSPT, the same heat treatments conducted on HSPT-sintered samples were performed on vacuum-sintered samples as well. Optical micrographs showing representative results of these experiments as well as the thermal profiles used in each experiment are shown in Figure 6.12. To elucidate the relative orientations of the grains in the as-sintered (HSPT and vacuum) and

heat treated (HSPT only) microstructures, inverse pole figure orientation maps as collected by EBSD are given in Figure 6.13.

Before heat treatment, the HSPT and vacuum-sintered samples were sintered using the corresponding standardized sintering profiles and atmospheres detailed in Figure 4.2. The as-sintered microstructure for both conditions was consistent with the expected results for both HSPT and vacuum sintering and, therefore, served as a reliable control in setting up these experiment. Further examples of both as-sintered microstructures are given in several figures throughout this dissertation as both optical micrographs and SEM micrographs (e.g. Figure 6.1-B and C for vacuum sintering and HSPT, respectively). However, it should be remembered that the phase contrast relationship is reversed in optical versus electron micrographs. That is, in an optical micrograph, α is the light phase and β is the dark phase, while the opposite is true for SEM micrographs.

As seen in Figure 6.12 and Figure 6.13, the microstructures achieved from HSPT samples were very different from those achieved from vacuum-sintered samples for the sub-transus heat treatments. However, the microstructures were essentially identical for HSPT and vacuum sintering for the β-annealed heat treatments. Such a result was expected, and the reasons for this are discussed in section 6.3.

#### 6.2.3.1 Globularized (Equiaxed) Microstructure

The sample shown in Figure 6.12-B and Figure 6.13-C was prepared by heat treating an as-sintered HSPT sample at 954 °C for 1 hour, furnace cooling to room temperature (~10 °C/min), and aged at 550 °C for 6 hours. As shown, the microstructure consisted of nearly all globularized α grains with a small aspect ratio (less than 3:1 on average) and a

very fine grain size. The individual dimensions of the grains shown in this micrograph range from 2~10 μm, with the average size of the equiaxed grains being approximately 5 μm. The retained β phase in this microstructure was largely confined to the triple points of the α grains.

It should be noted that the α grains in this microstructure were still slightly elongated, but had a very small aspect ratio. Additionally, the α grains had a morphology and size very similar to the size and shape of the α *colonies* in the as-sintered microstructure. The aspect ratio of α grains was much smaller than that of the α lamellae in what would be considered a lamellar structure, such as the as-sintered condition. Therefore, the term "globularized" was preferred by the author for naming this microstructure, as the term "equiaxed" did not strictly apply for all of the α grains. The rule of thumb for defining a globularized grain is generally thought to be an aspect ratio less than 3:1, which is consistent with this microstructure.

Figure 6.12-F is a micrograph of a vacuum-sintered sample subjected to an identical heat treatment used to produce the globularized microstructure shown in Figure 6.12-B. However, as clearly evident in the micrograph, the heat treatment had essentially no effect on the microstructure. It is true that proportion of α and β grains surely changed as the temperature approached the β transus. However, the continuous β grains that line the α grain boundaries simply thickened at the increased temperature and then correspondingly thinned as the temperature decreased, resulting in an unchanged microstructure after the treatment. The proposed mechanism by which the β phase thickens and thins during the heat treatment is illustrated in section 6.3. From these results, it can be concluded that this type of heat treatment was essentially ineffective for modifying the size and shape of the

coarse lamellar structure that is produced by vacuum sintering.

6.2.3.2 Bi-modal Microstructure

The samples shown in Figure 6.12-C and Figure 6.13-D are essentially repeats of the bi-modal structure produced in the preliminary heat treating experiments discussed in section 6.2.1. Therefore, these samples were a control for the experiments on vacuum-sintered samples which was based on the previous heat treatments on HSPT samples.

As discussed before, the bi-modal microstructure consisted of roughly 40 vol% $\alpha_p$ grains with a globularized morphology. The remainder of the microstructure consisted of very fine acicular α grains with retained β. As with the fully globularized structure, the globularized $\alpha_p$ grains had a size and shape very similar to the α *colonies* in the as-sintered structure. Additionally, while some of the $\alpha_p$ grains were still rather elongated, the aspect ratio of the $\alpha_p$ grains was less than 3:1 on average. Therefore, by the rule of thumb in the titanium industry, these grains were considered to be globularized. This microstructure closely resembles micrographs published in the literature of bi-modal α+β alloys produced via wrought processing as presented in section 2.6.2. However, wrought processing requires thermomechanical processing (TMP) to achieve formation of the globularized or equiaxed α grains, whereas this structure was formed by performing a simple heat treatment of the as-sintered HSPT microstructure.

The corresponding experimental results for this heat treatment on a vacuum-sintered sample is shown in Figure 6.12-G. As seen, this microstructure was also bi-modal, consisting of $\alpha_p$ grains constituting 30~40 vol% of the microstructure with the balance consisting of very fine acicular α grains with retained β such as that seen in the HSPT-

sintered sample. However, while this microstructure is clearly bimodal, the morphology of $\alpha_p$ grains was not desirable. The $\alpha_p$ grains were on the order of 100s of microns in length (similar to the length of the lamellar α in the as-sintered microstructure) and had an extremely high aspect ratio. This was likely due to the thickening of the β grains during the high temperature hold causing the α grains at the heat treatment temperature to be very long and skinny. Therefore, when the material was quenched, the β phase transformed into martensite, leaving the very long and skinny $\alpha_p$ grains. Upon aging, the martensite transformed into acicular α with retained β. The mechanisms for the phase evolution during these experiments are illustrated in section 6.3.

6.2.3.3 Fully Lamellar (β-annealed) Microstructure

The final heat treatment performed on HSPT and vacuum-sintered samples was a β-anneal. As shown in Figure 6.12, this heat treatment consisted of heating the specimen to a temperature just above the β transus (1050 °C in this case) for 1 hour and air cooling (~200 °C/min for the initial several hundred degrees). A representative orientation map for this heat treatment for both sintering processes is shown in Figure 6.13-E.

The β-annealed samples prepared from HSPT-sintered material discussed in this section were prepared in batches of 10 tensile and fatigue bars each weighing 50~60 grams (500~600 grams total weight) to be used for mechanical testing as well as metallography. Therefore, the air cooling rate for the β-annealed HSPT samples discussed in this section was slower than the cooling rate experienced by the sample shown in Figure 6.9-B, which was about 350 °C/min, due to the larger total thermal mass of the samples in these experiments. A cooling curve generated by taking the temperature of the samples every

30 to 60 seconds using a non-contact infrared thermometer is given in Figure 6.14.

The thermal profiles and results of heat treating HSPT material is shown in Figure 6.12-D, and the results of performing the same heat treatment on a vacuum-sintered sample is shown in Figure 6.12-H. Because this heat treatment was performed above the β-transus, the material was entirely β phase during the high temperature hold. Therefore, the entire microstructure after heat treatment is transformed β, in the form of lamellar α colonies. Because of this, the starting microstructure had little effect on the microstructure that resulted from this heat treatment. As discussed in section 2.6.1, the size of the lamellar α colonies, as well the size of the G.B. α, is a function of the cooling rate during the heat treatment. Therefore, because both the HSPT and vacuum-sintered samples were β-annealed using identical heat treatment parameters, the resulting microstructures were essentially identical.

As an additional comparison, the same heat treatment was performed on as-received (mill-annealed) wrought Ti-6Al-4V purchased from McMaster-Carr as 12.7 mm diameter round bar stock. The results of heat treating all three starting conditions are shown in Figure 6.15. As shown, the microstructures of all three samples after the β-annealed heat treatment were essentially identical, despite the different starting microstructures. Each microstructure had a fully lamellar α colony structure composed of lamellae with 1~5 μm widths and 10~40 μm lengths. The α colonies had dimensions nearly equal to the length of the individual lamellae. Additionally, the prior β grain boundaries were lined with a layer of G.B. α (less than 5 μm thick). From these experiments, it can be concluded that the size and morphology of the fully lamellar microstructure that forms via this particular β-annealing heat treatment is independent of the method by which the material was

originally produced.

### 6.2.4 Effect of Gaseous Isostatic Forging

As discussed in section 5.4, gaseous isostatic forging technology (GIFT), which was used to increase the density of Ti-6Al-4V after HSPT and vacuum sintering, requires the material to be heated to a temperature between 845 and 900 °C for several minutes. Therefore, because these temperatures are approaching those used in sub-transus heat treatments of Ti-6Al-4V, the effect GIFT has on the porosity and microstructure of HSPT and vacuum-sintered samples was investigated.

Figure 6.16 shows six EBSD micrographs of Ti-6Al-4V produced via HSPT before and GIFT. Micrographs A-C are as-sintered HSPT Ti-6Al-4V, and micrographs D-F are as-GIFT'd HSPT Ti-6Al-4V. Micrographs A and D are image quality maps (IQ). IQ micrographs show the electron diffraction intensity as contrast gradients. The areas of darker contrast correspond to a weaker diffraction signal. Because grain boundaries cause the diffraction signal to deteriorate, IQ micrographs are useful for highlighting low-angle grain boundaries between grains of very similar or identical orientation, which are typically not shown in an EBSD orientation map. Micrographs B and E are orientation maps that display relative grain orientations as a colored gradient, with like colored grains having closer orientation to one another. Finally, micrographs C and F are composite images showing the IQ contrast gradients overlaid on the orientation map. Additionally, C and F have been zoomed in by 200% to show finer detail.

6.2.4.1 Change in Porosity During GIFT

Figure 6.16-A shows typical pores found in as-sintered HSPT Ti-6Al-4V highlighted with red circles. An average pore after HSPT is typically under 10 μm. However, larger pores, up to 100 μm or larger, are often found as the point of crack initiation in fatigue fracture surface micrographs. This is discussed in further detail in section 7.2. Therefore, larger pores do exist, though they are few and far between. However, their presence has a definitive effect on the fatigue performance of the as-sintered material. GIFT is very effective at essentially removing all porosity in the as-sintered microstructures. The vast majority of pores close completely or are reduced in size below 1 μm and, therefore, are typically not observed on a polished surface. The porosity of as-sintered and as-GIFT'd samples and the effect they have on mechanical properties are discussed in detail in CHAPTER 7.

6.2.4.2 Effect of GIFT on Microstructure

As discussed previously in this chapter, the as-sintered microstructure of HSPT Ti-6Al-4V is composed of fine colonies of lamellar α grains. The average width of the α colonies is typically around 5 μm or less. When comparing the orientation maps of the as-sintered and as-GIFT'd samples in Figure 6.16, one may notice that the overall morphology of the microstructure appears to be very similar. That is, they appear to be composed of slightly elongated grains with an average width of about 5 μm. However, the IQ map shown in Figure 6.16-A and C show distinct striations within the α grains of the as-sintered microstructure. This is because the apparent α grains are actually colonies of ultrafine parallel α lamellae in the as-sintered microstructure. The individual α lamellae within the

colonies have a length equal to the size of the colony (~5 μm) and submicron widths. Additionally, as shown in Figure 6.16-D and F, these striations are absent in the as-GIFT'd microstructure. It has been proposed that the ultrafine dimensions of the α lamellae creates a high degree of surface energy within the colonies, generating a driving force for coalescence of the lamellae. Therefore, during GIFT and other heat treatments of HSPT Ti-6Al-4V, the α lamellae within a single colony coalesce to form a single α grain with a size and shape equivalent to the α colonies in the as-sintered microstructure. As such, the as-GIFT'd Ti-6Al-4V has a fine globularized microstructure, as opposed to the ultrafine lamellar structure of the as-sintered material. This phenomenon is discussed further in section 6.3.1.

The GIFT process has very little effect on the microstructure of vacuum-sintered samples. This is consistent with the fact that the GIFT process is similar to a sub-transus heat treatment with slow cooling, which was shown to have no effect on the microstructure of vacuum-sintered Ti-6Al-4V. However, the GIFT process does produce a change in the vacuum-sintered microstructure that is worth mention. As shown in Figure 6.17, the microstructure of vacuum-sintered sample after GIFT has regions at the triple points of the α grains composed of very fine lamellar grain. Therefore, as the vacuum-sintered sample is heated, the β phase thickens. Then, upon cooling during the GIFT process, some of the thickened β grains are cooled at a sufficient rate to form small region of fine lamellar grains. The effect of this phenomenon the mechanical properties of as-GIFT'd samples is discussed in CHAPTER 7.

Further evidence for the mechanism by which the globularized microstructure is formed during GIFT is found by analyzing the grain size distribution (GSD) of the as-

sintered and as-GIFT'd material. The GSD as a function of area fraction for both conditions is shown in Figure 6.18. The GSDs were calculated from the orientation maps shown in Figure 6.16-B and E using analysis software on the EBSD microscope. The software assumes that each of the colored areas, as shown in an orientation map, represents individual grains. Therefore, the GSD of the as-sintered microstructure represents the size of the α colonies, not the size of the individual lamellae, as EBSD is unable to differentiate between α lamellae within a colony. The as-GIFT'd GSD is slightly narrower, causing the curve shown in Figure 6.18 to be slightly higher about the mean grain size. However, the average grain size, calculated by area, for both conditions is essentially identical. The calculated average grain size for the as-sintered condition is 3.81 μm, while the average grain size for the as-GIFT'd condition is 3.79 μm, both of which round to an average grain size of 3.8 μm. Therefore, it can be assumed that the globularized 3.8 μm α grains shown in as-GIFT'd microstructure were likely formed by coalescence of the ultrafine α lamellae within the colonies of the as-sintered microstructure.

## 6.3 Mechanisms and Reactions During Heat Treatment

As the β phase in Ti-6Al-4V is cooled, it tends to form lamellar α colonies, due to the diffusion-controlled process of alloying elemental partitioning. Therefore, the key to forming a fully equiaxed (globularized) or bi-modal microstructure is the formation of globularized primary α grains during heat treatments. It has been shown in this chapter that globularized α grains can be formed using simple heat treatments of HSPT Ti-6Al-4V. Additionally, it was shown that the coarse lamellar microstructure produced via vacuum sintering is not conducive to forming globularized α grains. Because of this, vacuum

sintering is not capable of forming the fine wrought-like microstructures formed from HSPT Ti-6Al-4V that have been presented in this chapter. In this section, the mechanisms by which globularized α grains form during heat treatments of HSPT Ti-6Al-4V is discussed.

Traditionally, globularized α grains are formed by recrystallization reactions during wrought processing. That is, thermomechanical processing (TMP) is used to break up the microstructure before heat treatment and generate a high dislocation density throughout the material, which serves as the driving force for recrystallization. It has been proposed that some degree of recrystallization may occur during HSPT and subsequent heat treatments, resulting from localized plastic deformation of the matrix due to the formation of the less dense δ-$TiH_2$ phase[1]. However, contrary to other processing routes such as wrought processing and traditional PM, it has been determined that the vast majority of the microstructural evolution of HSPT Ti-6Al-4V is actually controlled by surface energy-driven coalescence of ultrafine grains and simple phase transformations during heat treatments. Following this logic, it has been proposed that instead of recrystallization, there are two governing mechanisms that determine the microstructural evolution during heat treatments of HSPT Ti-6Al-4V:

1. Coalescence of ultrafine α lamellae
2. Growth and transformation of β grains

The proposed microstructural evolution during heat treatments of HSPT Ti-6Al-4V is shown schematically in Figure 6.19. Additionally, the proposed microstructural evolution during heat treatments of vacuum-sintered Ti-6Al-4V is shown schematically in Figure 6.20. The microstructural evolution of these two materials during heat treatments, and the

mechanisms and enabling factors that lead to these phenomena, are discussed in the following sections.

### 6.3.1 Coalescence of Ultrafine α Lamellae

As shown in Figure 6.19, coalescence of the ultrafine lamellae in the α colonies has been proposed as the mechanism by which globularized $\alpha_p$ grains are formed during the high temperature hold of a heat treatment. Essentially, the elevated grain boundary energy caused by the ultrafine dimensions of the α lamellae serves as a driving force for these grains to coalesce, thereby reducing grain boundary surface area and overall energy. Because of this, the resulting $\alpha_p$ grains have a size and shape similar to the size and shape of the α colonies in the as-sintered condition. The as-sintered α colonies in HSPT Ti-6Al-4V have a small overall aspect ratio and a very fine size (~5 μm). Therefore, the $\alpha_p$ grains that form via this mechanisms are also very fine and have a low aspect ratio, resulting in fine globularized $\alpha_p$ forming during heat treatments. This mechanism also occurs during GIFT processing. In fact, the thermal profile used during GIFT is very similar to that used to produce a globularized microstructure shown in Figure 6.12-B. The GIFT temperature is slightly lower (≤ 900 °C) and the time is on the order of minutes, as opposed to an hour. However, the mechanism by which the α colonies coalesce into globularized $\alpha_p$ grains is the same. Therefore, this phenomenon is discussed in detail in section 6.2.4.2 and clear evidence of this mechanism is shown in Figure 6.16 and Figure 6.18.

As mentioned previously, vacuum sintering produces a very coarse lamellar microstructure, as shown in Figure 6.1-B and Figure 6.12-E. The individual lamellae have widths on the order of 10s of microns and lengths that regularly exceed 100 μm. Therefore,

the α colonies that form during vacuum sintering are much too coarse to provide sufficient driving force for coalescence. Additionally, the colonies are so large that if the lamellae were to somehow coalesce, the resulting microstructure would be undesirably coarse. Therefore, similar to wrought processing, the only way by which fine $\alpha_p$ grains could form from a vacuum-sintered microstructure would be to deform the material via thermomechanical processing (TMP) before heat treating. However, as mentioned throughout this dissertation, incorporating these energy intensive postprocessing steps would significantly increase the cost of the process.

### 6.3.2 Evolution of β Grains During Sub-transus Heat Treatments

The size and shape of the β grains at the heat treatment temperature has a strong effect on the resulting microstructure. As the material is cooled form the elevated heat treatment temperature, β grains transform into either α grains or martensite (as discussed in section 6.2.1.1), depending on the cooling rate. The aspect ratio of α grains formed during this process is governed by the diffusion length of the alloying elements as they partition into their respective phases (as discussed in section 2.5). In this section, the evolution of β grains during heat treatments of HSPT and vacuum-sintered Ti-6Al-4V will be discussed.

A pseudo-binary phase diagram for Ti-6Al as a function of vanadium content is shown in Figure 2.5[36]. A tie line has been drawn on this figure to calculate the phase fractions at 950 °C, which is the approximate temperature used in the majority of heat treatments that produced globularized and bi-modal microstructures from HSPT Ti-6Al-4V shown in Figure 6.12. At this temperature, the equilibrium phase fraction is 60 vol% β phase and 40 vol% α phase. Conversely, the phase fraction of as-sintered Ti-6Al-4V before heat

treatment is on the order of 10 vol%. Therefore, the β grains will grow substantially at the heat treatment temperature to accommodate the higher equilibrium phase fraction.

Figure 6.21 shows optical micrographs of Ti-6Al-4V produced via HSPT and vacuum sintering. Both of these samples have been etched with Kroll's reagent, which darkens β phase causing it to appear as dark regions on optical micrographs. Additionally, phase maps are shown for the two conditions as determined via EBSD, highlighted in red and blue. It should be mentioned that β phase is restricted to grain boundaries and grain boundaries tends to produce weak diffraction signals via EBSD. Therefore, the β grains tend to have relatively poor indexing, causing them to be underestimated via EBSD. In fact, it has been estimated in this study that only about $1/5^{th}$ of the actual β phase is identified on the EBSD phase maps shown in Figure 6.21. However, these micrographs are useful in verifying the distribution of β phase that is observed via optical microscopy. From these micrographs, it can be seen that the distribution and size of the β phase is vastly different between the two conditions. In the HSPT sample, the β phase is largely confined to the triple points of the α colonies and is dispersed throughout the matrix (discontinuous). Conversely, the β phase in the vacuum-sintered microstructure is present as a continuous layer between the α lamellae.

As discussed in section 2.5, as Ti-6Al-4V is cooled, the morphology of the α grains that form from β is dependent on the cooling rate due to alloying element partitioning. Therefore, it has been observed that during heat treatments the starting size, shape, and distribution of the β grains in as-sintered HSPT Ti-6Al-4V is conducive to forming globularized α grains when the material is cooled slowly (Figure 6.19). This, coupled with the globularized $\alpha_p$ grains that form as the α lamellae coalesce at the heat treatment

temperature, results in a fully globularized microstructure. Conversely, if the material is cooled quickly, a bi-modal microstructure is formed, which is composed of the globularized $\alpha_p$ grains and either acicular or lamellar α colonies that form from the β phase. A very fast cooling rate (quenching) results in the transformation of β into martensite, which then transforms into acicular α grains during ageing as discussed in section 6.2.1 and shown in Figure 6.7. If the material is cooled at a moderate rate (air cooling), fine lamellar α colonies form from the β grains.

It has been observed that the continuous layer of β phase in the vacuum-sintered material grows into large and elongated β grains. The remainder of the α grains become long and skinny $\alpha_p$ grains (Figure 6.20). If the material is cooled slowly, the skinny $\alpha_p$ grains thicken, essentially forming a microstructure identical to that present before the heat treatment. On the other hand, if the material is quenched, the elongated β grains transform into acicular grains or α colonies, similar to that observed in HSPT samples. Therefore, the resulting microstructure is bi-modal, as shown in Figure 6.12-G. However, contrary to what is observed with HSPT TI-6Al-4V, the bi-modal microstructure consists of large and skinny $\alpha_p$, which is undesirable.

### 6.3.3 Evolution of β Grains During Super-transus Heat Treatments

As shown in Figure 6.15, super-transus heat treatments (β-annealing) produce identical heat-treated microstructures for HSPT, vacuum-sintered, and wrought-processed Ti-6Al-4V. Because of the high temperature, which results in rapid diffusion, and the fact that the treatment temperature is above the β-transus, the intermediate microstructure at the heat treatment temperature is entirely coarse β grains. Therefore, the starting microstructure

has little effect on the morphology of the β grains at the heat treatment temperature as well as the resulting microstructure.

The average size of the β grains is a function of the heat treatment temperature. For the temperature used on the samples shown in Figure 6.15 (1050 °C), the β grains at the treatment temperature are on the order of 100 μm. As the material is cooled, the β grains transform into α colonies. The width of the lamellae is determined by the cooling rate. Similar to the other heat treatments, a slow cooling rate will produce large α lamellae with a relatively small aspect ratio, while faster cooling rates will forms fine lamellae until the critical cooling rate for martensite is reached (~1000 °C)[34]. For the samples shown in Figure 6.15, a moderate cooling rate (air cooling) was used, resulting in moderately coarse lamellar structure observed.

Table 6.1: Hydrogen concentration as a function of dehydrogenation time and temperature.

| **Temperature** | **Time** | **H (ppmw)** |
|---|---|---|
| 650 °C | 12 hours | 142.57 |
| 825 °C | 2 hours | 93.09 |
| 650 °C | 24 hours | 19.34 |
| 750 °C | 12 hours | 1.84 |
| 650 °C | 24 hours | 2.36 |

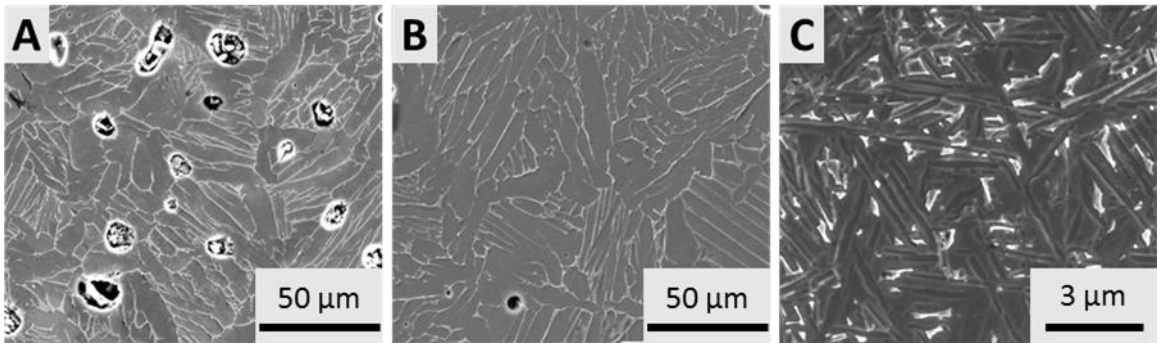


Figure 6.1: Micrographs of Ti-6Al-4V produced by blended elemental PM via A) vacuum sintering of metallic powder, B) vacuum sintering of hydrogenated powder, and C) HSPT of hydrogenated powder.

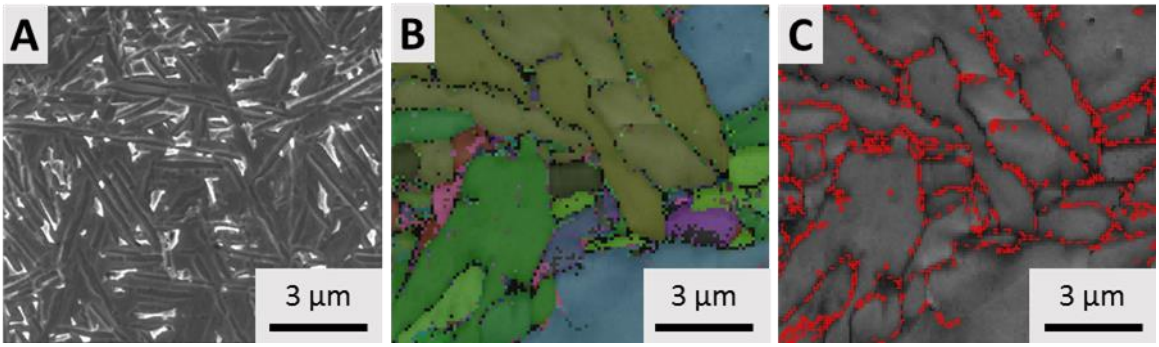


Figure 6.2: Micrographs of as-dehydrogenated Ti-6Al-4V produced via HSPT. A) SEM micrograph, B) Euler map of EBSD scan, and C) band contrast map showing HAGBs in red.

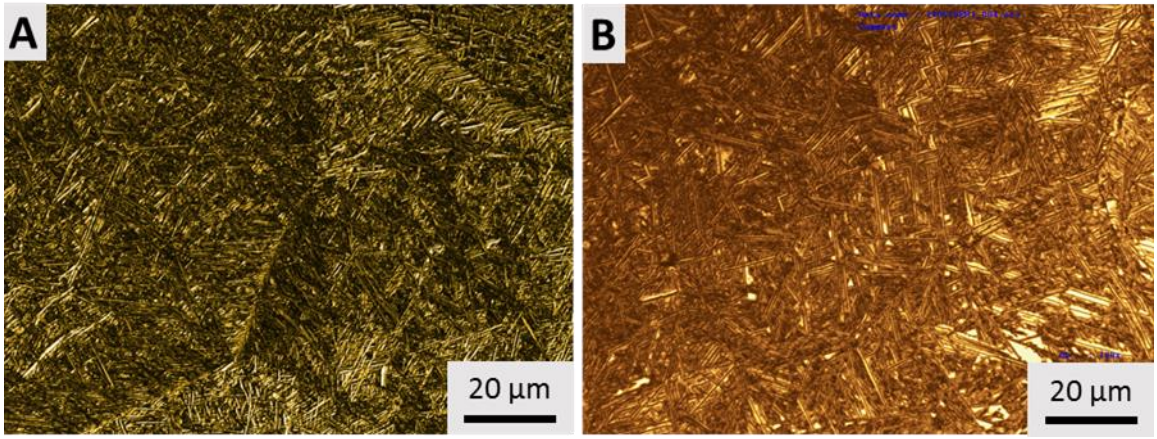


Figure 6.3: Confocal micrographs of as-sintered Ti-6Al-4V before dehydrogenation produced via HSPT.

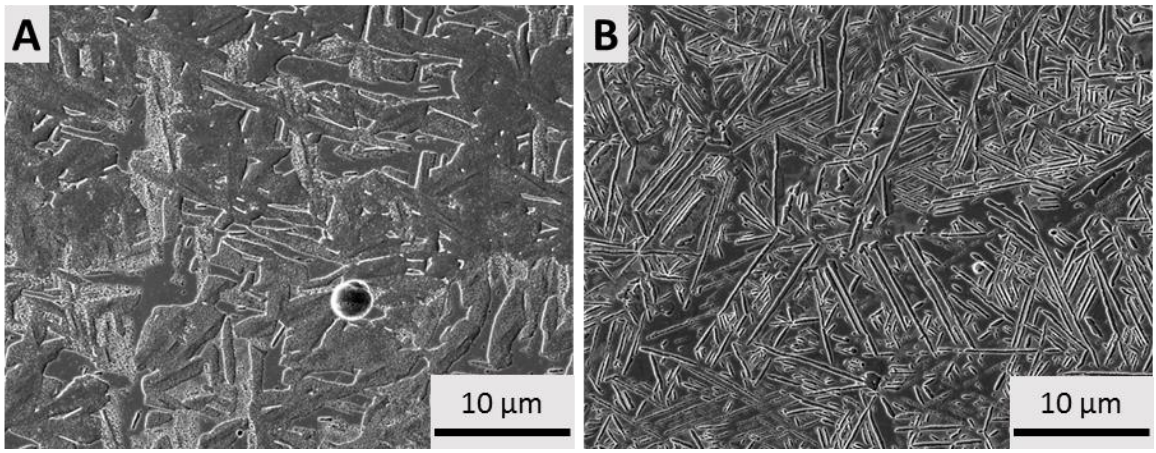


Figure 6.4: SEM micrographs of as-dehydrogenated Ti-6Al-4V. A) Dehydrogenated at 750 ºC, and B) dehydrogenated at 650 ºC.

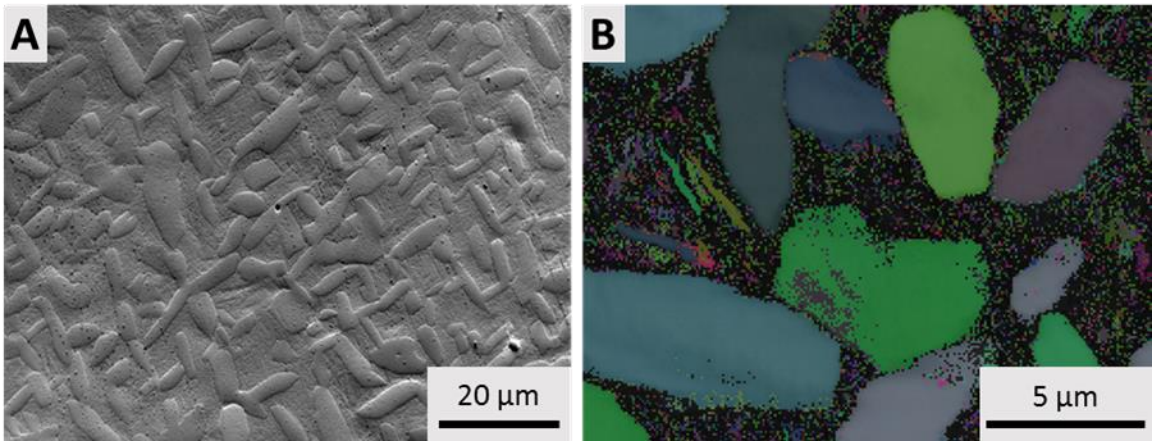


Figure 6.5: Micrographs of electropolished Ti-6Al-4V after heating treated at 954 ºC for 1 hour with a water quench. A) High-tilt SEM, and B) EBSD Euler map.

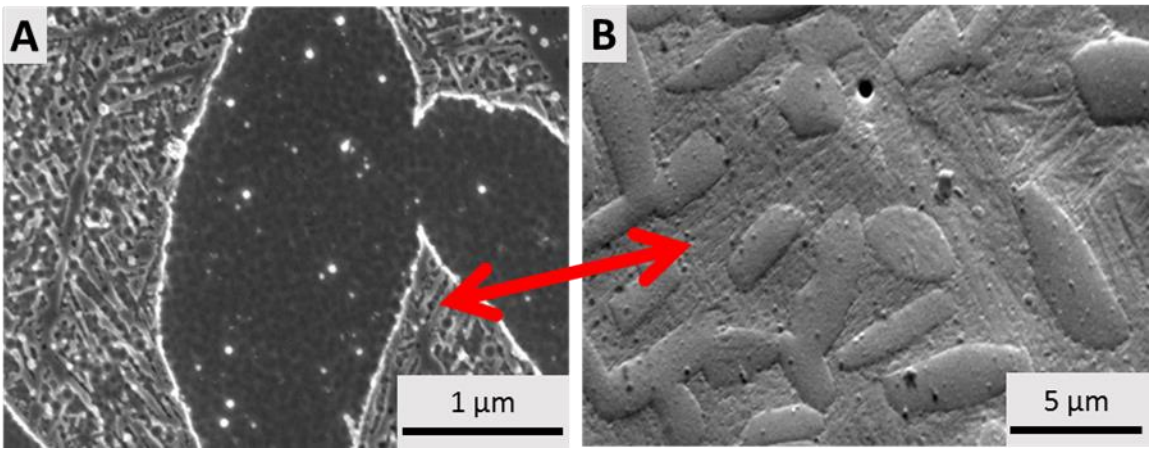


Figure 6.6: Micrographs of Ti-6Al-4V after heat treatment at 954 ºC for 1 hour with a water quench. A) High resolution SEM of mechanically polished and etched surface, and B) high-tilt SEM of electropolished surface.

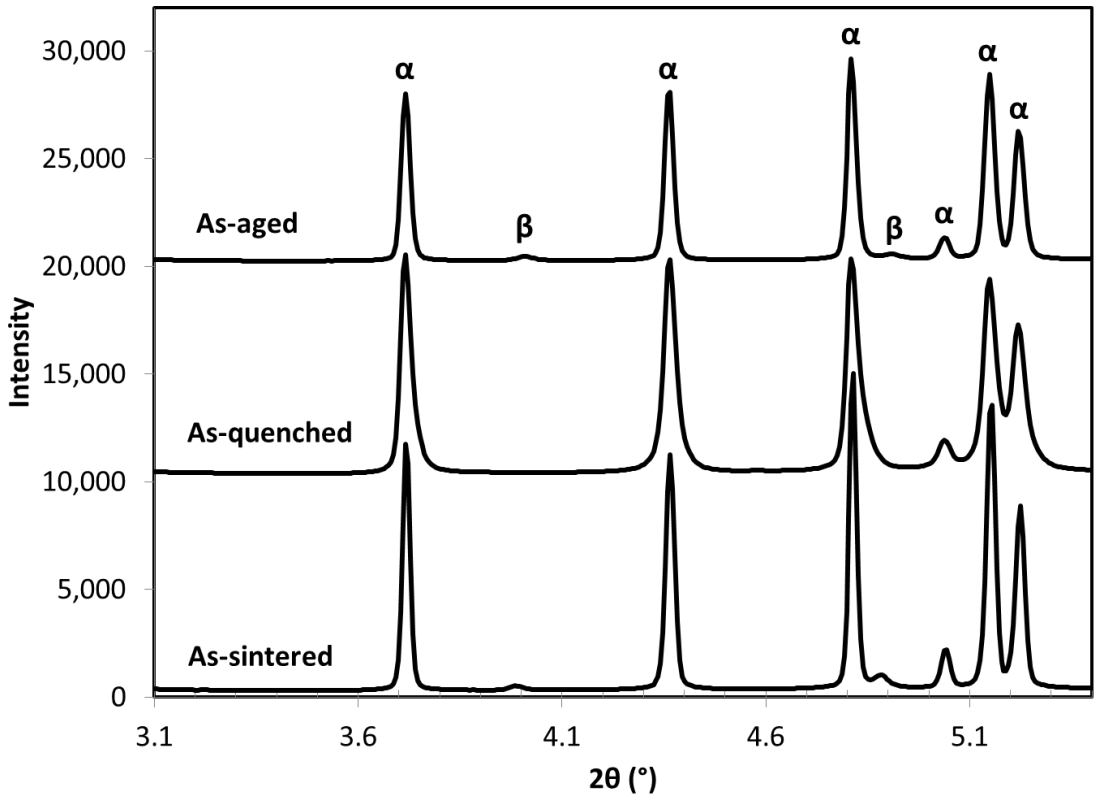


Figure 6.7: Synchrotron X-ray diffraction patterns of as-sintered Ti-6Al-4V produced via HSPT, the same sample after heat treating at 954 °C for 1 hour followed by water quenching, and then after ageing at 550 °C for 6 hours.

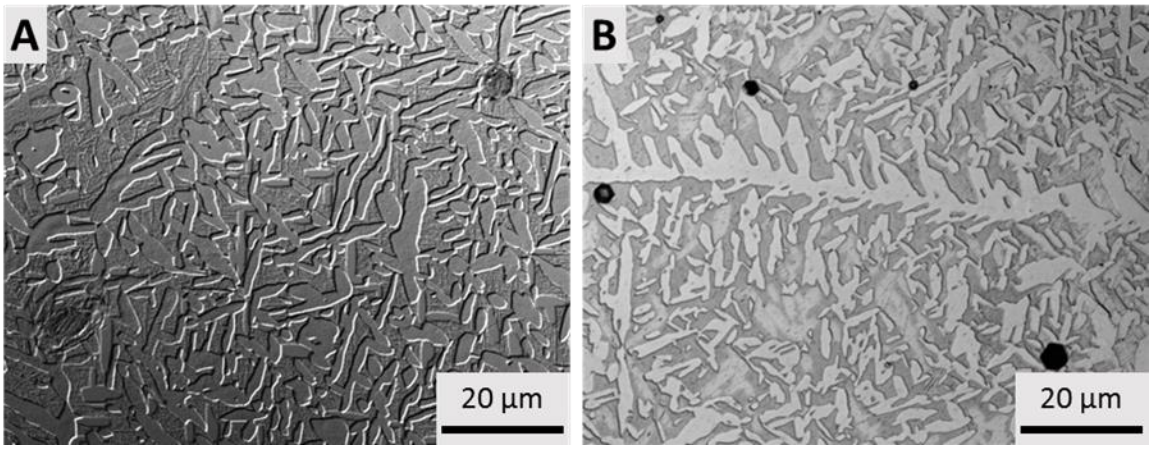


Figure 6.8: Confocal micrographs of mechanically polished and etched Ti-6Al-4V that has been heat treated at 954 ºC for 1 hour with a water quench. A) Dehydrogenated at 750 ºC and, B) dehydrogenated at 650 ºC.

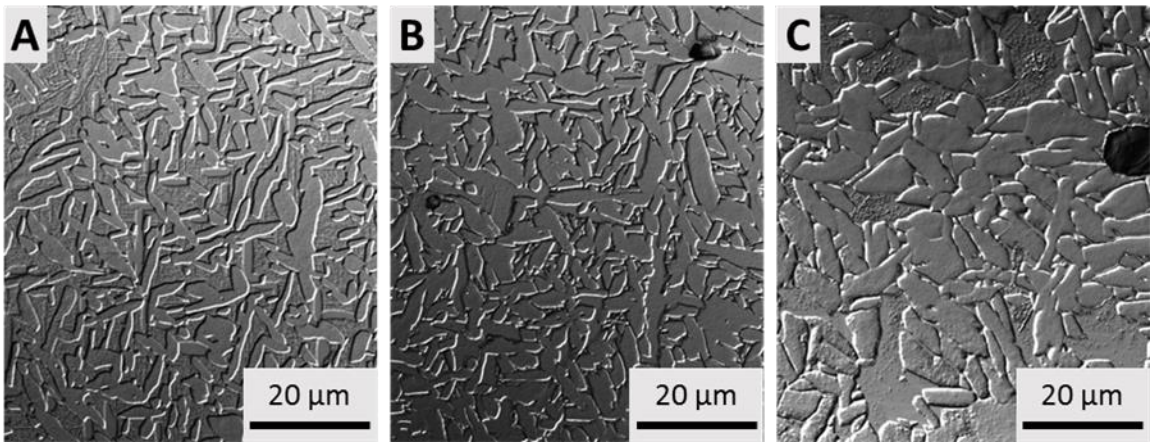


Figure 6.9: Confocal micrographs of mechanically polished and etched Ti-6Al-4V, dehydrogenated at 750 ºC, and heat treated at 954 ºC for 1 hour. A) Water quenched, B) air cooled, and C) furnace cooled.

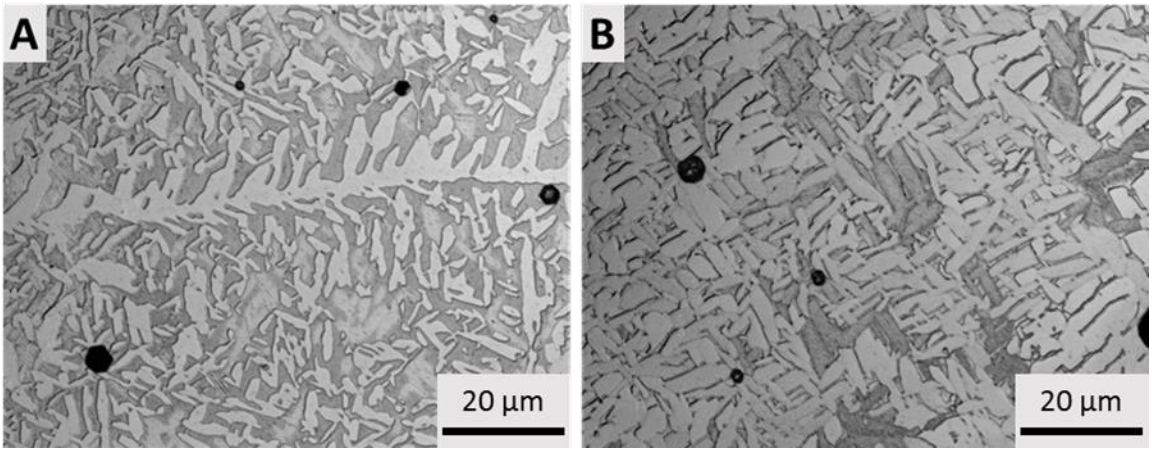


Figure 6.10: Optical micrographs of mechanically polished and etched Ti-6Al-4V, dehydrogenated at 650 ºC, and heat treated at 954 ºC for 1 hour. A) Water quenched, and B) furnace cooled.

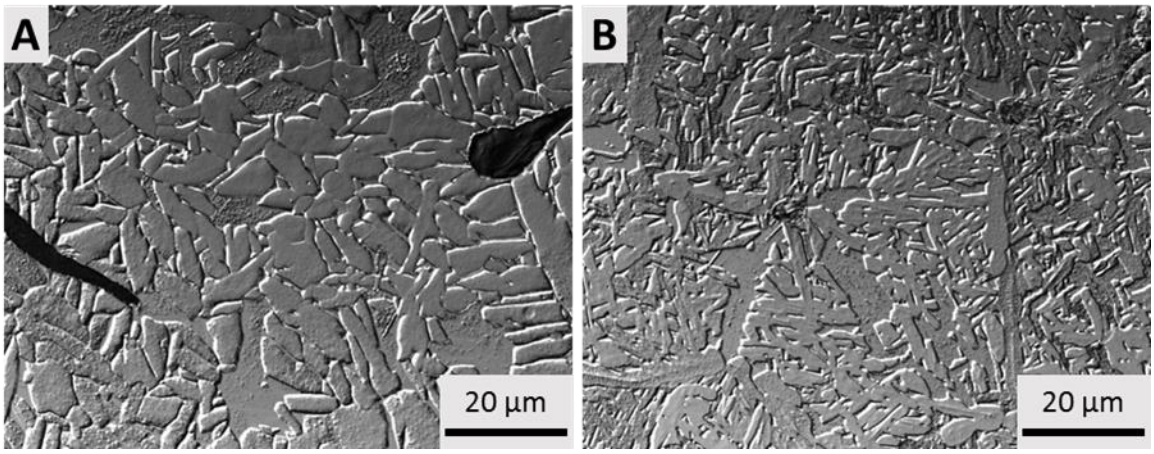


Figure 6.11: Confocal micrographs of mechanically polished and etched Ti-6Al-4V, sintered via HSPT with a dehydrogenation temperature of 750 °C. A) Heat treated at 954 °C for 1 hour and furnace cooled, and B) heat treated at 825 °C for 1 hour and furnace cooled.

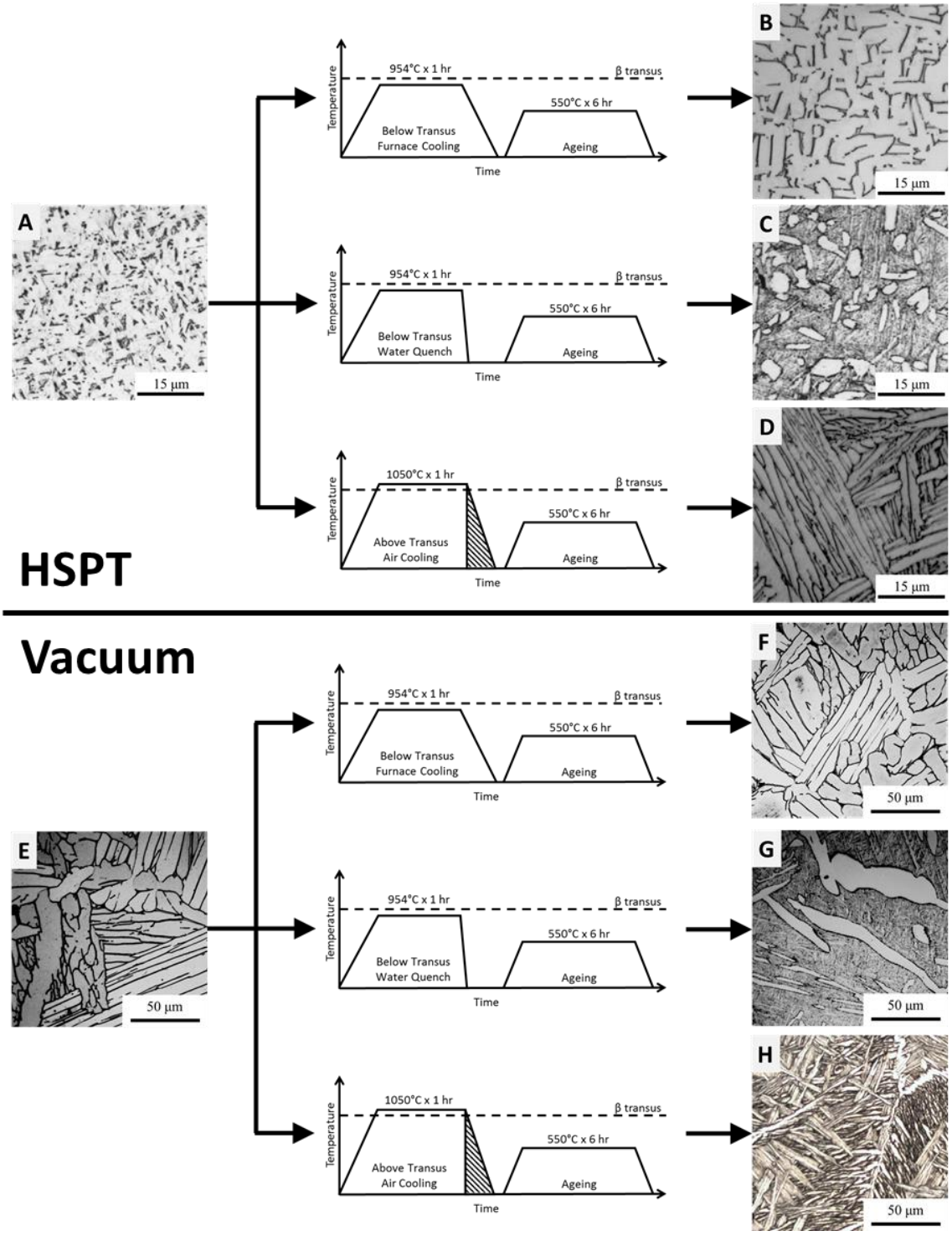


Figure 6.12: Comparison of microstructure achieved after heat treating HSPT vs. vacuum-sintered specimens.

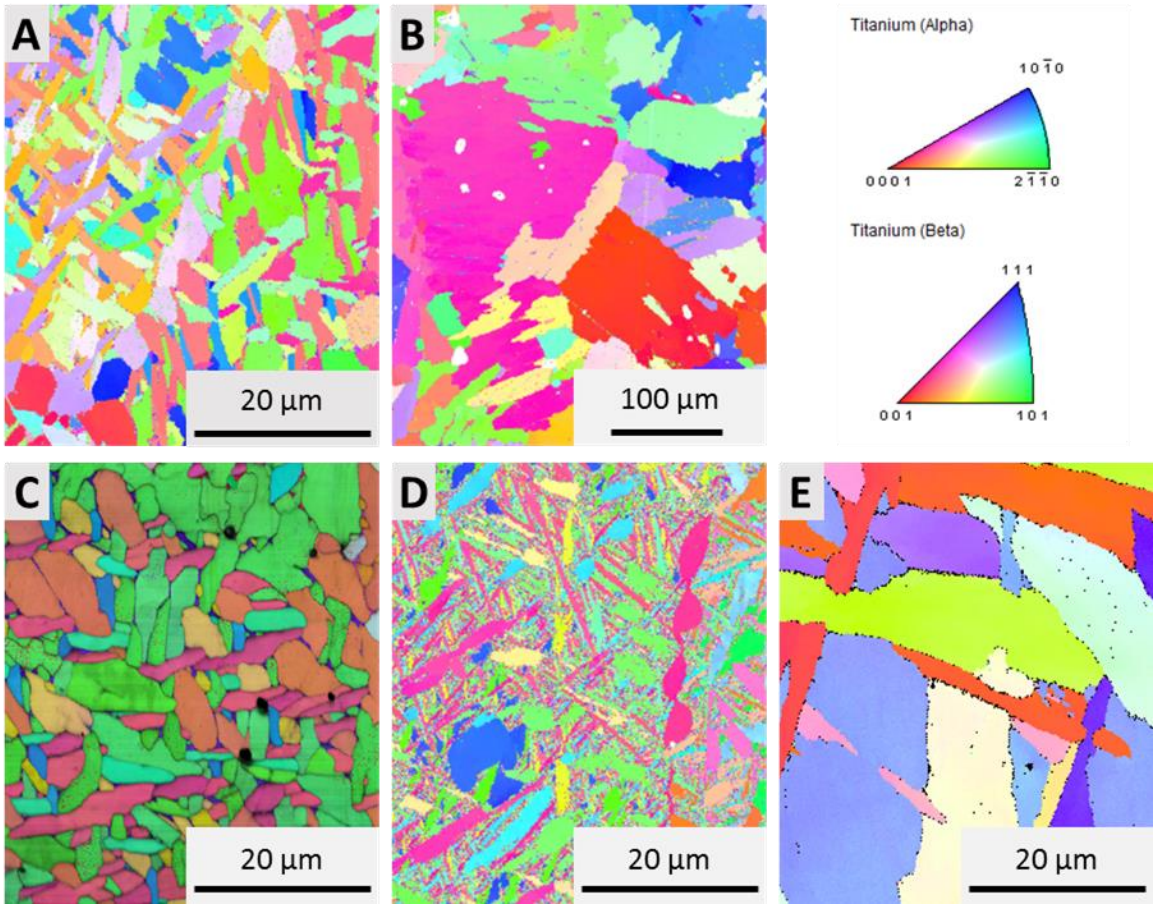


Figure 6.13: EBSD orientation color maps (inverse pole figure) of Ti-6Al-4V produced via HSPT, vacuum sintering, and HSPT with heat treatments. A) as-sintered HSPT, B) as-vacuum-sintered, C) globularized HSPT, D) bi-modal HSPT, and E) β-annealed HSPT. The inverse pole figure orientation legends for α and β phase correspond to all images.

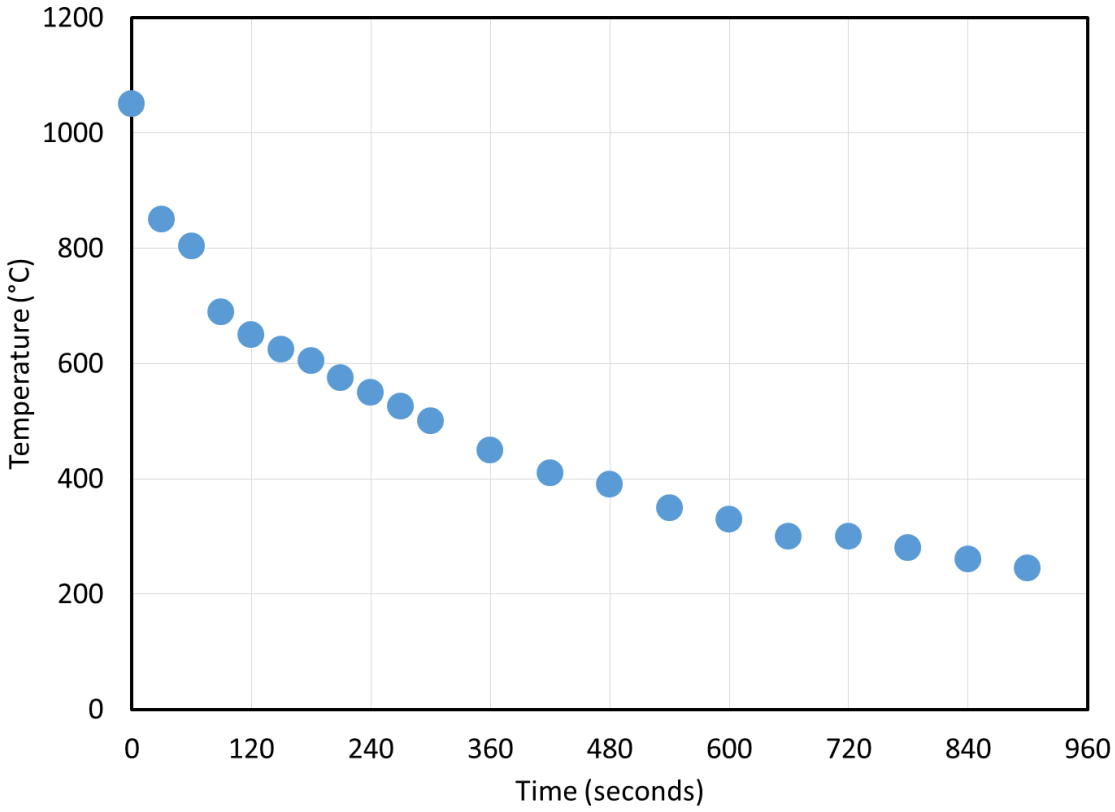


Figure 6.14: Cooling curve for β-anneal heat treatment with air cooling.

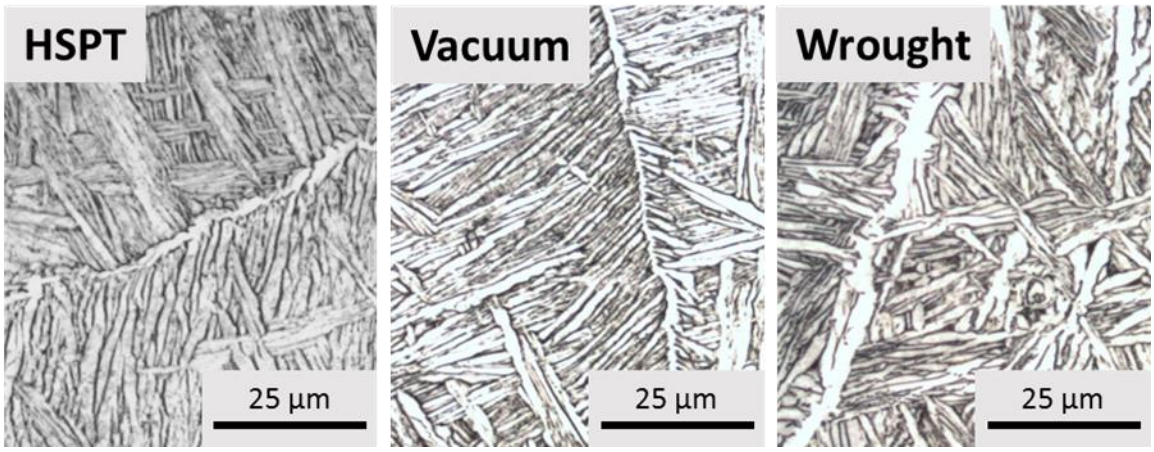


Figure 6.15: Fully lamellar microstructures produced by performing identical β-anneal heat treatments on as-sintered HSPT, as-vacuum-sintered, and as-received (mill-annealed) wrought Ti-6Al-4V.

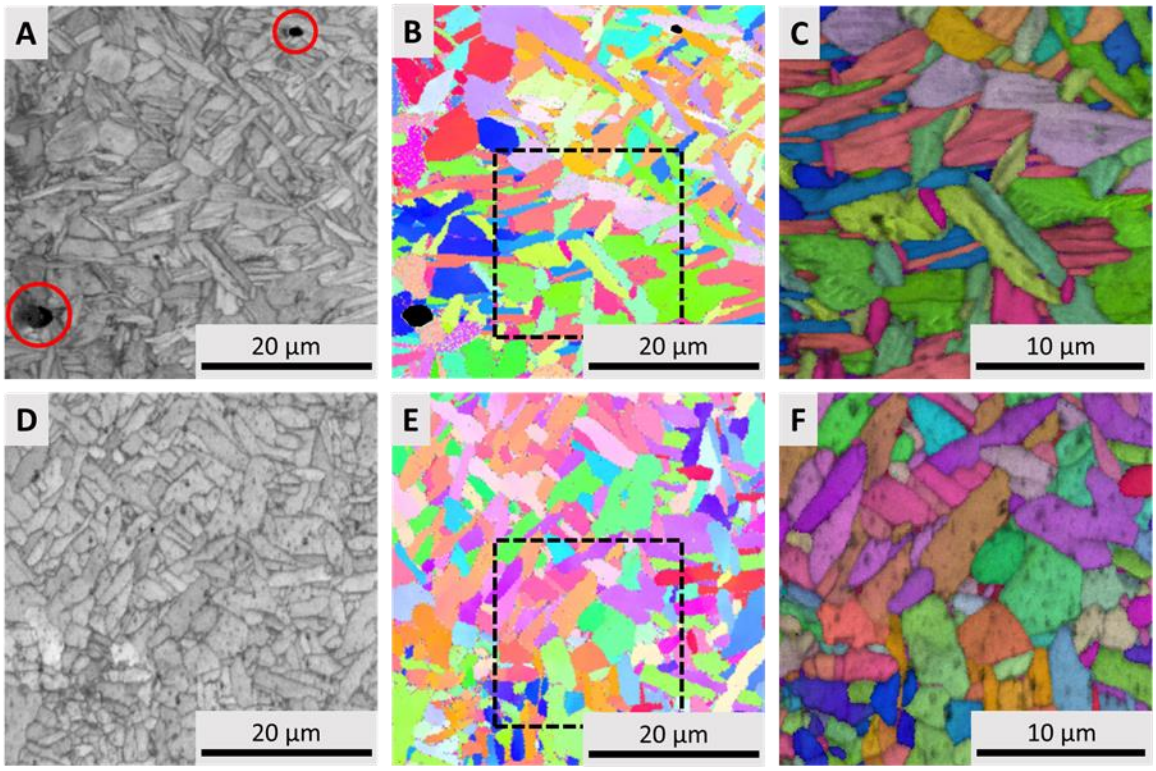


Figure 6.16: EBSD micrographs of HSPT Ti-6Al-4V: A) as-sintered image quality map (IQ), B) as-sintered orientation map, C) as-sintered IQ + orientation map composite of outlined area in B, D) as-GIFT'd IQ, E) as-GIFT'd orientation map, and F) as-GIFT'd IQ + orientation map composite of outline area in E. The dashed boxes in B and E correspond to the area shown in C and F, respectively.

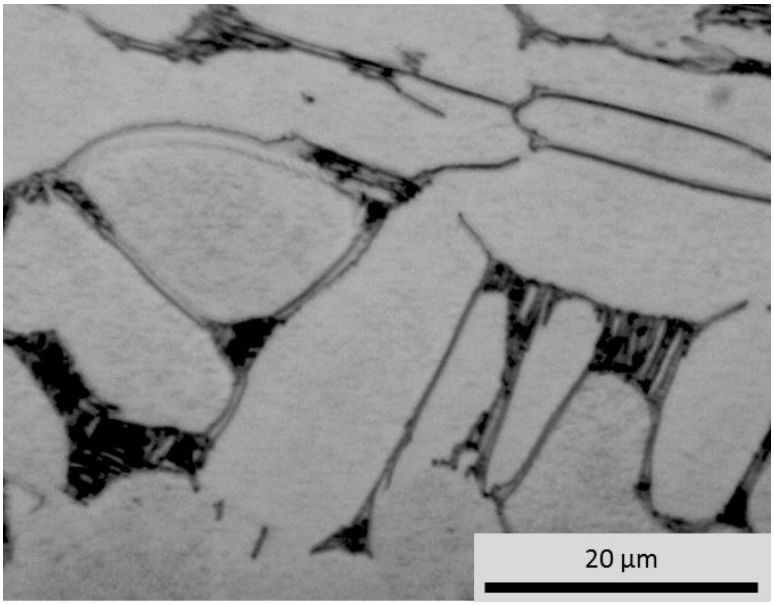


Figure 6.17: Microstructure of vacuum-sintered Ti-6Al-4V after GIFT showing regions of fine lamellar grains at the tripe points of the coarse α grains.

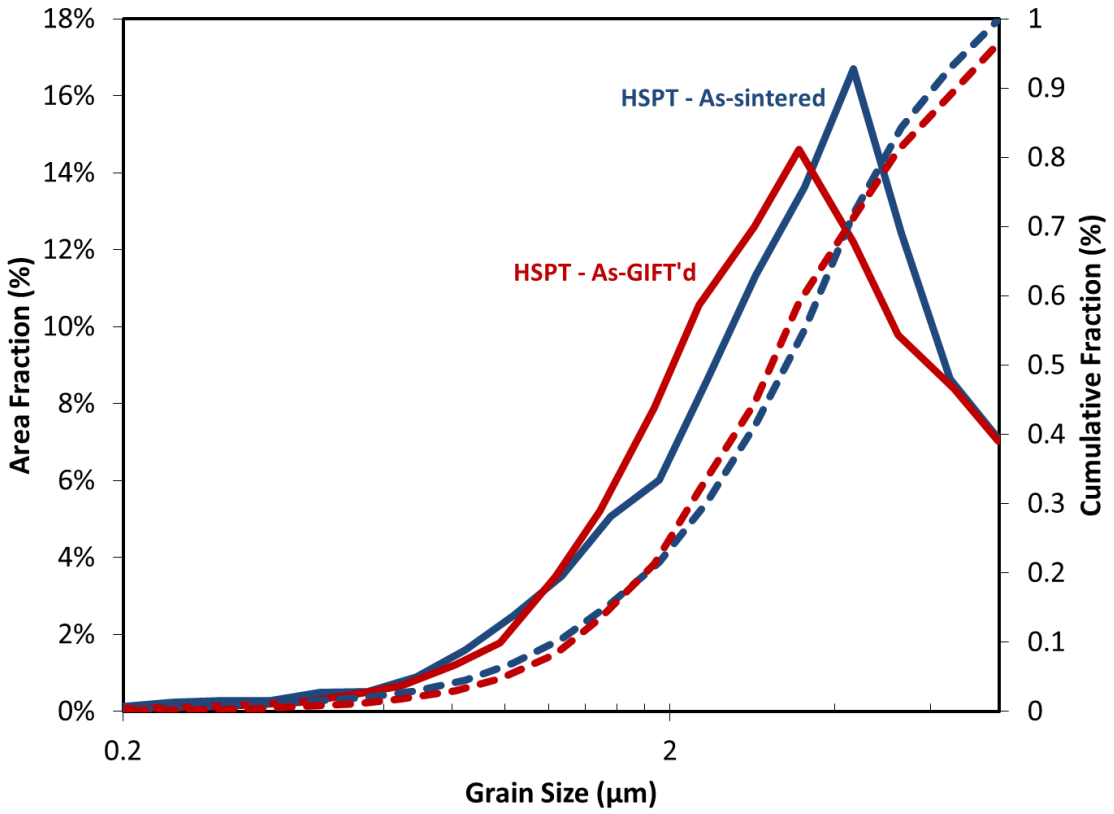


Figure 6.18: Grain size distribution of Ti-6Al-4V produced via HSPT before and after GIFT.

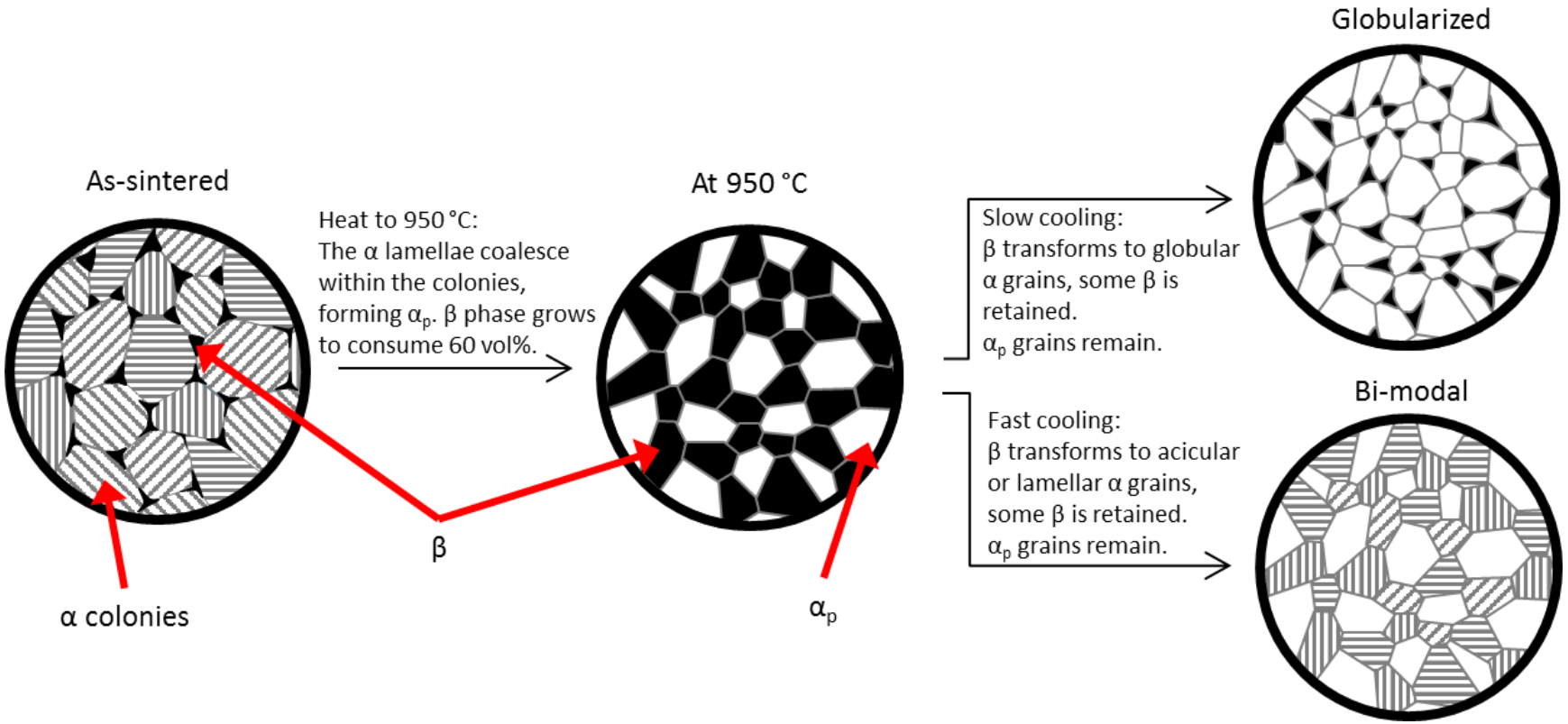


Figure 6.19: Schematic flow sheet showing microstructural evolution during heat treatments of HSPT Ti-6Al-4V. Grain sizes are not to scale.

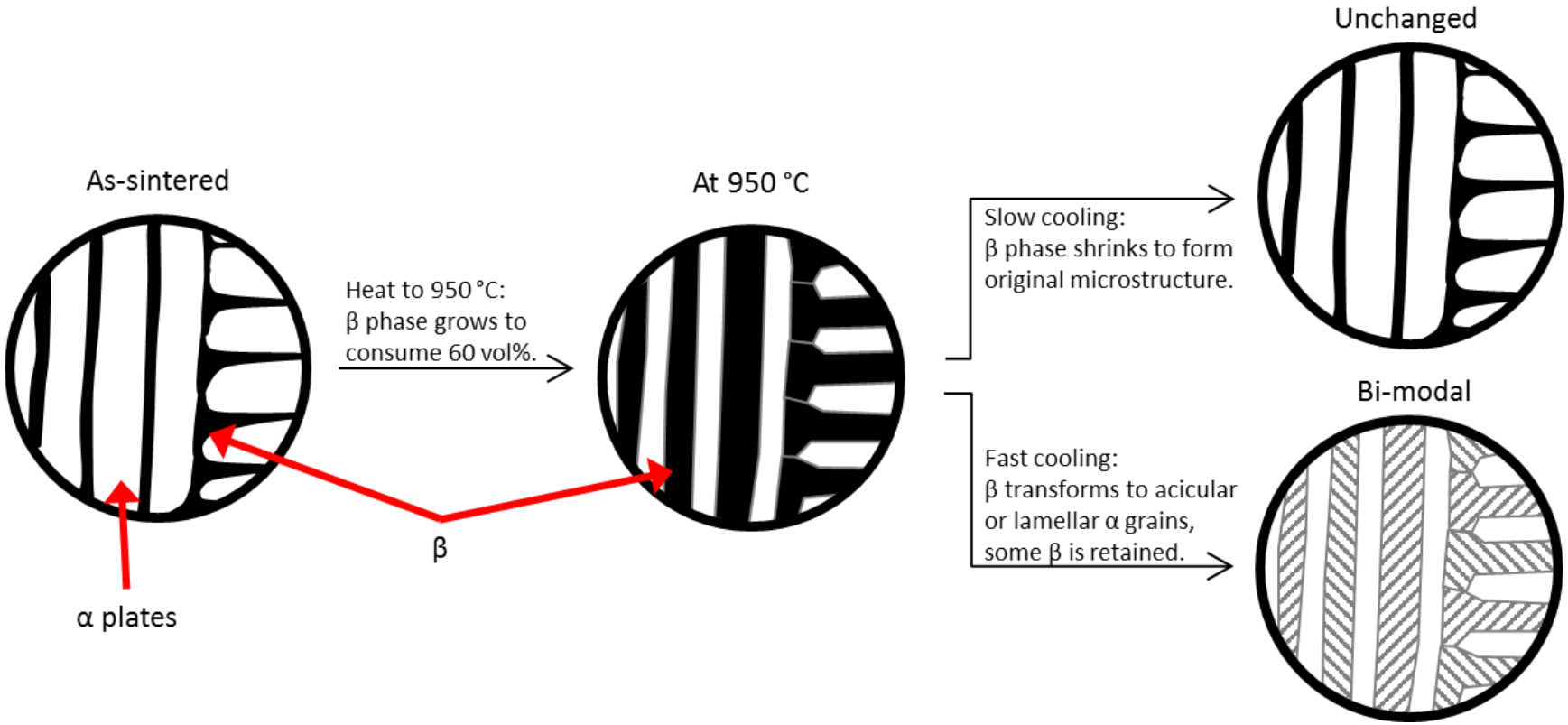


Figure 6.20: Schematic flow sheet showing microstructural evolution during heat treatments of vacuum-sintered Ti-6Al-4V. Grain sizes are not to scale.

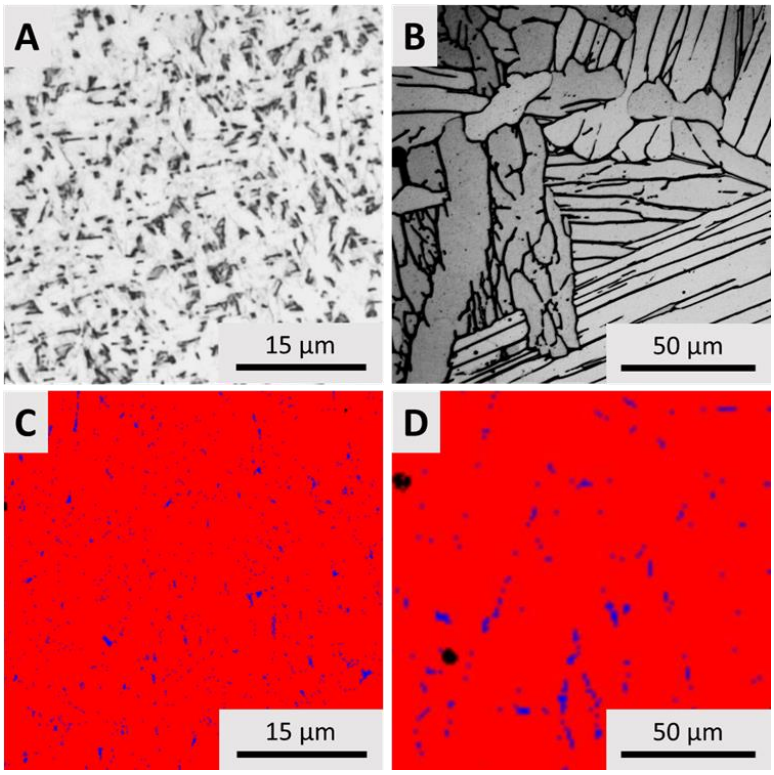


Figure 6.21: Optical micrographs and EBSD phase fraction calculations of as-sintered Ti-6Al-4V produced via HSPT (A and C) and vacuum sintering (B and D). The blue areas correspond to β-phase is C and D.

# CHAPTER 7

## RELATIONSHIP BETWEEN MICROSTRUCTURE AND MECHANICAL PROPERTIES OF Ti-6Al-4V PRODUCED VIA HSPT

In CHAPTER 6, the microstructures that are produced via HSPT with and without heat treatments were presented and compared with traditional processes, especially vacuum sintering and wrought processing. It was shown that wrought-like microstructures (globularized, bi-modal, and fully lamellar) are possible via HSPT with simple heat treatments without requiring thermomechanical processing (TMP). However, the merit in controlling the microstructure of a structural metal is only warranted if the microstructural changes have a measurable effect on the mechanical properties. Therefore, an important area of this dissertation is defining how the microstructures that are possible via HSPT and subsequent heat treatments translate into mechanical properties.

In this chapter, the mechanical properties associated with the various microstructures discussed in the previous chapter will be presented. Both the static properties (strength and ductility) as well as the dynamic properties (fatigue performance) of Ti-6Al-4V produced via HSPT and vacuum sintering will be presented. Because of the large amount of information discussed in this chapter, a summary of the important findings presented in this chapter and previous chapters is presented in CHAPTER 8.

## 7.1 Static Mechanical Properties

As discussed in CHAPTER 4, all the tensile bars used to generate the data in this chapter were prepared conforming to the ASTM E8 standard[133]. All samples were prepared as cylindrical blanks which were pressed as green parts using a cold isostatic press (CIP) before sintering. Sintering was performed using the standard HSPT or vacuum sintering profiles shown in Figure 4.2, followed by gaseous isostatic forging (GIFT) and/or heat treatments, when applicable. The GIFT process is shown schematically in Figure 4.5. Additionally, all heat treatments used on samples followed one of the three basic heat treatments presented in Figure 4.4, which have all been borrowed from typical heat treatments used in wrought processed as defined in the literature[34–37]. After thermal processing, the cylindrical blanks were sent out for machining and made into round "dog-bone" tensile bars with a 25.4 mm (1 inch) long by 6.35 mm (0.25 inch) diameter gauge and 3/8-16" threaded grips. The tensile tests were performed on the MTS Landmark test frame discussed in section 4.5 at a strain rate of $3 \times 10^{-4}\ s^{-1}$, as designated by the ASTM B348 standard for titanium alloys[96].

### 7.1.1 As-Sintered HSPT vs. Vacuum Sintering

The static mechanical properties of as-sintered HSPT Ti-6Al-4V have been previously published and compared with vacuum-sintered material produced using identical powder preparation and compaction techniques[2,5,8,14,15,17]. Ti-6Al-4V produced using the standard HSPT sintering profile and atmosphere (Figure 4.2) will have an average tensile strength exceeding 1 GPa and exhibit 15% elongation at failure. Conversely, vacuum-sintered Ti-6Al-4V will have significantly lower ultimate tensile strength (~900 MPa) but similar

ductility. In this section, the as-sintered mechanical properties of Ti-6Al-4V produced using both sintering technologies will be discussed, both as a baseline to compare with the new heat treating and GIFT results and as further verification of the published data.

Figure 7.1 shows stress-strains curves for as-sintered Ti-6Al-4V produced via HSPT and vacuum sintering. The respective thermal profiles and atmospheres used to sinter these samples are given in Figure 4.2. Both the shape of the stress-strain curve and the mechanical properties reported agree well with previously published results for HSPT and vacuum sintering[2,5,8,14,15,17]. As shown in Figure 7.1, HSPT produces significantly higher strength than vacuum sintering with minimal sacrifice in ductility. The overall range of values for as-sintered specimens prepared by these two methods is presented in section 8.4. From these data, it can be deduced that the much finer microstructure plays an important role in improving the static strength of PM Ti-6Al-4V without sacrificing ductility.

It should be pointed out that the stress-strain curves for both HSPT and vacuum-sintered Ti-6Al-4V are very flat throughout the plastic region of the curve. This is indicative of a homogenous microstructure, which is consistent with what has been observed during metallographic analysis of such samples. It has been found that the homogeneity of the microstructure for HSPT Ti-6Al-4V is dependent on the partial pressure of atmosphere used during the sintering process. That is, it was found that hydrogen partial pressure of 0.5 atm or more consistently produced a fine microstructure that was homogenous across the sample's interior. However, smaller hydrogen partial pressures resulted in a slightly coarser microstructure towards the center of the samples. It has been determined that the lower hydrogen partial pressure results in a hydrogen concentration gradient across the sample. Because the presence of hydrogen is key to

controlling the phase transformations that result in the ultrafine as-sintered microstructure[5], it is necessary to maintain a sufficient hydrogen concentration across the entire sample to produce the desired microstructure.

### 7.1.2 Effect of Gaseous Isostatic Forging Technology (GIFT)

Stress-strain curves of samples produced via HSPT before and after GIFT processing are given in Figure 7.2. Additionally, stress-strain curves of samples produced via vacuum sintering before and after GIFT are given in Figure 7.3. The range of values for mechanical properties of samples tested in all four conditions are discussed in detail in section 8.4.

GIFT has a measurable effect on the ductility of HSPT Ti-6Al-4V while not affecting the strength in any significant degree. As shown in the shape of the stress-strain curve in Figure 7.2 and the range of values reported in section 8.4, HSPT Ti-6Al-4V has a tensile strength exceeding 1 GPa both before and after GIFT. However, the ductility increases by several percent elongation (%EL), and is increased by a factor of almost 1.5 with regard to reduction in area (%RA).

As discussed later in this chapter in section 7.2.1, as-sintered HSPT Ti-6Al-4V will have rogue pores on the order of 100 μm. Such pores are often found on the fracture surface of HSPT tensile specimens. Therefore, it is assumed that they tend to play a role in governing the failure of this material during tensile tests. The fact that GIFT closes these large pores, indicated by the lack of pores on fracture surfaces of both tensile and fatigue bars after GIFT, it is likely that removal of the pores plays at a significant role in improving the ductility of HSPT Ti-6Al-4V.

It has also been shown in section 6.2.4.2 that the high temperatures used during GIFT

cause the ultrafine α lamellae in the as-sintered microstructure to coalesce, forming fine $\alpha_p$ grains. It is shown in the literature that the formation of $\alpha_p$ has ductilizing effect[35]. As shown in Figure 2.18, cracks tends to form within the lamellar region of α+β Ti microstructures. Therefore, for these reasons, it stands to reason that the microstructural evolution that occurs during GIFT is part of the reason for the significant change in ductility.

As shown in the following section, a pressure-less heat treatment to produce globularized $\alpha_p$ grains improves %EL but not %RA of HSPT Ti-6Al-4V. Therefore, the closing of porosity has the greatest effect on %RA, while the change in microstructure has the greatest effect on %EL.

As opposed to HSPT, vacuum-sintered Ti-6Al-4V does not experience the same change in ductility as a result of GIFT. With respect to both %EL and %RA, vacuum-sintered Ti-6Al-4V has very similar ductility both before and after GIFT. However, there is a measurable change in strength of about 40 MPa with regards to both UTS and yield strength. As shown in Figure 6.17, GIFT causes the vacuum-sintered microstructure to change slightly from the as-sintered condition. That is, small regions of fine lamellar grains are visible at the triple points of the coarse α grains. Therefore, it is likely that these small regions of refined microstructure that result from the GIFT process cause the slight increase in strength.

### 7.1.3 Effect of Heat Treatments

In order to study the effect of heat treating on mechanical properties, samples were prepared with globularized (equiaxed), bi-modal, and fully lamellar (β-annealed) microstructures. For these experiments, samples were prepared using the standard HSPT

profile shown in Figure 4.2. The heat treatment and ageing profiles and resulting microstructure of the samples discussed in this section with the corresponding globularized, bi-modal, and β-annealed microstructures are shown in Figure 6.12. Therefore, Figure 6.12 can be used to reference both the heat treating profiles and the corresponding microstructures of all the samples discussed in this section.

Figure 7.4 shows representative stress-strain curves for samples with an as-sintered, bi-modal, and "globularized" microstructure that results from HSPT with and without heat treatment. The as-sintered condition falls in the middle of the heat treated conditions with respect to both strength and ductility. As shown in the micrograph, the "globularized" microstructure improves ductility but lowers strength. Conversely, the bi-modal microstructure has the greatest strength, but at a sacrifice in ductility of both %EL and %RA.

As discussed in detail in section 8.4, the formation of a "globularized" microstructure improves the average %EL of HSPT Ti-6Al-4V, but has little effect on the %RA. Because the formation of globularized $\alpha_p$ has a ductilizing effect on the microstructure by eliminating areas prone to crack formation within the lamellar regions of the microstructure, it is expected that the %EL should increase with a corresponding decrease in strength. However, it should be pointed out that this heat treatment does not close large pores. Therefore, the "globularized" Ti-6Al-4V produced via this heat treatment will still have the rogue pores that are present in the as-sintered condition. The fact that the large pores and %RA are the constant between the as-sintered and "globularized" microstructure, it is logical that the large pores primarily effect the %RA of HSPT Ti-6Al-4V with regard to static properties.

The bi-modal microstructures prepared and tested in this study were the result of an STA heat treatment with a water quench. As shown in the XRD data and discussed in section 6.2.1.1, the water quench causes the formation of martensite, which transforms to acicular α regions during ageing. Acicular α is known to have high strength but tends to be rather brittle[34,35]. Therefore, the presence of this phase in the tensile samples is the cause of both the increase in strength and the sacrifice of ductility. It should be pointed out that the "globularized" $\alpha_p$ grains that form during the heat treatment will ductilize the resulting microstructure. Therefore, if this material was entirely acicular α, which could be formed by heat treating above the transus temperature and then water quenching, it would likely have significantly greater strength but ductility below 10 %EL, which is the threshold of the ASTM standard[96]. For reference, this is observed in the fully acicular tensile data prepared from samples by such a heat treatment as discussed on page 526 of the ASM handbook of titanium properties[35].

7.1.3.1 Effect of Heat Treatments Following GIFT

In addition to heat treating as-sintered HSPT Ti-6Al-4V, samples were also prepared by first processing HSPT Ti-6Al-4V with GIFT and then subjecting it to three different heat treatments to produce "globularized", bi-modal, and β-annealed (fully lamellar) microstructures. The heat treatments used and the corresponding microstructures produced are identical to those produced from the as-sintered condition as shown in Figure 6.12. The results of these experiments on tensile properties are discussed in this section.

Figure 7.5 shows the stress-strain curves of representative samples produced via HSPT + GIFT with the three different heat treatments and microstructures. Additionally, the

range of values for all samples produced with these conditions is discussed in section 8.4. As expected from the previous results, the "globularized" sample exhibited a significant increase in ductility and a measurable loss in strength. The bi-modal microstructure has the greatest strength, approaching 1100 MPa, but suffers a loss in ductility form the as-GIFT'd condition. The β-annealed samples exhibited the worst mechanical properties when considering the trade-off between strength and ductility. While the samples shown in Figure 7.5 seem to indicate that β-annealed falls in the middle of bi-modal and "globularized" mechanical properties, the range of values for all samples produced actually show a different trend. As discussed in section 8.4, there were some β-annealed samples with greater ductility than some bi-modal samples, but there were also bi-modal and "globularized" samples which exhibited both better strength and ductility than some β-annealed samples. Therefore, when considering the total trade-off between strength and ductility, the β-annealed condition produces the worst mechanical properties.

The mechanical properties observed from the "globularized" microstructure produced by GIFT and heat treatment were rather remarkable. The strength and %EL are changed from the as-GIFT'd condition by further evolution of the microstructure to form slightly larger, globularized $\alpha_p$ grains. However, the %RA does not change due to the fact that the porosity of the samples before and after heat treatment is essentially unchanged. As mentioned, there was a measurable loss in strength from the as-GIFT'd condition, but not as much as was seen when the as-sintered material was subjected to the same heat treatment. It is likely that the two-step heat treatment that occurs by first processing with GIFT and then an STA heat treatment retarded the process, which lowers the strength during STA. Therefore, this material had a tensile strength approaching 1 GPa and ductility exceeding

21 %EL and 46 %RA.

Compared to the as-GIFT'd condition, the bi-modal microstructure produced in this study has improved strength, but decreased %EL and %RA. It is known that the acicular α regions that form as a result of the bi-modal heat treatment are both strong and relatively brittle, explaining the change in mechanical properties. It should be noted that the ductility of the bi-modal microstructure produced after GIFT is significantly better than the bi-modal microstructure produced from the as-sintered condition. Therefore, it is likely that the porosity present in the as-sintered condition has a greater effect on the acicular grains, causing the bi-modal microstructure in the GIFT samples to exhibit improved mechanical properties than that generated from the as-sintered microstructure.

An interesting result of these experiments is the microstructure and corresponding mechanical properties that resulted from β-annealing. This heat treatment produced a fully lamellar microstructure that is significantly coarser after heat treatment (Figure 6.12-D). Therefore, as expected, this heat treatment has deleterious effect on mechanical properties due to the formation of a relatively coarse lamellar structure. It should be noted that the β-annealed structure formed from as-GIFT'd Ti-6Al-4V has both average strength and elongation that are on-par with as-sintered HSPT Ti-6Al-4V (approximately 1 GPa and 15 %EL). However, the GIFT and β-annealed condition has a reduction in area that is inferior to the as-sintered HSPT condition. Additionally, it should be remembered that the as-sintered HSPT condition has porosity which has been shown to have a damaging effect on ductility, particularly %RA. Therefore, it is likely that the β-annealed structure, if tested on samples that were β-annealed without GIFT, would have measurably lower mechanical properties than the as-sintered condition owing to the coarsening of the microstructure.

Such an experiment has been recommended as future work in CHAPTER 9.

### 7.1.4 Effect of Dehydrogenation Temperature

It has been shown that there is a strong correlation between the dehydrogenation temperature and microstructure (Figure 6.4). Therefore, the effect of these different microstructures on mechanical properties was tested. Ti-6Al-4V samples were produced using the standard HSPT profile shown in Figure 4.2, except with a lower dehydrogenation temperature of 650 ºC. All other parameters for these experiments were identical to those used for HSPT samples produced with the standard dehydrogenation temperature of 750°C. The static mechanical properties of the as-dehydrogenated samples were then tested.

Figure 7.6 shows the stress-strain curves of HSPT Ti-6Al-4V produced with the two different dehydrogenation temperatures. The sample dehydrogenated at 650 °C had the very fine acicular microstructure that is typical of this processing condition (Figure 6.4-B). The finer and more acicular microstructure had a strong effect on mechanical properties. Versus the standard HSPT microstructure (Figure 6.4-A), the tensile strength of the material was increased to about 1100 MPa, but the increased strength was accompanied by a decrease in ductility to 11.5%. Therefore, consistent with the literature[34,35], the acicular α structure is strong but relatively brittle.

#### 7.1.4.1 Effect of Dehydrogenation Temperature on Heat Treatments

For comparison with the standard HSPT profile (Figure 4.2), samples were heat treated after HSPT with a dehydrogenation temperature of 650 ºC. Identical heat treatments were used in this study as those used to heat treat the standard HSPT samples dehydrogenated

at 750 °C. That is, the as-dehydrogenated samples were all heat treated at 954 for 1 hour. One set of samples was water quenched to form a bi-modal microstructure (Figure 6.10-A), while the other set of samples were furnace cooled to form a "globularized" microstructure (Figure 6.10-B). Both sets of samples were aged at 550 ºC for 6 hours. Representative stress-strain curves for all three conditions are shown in Figure 7.7.

Compared to the as-sintered condition, the "globularized" sample had ductility that was increased significantly to 15 %EL and 31 %RA. However, the increase in ductility was met with a decrease in tensile strength from roughly 1100 MPa to just under 1000 MPa.

Interestingly, despite the change in microstructure, the bi-modal heat treatment had very little effect on the mechanical properties. The acicular α that forms as a result of heat treatment is considerably finer and, therefore, harder and more brittle than the acicular α that forms during dehydrogenation at 650 °C. Because of this, the combined effect of the fine acicular α and the relatively softer and ductile $\alpha_p$ the forms during the heat treatment resulted in static mechanical properties that were very similar to the as-sintered condition, which had a coarser fully acicular structure.

## 7.2 Fatigue Properties

For many applications, specifically aerospace, the fatigue performance of titanium alloys is a more critical consideration than the static properties. Traditional PM titanium alloys typically have unacceptable levels of porosity and a very coarse microstructure, resulting in poor fatigue performance. Therefore, traditionally, wrought alloys were the only option for fatigue-critical applications. It has been shown in CHAPTER 6 that HSPT is capable of forming an ultrafine microstructure in the as-sintered condition which may be

further evolved via simple heat treatments to produce wrought-like microstructures and static properties. As such, an important part of this research was to determine the fatigue performance of HSPT Ti-6Al-4V with the as-sintered, as-GIFT'd, and GIFT plus heat treated microstructures. For comparison, the fatigue performance of Ti-6Al-4V produced using vacuum sintering with all other processing conditions identical was also investigated to identify the role of both porosity and microstructure on the fatigue performance of Ti-6Al-4V.

The details of the experimental methods used for analyzing fatigue performance in this study is described in section 4.5. The dimensions of the fatigue bars used in this study are shown in Figure 4.6. For consistency, all samples were tested using a maximum frequency of 35 Hz and a stress ratio of R = 0.1. Because of the large volume of samples due to the many conditions tested, high cycle fatigue tests were limited to 20 million cycles or less. Therefore, for comparison, the stress at which a condition reached 10 million cycles ($S_{10^7}$) was used as the metric for comparing high cycle fatigue performance of the various conditions. This value was chosen because it is often used in practice for defining the threshold for endurance limit[102]. To compare HSPT and vacuum sintering with commercially available Ti-6Al-4V, all the S-N data presented in this section have been overlaid on the scatter-bands of fatigue properties as reported in the literature for both wrought Ti-6Al-4V with a mill-annealed condition as well as PM Ti-6Al-4V produced from both blended elemental (BE) and pre-alloyed (PA) powders[23].

### 7.2.1 As-sintered HSPT vs. Vacuum

The S-N curves for as-sintered Ti-6Al-4V produced via HSPT and vacuum sintering are given in Figure 7.8. The as-sintered HSPT given in this dissertation is limited. These results were generated as a verification of extensive data prepared by the author's colleague, Fei Cao. The results generated by Fei Cao will be included in his dissertation, and have been omitted from this dissertation. However, the data presented herein are very consisted with those generated by Fei Cao. Therefore, while the actual data points for as-sintered HSPT Ti-6Al-4V presented in this dissertation are limited, the trends discussed for this condition have been vetted by extensive experimentation.

The HSPT samples typically fell right within the scatter-bands for wrought Ti-6Al-4V and pre-alloyed PM Ti-6Al-4V. The HSPT S-N curve levels off at around 500 MPa, with several samples at this stress exceeding 10 million cycles. Therefore, 500 MPa has been identified as the 10 million cycle strength ($S_{10^7}$) for as-sintered HSPT Ti-6Al-4V.

Vacuum sintering produced significantly worse fatigue performance. The vacuum-sintered curve falls well to the left of the HSPT curve, indicating failure at less cycles for a corresponding stress. The two curves begin to converge at a stress around 600 MPa, but diverge again as the stress approaches the yield strength of vacuum-sintered Ti-6Al-4V (~800 MPa). The vacuum-sintered Ti-6Al-4V falls within the blended elemental (BE) scatter band for high stresses (~700 MPa) and also for 400~450 MPa range. However, the vacuum-sintered specimens tested over 10 million cycles only when the stress was below 300 MPa. Therefore, the 10 million cycle strength ($S_{10^7}$) for vacuum sintering has been identified as 300 MPa.

An HCF fracture surface of HSPT Ti-6Al-4V is shown in Figure 7.9. This sample was

tested at 500 MPa and failed at just over 10 million cycles. In HSPT samples, the HCF crack initiation point is almost always a large pore, usually with dimensions on the order of 100 μm. As shown in the fracture surface, the pore at the initiation site has an irregular shape, indicating that is actually several connected smaller pores. The interior of the pore is smooth, indicating the pore was present during sintering. Therefore, the large pores in HSPT Ti-6Al-4V, which control the fatigue performance, result from pressing defects in the green samples before sintering. Also shown in Figure 7.9 is the plastic region in the fracture surface, which resulted from the yield strength being reached as the cross section area decreased during crack propagation. The plastic region shows dimpling that is indicative of microvoid coalescence, which occurs in ductile materials. This region of the fracture surface is extremely similar to and consistent with tensile ductile fracture surfaces of the same material that are produced from quasi-static testing. As the material fails and the yield strength is exceeded, a shear lip forms around the edge of the sample farthest from the initiation site. Therefore, small shear lips are commonly found on the fracture surfaces of this material after fatigue testing.

Figure 7.10 shows the fracture surface of an as-sintered samples produced via vacuum sintering. This sample was tested at 400 MPa and failed and 3.4 million cycles. As opposed to HSPT, no obvious pores are found at the initiation site. Therefore, as opposed to HSPT samples, porosity does not seem to be the controlling facture in fatigue performance of vacuum-sintered samples, even though it is present. Instead, the crack initiation sites are identified by a smooth region, in which the morphology of the coarse lamellar microstructure can be seen (Figure 7.10-B). As discussed in detail in CHAPTER 6, the as-sintered microstructure produced from vacuum sintering is very coarse, with α

grains often exceeding 100 μm in length. Because of this, the grain size of vacuum-sintered material is more profound than the porosity. It is known that cracks tends to form by fracture of α grains in lamellar regions of the microstructure, as shown in Figure 2.18. When an individual α grain fractures in the vacuum-sintered microstructure, the individual crack is sufficiently large to induce crack propagation which eventually leads to failure. The cracks propagate transgranularly across the colony, leading to the type of crack initiation site shown in the micrograph. Therefore, the coarse microstructure in vacuum-sintered samples is the controlling factor with regards to fatigue performance.

Figure 7.10-C shows the plastic region in the shear lip in the vacuum-sintered fracture surface. Similar to the HSPT sample, the shear lip shows dimpling that is consistent with microvoid coalescence due to the yield strength of the material being exceeded. Therefore, the plastic region of the fracture surface is indicative of a ductile material and has the same appearance as a tensile fracture surface that results from quasi-static testing of the same condition.

### 7.2.2 Effect of Gaseous Isostatic Forging Technology (GIFT)

In order to determine the degree at which porosity effects the fatigue performance of Ti-6Al-4V produced via HSPT and vacuum sintering, samples were prepared using the two sintering methods and processed via GIFT to close the remaining porosity. The results of these samples are discussed in this section.

7.2.2.1 HSPT with GIFT

Similar to the as-sintered HSPT Ti-6Al-4V data, the data presented in this section for HSPT Ti-6Al-4V after GIFT processing is a verification of data generated by the author's colleague, Fei Cao. Because Fei Cao's data will be presented in his dissertation, it has been omitted from this dissertation. Therefore, even though the actual data points presented in this dissertation are limited, the trends that are discussed have been vetted by extensive experimentation.

Figure 7.11 shows the S-N curve for as-sintered HSPT Ti-6Al-4V and HSPT Ti-6Al-4V that has been processed via GIFT to close the remaining porosity. For similar stresses, the as-GIFT'd curve falls consistently to the right of the as-sintered curve. Therefore, GIFT does have a measureable effect on the fatigue performance of HSPT Ti-6Al-4V. As expected, the curves converge at the higher stresses, due to the fact that both materials have similar tensile strength. Additionally, the curves begin to converge as the testing stress approaches 500 MPa. Therefore, from these data, it can be concluded that GIFT has the greatest effect on lower cycle fatigue performance, with the greatest improvement in the 1 million cycle region. The as-GIFT'd samples typically exceed 1 million cycles at around 800 MPa, while the as-sintered samples typically exceed 1 million cycles at around 650 MPa.

The reason for the convergence of the two curves at very high cycles ($>10^7$) is evident in the HCF fracture surfaces of as-GIFT'd Ti-6Al-4V. Figure 7.12 shows a HCF fracture surface of Ti-6Al-4V produced via HSPT with GIFT processing to close the porosity. The crack initiation point on this fracture surface appears to be porosity, with dimensions similar to the porosity seen in the as-sintered material. However, the pores in the as-

GIFT'd material have a significantly different appearance than those found in the as-sintered condition. First off, the pore does not have a smooth interior surface. Therefore, it can be deduced that this pore was not present, at least not in its current condition, during sintering. Additionally, the geometry of the pore is angular, having a triangular shape in this specific sample. Because of these features, it has been determined that this pore actually opened up during the fatigue test. Therefore, it is likely that this feature was a pore that was closed during GIFT, but then reopened during the fatigue test due to cyclic loading, eventually leading to failure of the sample. While GIFT is effective at closing porosity, it is likely that the material is not held at an elevated temperature for long enough to facilitate welding of the interface due to diffusion bonding. As such, the closed pores open back up during fatigue tests. The process of opening of the pore is likely very slow, which is why GIFT has a profound effect on lower cycle fatigue performance but not when the number of cycles is sufficient to allow for significant reopening of the pores.

Figure 7.12-C shows a high resolution SEM micrograph taken in the shear lip of the fracture surface. This micrograph is chosen to show the typical pores that are left from GIFT processing before reopening due to cyclic loading. As shown in Figure 5.6, GIFT produces a relative density of essentially 100%. However, while GIFT significantly reduces the size and volume fraction of porosity in the sample, resulting in the very high relative density, very fine pores are still left after this process. The pores left after GIFT are typically on the order of 1~2 μm in diameter.

7.2.2.2 Vacuum Sintering with GIFT

The S-N curves for vacuum-sintered Ti-6Al-4V both in the as-sintered and as-GIFT'd condition are shown in Figure 7.13. As opposed to HSPT, the GIFT process has very little effect on the fatigue performance of the vacuum-sintered material. This makes sense considering the failure mechanism in as-sintered Ti-6Al-4V produced by vacuum sintering is not controlled by porosity and that the microstructure before and after GIFT is identical. Therefore, the fact that GIFT closes the porosity of vacuum-sintered material does not affect the fatigue performance.

Figure 7.14 shows an HCF fracture surface of an as-GIFT'd Ti-6Al-4V sample produced via vacuum sintering. This sample failed at 7.4 million at 350 MPa stress. As expected from the S-N curves, the fracture surfaces of as-GIFT'd samples are very similar to the as-vacuum-sintered samples. In this figure, the initiation site is evident as a flat area in the fracture surface, in which the form of the coarse lamellar microstructure can be made out. From the micrograph, it can be seen that the material failed by transgranular crack propagation. This is clearly seen as striations across the cross-section of the α grains that are visible in the fracture surface. Therefore, as with the as-sintered sample produced via vacuum sintering, failure probably initiated as a single α grain fracturing. Then, because of the large size of the α grain, this initial fracture led to transgranular propagation across the colony and eventual failure of the sample.

Figure 7.14-C shows a micrograph taken from the shear lip in the fracture surface. As with the other samples, the morphology of the plastic region is consistent with a ductile material and has an identical appearance to a fracture surface produced by quasi-static testing of the same material.

### 7.2.3 Effect of Heat Treatments on Fatigue Performance of HSPT Ti-6Al-4V

In this section, the fatigue performance of the wrought-like "globularized", bi-modal, and fully lamellar (β-annealed) microstructures produced via simple heat treatments of HSPT Ti-6Al-4V is discussed. All the heat treatments discussed in this section followed the same profiles and resulted in the same microstructures as those shown in Figure 6.12.

As discussed in section 7.2.1, the large rogue pores that are present in as-sintered HSPT Ti-6Al-4V are the controlling factor with regards to fatigue performance. In an attempt to eliminate the effect of these large pores, all the heat treated fatigue bars were first processed via GIFT to close any rogue pores. This was done as means to eliminate the effect of large pores and, therefore, evaluate the effect of microstructure alone on the fatigue performance of HSPT Ti-6Al-4V with wrought-like microstructures produced via simple heat treatments.

The S-N curves for all three microstructures discussed in this section are shown in Figure 7.15. As with all of the other S-N plots, the fatigue data are overlaid on the scatter-bands of the literature values for fatigue performance of Ti-6Al-4V produced via wrought processing and traditional PM from pre-alloyed (PA) and blended elemental (BE) powders. Further testing was performed using lower stresses than those presented in Figure 7.15, but these samples were tested to 20~30 million cycles without failure. Therefore, the fatigue tests were terminated due to time constraints and these data are not presented on the S-N curves.

7.2.3.1 Globularized Microstructure

The “globularized” microstructure’s S-N curve is presented as black circles in Figure 7.15. As shown, the S-N curve for this microstructure falls within the upper half of the scatter-band for wrought Ti-6Al-4V, and is well beyond the range of values reported for other BE processes. Along this point, it is important to note that HSPT is a BE process, which is key to developing a low-cost PM process. In addition to having a wrought-like “globularized” microstructure and static mechanical properties, these data indicated that this heat treatment also produces fatigue performance that is competitive with wrought Ti-6Al-4V.

The “globularized” microstructure’s fatigue performance is well above that observed in as-sintered HSPT Ti-6Al-4V, as shown in Figure 7.8. However, it lies below the as-GIFT’d curve in the range 100,000 to about 5 million cycles. This is to be expected, as the tensile strength of the globularized condition is about 30~40 MPa lower than the as-GIFT’d condition. However, the globularized condition exceeds 10 million cycles at a higher stress than the as-GIFT’d condition and does not converge as dramatically with the as-sintered HSPT curve. The 10 million cycle fatigue strength ($S_{10^7}$) of the globularized microstructure has been determined to be 550 MPa from the data presented in this section.

The HCF fracture surface shown in Figure 7.16 is from a globularized sample that was tested at 600 MPa and failed at 6.3 million cycles. This fracture surface shows a different failure mechanism than that which was observed for the as-sintered and as-GIFT’d HSPT samples. The other two conditions had fatigue performance controlled by porosity, which was reopened in the as-GIFT’d condition as a function of the cyclic loading. However, the fracture surface for the globularized microstructure does now show this phenomenon.

During the heat treatment, this sample was exposed to an elevated temperature for a longer time than that used during GIFT. It is likely that the additional diffusion bonding which occurs during the 1 hour hold at 954 °C was effective in welding the interfaces left by the collapsed pores. Therefore, it appears that the crack initiation resulted from microstructural features in the heat treated samples. As shown in Figure 7.16, there is a flat area measuring about 100 μm across with striations along its surface at the initiation site. Grain boundary α (G.B. α) forms during dehydrogenation at 750°C in the HSPT sintering process. Additionally, the G.B. α grows during heat treatments, meaning the heat treated microstructures are plagued by large α grains along the prior β grain boundaries. Therefore, it is likely that because all porosity was effectively closed, or reduced to a size that is insignificant with regards to mechanical properties, the G.B. α is the controlling factor for fatigue performance of the heat treated microstructures. Therefore, failure was likely initiated by fracture of a large G.B. α grain, which served as a stress concentrator, leading to crack propagation and eventual failure in this sample.

Figure 7.16-C is a high resolution SEM micrograph of the plastic region within the shear lip of the fracture surface. As with all the other samples, the plastic region's fracture surface is consistent with the ductile fracture surfaces seen in quasi-static tensile specimens of the same microstructure. That is, the plastic region shows dimpling of the surface that is characteristic of ductile failure.

#### 7.2.3.2 Bi-modal Microstructure

The red squares in Figure 7.15 and Figure 7.17 show the S-N curve for the bi-modal microstructure. This structure exhibited the best fatigue performance of all the conditions

tested in this study. This is consistent with the static properties, as this material exhibited the greatest strength of all the conditions tested for fatigue performance while still having ductility on the order of 15 %EL and 30 %RA. As shown, the S-N curve for the bi-modal microstructure follows the upper limit of the scatter-band for mill-annealed wrought Ti-6Al-4V. Therefore, this microstructure can be considered to be highly competitive with wrought Ti-6Al-4V. It should be pointed out that some of the samples tested fell well beyond the scatter-band for wrought Ti-6Al-4V; one of these samples is circled on Figure 7.15 to highlight it. This particular sample went to over half a million cycles at 850 MPa, which is 80% of the ultimate tensile strength (UTS) and 85% of the yield strength. It is likely that these samples were devoid of the microstructural features which typically lead to failure. While this is a statistical anomaly with regards to the trend, it indicates the possibility of this microstructure to have a much higher fatigue strength than that which is currently reported. From the data presented, the bi-modal microstructure exhibited the highest 10 million cycle fatigue strength ($S_{10^7}$), which was 600 MPa.

The HCF fracture surface for a bi-modal sample tested at 600 MPa, which failed via sub-surface initiation at 12 million cycles, is shown in Figure 7.18. While grain boundary α (G.B. α) is present in the bi-modal microstructure and shows up distinctly on polished surfaces, it does not appear to be the mechanism for initiation in this fractograph. It should be noted that the majority of bi-modal samples failed due to surface initiation, despite thorough grinding to remove 200 μm from the machined surface and polishing procedures used to eliminate surface imperfections. In the sample shown, it is likely that a crack was initiated within the brittle acicular α regions of the microstructure. Fine microstructural features can be made out on the fractograph at the initiation site, and cracks can be seen

emanating from this area. Therefore, this fracture surface is consistent with crack initiation within the acicular region of the microstructure.

The plastic region within the shear lip of the fracture surface is shown in Figure 7.18-C. Again, the dimpled surface is consistent with ductile fracture that is seen on quasi-static tensile specimens with the same microstructure. This micrograph also shows the very fine porosity that is left from the GIFT process. The pore shown on this micrograph is approximately 2 μm across.

#### 7.2.3.3 β-annealed Microstructure

The final microstructure tested for fatigue performance is the fully lamellar structure that forms from β-annealing. The S-N curve for this microstructure is shown as orange triangles in Figure 7.15. All three heat-treated microstructure have S-N curves which converge as the stress approaches 1000 MPa, which is approaching the tensile strength for all three microstructures. However, the β-annealed microstructure performs much more poorly than the globularized and bi-modal microstructures. For moderate cycle ranges (10,000 to 500,000), the β-annealed material falls well within the scatter-band for wrought Ti-6Al-4V. However, as the number of cycles exceeds 1 million, the S-N curve quickly falls. It is known that the microstructure of a material has strong influence on crack growth for smaller applied stresses[135,136]. Additionally, the β-annealed heat treatment essentially undoes the microstructural refinement achieved by the HSPT sintering process. That is, the β-annealing heat treatment forms an entirely β phase microstructure during the heat treatment, which transforms into a relatively coarse lamellar structure as the material is cooled. In fact, as discussed in section 6.2.3.3, the β-annealed microstructure is very

similar to the vacuum-sintered microstructure, but not quite as coarse. Because of this, the β-annealed microstructure has a 10 million cycle fatigue strength ($S_{10^7}$) of 350 MPa, which is approaching that observed in vacuum-sintered samples.

The HCF fracture surface for a β-annealed sample that was tested at 400 MPa and failed at 6.5 million cycles is shown in Figure 7.19. As expected, based on the form of the microstructure, the β-annealed samples have very similar HCF fracture surfaces to vacuum-sintered samples. For this specific sample, it appears that failure was initiated by fracturing the grain boundary α (G.B. α) grains. Additionally, there is transgranular fracture emanating from the point of initiation, and the fully lamellar structure can be observed in areas where a crack propagated across the α colonies.

Figure 7.19-C shows the plastic region found within the shear lip of the fracture surface. This, as with the other samples, is consistent with the fracture surface that is observed from a quasi-static tensile specimen of the same material. The plastic region shows dimpling that is characteristic of microvoid coalescence that occurs during failure of ductile materials when the yield strength is exceeded.

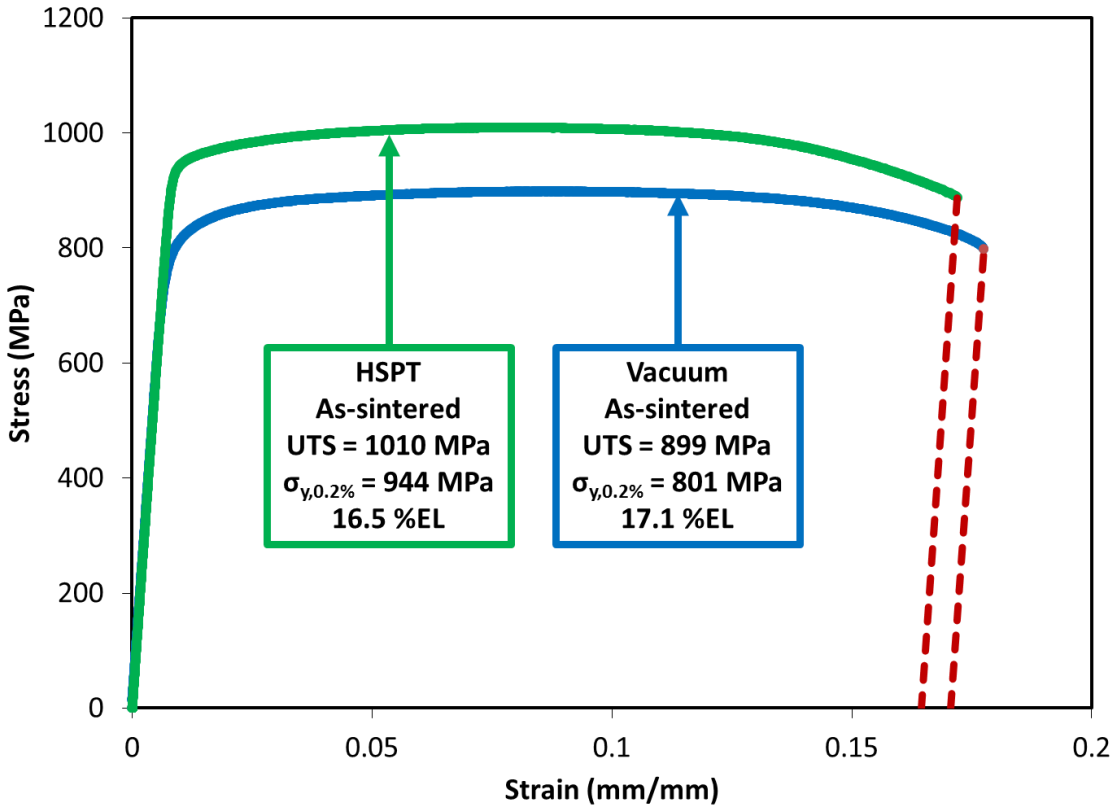


Figure 7.1: Stress-strain curves of representative as-sintered Ti-6Al-4V samples produced via HSPT versus vacuum sintering.

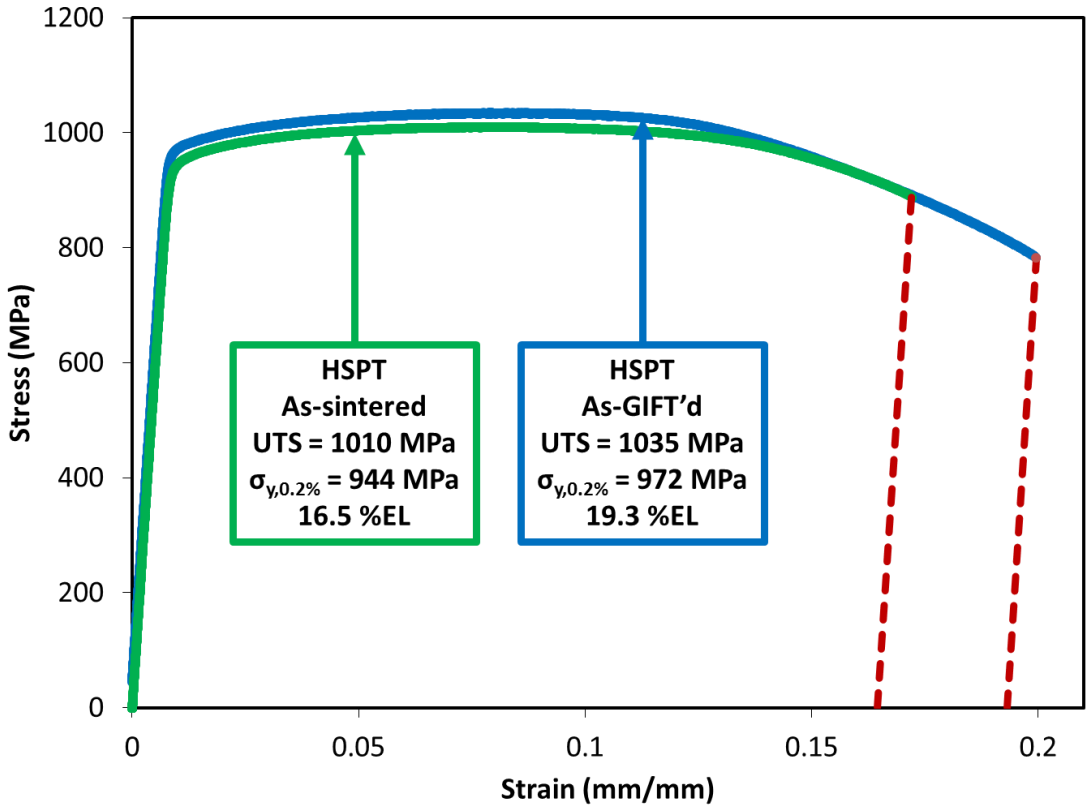


Figure 7.2: Stress-strain curves of representative as-sintered versus as-GIFT'd Ti-6Al-4V samples produced via HSPT.

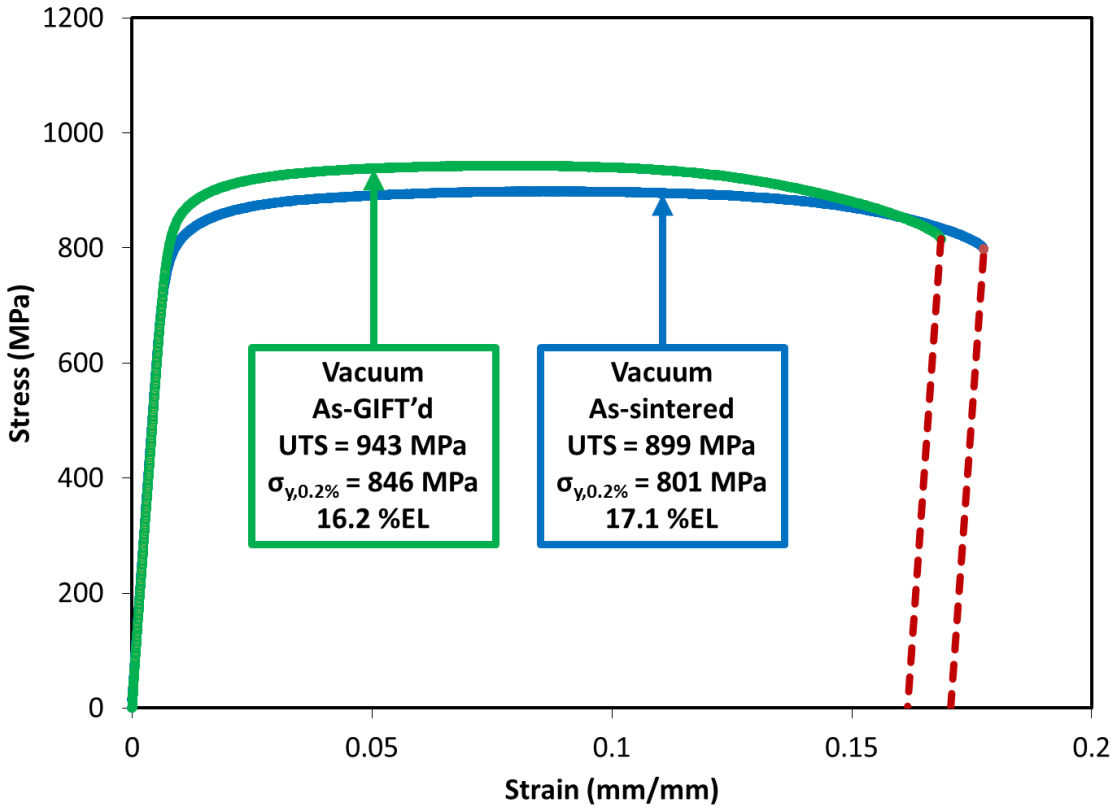


Figure 7.3: Stress-strain curves of representative as-sintered versus as-GIFT'd Ti-6Al-4V samples produced via vacuum sintering.

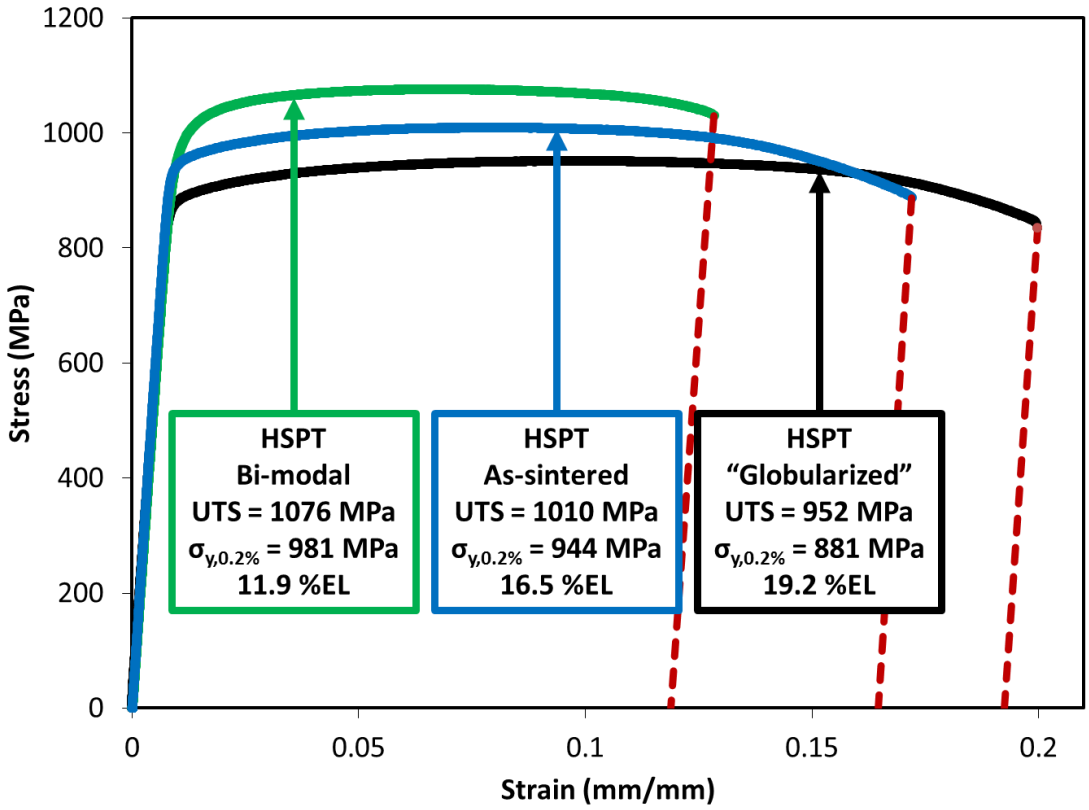


Figure 7.4: Stress-strain curves of representative Ti-6Al-4V samples produced via HSPT with as-sintered versus bi-modal versus "globularized" microstructures.

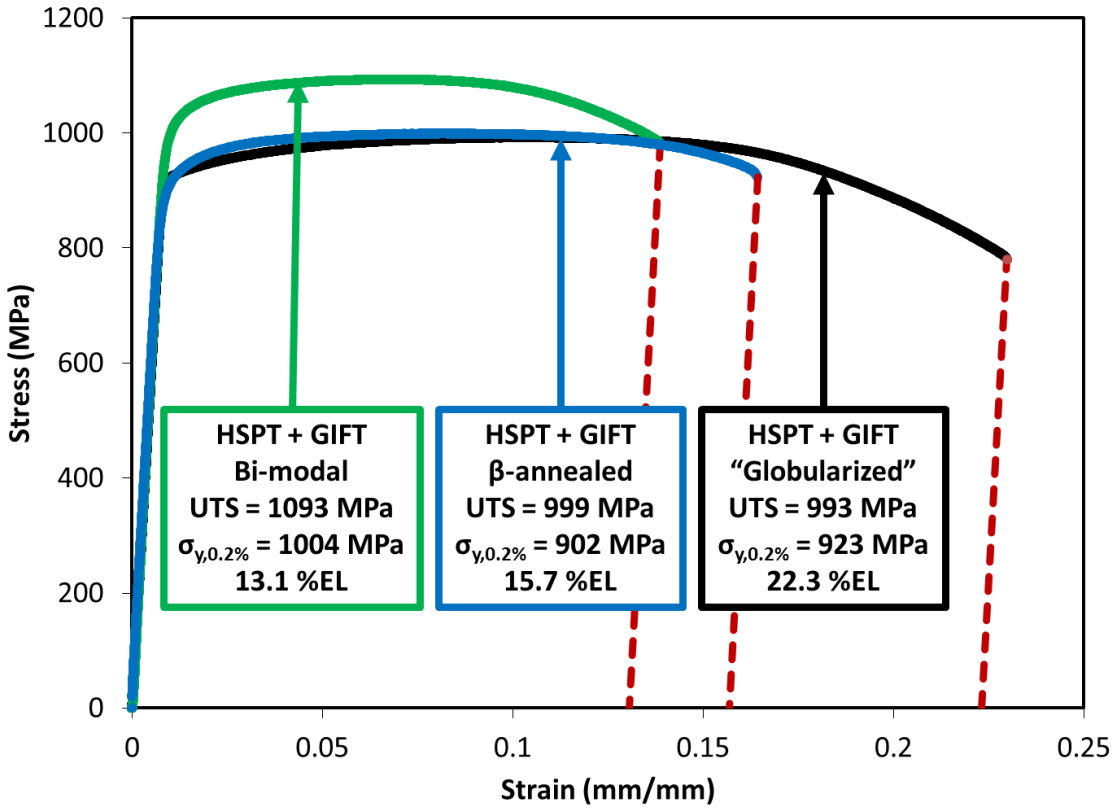


Figure 7.5: Stress-strain curves of representative Ti-6Al-4V samples produced via HSPT followed by GIFT and heat treatments to produce bi-modal versus β-annealed versus "globularized" microstructures.

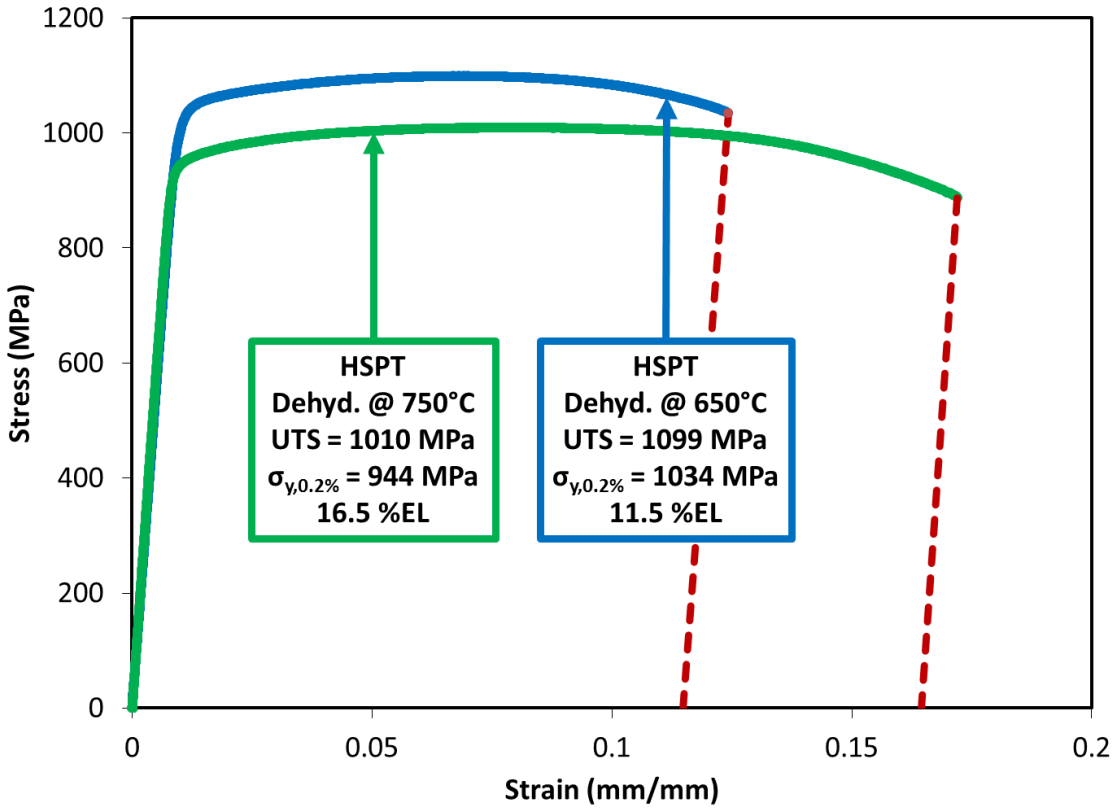


Figure 7.6: Stress-strain curves of representative as-sintered Ti-6Al-4V samples produced via HSPT and dehydrogenated at 750 °C versus 650 °C.

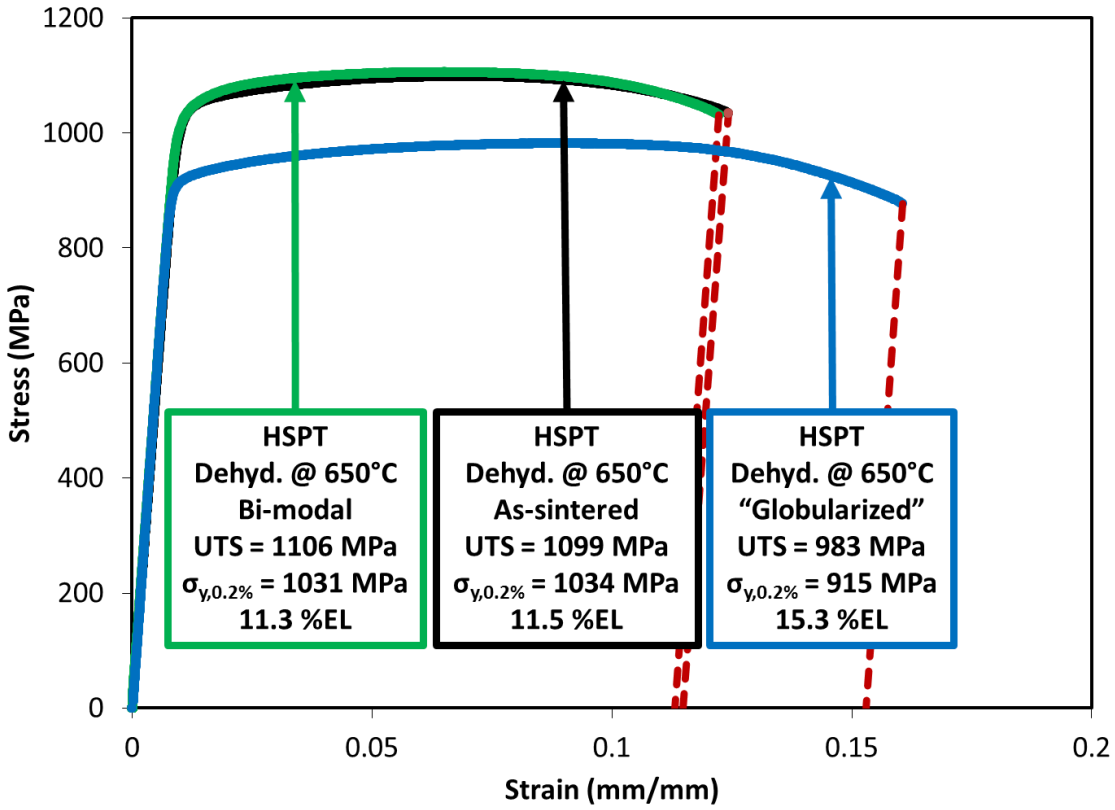


Figure 7.7: Stress-strain curves of representative as-sintered Ti-6Al-4V samples produced via HSPT that have been dehydrogenated at 650 °C and heat treated to produce various microstructures: as-sintered versus bi-modal versus "globularized".

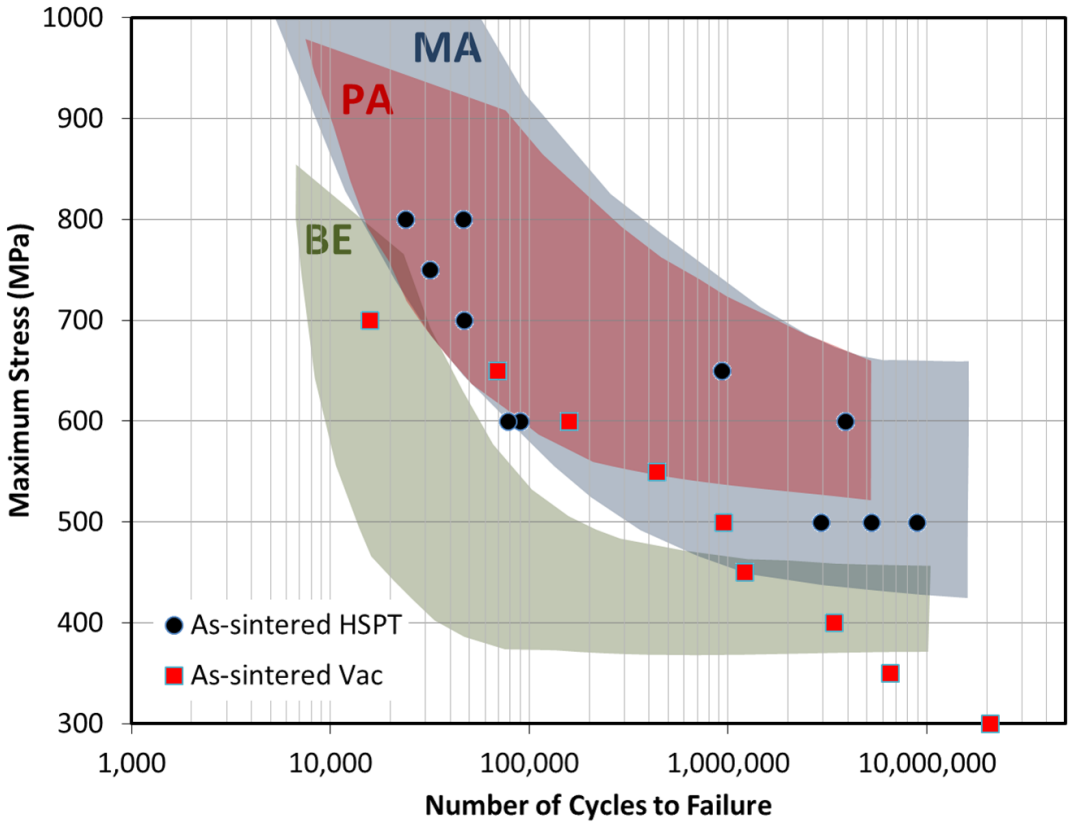


Figure 7.8: S-N curves for as-sintered Ti-6Al-4V produced via HSPT versus vacuum sintering. For reference, these data are overlaid on the fatigue life scatter-bands (prepared from data in the ASM Handbooks[23]) for Ti-6Al-4V produced via wrought processing with a mill-annealed microstructure (MA), pre-alloyed powder metallurgy (PA), and blended elemental powder metallurgy (BE).

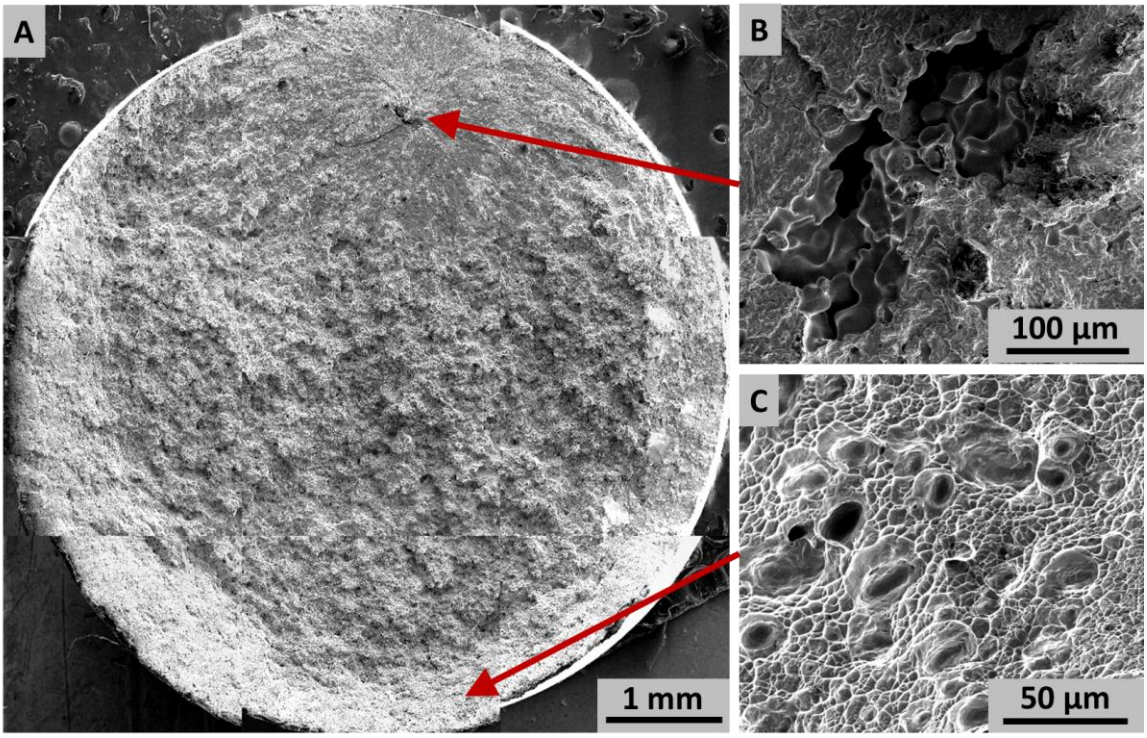


Figure 7.9: High cycle fatigue ($1.0x10^7$ cycles at 500 MPa) SEM fractographs of as-sintered Ti-6Al-4V produced via HSPT: A) montage of entire surface, B) crack initiation site, and C) plastic region in shear lip.

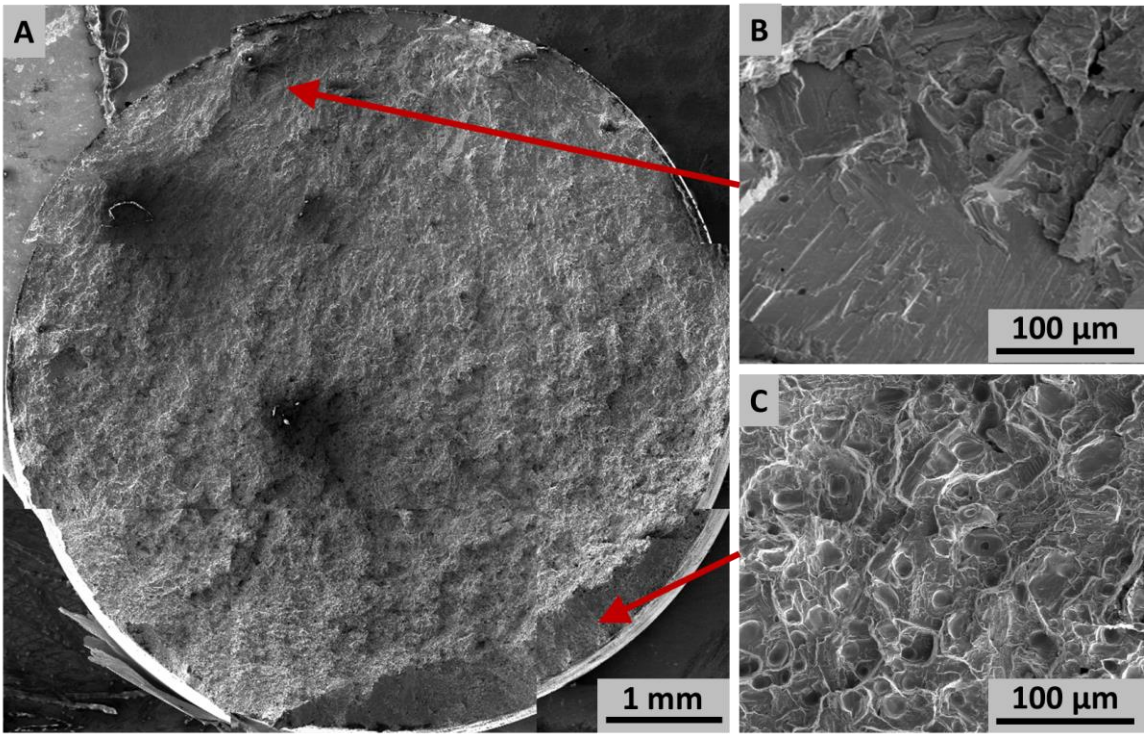


Figure 7.10: High cycle fatigue ($3.4x10^6$ cycles at 400 MPa) SEM fractographs of as-sintered Ti-6Al-4V produced via vacuum sintering: A) montage of entire surface, B) crack initiation site, and C) plastic region in shear lip.

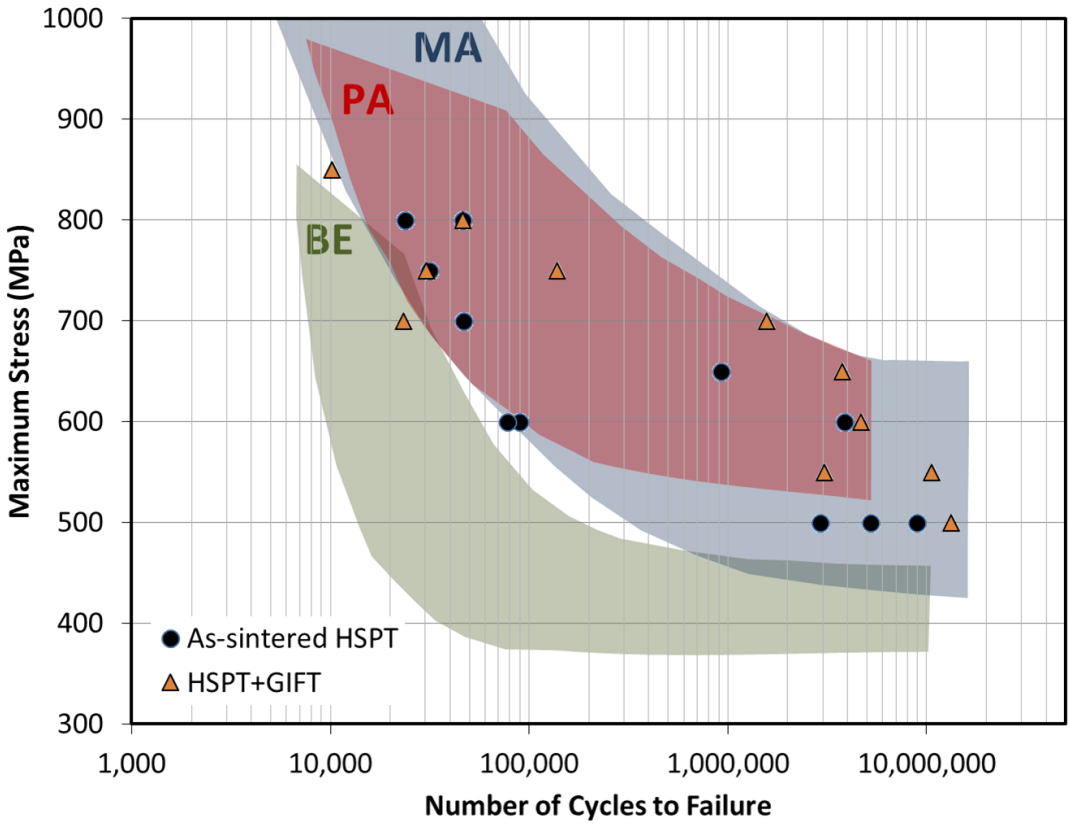


Figure 7.11: S-N curves for as-sintered versus as-GIFT'd Ti-6Al-4V produced via HSPT. For reference, these data are overlaid on the fatigue life scatter-bands (prepared from data in the ASM Handbooks[23]) for Ti-6Al-4V produced via wrought processing with a mill-annealed microstructure (MA), pre-alloyed powder metallurgy (PA), and blended elemental powder metallurgy (BE).

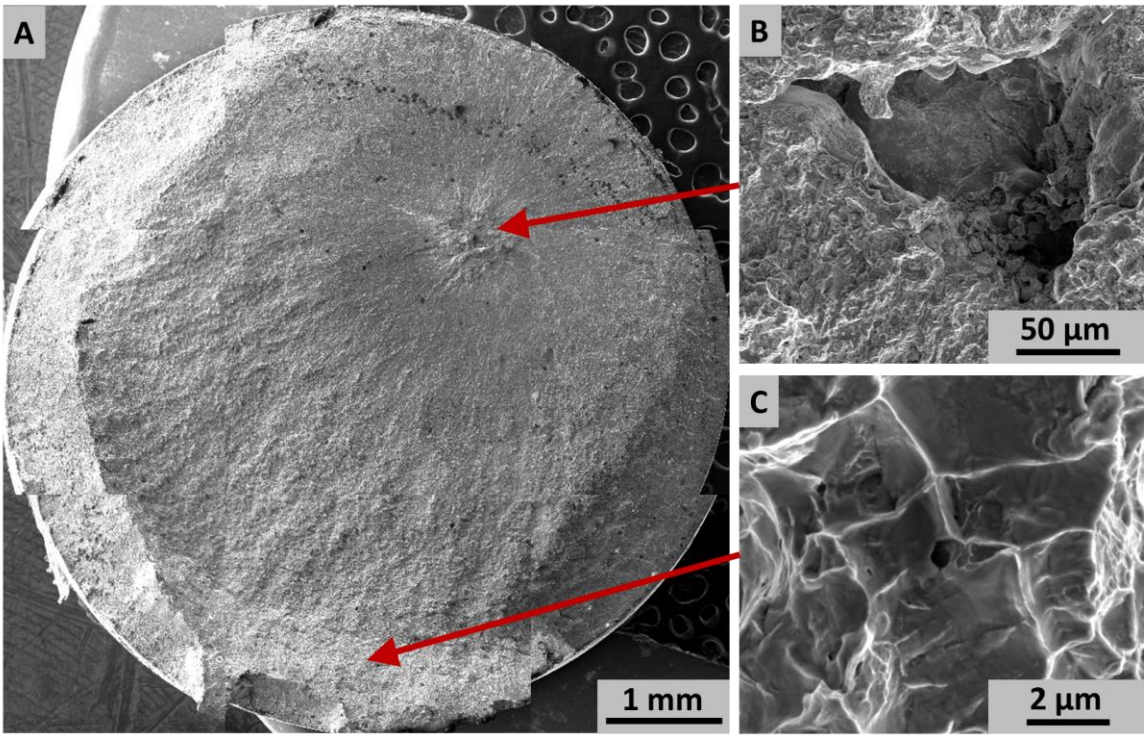


Figure 7.12: High cycle fatigue ($1.3x10^7$ cycles at 500 MPa) SEM fractographs of Ti-6Al-4V produced via HSPT followed by GIFT to close porosity: A) montage of entire surface, B) crack initiation site, and C) high resolution micrograph of plastic region showing submicron porosity left after GIFT.

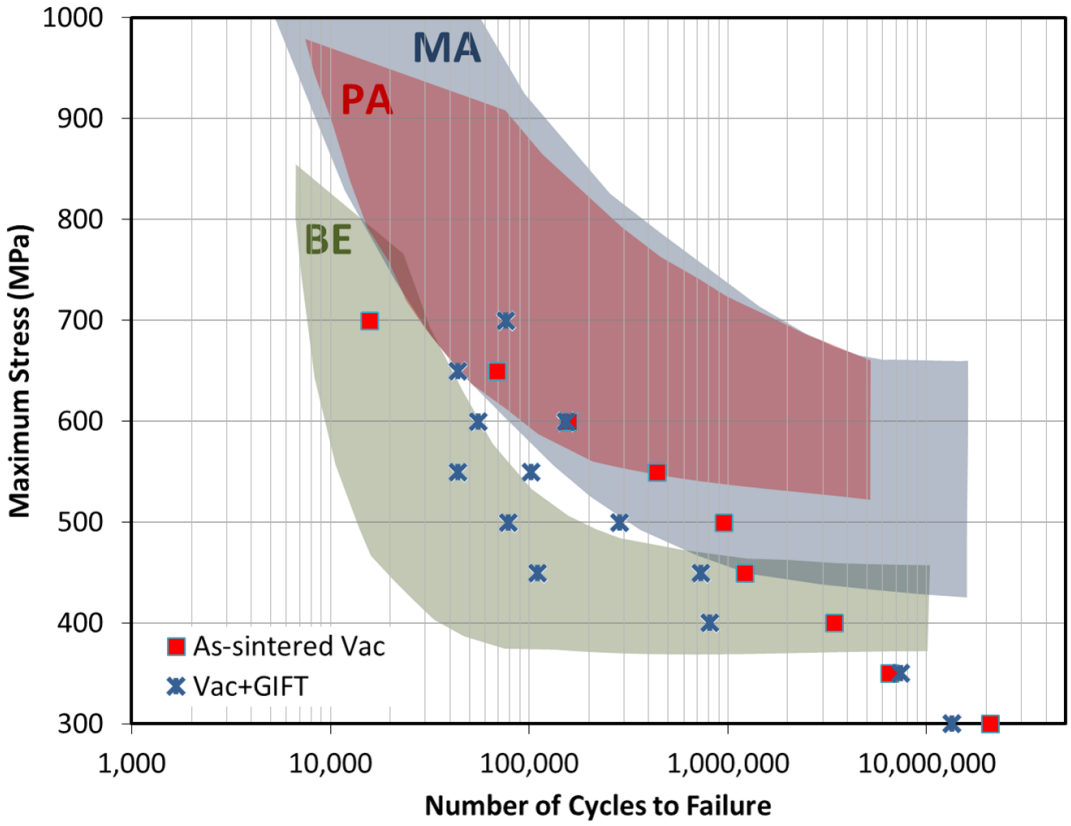


Figure 7.13: S-N curves for as-sintered versus as-GIFT'd Ti-6Al-4V produced via vacuum sintering. For reference, these data are overlaid on the fatigue life scatter-bands (prepared from data in the ASM Handbooks[23]) for Ti-6Al-4V produced via wrought processing with a mill-annealed microstructure (MA), pre-alloyed powder metallurgy (PA), and blended elemental powder metallurgy (BE).

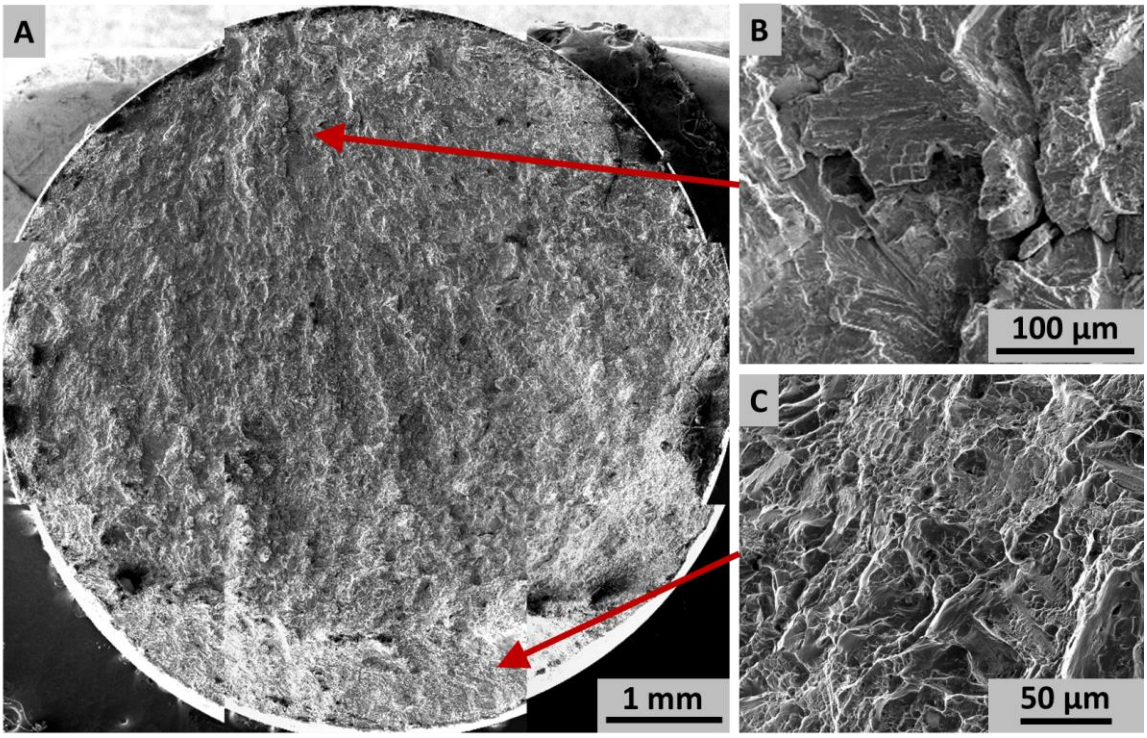


Figure 7.14: High cycle fatigue ($7.4x10^6$ cycles at 350 MPa) SEM fractographs of Ti-6Al-4V produced via vacuum sintering followed by GIFT to close porosity: A) montage of entire surface, B) crack initiation site, and C) plastic region in shear lip.

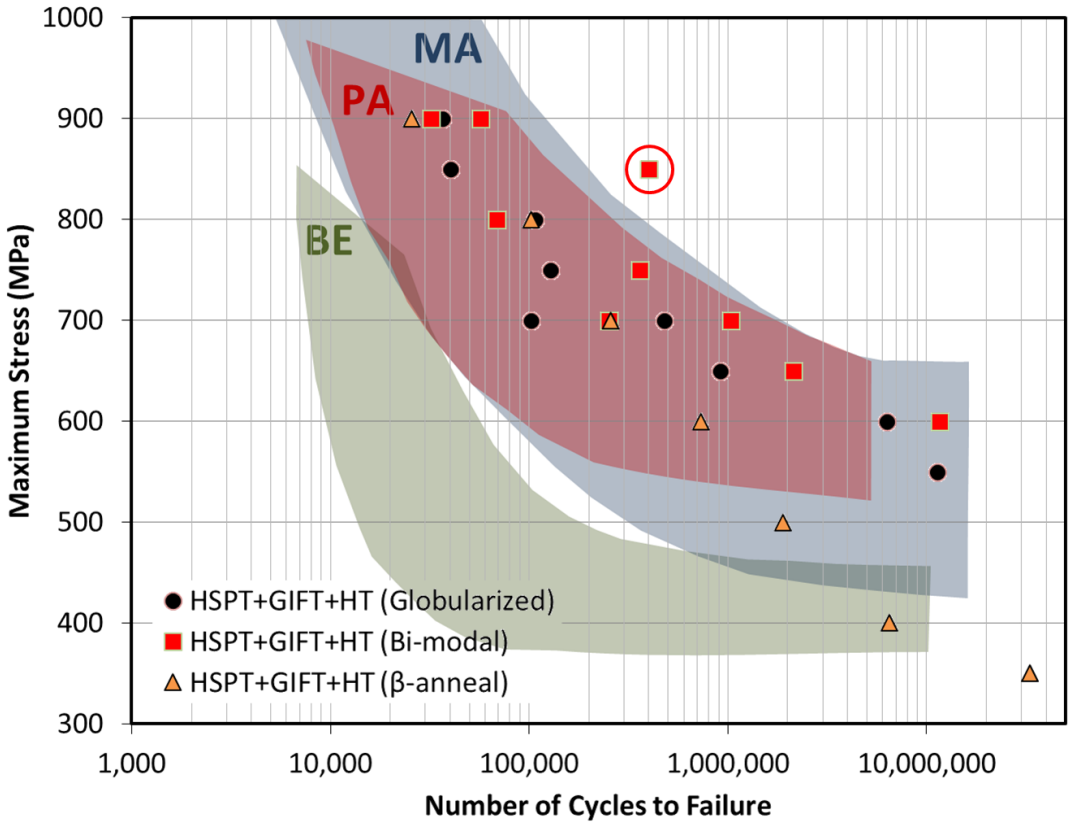


Figure 7.15: S-N curves for Ti-6Al-4V produced via HSPT followed by GIFT and heat treated to produce "globularized" versus bi-modal versus β-annealed microstructures. For reference, these data are overlaid on the fatigue life scatter-bands (prepared from data in the ASM Handbooks[23]) for Ti-6Al-4V produced via wrought processing with a mill-annealed microstructure (MA), pre-alloyed powder metallurgy (PA), and blended elemental powder metallurgy (BE).

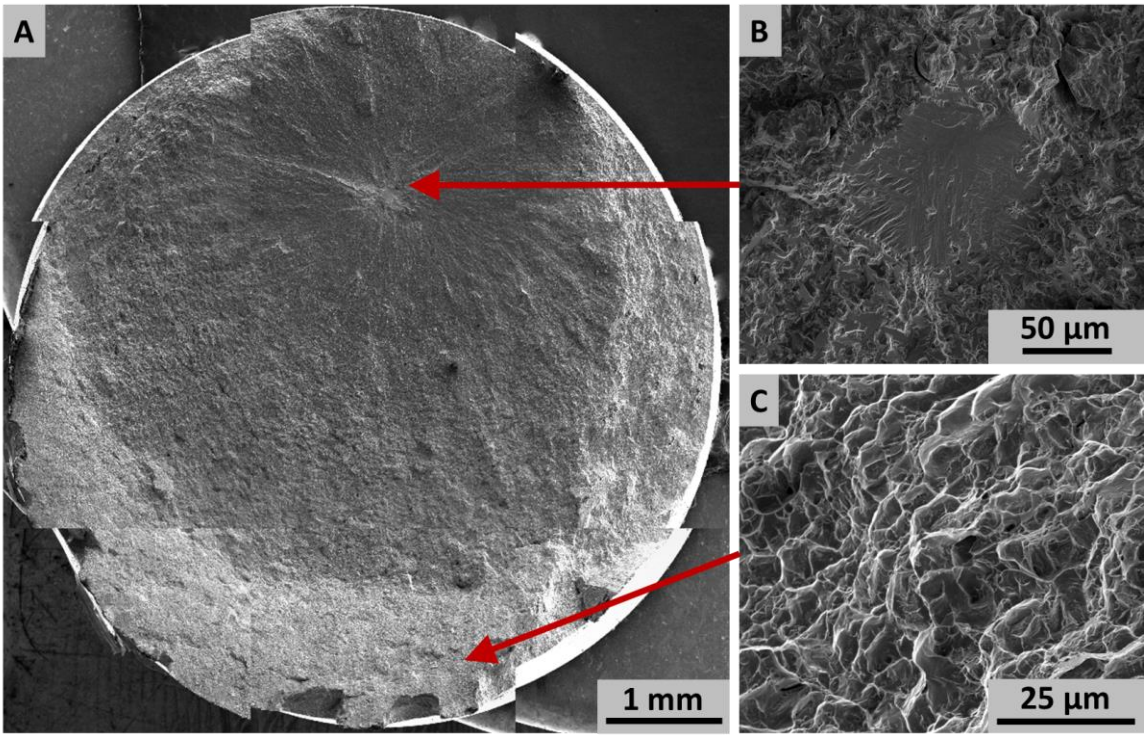


Figure 7.16: High cycle fatigue ($6.3x10^6$ cycles at 600 MPa) SEM fractographs of Ti-6Al-4V produced via HSPT followed by GIFT and heat treatment to produce a "globularized" microstructure: A) montage of entire fracture surface, B) crack initiation site, and C) plastic region in shear lip.

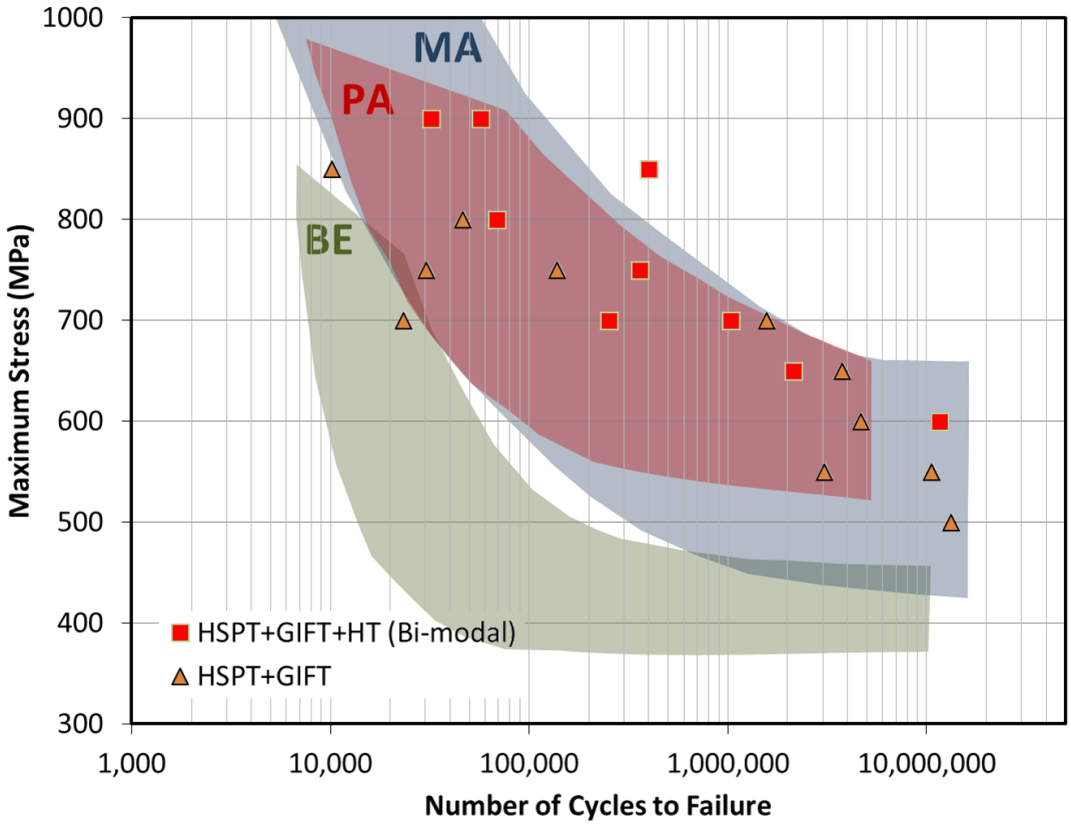


Figure 7.17: S-N curves for as-sintered versus as-GIFT'd Ti-6Al-4V produced via HSPT with the as-GIFT'd versus heat treated and aged bi-modal microstructure. For reference, these data are overlaid on the fatigue life scatter-bands (prepared from data in the ASM Handbooks[23]) for Ti-6Al-4V produced via wrought processing with a mill-annealed microstructure (MA), pre-alloyed powder metallurgy (PA), and blended elemental powder metallurgy (BE).

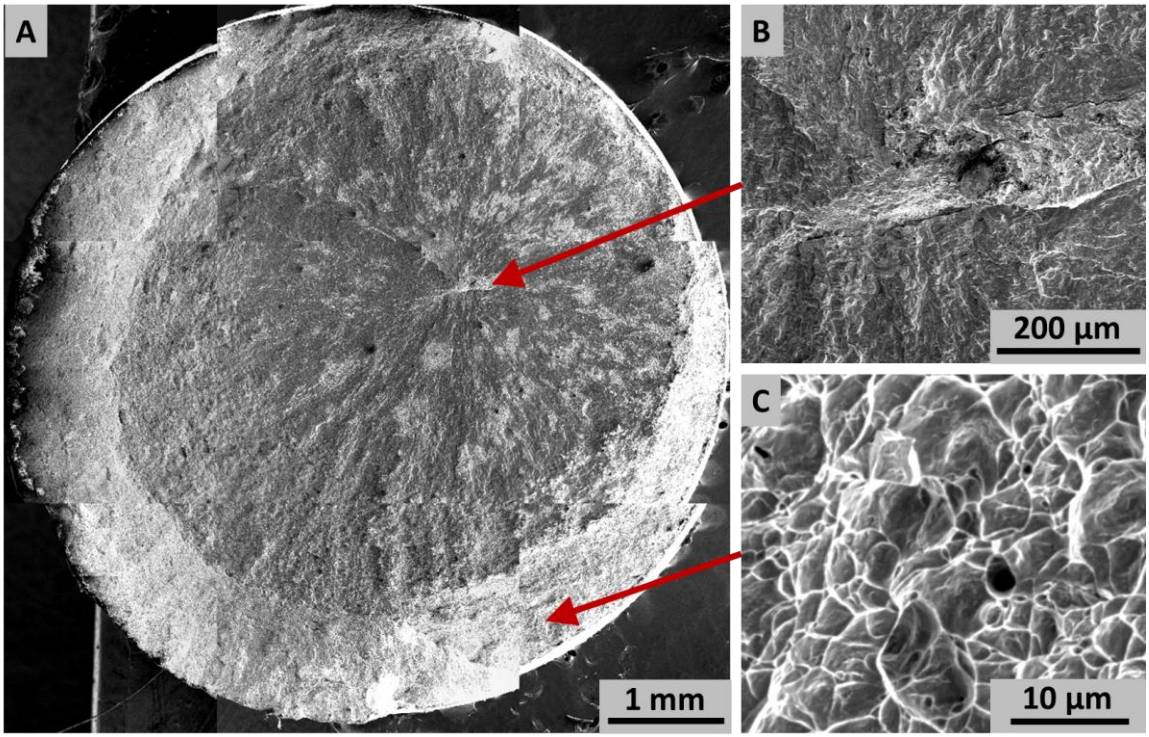


Figure 7.18: High cycle fatigue ($1.2x10^7$ cycles at 600 MPa) SEM fractographs of Ti-6Al-4V produced via HSPT followed by GIFT and heat treatment to produce a bi-modal microstructure: A) montage of entire fracture surface, B) initiation site, and C) plastic region in shear lip showing very fine porosity left after GIFT processing.

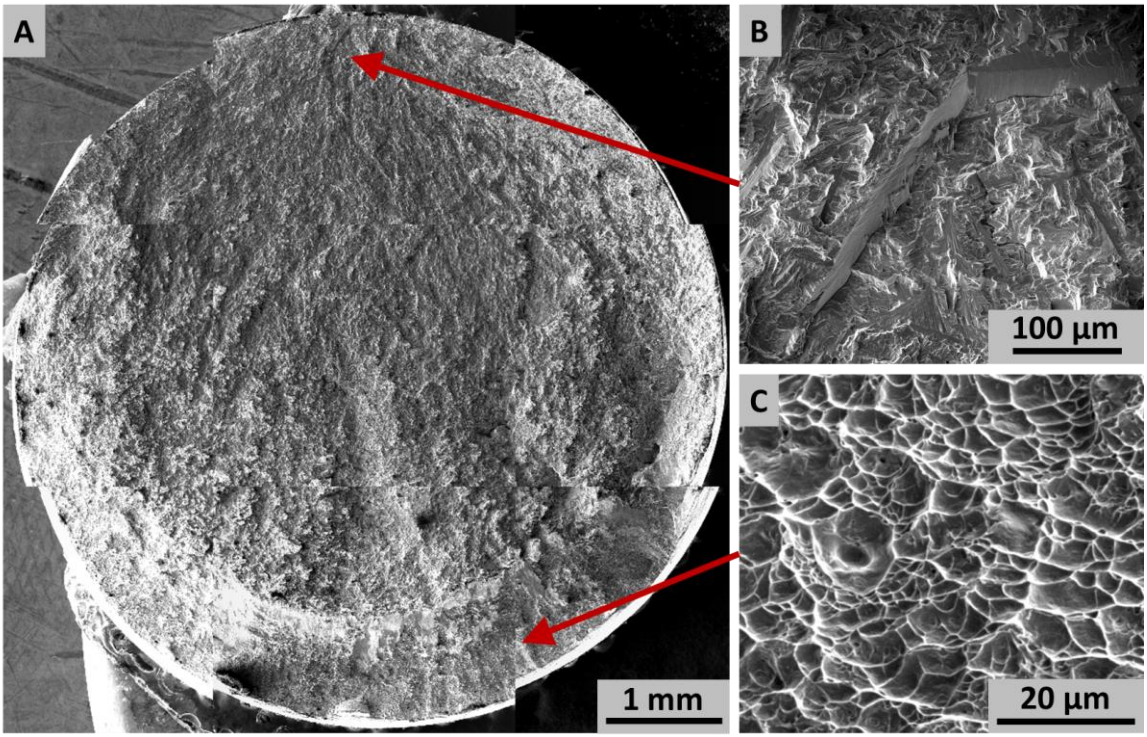


Figure 7.19: High cycle fatigue ($6.5x10^6$ cycles at 400 MPa) fractograph of as-sintered Ti-6Al-4V produced via HSPT followed by GIFT and heat treatment to produce a fully lamellar (β-annealed) microstructure: A) montage of entire fracture surface, B) initiation site, and C) plastic region in shear lip.

# CHAPTER 8

## SUMMARY OF KEY FINDINGS AND CONCLUSIONS

In this dissertation, the feasibility of producing Ti-6Al-4V with wrought-like microstructures and mechanical properties via a low-cost powder metallurgy process named hydrogen sintering and phase transformation (HSPT) was investigated. To date, wrought processing is the state of the art for producing titanium alloys. However, wrought processing is cost prohibitive for many commercial applications. It was found that HSPT is a viable alternative to wrought processing for the production of titanium components with superior mechanical properties. Additionally, the fundamental relationship between the processing, structure, and properties of titanium alloys, specifically Ti-6Al-4V, produced via this process were identified. It was found that HSPT can produce Ti-6Al-4V with very fine wrought-like microstructures by utilizing the novel sintering process and simple heat treatments. The key to this finding was that the desired microstructures can be achieved without resorting the thermomechanical processing (TMP). TMP is compulsory to producing high performance titanium alloys via tradition processing routes such as wrought processing and traditional PM, and is the source for the majority of the energy consumption and price of many titanium components. Therefore, the ability to produce titanium alloys with the properties that are necessary for critical applications without resorting to TMP has the ability to transform the titanium industry.

In this dissertation, HSPT has been shown capable of producing a range of microstructures and corresponding mechanical properties that are competitive with wrought Ti-6Al-4V. Ti-6Al-4V is by the far the most utilized titanium alloy in the industry. This is not because the alloy is specifically the best for any particular application, but that it is very versatile and can be easily engineered to meet the mechanical property demands of a wide range of applications. Therefore, the ability for HSPT to produce Ti-6Al-4V with engineered microstructures for application-tailored mechanical properties is important concerning the feasibility of the process serving as an alternative to wrought processing.

## 8.1 Energy Model

As an initial verification of the low-cost nature of HSPT, an intensive quantitative energy model was prepared by the author in the early stages of this research. The model is based on thermodynamic calculations of energy consumed during the various processing steps, as well as literature values for both the energy consumed and efficiency of typical processing equipment that would be employed in a commercialized process. From this model, it was found that HSPT is capable of producing 2” round bar stock of titanium alloys using less than half the energy required for a typical wrought process (Table 3.2).

The energy consumed in an industrial process is directly related to price. Therefore, employing a process with these energy savings could overcome the price barrier that currently limits the applications for which titanium is used. In so doing, the titanium market share would be significantly increased. Therefore, the implications for environmental impact and sustainability could be significant. Firstly, titanium components improve the efficiency and sustainability of a process when used as a replacement for steel,

due to the significant weight savings achieved by using a low-density material. Currently, the titanium industry is a comparatively small metals market, and has minimal environmental impact. However, as the cost of titanium is decreased, the market share will be significantly increased. Therefore, the positive environmental impact of employing an energy efficient production process for titanium components would become significant.

### 8.2 Powder Preparation, Compaction Behavior, and Densification

This study focused primary on the relationship between process, microstructure, and properties of Ti-6Al-4V as a function of the sintering profile and subsequent thermal treatments. However, as a powder metallurgical process, the behavior of the powder during powder preparation (i.e. hydrogenation, milling, and sieving), compaction, and densification are equally important. Therefore, these areas were also studied and the results of this investigation are detailed in CHAPTER 5. From the study, methods to both prepare the powder in order to achieve a beneficial particle size distribution and morphology were identified. Additionally, the behavior of the powder during compaction was investigated. Compaction methods that would be suitable for commercialization were identified and discussed, including cold isostatic pressing (CIP) and traditional die pressing. Finally, the densification behavior of the material during sintering was investigated for both HSPT and traditional vacuum sintering. From this study, the methods necessary for achieving fully densification (>99% relative density) while maintaining the necessary purity of the sintered material were determined and discussed.

### 8.3 Relationship Between Microstructure and Processing

The relationship between the sintering process and subsequent thermal treatments (i.e. gaseous isostatic forging, GIFT, and solution treatments and ageing, STA) to the resulting microstructure is discussed in detail in CHAPTER 6. Additionally, the mechanisms by which the various wrought-like microstructures are produced via these processes are also presented. From this study, it was found that HSPT with and without subsequent thermal treatments is capable of producing a range of wrought-like microstructures of the "globularized", bi-modal, and fully lamellar varieties. Additionally, it was determined that a range of grain sizes can be achieved for the various microstructures. For each type of microstructure, the necessary methods for producing very fine (<10 μm) globularized α grain or lamellar α colonies were discussed. Additionally, results from similar investigations using the traditional method of vacuum sintering were presented. From this study, it was determined that the wrought-like microstructure produced via these processes are unique to HSPT, as traditional vacuum sintering processing results in microstructures that are too coarse and not conducive to the necessary phase transformations and microstructure evolution. The microstructures available from heat treating HSPT Ti-6Al-4V, the processing parameters required, and the comparison of these results to those obtained from vacuum sintering are summarized in Figure 6.12.

### 8.4 Relationship Between Mechanical Properties and Microstructure

A comprehensive summary of the mechanical properties, including static and dynamic properties, microstructure, density, and purity, are given in Table 8.1. All the experimental data presented in this table were generated using the standard HSPT or vacuum sintering

profile (Figure 4.2) unless otherwise noted (i.e. HSPT samples dehydrogenated at 650 °C). In Table 8.1, the static mechanical properties of the samples produced in this study are given as a range representing the maximum and minimum values of the entire experimental population of the corresponding microstructure and processing route utilized. This method of presenting the data was chosen to give the reader an idea of the repeatability of the experiments, as well as the variability that is intrinsic to mechanical properties produced via powder metallurgy. The density and purity data are presented as averages, as the methods developed to control these values are standard to PM processing. Therefore, these properties were reproduced with excellent repeatability.

From the data presented in Table 8.1, it can be seen that a range of mechanical properties are achieved by producing the different microstructures available via the processing routes demonstrated. For convenience, the average strength and ductility that are produced by the various processing routes investigated in this dissertation are plotted in Figure 8.1. These data are grouped based on the method used to prepare the material before heat treatments. These data are grouped as HSPT-sintered Ti-6Al-4V dehydrogenated at 750 °C (standard), dehydrogenated at 650 °C, HSPT plus GIFT, vacuum-sintered, vacuum-sintered plus GIFT, and samples that have been β-annealed. As shown, the range of properties corresponding to different microstructures of a specific starting condition before heat treatment follows linear trends regarding the trade-off between strength and ductility. The most desirable points on this plot would be located towards the upper-right corner of the plot. Based on this logic, it can be seen that the HSPT plus GIFT produces the highest strength-to-ductility ratio.

The β-annealed condition was not included in any other group in Figure 8.1. As shown

in section 6.2.3.3, this heat treatment essentially undoes any of the microstructural refinement of the HSPT process before heat treatment. Therefore, these samples stand on their own regarding the resulting mechanical properties.

The fatigue performance of each condition is simplified in Table 8.1 and given as a value that corresponds to the fatigue strength at 10 million cycles ($S_{10^7}$). The $S_{10^7}$ value corresponds to the maximum stress at which the sample will survive at least 10 million cycles during cyclic loading. The fatigue data generated in this study are also given as S-N trends in Figure 8.2. The $S_{10^7}$ for each microstructure is also identified in Figure 8.2. From these data, the various microstructures follow the trend given below for fatigue strength, from highest to lowest:

Bi-modal > Globularized > HSPT (fine lamellar) >

β-annealed (moderate lamellar) > Vacuum-Sintered (coarse lamellar)

This trend is very interesting, as it follows the trend for fatigue strength of wrought Ti-6Al-4V as shown in Figure 2.17. Therefore, not only is HSPT capable of producing mechanical properties that are competitive to wrought processing, but the general trend for the fatigue performance as related to microstructure follows the same trend as wrought titanium alloys.

Table 8.1: Summary of properties of all samples produced in this study via HSPT and vacuum sintering. For reference, typical literature values[35] and the ASTM standard[96] for grade 5 wrought Ti-6Al-4V are also given.

| Process | Condition | Source | Microstructure | | | | Density | | Static Mechanical Properties | | | | | Fatigue | Interstitials | | |
|---|---|---|---|---|---|---|---|---|---|---|---|---|---|---|---|---|---|
| | | | Morphology | $\alpha_P$ Size (μm) | α Colony Width (μm) | α Lamellae Width (μm) | ρ ($g/cm^3$) | $\rho_{relative}$ (%) | UTS (MPa) | $\sigma_{y,0.2\%}$ (MPa) | %EL | %RA | E (GPa) | $S_{10^7}$ (MPa) | O (wt%) | N (wt%) | H (ppmw) |
| HSPT | As-Sintered | Experiment | Ultrafine Lamellar | – | 4 | <1 | 4.380 | 99.0% | 994-1026 | 930-976 | 13.8%-17.8% | 29.7%-33.0% | 105-119 | 500 | 0.230 | 0.015 | 3.1 |
| | As-GIFT | Experiment | Fine "Globularized" | 4 | – | – | 4.426 | 100.0% | **1022-1035** | **950-972** | **19.3%-19.5%** | **46.4%-47.1%** | **121-140** | **550** | 0.248 | 0.013 | 9.4 |
| | STA (954°C) Furnace Cooled 550°C x 6 hr | Experiment | Fine "Globularized" | 5 | – | – | 4.373 | 98.8% | 949-952 | 872-881 | 17.6%-19.2% | 32.0%-34.1% | 109-113 | – | 0.232 | 0.020 | 4.0 |
| | STA (954°C) Water Quenched 550°C x 6 hr | Experiment | Fine Bi-Modal | 4 | 4 | <1 | 4.373 | 98.8% | 1070-1076 | 981-981 | 10.7%-11.9% | 20.0%-20.5% | 108-113 | – | 0.230 | 0.020 | 15.9 |
| | GIFT + STA (954°C) Furnace Cooled 550°C x 6 hr | Experiment | Fine "Globularized" | 5 | – | – | 4.426 | 100.0% | **993-999** | **923-930** | **21.0%-22.3%** | **45.2%-47.6%** | **115-124** | **550** | 0.246 | 0.015 | 9.1 |
| | GIFT + STA (954°C) Water Quenched 550°C x 6 hr | Experiment | Fine Bi-Modal | 4 | 4 | <1 | 4.426 | 100.0% | **1058-1093** | **984-1004** | **13.1%-16.2%** | **28.4%-34.5%** | **109-120** | **600** | 0.254 | 0.015 | 21.2 |
| | GIFT + β-annealed (1050°C) Air Cooled 550°C x 6 hr | Experiment | Lamellar | – | 30 | 2 | 4.426 | 100.0% | 999-1015 | 902-920 | 15.7%-15.7% | 25.4%-26.0% | 115-124 | 300 | 0.254 | 0.012 | 21.7 |
| | As-Sintered Dehydrogenated at 650°C | Experiment | Ultrafine Acicular | – | – | <1 | 4.380 | 99.0% | 1097-1099 | 1030-1034 | 11.4%-11.5% | 22.8%-23.1% | 107-110 | – | 0.230 | 0.015 | 2.4 |
| | Dehydrogenated at 650°C STA (954 °C) Furnace Cooled 500 °C x 6 hr | Experiment | Fine Elongated α | 4 | – | – | 4.380 | 99.0% | 983-985 | 915-919 | 15.1%-15.3% | 31.3%-31.7% | 115-117 | – | 0.230 | 0.015 | 3.1 |

Table 8.1: continued

| Process | Condition | Source | Microstructure | | | | Density | | Static Mechanical Properties | | | | | Fatigue | Interstitials | | |
|---|---|---|---|---|---|---|---|---|---|---|---|---|---|---|---|---|---|
| | | | Morphology | $\alpha_P$ Size (μm) | α Colony Width (μm) | α Lamellae Width (μm) | ρ ($g/cm^3$) | $\rho_{relative}$ (%) | UTS (MPa) | $\sigma_{y,0.2\%}$ (MPa) | %EL | %RA | E (GPa) | $S_{10^7}$ (MPa) | O (wt%) | N (wt%) | H (ppmw) |
| HSPT | Dehydrogenated at 650°C STA (954 °C) Water Quenched 500 °C x 6 hr | Experiment | Fine Bi-Modal | 4 | 4 | <1 | 4.380 | 99.0% | 1106-1109 | 1031-1036 | 10.9%-11.3% | 22.5%-22.7% | 113-115 | – | 0.237 | 0.012 | 8.6 |
| Vacuum Sintering | As-Sintered | Experiment | Coarse Lamellar | – | 100 | 10 | 4.395 | 99.3% | 899-906 | 796-807 | 17.1%-18.8% | 31.0%-33.0% | 112-115 | 300 | 0.238 | 0.019 | 4.4 |
| | As-GIFT | Experiment | Coarse Lamellar | – | 100 | 10 | 4.426 | 100.0% | 937-943 | 834-846 | 16.2%-16.8% | 30.2%-34.0% | 116-117 | 300 | 0.252 | 0.015 | 11.1 |
| Wrought | α + β Forged and Recyrs-tallization Annealed (RA) | Literature | Fine Equiaxed | <10 | – | – | 4.425 | 100.0% | 876 | 711 | 12.4% | 36.0% | – | – | – | – | – |
| | α + β Forged and Solution Treated and Aged (STA) | Literature | Fine Equiaxed | <10 | – | – | 4.425 | 100.0% | 938 | 876 | 15.2% | 34.0% | – | – | – | – | – |
| | α + β Forged and Duplex Annealed | Literature | Fine Bi-Modal | <10 | <10 | <1 | 4.425 | 100.0% | 911 | 856 | 15.3% | 47.0% | – | – | – | – | – |
| ASTM B348 | Grade 5 Ti-6Al-4V | Standard | – | – | – | – | – | – | 895 min. | 828 min. | 10 min. | 25 min. | – | – | 0.200 max. | 0.050 max. | 150 max. |

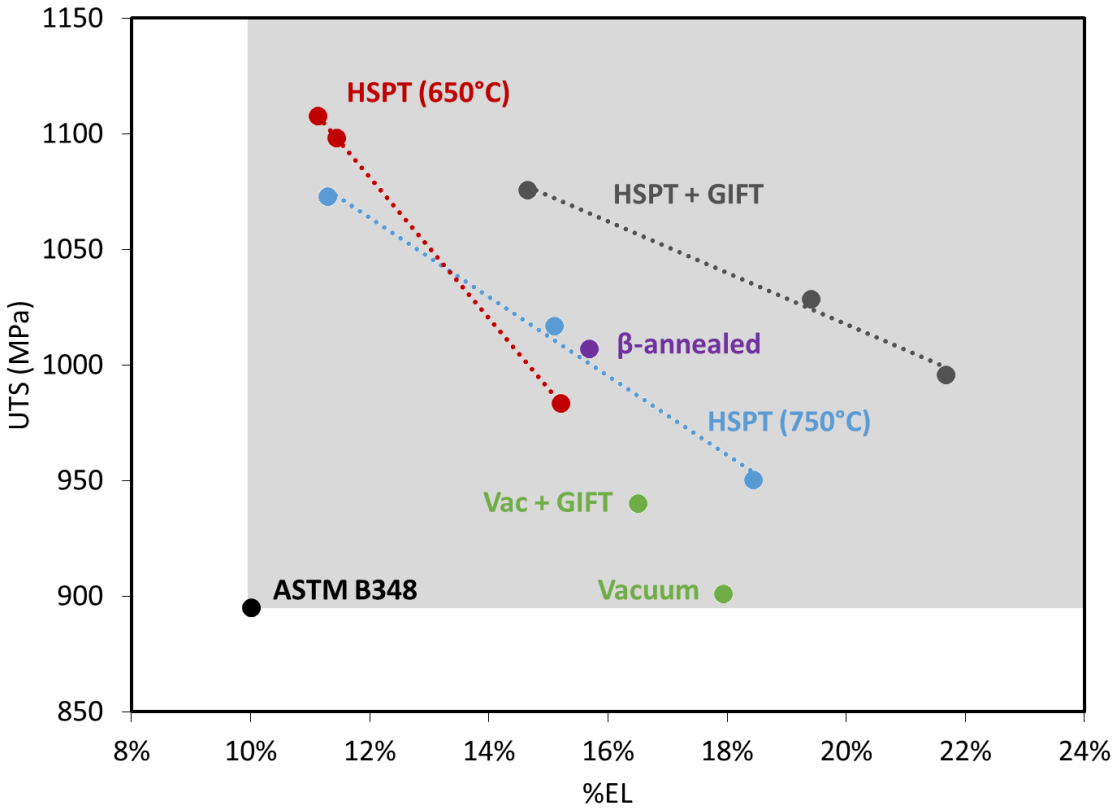


Figure 8.1: Average values of UTS versus %EL for all conditions discussed in this study.

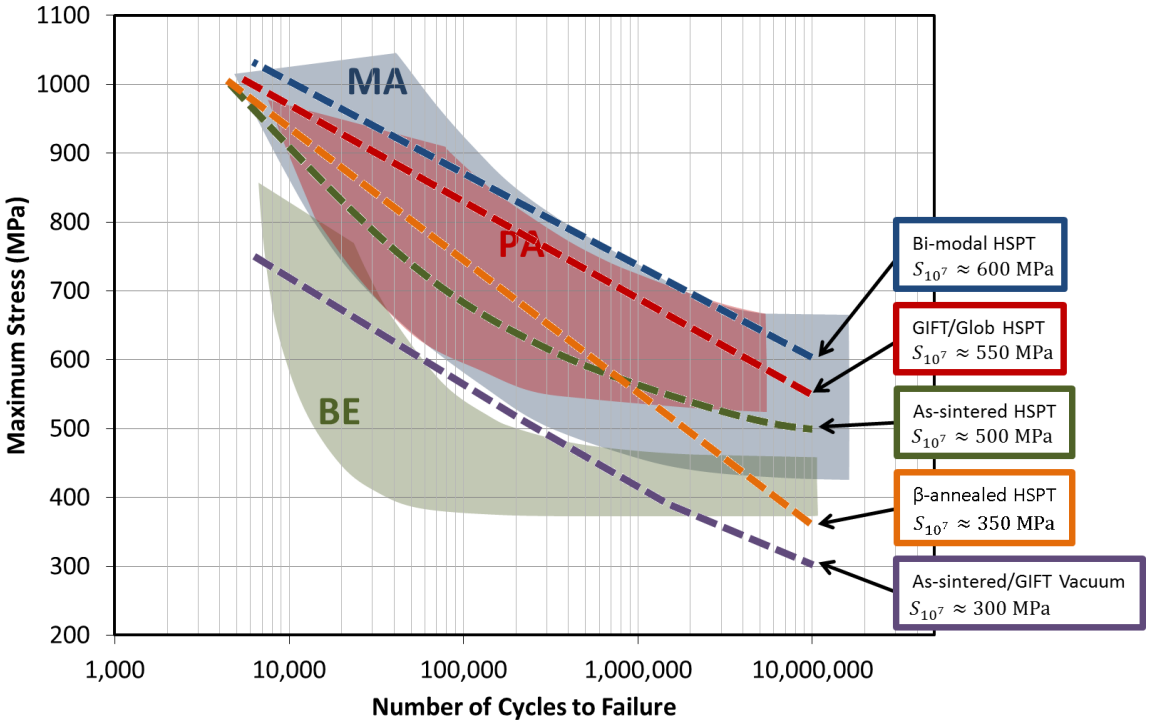


Figure 8.2: S-N plot showing general trends for Ti-6Al-4V produced in this study with various processes of vacuum sintering, HSPT, GIFT, and heat treatments. For reference, these data are overlaid on the fatigue life scatter-bands (prepared from data in the ASM Handbooks[23]) for Ti-6Al-4V produced via wrought processing with a mill-annealed microstructure (MA), pre-alloyed powder metallurgy (PA), and blended elemental powder metallurgy (BE).

# CHAPTER 9

## FUTURE WORK

The author would like to recommend the following future work:

(1) A common feature in the microstructures presented in this dissertation is coarse grain boundary α (G.B. α). G.B. α has been shown to have deleterious effects on mechanical properties, and was identified as the source of crack initiation in the globularized microstructure in section 7.2.3.1. It was shown that G.B. α forms primarily during dehydrogenation, and that G.B. α can be minimized by dehydrogenating at a lower temperature. However, these experiments also sacrificed ductility. Therefore, further investigation is required to determine a method to eliminate G.B α while maintaining ductility.

(2) In this study, the fatigue performance of various microstructures produced via heat treatments of HSPT Ti-6Al-4V was determined. However, all the heat-treated fatigue bars were first subjected to GIFT in order to close the porosity and enable the study to focus on the effect of the grain structure alone on fatigue performance. Therefore, a useful addition to this research would be to study the effect of heat treatments without GIFT.

(3) For the sake of workload and time, specific high priority heat treatments and microstructures were identified for this study. However, there are countless

modifications to the heat treatments used in this study that would further the process-structure-property understanding of Ti-6Al-4V including:

a. β-annealing with oil and water quenching to produce finer fully lamellar structures than those prepared in this study
b. Solution treatment and ageing with oil quenching and air cooling to produce a bi-modal structure with coarser lamellar regions than those prepared in this study

(4) The HSPT sintering profile used in this study was established as a best practice and control for heat treatment experiments. However, further research is warranted to understand the process-structure-property relationship as a function of the HSPT sintering parameters, including:

a. Dehydrogenation temperature
b. Phase transformation temperature
c. Cooling rate form sintering temperature to phase transformation temperature

(5) The overall processes discussed in this dissertation could be simplified by combining processing steps, such as

a. Using a higher dehydrogenation temperature to simultaneously heat treat the microstructure during dehydrogenation to produce a globularized or bi-modal microstructure
b. Applying pressure during dehydrogenation to achieve GIFT simultaneously

## REFERENCES


1 Paramore, J. D.; Fang, Z. Z.; Sun, P. In *Titanium Powder Metallurgy*; Qian, M., Froes, F. H. (Sam), Eds.; Butterworth-Heinemann: Oxford, 2015; pp 163–182.

2 Paramore, J. D.; Fang, Z. Z.; Sun, P.; Koopman, M.; Chandran, K. S. R.; Dunstan, M. *Scr. Mater.* **2015**, *107*, 103–106.

3 Paramore, J. D.; Sun, P.; Dunstan, M.; Fang, Z. Z.; Koopman, M.; Yang, L. In *The 13th World Conference on Titanium*; TMS: San Diego, CA, 2015.

4 Sun, P.; Fang, Z. Z.; Koopman, M.; Xia, Y.; Paramore, J.; Ravi Chandran, K. S.; Ren, Y.; Lu, J. *Metall. Mater. Trans. A* **2015**, *September* .

5 Sun, P.; Fang, Z. Z.; Koopman, M.; Paramore, J.; Chandran, K. S. R.; Yang, R.; Lu, J. *Acta Mater.* **2015**, *84*, 29–41.

6 Sun, P. Powder Metallurgy Titanium by the Hydrogen Sintering and Phase Transformation (HSPT) Process. Ph.D. Dissertation, University of Utah, 2015.

7 Yang, L. Effect of Particle Size on Oxygen Content and Porosity of Sintered Ti-6Al-4V. M.S. Thesis, University of Utah, 2015.

8 Fang, Z. Z.; Sun, P.; Paramore, J.; Wang, H.; Koopman, M.; Yang, L. Powder Metallurgy Methods for the Production of Fine and Ultrafine Grain Ti and Ti Alloys. U.S. Patent Appl. 14/152,787, 2014.

9 Dunstan, M.; Paramore, J.; Koopman, M.; Fang, Z. Z. *Adv. Powder Metall. Part. Mater.* **2014**, *2014*.

10 Paramore, J.; Sun, P.; Fang, Z. Z.; Koopman, M.; Dunstan, M. In *25th Advanced Aerospace Materials and Processes (AeroMat) Conference and Exposition*; ASM International: Orlando, FL, 2014.

11 Paramore, J.; Sun, P.; Fang, Z. Z.; Koopman, M. In *Materials Science & Technology Conference and Exhibition 2013 (MS&T'13)*; TMS, ASM: Montreal, Quebec, Canada, 2013.

12 Paramore, J.; Sun, P.; Fang, Z. Z.; Koopman, M. In *TITANIUM 2013: 29th Annual Conference and Exhibition*; ITA: Las Vegas, NV, 2013.

13 Sun, P.; Fang, Z. Z.; Koopman, M. *Adv. Eng. Mater.* **2013**, *15* (10), 1007–1013.

14 Fang, Z. Z.; Sun, P. *Key Eng. Mater.* **2012**, *520*, 15–23.

15 Fang, Z. Z.; Sun, P.; Wang, H. *Adv. Eng. Mater.* **2012**, *14* (6), 383–387.

16 Sachdev, A. K.; Kulkarni, K.; Fang, Z. Z.; Yang, R.; Girshov, V. *JOM* **2012**, *64* (5), 553–565.

17 Wang, H.; Lefler, M.; Fang, Z. Z.; Lei, T.; Fang, S.; Zhang, J.; Zhao, Q. *Key Eng. Mater.* **2010**, *436*, 157–163.

18 Ivasishin, O. M.; Anokhin, V. M.; Demidik, A. N.; Savvakin, D. G. *Key Eng. Mater.* **2000**, *188*, 55–62.

19 Ivasishin, O. M.; Savvakin, D. G.; Moxson, V. S.; Bondareva, K. A.; Froes, F. H. (Sam). *Mater. Technol.* **2002**, *17* (1), 20–25.

20 Ivasishin, O. M.; Savvakin, D. G.; Moxson, V. S.; Duz, V. A.; Davies, R. In *TMS-2005 134th Annual Meeting & Exhibition*; San Francisco, CA, 2005.

21 Duz, V. A.; Ivasishin, O. M.; Lavender, C.; Moxson, V. S.; Telin, V. V. In *Titanium 2008 24th Annual ITA Conference & Exhibition*; Las Vegas, NV, 2008.

22 Savvakin, D. H.; Humenyak, M. M.; Matviichuk, M. V.; Molyar, O. H. *Mater. Sci.* **2012**, *47* (5), 651–661.

23 Eylon, D.; Froes, F. H. (Sam); Abkowitz, S. In *ASM Handbook, Volume 7: Powder Metal Technologies and Applications*; ASM, 1998; Vol. 7, pp 874–886.

24 Froes, F. H. (Sam); Eylon, D. *Int. Mater. Rev.* **1990**, *35* (3), 162–182.

25 Wang, H.; Fang, Z. Z.; Sun, P. *Int. J. Powder Metall.* **2010**, *46* (5), 45–57.

26 Heaney, D. F.; German, R. M. In *Powder Metallurgy World Congress and Exhibition (PM2004)*; Vienna, Austria, 2004.

27 German, R. M. *Powder Metallurgy Science*; MPIF: Princeton, New Jersey, 1994.

28 Ellingham, H. J. T. *J. Soc. Chem. Ind.* **1944**, *63* (5), 125–133.

29 Froes, F. H.; Imam, M. A. *Key Eng. Mater.* **2010**, *436*, 1–11.

30 Froes, F. H. (Sam). *JOM* **2004**, *56* (2), 39–39.

31 Froes, F. H. *JOM* **1998**, *50* (9), 15–15.

32 Froes, F. H. S.; Gungor, M. N.; Imam, M. A. *JOM* **2007**, *59* (6), 28–31.

33 Froes, F. H.; Friedrich, H.; Kiese, J.; Bergoint, D. *JOM* **2004**, *56* (2), 40–44.

34 Lütjering, G.; Williams, J. C. *Titanium*, 2nd ed.; Springer: Berlin Heidelberg New York, 2007.

35 Boyer, R.; Welsch, G.; Collings, E. W. *Materials Properties Handbook - Titanium Alloys*; ASM International, 1994.

36 Leyens, C.; Peters, M. *Titanium and Titanium Alloys: Fundamentals and Applications*; John Wiley & Sons: Weinheim, 2003.

37 Donachie, M. J. *Titanium: A Technical Guide*; ASM International: Materials Park, OH, 2000.

38 Okamoto, H. In *ASM Handbook Volume 3: Alloy Phase Diagrams*; ASM, 1992; p 2.238.

39 McCracken, C. G.; Motchenbacher, C.; Barbis, D. P. *Int. J. Powder Metall.* **2010**, *46* (5), 19–26.

40 Ivasishin, O. M.; Savvakin, D. G.; Gumenyak, M. M.; Bondarchuk, O. B. *Key Eng. Mater.* **2012**, *520*, 121–132.

41 Duz, V. A.; Ivasishin, O. M.; Moxson, V. S.; Savvakin, D. G.; Telin, V. V. Cost-Effective Titanium Alloy Powder Compositions and Method for Manufacturing Flat or Shaped Articles from These Powders. U.S. Patent 7,993,577, 2011.

42 Robertson, I. M.; Schaffer, G. B. *Powder Metall.* **2010**, *53* (1), 12–19.

43 Ivasishin, O. M.; Savvakin, D. G.; Froes, F.; Mokson, V. C.; Bondareva, K. A. *Powder Metall. Met. Ceram.* **2002**, *41* (7-8), 382–390.

44 Gregory, E. Fabrication of Niobium Superconductor Alloys. U.S. Patent 3,472,705, 1969.

45 Greenspan, J.; Rizzitano, F.; Scala, E. *Metal Matrix Composites by Decomposition Sintering of Titanium Hydride.*; Army Materials and Mechanics Research Center: Watertown, MA, 1970.

46 Greenspan, J.; Rizzitano, F.; Scala, E. In *Titanium, Science and Technology: Proceedings of the Second International Conference*; 1973; pp 365–379.

47 Obara, K.; Nishino, Y.; Matsumoto, S. Process for Producing a Sintered Article of a Titanium Alloy. U.S. Patent 3,950,166, 1976.

48 Yolton, C. F.; Froes, F. H. Method for Producing Powder Metallurgy Articles. U.S. Patent 4,219,357, 1980.

49 Pankevich, A. P.; Chertovich, A. F.; Libenson, G. A. *Sov. Powder Metall. Met. Ceram.* **1986**, *25* (2), 89–92.

50 Li, Y.; Chou, X. M.; Yu, L. *Powder Metall.* **2006**, *49* (3), 236–239.

51 Taddei, E.; Henriques, V. *Mater. Sci. Forum* **2006**, *530-531*, 341–346.

52 Carreño-Morelli, E.; Krstev, W. *Euro PM2009 Proc.* **2009**, *2* (4298), 1–6.

53 Robertson, I. M.; Schaffer, G. B. *Powder Metall.* **2010**, *53* (1), 27–33.

54 Zhang, J. M.; Yi, J. H.; Gan, G. Y.; Yan, J. K.; Du, J. H.; Liu, Y. C. *Adv. Mater. Res.* **2013**, *616*, 1823–1829.

55 Dunlop, J.; Rensing, H. Method for Making Tungsten-Titanium Sputtering Targets and Product. U.S. Patent 4,838,935, 1989.

56 Gladden, T. Process for the Manufacture by Sintering of a Titanium Part and a Decorative Article Made Using a Process of This Type. U.S. Patent 5,441,695, 1995.

57 Bertheville, B.; Neudenberger, M.; Bidaux, J.-E. *Mater. Sci. Eng. A* **2004**, *384* (1-2), 143–150.

58 Ivasishin, O. M.; Bondareva, K. A.; Bondarchuk, V. I.; Gerasimchuk, O. N.; Savvakin, D. G.; Gryaznov, B. A. *Strength Mater.* **2004**, *36* (4), 225–230.

59 Ivasishin, O. M.; Savvakin, D. G.; Bielov, I. S.; Moxson, V. S.; Duz, V. A.; Davies, R.; Lavender, C. *Mater. Sci. Technol. 2005 Proc.* **2005**, 151–158.

60 Ivasishin, O. M.; Eylon, D.; Bondarchuk, V. I.; Savvakin, D. G. *Defect Diffus. Forum* **2008**, *277*, 177–185.

61 Ivasishin, O. M.; Savvakin, D. G. *Key Eng. Mater.* **2010**, *436*, 113–121.

62 Klevtsov, A.; Nikishin, A.; Shuvalov, J. Continuous and Semi-Continuous Process of Manufacturing Titanium Hydride Using Titanium Chlorides of Different Valency. U.S. Patent 8,388,727, 2013.

63 Kasparov, S.; Klevtsov, A.; Cheprasov, A.; Moxson, V.; Duz, V. Semi-Continuous Magnesium-Hydrogen Reduction Process for Manufacturing of Hydrogenated, Purified Titanium Powder. U.S. Patent 8,007,562, 2011.

64 Moxson, V.; Ivanov, E. Method for Manufacturing Fully Dense Metal Sheets and Layered Composites from Reactive Alloy Powders. U.S. Patent 7,566,415, 2009.

65 Moxson, V.; Duz, V. Process of Direct Powder Rolling of Blended Titanium Alloys, Titanium Matrix Composites, and Titanium Aluminides. U.S. Patent 7,311,873, 2007.

66 Drozdenko, V.; Petrunko, A.; Adreev, A.; Yatsenko, O.; Ivasishin, O.; Savvakin, D.; Moxson, V.; Froes, F. Manufacture of Cost-Effective Titanium Powder from Magnesium Reduced Sponge. U.S. Patent 6,638,336, 2003.

67 Zwicker, U.; Schleicher, H. W. Process for Improving the Workability of Titanium Alloys. U.S. Patent 2,892,742, 1959.

68 Kerr, W. R.; Smith, P. R.; Rosenblum, M. E.; Gurney, F. J.; Mahajan, Y. R.; Bidwell, L. R. In *Titanium '80, Science and Technology; Proceedings of the Fourth International Conference on Titanium*; Kyoto, Japan, 1980; pp 2477–2486.

69 Kerr, W. *Metall. Trans. A* **1985**, *16A*, 1077–1087.

70 Kao, W. H.; Eylon, D.; Yolton, C. F.; Froes, F. H. *Prog. Powder Metall. 1981*. **1981**, *37*, 289–301.

71 Smickley, R.; Dardi, L. Microstructural Refinement of Cast Titanium. U.S. Patent 4,505,764, 1985.

72 Kohn, D.; Ducheyne, P. *J. Mater. Sci.* **1991**, *26*, 534–544.

73 Kohn, D.; Ducheyne, P. *J. Mater. Sci.* **1991**, *26*, 328–334.

74 Zhang, C.; Bian, W.; Lai, Z.; Gong, B. *Acta Metall. Sin.* **1992**, *5* (5), 362–368.

75 Ilyn, A. A.; Kolachev, B. A.; Mamonov, A. M. In *Titanium '92, Science and Technology; Proceedings*; 1992.

76 Gong, B.; Mitsuo, N.; Kobayashi, T.; Yukitoshi, O. *J. Japan Inst. Light Met.* **1992**, *42*, 638–643.

77 Yang, K.; Guo, Z.; Edmonds, D. *Scr. Metall. Mater.* **1992**, *27* (c), 1695–1700.

78 Yoshimura, H.; Kimura, K.; Hayashi, M.; Ishii, M.; Hanamura, T.; Takamura, J. *Mater. Trans.* **1994**, *35* (4), 266–272.

79 Niinomi, M.; Gong, B.; Kobayashi, T. *Metall. Mater. Trans. A* **1995**, *26A* (May), 1141–1151.

80 Zhang, Y.; Zhang, S. Q. *Int. J. Hydrogen Energy* **1997**, *22* (2/3), 161–168.

81 Yoshimura, H. *Int. J. Hydrogen Energy* **1997**, *22* (213), 145–150.

82 Fang, T.; Wang, W. *Mater. Chem. Phys.* **1998**, *56* (98), 35–47.

83 Qazi, J. I.; Senkov, O. N.; Rahim, J.; Genc, A.; Froes, F. H. (Sam). *Metall. Mater. Trans. A* **2001**, *32A* (October), 2453–2463.

84 Qazi, J. Thermohydrogen Processing (THP) of Ti-6Al-4V and TiAl Alloys. Ph.D. Dissertation, University of Idaho, 2002.

85 Qazi, J. I.; Senkov, O. N.; Rahim, J.; (Sam) Froes, F. H. *Mater. Sci. Eng. A* **2003**, *A359* (1-2), 137–149.

86 Yu, C.; Shen, C.; Perng, T. *Scr. Mater.* **2006**, *55*, 1023–1026.

87 Il'in, A. A.; Skvortsova, S. V.; Mamonov, A. M. *Mater. Sci.* **2008**, *44* (3), 336–341.

88 Sun, Z.; Zhou, W.; Hou, H. *Int. J. Hydrogen Energy* **2009**, *34* (4), 1971–1976.

89 Zhu, T.; Li, M. *J. Alloys Compd.* **2009**, *481* (1-2), 480–485.

90 Ilyin, A. A.; Polkin, I. S.; Manonov, A. M.; Nosov, V. K. In *Titanium '95: Science and Technology: Proceedings of the Eighth World Conference on Titanium*; Birmingham, UK, 1995; pp 2462–2469.

91 Guitar, A.; Vigna, G.; Luppo, M. I. *J. Mech. Behav. Biomed. Mater.* **2009**, *2* (2), 156–163.

92 Froes, F. H.; Senkov, O. N.; Qazi, J. I. *Int. Mater. Rev.* **2004**, *49* (3-4), 227–245.

93 Wang, W.-E. *J. Alloys Compd.* **1996**, *238* (1-2), 6–12.

94 Stickels, C. In *ASM Handbook, Volume 4: Heat Treating*; ASM, 1991; Vol. 4, pp 312–324.

95 Shen, C. C.; Perng, T.-P. *Acta Mater.* **2007**, *55* (3), 1053–1058.

96 ASTM. *B348-10: Standard Specification for Titanium and Titanium Alloy Bars and Billets*; ASTM: West Conshohocken, PA, 2010.

97 Lütjering, G. *Mater. Sci. Eng. A* **1998**, *243*, 32–45.

98 Porter, D. A.; Easterling, K. E.; Sherif, M. *Phase Transformations in Metals and Alloys, Third Edition (Revised Reprint)*; CRC Press, 2009.

99 Peters, M.; Lütjering, G.; Ziegler, G. *Zeitschrift fuer Met.* **1983**, *74* (5), 274–282.

100 Peters, M.; Lütjering, G. In *Titanium '80, Science and Technology; Proceedings of the Fourth International Conference on Titanium*; AIME: Warrendale, 1980; p 925.

101 Callister Jr., W. D.; Rethwisch, D. G. *Materials Science and Engineering: An Introduction*, 8th ed.; Wiley: New York, 2009.

102 Dieter, G. E.; Bacon, D. *Mechanical Metallurgy*; McGraw-Hill, 1988.

103 Kanninen, M. F.; Popelar, C. H. *Advanced Fracture Mechanics*; Oxford University Press, 1985.

104 Norgate, T. E.; Wellwood, G. *JOM* **2006**, *58* (9), 58–63.

105 Kirchain, R.; Roth, R.; Camanoe Associates. *Report : The Role of Titanium in the Automobile*; Northwest Alliance for Transportation Technology: Cambridge, MA, 2002.

106 Faller, K.; Froes, F. H. (Sam). *JOM* **2001**, *53* (4), 27–28.

107 Kraft, E. H. *Summary of Emerging Titanium Cost Reduction Technologies*; EHK Technologies for DOE/ORNL: Vancouver, WA, 2003.

108 Froes, F. H. S. *Powder Metall. Met. Ceram.* **2007**, *46* (5-6), 303–310.

109 TOHO Titanium Co. Titanium Metals - Titanium Sponge http://www.toho-titanium.co.jp/en/products/sponge_en.html (accessed Apr 24, 2015).

110 Zhao, J.; Ding, H.; Tian, X.; Zhao, W.; Hou, H. *Chinese J. Chem. Phys.* **2008**, *21* (6), 569–574.

111 Nozaki, T.; Muto, N.; Kado, S.; Okazaki, K. *Am. Chem. Soc. Div. Fuel Chem.* **2004**, *49* (1), 179–180.

112 Wills, B. A.; Napier-Munn, T. J. *Wills' Mineral Processing Technology*; Butterworth-Heinemann: Oxford, 2006.

113 Haffez, G. S. A. *J. Eng. Sci. Assiut Univ.* **2012**, *40* (1), 271–280.

114 Setoyama, D.; Matsunaga, J.; Muta, H.; Uno, M.; Yamanaka, S. *J. Alloys Compd.* **2004**, *381* (1-2), 215–220.

115 Akers, A.; Gassman, M. *Hydraulic Power Systems Analysis*; Taylor and Francis: New York, 2006.

116 Raffeinner, T. J.; Feldbauer, S. L. *Budgetary Proposal #122926: Continuous Belt Sintering Furnace Quote*; Abbott Furnace Co. for University of Utah, 2015.

117 Chase Jr., M. W. *NIST-JANAF Thermochemical Tables*; American Chemical Society: Woodbury, NY, 1998.

118 Nandi, H. K.; Thomason, M. C.; Delhunty, M. R. *Heat Treat. Prog.* **2002**, *2* (8), 17–21.

119 *CRC Handbook of Chemistry and Physics*, 96th ed.; Haynes, W. M., Ed.; CRC Press: Boca Raton, FL, 2015.

120 Weir, G.; Muneer, T. *Energy Convers. Manag.* **1998**, *39* (3-4), 243–256.

121 Refractory Specialties Inc. Technical Data Sheet: Gemcolite® FG23-101, FG23-112 http://www.rsifibre.com/technical-data-sheets/Gemcolite-FG23-101-tech-sheet.pdf (accessed Jul 1, 2015).

122 Mueller-Aue, H. J. *J. Vac. Sci. Technol.* **1971**, *8* (6), VM19–VM23.

123 TIMET. Ingot http://www.timet.com/products/ingot (accessed Jan 2, 2015).

124 Semiatin, S. L. *ASM Handbook, Volume 14A - Metalworking: Bulk Forming*; ASM International: Materials Park, OH, 2010.

125 Thekdi, A. C. In *Forging Industry Energy Workshop*; Canton, OH, 2010.

126 U.S. Energy Information Administration. *Annual Energy Review: 2013*; U.S. Department of Energy: Washington, DC, 2013.

127 Moxson, V. S.; Qazi, J.; Patankar, S. N.; Senkov, O. N.; Froes, F. H. *Key Eng. Mater.* **2002**, *230-232*, 339–343.

128 Linseis Inc. Dilatometer - L76 - L75 Horizontal - L75 Vertical http://www.linseis.com/fileadmin/_migrated/content_uploads/Dilatometer_L76_L75H_L75V_Brochure_.pdf (accessed Apr 2, 2015).

129 Pfeiffer Vacuum GmbH. HiCube Eco http://www.pfeiffer-vacuum.com/productPdfs/PMS03550.en.pdf (accessed Mar 2, 2015).

130 Hodge, E. S.; Tavenner, R. F. Method for Pneumatic Isostatic Processing of a Workpiece. U.S. Patent 5,816,090, 1998.

131 Struers A/S. LectroPol-5 http://www.struers.com/resources/elements/12/287650/LectroPol-5 14937001.pdf (accessed Apr 3, 2015).

132 Westmoreland Testing and Research Inc. Accreditations http://www.wmtr.com/en.accreditations.html (accessed Jun 17, 2015).

133 ASTM. *E8/E8M-11: Standard Test Methods for Tension Testing of Metallic Materials*; ASTM: West Conshohocken, PA, 2011.

134 MTS Systems Corporation. MTS Landmark Testing Solutions http://www.mts.com/ucm/groups/public/documents/library/dev_004324.pdf (accessed May 30, 2015).

135 Ritchie, R. O. *Int. J. Fract.* **1999**, *100*, 55–83.

136 Nalla, R. K.; Boyce, B. L.; Campbell, J. P.; Peters, J. O.; Ritchie, R. O. *Metall. Mater. Trans. A* **2002**, *33* (13), 899–918.